TECHNISCHE UNIVERSITÄT MÜNCHEN

Physik-Department
Lehrstuhl für Experimentalphysik IV

Dynamics at the Onset of Self-Diffusion in Molecular Liquids

Humphrey Morhenn

Vollständiger Abdruck der von der Fakultät für Physik der Technischen Universität München zur Erlangung des akademischen Grades eines

Doktors der Naturwissenschaften (Dr. rer. nat.)

genehmigten Dissertation.

Vorsitzender:		Univ.-Prof. Dr. Martin Zacharias
Prüfer der Dissertation:	1.	Univ.-Prof. Dr. Winfried Petry
	2.	Univ.-Prof. Dr. Tobias Unruh (Friedrich-Alexander-Universität Erlangen-Nürnberg)

Diese Dissertation wurde am 21. Oktober 2013 bei der Technischen Universität München eingereicht und durch die Fakultät für Physik am 16. Dezember 2013 angenommen.

Contents

Summary

Molecular self-diffusion is the result of different molecular dynamics. These include both inter- and intramolecular motions, which take place on a large range of length and time scales. It is most likely that these motions are not independent of each other and can partially occur on the same time and length scale with similar activation energies. It is hence quite challenging to describe the resulting transport mechanism in molecular liquids.

The dynamics of unentangled, linear molecules were studied on the pico- to nanosecond time scale to identify the prevailing dynamics leading to molecular self-diffusion. In this context neutron scattering experiments and computer simulations were performed to obtain a comprehensive picture. The neutron scattering data proved to be eminently suitable to validate and improve the simulation procedure, while the computational power available nowadays allows for the modeling of large ensembles, making among others the formation and evaluation of correlated motions in large volumes possible.

Quasielastic neutron scattering experiments were conducted at the time-of-flight spectrometer TOFTOF at the Heinz Maier-Leibnitz Zentrum. By changing temperature, observation time, and molecular weight of the sample molecules, different motions were characterized. They could be attributed to local and global dynamics at the crossover to self-diffusion. The experimentally measured spectra could be reproduced with great accuracy by complementary state-of-the-art molecular dynamics (MD) simulations. The study of local bond reorientations reveals distinct relaxation processes.

The molecular dynamics in n-alkane melts are mainly due to local bond rotations and a rotational motion of the entire chains. The characteristic relaxation times of these processes separate when longer alkane chains are studied, revealing a third clear relaxation process occurring on intermediate time scales. By constructing special correlation functions the respective dynamics could be characterized as a result of intermolecular flow-like collective motions of many atoms in large clusters. The

characteristic time scale of these motions is associated with the breakdown of the Rouse theory, which fails to model the chain dynamics on time scales where these flow-like motions are dominant. This observation disproves the concept of total hydrodynamic screening in polymer melts, as stated by de Gennes. Moreover, first comparisons show a great agreement of the present dynamics with the findings of a recent theory accounting for viscoelastic and hydrodynamic interactions to model the subdiffusive behavior of the molecular dynamics.

Zusammenfassung

Molekulare Selbstdiffusion resultiert aus dem Zusammenspiel verschiedener inter- und intramolekularer Bewegungen, die auf weiten Längen- und Zeitskalen stattfinden. Es ist davon auszugehen, dass diese Bewegungen nicht unabhängig voneinander stattfinden und die entsprechenden dynamischen Relaxationen teilweise durch ähnliche Relaxationszeiten und Aktivierungsenergien gekennzeichnet sind. Dementsprechend ist die Beschreibung des Transportmechanismuses in molekularen Flüssigkeiten eine große Herausforderung.

Um den Übergang zu molekularer Selbstdiffusion zu beschreiben, wurde die Dynamik linearer, nicht verschlaufter Moleküle auf einer Zeitskala im Piko- bis Nanosekundenbereich untersucht. Hierfür wurden umfassende Neutronenstreuexperimente und Computersimulationen durchgeführt. Dabei konnten anhand der Neutronenstreudaten die Simulationen mit hoher Genauigkeit validiert und verfeinert werden. Daneben erlaubt es die heute verfügbare Rechenleistung große Ensembles zu simulieren.

Quasielastische Neutronenstreuung wurde am Flugzeitspektrometer TOFTOF des Heinz Maier-Leibnitz Zentrums durchgeführt. Durch Variation der Temperatur, der Beobachtungszeit und des Molekulargewichts der Probenmoleküle konnten unterschiedliche Bewegungen ausgemacht und als lokale und globale Bewegungen am Übergang zur molekularen Selbstdiffusion charakterisiert werden. Zusätzlich wurden ausführliche molekülдynamische (MD) Simulationen durchgeführt. Dabei konnten die mit Neutronenstreuung gemessenen Spektren hervorragend durch die Simulationen reproduziert werden. Durch die Auswertung der Reorientierungen einzelner Bindungen konnten eindeutige Relaxationsprozesse analysiert werden.

In Schmelzen aus n-Alkanen finden hauptsächlich Bewegungen der Diederwinkel statt, die von einer Rotation des gesamten Moleküls begleitet werden. Die Relaxationszeiten der beiden Prozesse trennen sich deutlich, wenn längere Alkanketten betrachtet werden. Dabei kann eine weitere Relaxation auf einer intermediären Zeitskala beobachtet werden, die mittels einer speziellen Korrelationsfunktion als

Zusammenfassung

Folge einer intermolekularen flussartigen Strömung vieler Atome beschrieben werden kann. Diese Beobachtung kann direkt mit dem Scheitern des Rouse-Modells verbunden werden. Die Vorhersagen des Rouse-Modells entsprechen erst wieder für längeren Zeiten der beobachteten Kettendynamik, lange nachdem diese kollektiven Flüsse nachgelassen haben. Dies widerlegt das Konzept der hydrodynamischen Abschirmung, welches von de Gennes für Polymerschmelzen abgeleitet wurde. Weiterhin unterstützen die Ergebnisse die Vorhersagen eines jüngeren Ansatzes, in welchem explizit viskoelastische und hydrodynamische Wechselwirkungen berücksichtigt werden um die anomale subdiffusive Molekül̈dynamik zu beschreiben.

1 Introduction

It is easy to imagine that all observed motions in molecular liquids depend on the time scale on which the motions are detected. On very short times the single atoms move ballistically until they feel the chemical bonds. Eventually, on a much longer time scale, the whole molecules are self-diffusing through the melt. Now the fast, local motions, which dominate the short-time dynamics, are hardly distinguishable, as the atomic motion is mainly governed by the translation of the molecules. However, it is the local dynamics which eventually result in the global dynamics of the molecules. The knowledge about these short-time motions is essential for understanding the mechanism of molecular self-diffusion. Its description is quite complex due to the interplay of several inter- and intramolecular processes. In order to understand the onset of molecular self-diffusion, atomic motions must be studied on short length and time scales.

In this thesis the dynamics of rather simple systems are studied: Melts of n-alkanes and poly(ethylene oxide) (PEO). Alkanes are the basic component of biological molecules, and PEO is also used in pharmaceutical industry. Understanding the dynamics in these systems is relevant among others for the design of novel drug delivery systems, where drug molecules (which are typically not water soluble) are incorporated in e. g. a lipid emulsion [1–3]. In this context the knowledge about the dynamics causing translational motion of the molecules is essential to control the release of the drug molecules from the carrier.

The results presented in the framework of this thesis are mainly obtained utilizing two methods: Time-of-flight (TOF) quasielastic neutron scattering (QENS) experiments and molecular dynamics (MD) simulations. The TOF-QENS experiments were performed at the neutron time-of-flight spectrometer TOFTOF at the new German high-flux neutron source Forschungs-Neutronenquelle Heinz Maier-Leibnitz (FRM II). This instrument allows for probing dynamics on the sub-pico- to nanoseconds time scale with high statistics, as will be demonstrated in this thesis. Since the sample molecules have traveled a few angstroms to several nanometers during that

extended time frame, TOFTOF is perfectly suited for the study of the dynamics at the onset of molecular self-diffusion.

Neutron scattering data allows to characterize molecular motions in reciprocal space. To probe real space dynamics, MD simulations become increasingly popular. The continuous advance in computer power makes this technique more and more feasible. The first programmable computer, the Z3 designed by Konrad Zuse in 1941, achieved 2 flop/s with a clock speed of approximately 5 Hz [4]. Since then computing capacity has increased magnificently: The new supercomputer SuperMUC of the Leibniz-Rechenzentrum, which started operation in summer 2012, reaches a performance of 2.9 petaflop/s [5].

MD simulations are one of the methods of computational chemistry*. They allow for the study of the time-dependent behavior of systems, including vibrations or Brownian motion, by integrating Newton's equations of motion over time [7]. Large ensembles containing more than 1 million atoms can be simulated with computation speeds of the order of nanoseconds/day on supercomputers. A crucial point of MD simulations is the validation of the properties under interest. Novel, unexpected or strange simulation results can simply be wrong, e. g. a simulation artifact [8]. This option must be ruled out before any simulated phenomena can be accepted. Otherwise the simulations are useless if they do not model the reality correctly to some extend. The simulated dynamics presented in this thesis were validated by a careful comparison of computed scattering spectra with experimental QENS data. This method has proven to be very sensitive to small changes of simulation parameters, as already minor variations of the simulation procedure result in noticeable deviations from the measured data. Hence neutron scattering experiments allow for a fundamental verification of MD simulations.

Despite their simple structure, the transport mechanism in melts of linear medium-sized molecules is not fully understood yet. On the one hand the long-range long-time behavior, characterized by a diffusion coefficient D, is well known from pulsed-field gradient nuclear magnetic resonance (PFG-NMR) for many n-alkanes (cf. e. g. [1, 9–11]). On the other hand, the short-time dynamics of n-alkanes are not well characterized yet. Typically the Rouse model [12] is used to describe the dynamics of short polymer chains. However, this theory fails if the molecules are too short to fulfill the Gaussian chain statistics which are already presupposed in the Rouse model. In line with this, deviations from the Rouse predictions were reported in an

*Computational chemistry implements theoretical chemistry into computer programs to solve chemical problems [6].

early QENS work on the dynamics of medium-sized alkanes in a polyethylene (PE) melt [13].

It is conceivable that the dynamics at the onset of molecular self-diffusion cannot be modeled by the coarse grained Rouse model alone, which describes internal motions by introducing orthogonal modes. Although this abstract model is capable of predicting concrete motions such as global molecular rotation, specific intermolecular interactions are not explicitly taken into account. However, it is to be expected that such intermolecular correlations prevail the atomic motions at the onset of molecular self-diffusion.

Several QENS measurements of short- and medium-chain alkane melts can be found in the literature [14–20], which are partially not consistent with PFG-NMR results [1]. In a systematic QENS study of several different-sized n-alkanes Smuda et al. tried to extract only the contribution due to molecular long-range diffusion from the scattering functions [18]. For short n-alkanes at high temperatures the same long-range diffusion coefficients were extracted as measured on longer time scales with PFG-NMR. But with increasing chain length and decreasing temperature the observed dynamics were too fast compared to the PFG-NMR results. Hence the authors concluded that a crossover of several diffusive motions with similar relaxation times is present on the picosecond time scale. A decoupling of these dynamics is quite challenging, since they are not independent of each other and have similar relaxation times [1].

Besides the sporadic number of QENS articles many MD simulation studies on various alkane systems have been published (cf. e. g. [19, 21–31]). The simulations present a detailed picture of the diffusion behavior, which was used to examine the failure of the Rouse model [26, 28]. Some studies carefully validated their simulations and investigated the short-time dynamics. Such combined neutron scattering measurements and MD simulations of longer n-alkane chains showed that the single broad relaxation process observed with QENS is not due to long-range diffusion, but rather a combination of two local motions: Torsional librations and conformational jumps [17, 29, 30]. With the information from MD simulations and the improved data quality from modern neutron scattering instruments it was recently possible to distinguish these motions as two separate relaxation processes also with QENS [18, 20]. The effect of these local conformational transitions on the long-range molecular displacement is the subject of controversial discussion: Local chain dynamics are reported to occur independent from the neighboring chains and without causing

large-scale chain reorientations [32], and on the contrary found to be closely linked to long-range motion [20].

Most of the MD simulation studies quoted above simulated relatively small ensembles, consisting of e. g. 40 $C_{100}H_{202}$ chains [29]. The corresponding $C_{100}H_{202}$ simulation study presented in this thesis simulates significantly larger systems, containing 4096 $C_{100}H_{202}$ molecules, which allows for hydrodynamic interactions to fully develop and makes an analysis of collective motions unimpeded of influences of boundary effects possible.

Small- and medium-sized *n*-alkanes are known to be in an elongated conformation [19, 24, 33], making the Rouse model inapplicable. But even longer polyethylene chains, which should be ideal Rouse chains, cannot be described satisfactorily in terms of the Rouse model [31]. It is mainly an unexpected subdiffusive behavior of the whole molecules which occurs on time scales before long-range Fickean diffusion dominates the overall dynamics. This effect has been observed in many simulations and experimental works on polymer melts (cf. e. g. [31, 34–41]). More elaborated theories have been developed to describe the deviations from the Rouse theory (cf. e. g. [42–46] and discussions therein). These theories mainly try to model the global motion of the molecules correctly. First comparisons with experimental data look promising [39], underlining that taking cooperative dynamics into account is a step in the right direction to describe the overall molecular dynamics. However, detailed predictions on the local, short-time dynamics, are not explicitly made within the framework of the advanced theories.

The concept of modeling cooperative dynamics in molecular melts is based on insights from glass physics. In a glassy state, which is reached by approaching the glass transition temperature of a viscous liquid through cooling, the molecules become localized i. e. trapped in their surroundings, and the system appears "frozen" [3]. In this state the liquid is mainly dynamically heterogeneous (cf. e. g. [47–49]). The time scale on which such dynamic correlations take place depends on the temperature. Even at temperatures far above the glass transition temperature a glass forming system may appear frozen, if adequately short observation times are chosen [3]. Similarities between the correlated dynamics in a metallic glass former and a polymer melt suggest that these collective features are barely affected by chain connectivity [50] and suggests that this behavior is universal. The concept of collective dynamics is applied by many research groups to describe various phenomena, as e. g. huddling dynamics of Emperor penguins [51] or motion in schools of fish [52].

In the following chapter relevant models to describe molecular conformation and dynamics will be outlined. Following the basics of neutron scattering and MD simulations will be briefly described. The subsequent analysis of the QENS data points out that different motions are observed by variation of observation time, temperature and molecular weight of the sample. After characterizing these motions with QENS a comprehensive MD simulation study of *n*-alkanes will be presented, which was applied to identify the prevailing dynamics. In doing so the initial steps of molecular self-diffusion are disentangled. It will thereby turn out that not only single-chain dynamics take place. In particular intermolecular collective flow-like motions of the atoms dominate the observed dynamics on the pico- to nanosecond time scale.

2 Molecular Liquids

Several models are available to describe static and dynamic properties of polymers in solution and in the melt. The Rouse theory, which is commonly used as a starting point to describe polymer dynamics, is based on the model of a Gaussian chain. In this chapter the Gaussian chain model will be introduced before the Rouse model and its characteristics will be explained. Finally a brief overview of recent theoretical advancements to overcome the well-known shortcomings of the Rouse model will be given.

2.1 Flexible and Semiflexible Chain Conformations

A molecule is formed by at least 2 covalently bonded atoms. The molecules studied in this thesis are linear molecules, meaning that they are built up by small repeating units interconnected to form a single backbone without sidechains and crosslinks. The basic units are called monomers, with mass m_n and position vector of their center of mass $\vec{r}_n(t)$. Polymers are composed of many monomers connected by covalent bonds of length b_0. Short polymers formed by only a few monomers are called oligomers. The center-of-mass (com) of a molecule consisting of N monomers is given by the position vector

$$\vec{r}_{\mathrm{com}}(t) = \frac{\sum_{n=1}^{N} m_n \vec{r}_n(t)}{\sum_{n=1}^{N} m_n}. \tag{2.1}$$

The displacement of the com coordinates is affected by both intra- and intermolecular motions: At short times the vibrations of covalent bonds effect the behavior of $\vec{r}_{\mathrm{com}}(t)$. Later the reorientation of smaller or larger intramolecular subgroups, as e. g. a stretching of a folded molecule results in a displacement of $\vec{r}_{\mathrm{com}}(t)$. Tracing the com coordinates for a long time provides information on the translational motion of the whole molecule. A rotational motion of a rodlike molecule, however, has no effect on $\vec{r}_{\mathrm{com}}(t)$.

The global conformation of the molecule and its size is linked to the end-to-end distance of the chain, which is the norm of the end-to-end vector given by

$$\vec{r}_{\mathrm{ee}}(t) = \vec{r}_N(t) - \vec{r}_1(t). \tag{2.2}$$

A rotational motions of whole molecules, which has no effect on the center-of-mass translation, results in an unambiguous reorientation of the end-to-end vector.

In the so-called freely jointed (fj) chain model excluded volume interactions are neglected, meaning that two monomers can occupy the same space. Furthermore the covalent bond length is assumed to be constant and the bond angles exhibit no restrictions. In this model the orientation of the backbone bonds along a polymer chain is described by three-dimensional random walk statistics, and the resulting mean end-to-end distance is zero. The second moment of the end-to-end distance is given by $\langle \vec{r}_{\mathrm{ee}}^{\,2} \rangle^{\mathrm{fj}} = (N-1)b_0^2$ for this model [53]. The brackets denote the ensemble average of the value.

Real molecules are not fully flexible. The orientation of the bonds depends on the chemical structure and hence shows preferred orientations. This causes a local stiffness of the chain on local length scales. Taking this stiffness into consideration leads to the characteristic ratio, which is defined as the ratio of the mean-square end-to-end distance to the value of a freely-jointed chain [54]

$$C_\infty = \frac{\langle \vec{r}_{\mathrm{ee}}^{\,2} \rangle}{(N-1)b_0^2}. \tag{2.3}$$

Hence a long, not fully flexible molecule can again be treated as a coarse grained freely-jointed chain formed by segments, which consist of several monomers. An increasing rigidity of the chain results in a larger C_∞, meaning that larger segments are necessary to treat the stiff chain in terms of the freely-jointed chain model. The length of a segment is $b = b_0\sqrt{C_\infty}$.

In the framework of the freely-jointed chain model the molecular end-to-end distance distribution is given by a Gaussian. Taking the effective bond length b into account results in

$$P(\vec{r}_{\mathrm{ee}}) = \left(\frac{3}{2\pi N b^2}\right)^{3/2} \exp\left(-\frac{3\vec{r}_{\mathrm{ee}}^{\,2}}{2Nb^2}\right). \tag{2.4}$$

The Rouse model, which will be described next, starts from such a Gaussian chain.

2.2 The Rouse Model

In 1948 Kargin and Slonimskii published a "bead and spring" model for the dynamics of linear polymers [55]. The Kargin-Slonimskii model was only published in Russian and hence did not make a strong international impact. In 1953 Prince Earl Rouse, Jr. published his "theory of linear viscoelastic properties of dilute solutions of coiling polymers" [12]. In this model Brownian fluctuating forces are included, which were not considered in the model of Kargin and Slonimskii [56]. The theory has been termed the Rouse model, and has turned out to be one of the most cited publications in polymer physics*. It is the standard starting point for the description of dynamics in unentangled polymer melts. For entangled chains the reptation model of de Gennes applies [57]. Since the molecules studied in this thesis are unentangled, reptation will not be further considered.

In the Rouse model the molecule chain is build up of so-called subchains, or segments, forming a Gaussian chain. The segments themselves contain several chemical monomers, as described before. These beads are connected by entropic springs and random forces model thermal fluctuations. In the Rouse model the length ℓ of the springs is again described by a Gaussian as

$$P(\vec{\ell}) = \left(\frac{3}{2\pi\ell_0^2}\right)^{3/2} \exp\left(-\frac{3\vec{\ell}^{\,2}}{2\ell_0^2}\right), \tag{2.5}$$

with $\ell_0^2 = \langle \ell^2 \rangle$ [58]. This coarse-graining of the molecule is illustrated in figure 2.1.

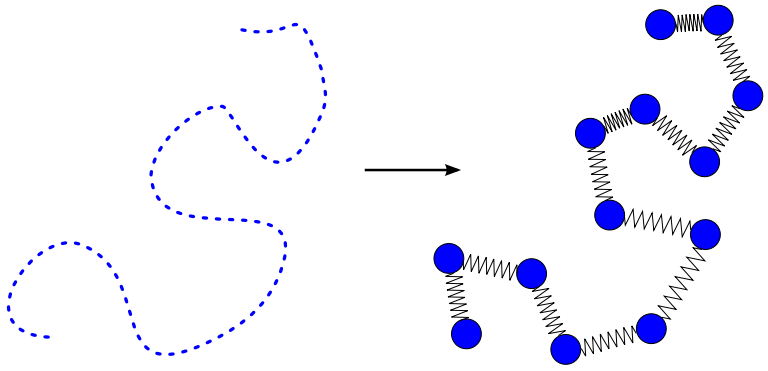

Figure 2.1: Coarse-graining of the molecule. The segments at position $R_n(t)$ are connected by springs, with a Gaussian distribution of length ℓ and a spring constant $k = 3k_\mathrm{B}T/\ell^2$.

*Cited more than 2700 times (02/13).

In the Rouse model excluded volume interactions and explicit hydrodynamic interactions are disregarded [59]. Only neighboring intramolecular segments, i. e. neighboring segments of the same molecule interact with each other. The motion of bead n is described by the Langevin equation of the form

$$\zeta \frac{\mathrm{d}\vec{R}_n(t)}{\mathrm{d}t} = -\frac{\mathrm{d}V}{\mathrm{d}\vec{R}_n(t)} + \vec{f}_n(t). \tag{2.6}$$

In this equation $\vec{f}_n(t)$ denotes a stochastic force reflecting thermal fluctuations, which includes a friction coefficient ζ representing a background friction due to the surrounding chains [37]. The entropic force on a segment is described by the potential V, which models the conformational energy for a Gaussian chain of beads connected with harmonic springs [60]

$$\begin{aligned} V &= \frac{3k_\mathrm{B}T}{2\ell^2} \sum_{n=2}^{N} \left(\vec{R}_n(t) - \vec{R}_{n-1}(t) \right)^2 \\ &= \frac{3k_\mathrm{B}T}{2\ell^2} A_{nm} \vec{R}_n(t) \vec{R}_m(t), \end{aligned} \tag{2.7}$$

using Einstein's notation with the so-called connectivity matrix or adjacent matrix [61, 62]

$$\mathbf{A} = (A_{nm}) = \begin{pmatrix} 1 & -1 & & & & & \\ -1 & 2 & -1 & & & 0 & \\ & -1 & 2 & -1 & & & \\ & & \ddots & \ddots & \ddots & & \\ & & & -1 & 2 & -1 & \\ & 0 & & & -1 & 2 & -1 \\ & & & & & -1 & 1 \end{pmatrix}. \tag{2.8}$$

This matrix is symmetric and its diagonal elements A_{ii} describe the number of bonds or springs connected to the i^{th} bead. The off-diagonal elements A_{ij} are -1 in case bead i and j are connected, or zero otherwise.

The stochastic force $\vec{f}_n(t)$ is defined as

$$\left\langle \vec{f}_n(t) \right\rangle = 0, \quad \left\langle f_{n,\alpha}(t) f_{m,\beta}(t') \right\rangle = 2k_\mathrm{B}T\zeta\delta_{nm}\delta_{\alpha\beta}\delta(t-t'), \tag{2.9}$$

with the Cartesian components α, β.

For internal beads the Langevin equation becomes

$$\zeta \frac{\mathrm{d}\vec{R}_n(t)}{\mathrm{d}t} = -\frac{3k_\mathrm{B}T}{\ell^2}\left(2\vec{R}_n(t) - \vec{R}_{n+1(t)} - \vec{R}_{n-1}(t)\right) + \vec{f}_n(t). \tag{2.10}$$

For the beads at the ends of the chain ($n = 1, N$) the segment motion is assumed as

$$\zeta \frac{\mathrm{d}\vec{R}_1(t)}{\mathrm{d}t} = -\frac{3k_\mathrm{B}T}{\ell^2}\left(\vec{R}_1(t) - \vec{R}_2(t)\right) + \vec{f}_1(t), \tag{2.11a}$$

$$\zeta \frac{\mathrm{d}\vec{R}_N(t)}{\mathrm{d}t} = -\frac{3k_\mathrm{B}T}{\ell^2}\left(\vec{R}_N(t) - \vec{R}_{N-1}(t)\right) + \vec{f}_N(t). \tag{2.11b}$$

The above equations 2.10 and 2.11 can be rewritten using the connectivity matrix to obtain

$$\zeta \frac{\mathrm{d}\vec{R}_n(t)}{\mathrm{d}t} = -\frac{3k_\mathrm{B}T}{\ell^2}\sum_{m=1}^{N} A_{nm}\vec{R}_m(t) + \vec{f}_n(t). \tag{2.12}$$

This expression describes a Brownian motion of coupled oscillators [59].

Normal Coordinates Equation 2.12 can be analytically solved by multiplying $\vec{R}_n(t)$ with a matrix consisting of the eigenvectors of $\mathbf{A}$ [60]. As a result the so-called normal coordinates $\vec{X}_p(t)$, which are eventually the Fourier-transformed real space coordinates, are introduced as [40, 63]

$$\vec{X}_p(t) = \frac{1}{N}\sum_{n=1}^{N} \cos\left[\frac{\pi p}{N}\left(n - \frac{1}{2}\right)\right]\vec{R}_n(t). \tag{2.13}$$

By this approach the motion of the molecule is decomposed into independent modes $p = 0, 1, 2, ..., (N\text{-}1)$. The inverse transformation is

$$\vec{R}_n(t) = \vec{X}_0(t) + 2\sum_{p=1}^{N} \vec{X}_p(t)\cos\left[\frac{\pi p}{N}\left(n - \frac{1}{2}\right)\right], \tag{2.14}$$

which is the linear combination of all orthogonal, i. e. independent solutions of equation 2.12.

The normal coordinate of the zeroth mode $\vec{X}_{p=0}(t)$ corresponds to the center-of-mass (com) position of the chain. With increasing mode number more local dynamics are described. The end-to-end vector of the chain can be expressed as $-4 \cdot \sum_{p_\mathrm{odd}} \vec{X}_p(t)$, summing only over odd mode numbers p [59].

Using the normal coordinates $\vec{X}_p(t)$, the Langevin equation becomes

$$\zeta_p \frac{\partial \vec{X}_p(t)}{\partial t} = -k_p \vec{X}_p(t) + \vec{f}_p(t), \tag{2.15}$$

with the transformed spring constant k_p, friction coefficient ζ_p and stochastic force $f_p(t)$ similar to definition 2.9

$$k_p = 8Nk \sin^2\left(\frac{p\pi}{2N}\right) \underset{p \ll N}{\approx} 8N \frac{3k_\mathrm{B}T}{\ell^2} \frac{p^2\pi^2}{4N^2} = \frac{6\pi^2 k_\mathrm{B}T}{N\ell^2} p^2 \tag{2.16}$$

$$\zeta_{p=0} = N\zeta, \quad \zeta_{p>0} = 2N\zeta \tag{2.17}$$

$$\left\langle f_{p,\alpha}(t) \right\rangle = 0, \quad \left\langle f_{p,\alpha}(t) f_{q,\beta}(t') \right\rangle = 2k_\mathrm{B}T\zeta_p \delta_{pq} \delta_{\alpha\beta} \delta(t-t'). \tag{2.18}$$

The approximation $\sin(p\pi/(2N)) \approx p\pi/(2N)$ is valid if N is large and allows for a simplified study of the lower modes[†]. The spectrum of relaxation times τ_p is given by k_p and ζ_p through

$$\tau_p = \frac{\zeta_p}{k_p} = \frac{\zeta\ell^2}{12k_\mathrm{B}T \sin^2\left(\frac{p\pi}{2N}\right)} \underset{p \ll N}{\approx} \frac{\zeta N^2 \ell^2}{3\pi^2 k_\mathrm{B}T p^2} = \frac{N^2}{W\pi^2 p^2} \sim p^{-2}, \tag{2.19}$$

with the elementary Rouse rate $W = k/\zeta$. The longest time in the relaxation spectrum $\tau_{p=1}$ is called the Rouse time τ_R, while $\tau_{p=N-1}$ corresponds to the fastest relaxation time in terms of the Rouse model.

The dynamics of the chain are now described by time correlation functions of the normal coordinates as [58]

$$\left\langle \vec{X}_p(t) \vec{X}_p(0) \right\rangle = \frac{2k_\mathrm{B}T}{N\zeta} t \qquad p = 0, \tag{2.20}$$

$$\left\langle \vec{X}_p(t) \vec{X}_p(0) \right\rangle = \frac{k_\mathrm{B}T}{k_p} \exp\left(-\frac{t}{\tau_p}\right). \qquad p > 0. \tag{2.21}$$

Consequently the com ($p = 0$) motion is always freely diffusive, since the dynamics modeled with equation 2.20 scale linear with time [59]. The amplitudes of the normal coordinates are given by

$$\left\langle \vec{X}_p(0) \vec{X}_p(0) \right\rangle = \frac{N\ell^2}{6\pi^2 p^2}. \tag{2.22}$$

[†]The error of this approximation is less 1 % already for $N = 9$ [60].

They are independent of temperature and scale with p^{-2}, just as the relaxation time τ_p (compare eq. 2.19). In this thesis the validity of the Rouse model will be analyzed by calculating the Rouse correlators ($p > 0$), defined as [58]

$$\Phi_p = \frac{\left\langle \vec{X}_p(t)\vec{X}_p(0)\right\rangle}{\left\langle \vec{X}_p^2(0)\right\rangle}. \tag{2.23}$$

Rouse-MSD The mean-square displacement (MSD) is a measure for the average distance a particle has traveled during a certain time span. The corresponding expression is obtained by back-transforming the normal coordinates into real-space, resulting in [58]

$$\left\langle R_n^2(t)\right\rangle = 6D_{\mathrm{R}}t + \frac{4N\ell^2}{\pi^2}\sum_{p=1}^{N-1}\frac{1}{p^2}\cos^2\left(\frac{p\pi n}{N}\right)\left[1-\exp\left(-\frac{p^2}{\tau_{\mathrm{R}}}t\right)\right] \tag{2.24}$$

$$\underset{\text{large}\,p}{\approx}\left\langle R_{\mathrm{R}}^2(t)\right\rangle = 6D_{\mathrm{R}}t + 2\ell^2\left(\frac{3k_{\mathrm{B}}T}{\pi\zeta\ell^2}t\right)^{1/2} = 6D_{\mathrm{R}}t + \left(\frac{4W\ell^4}{\pi}t\right)^{1/2}, \tag{2.25}$$

with the Rouse diffusion coefficient

$$D_{\mathrm{R}} = \left\langle\left(\vec{X}_0(t)-\vec{X}_0(0)\right)^2\right\rangle(6t)^{-1} = k_{\mathrm{B}}TN^{-1}\zeta^{-1}. \tag{2.26}$$

The first summand scaling linear with time describes the center-of-mass self-diffusivity. This term dominates the MSD on a long time scale. In the approximation of large mode numbers p the segmental MSD increases with $\sqrt{t}$ in the Rouse regime ($t < \tau_{\mathrm{R}}$).

2.3 Hydrodynamic Interactions

The Rouse model described before was developed to describe the dynamics in unentangled polymer melts, neglecting explicit hydrodynamic interactions between monomers. The diffusion coefficient scales with the length of the molecule as $D \propto N^{-1}$ (cf. eq. 2.26). For polymer chains in a solvent hydrodynamic interactions must be included, resulting in a $D \propto N^{-1/2}$ scaling in the so-called Zimm model [59, 64]. This scaling results from the assumption that the molecule drags the neighboring solvent molecules.

The theoretical predictions for the dilute limit [59] have been confirmed by both experiments and computer simulations (see discussion in [65]). For finite concentrations, however, the dynamics become more complex due to the interplay of excluded-volume interactions, hydrodynamic interactions and entanglement [65]. For semidilute solutions de Gennes derived that hydrodynamic interactions are more and more screened with increasing concentrations, until they are finally screened out completely in the limit of the Rouse model [66]. The interactions between a polymer and the surrounding solvent is screened by the presence of further polymer chains, which are treated as static and absorb the momentum passed from the first polymer to its surroundings [67]. A total screening then results in the smaller diffusion coefficient $D \propto N^{-1}$ in the Rouse model [68].

For the high concentration limit, i. e. for polymer melts, this picture becomes questionable, since the momentum of a polymer should somehow be passed to its neighbors. A serious deviation from the classical Rouse model is the presence of a subdiffusive behavior of the center-of-mass (com) motions on time scales shorter than the Rouse time. The mean-square displacement (MSD) of the whole molecules scales with $t^{<1}$ [34, 35, 37, 39, 40, 69], contrary to the linear scaling as predicted by the Rouse model (see first term in eq. 2.25).

Different theories have been developed to account for the subdiffusive behavior of the molecules. In an approach by Guenza true com self-diffusion sets in after the whole molecule has left its old place, and thereby creating a vacancy [42, 43]. The resulting potential then accounts for the penetration of other chains into the first molecule [70]. However, the numerical solution of this theory is hardly applicable [71].

In a recent analytical theory Farago et al. explicitly considered viscoelastic properties of the polymers in a melt [44–46]. Here the authors suggest that the relative motion of the individual chains cause transverse collective modes, resulting in de-

viations from the Rouse predictions. In this context viscoelastic hydrodynamic interactions (VHIs) are not screened, but result in a transient collective flow. Two time regions can be determined: At very short times the momentum of an atom is spread along the molecular chain, and at longer times the momentum is passed to the surrounding chains. This results in a crossover of the center-of-mass velocity autocorrelation function (VAF) from positive to negative values. In the first part, the positive VAF scales as $-N^{-1}t^{-5/4}$. For longer times the behavior is predicted as $-N^{-1/2}t^{-3/2}$.

Farago et al. derived an expression for the com MSD incorporating the effect of VHIs [46]

$$\langle r^2(t)\rangle_{\mathrm{com}}^{\mathrm{VHI}} \simeq 6\ell^2 \left[\frac{\pi}{12}\frac{Wt}{N} + \frac{16}{(3\pi)^{3/2}}\frac{1}{n\ell^3}\left(\frac{Wt}{N}\right)^{1/2}\right], \tag{2.27}$$

with an microscopic timescale W and the monomer number density n. Besides the linear Fickean scaling in the first summand, a $t^{1/2}$-term appears, which is due to the VHIs. The effective apparent scaling of $t^{\simeq 3/4}$ then corresponds to the observed subdiffusive behavior.

A second model by Farago et al. is a density-based mode-coupling theory approach to catch the origin of the subdiffusive com motion. This approach is based on interactions between chains, causing longitudinal collective modes related to density fluctuations. This model also predicts a crossover of the com VAF, with a short time scaling of $-N^{-1}t^{-5/4}$, and $-t^{-5/4}$ for longer times. Note that the long time scaling is now independent of chain length. Hence a comparison of the long-time tails of the com VAF can be used to distinguish between the two theories.

Using a density-based mode-coupling theory Farago et al. obtained the following expression for the com MSD [72]

$$\langle r^2(t)\rangle_{\mathrm{com}}^{\mathrm{df}} \simeq 6\frac{\ell^2 Wt}{N}\left[1 + 0.752\frac{(Wt)^{-1/4}}{n\ell^3}\right]. \tag{2.28}$$

The second summand in this equation again leads to a $t^{3/4}$ scaling of the MSD. However, this correction is relatively weak in contrast to equation 2.27.

The theories of Farago et al. are exact for very long, flexible and unentangled chains. Their applicability to describe the dynamics of rather stiff molecules of finite size will be tested in this thesis.

3 Samples

In this thesis two different molecular structures were studied: Short polyethylene chains (n-alkanes) and poly(ethylene oxide) (PEO). n-Alkanes are saturated hydrocarbons with the chemical formula C_nH_{2n+2}. Their chemical structure is composed of methanediyl and methyl end groups. Hexadecane ($C_{16}H_{34}$, >99 %), was purchased from Merck and used as received. Hectane ($C_{100}H_{202}$) was kindly provided by D. Richter (Forschungszentrum Jülich). It was synthesized in this group by anionic polymerization from a 1,4-polybutadiene parent and subsequent hydrogenation [31].

PEO has the chemical formula $(C_2H_4O)_nH_2O$. Its structure is similar to the one of n-alkanes, with every third methanediyl group substituted by an oxygen atom (cf. fig. 3.1). PEO was purchased from Sigma-Aldrich, with molecular weights similar to the ones of the n-alkane samples, as listed in table 3.1.

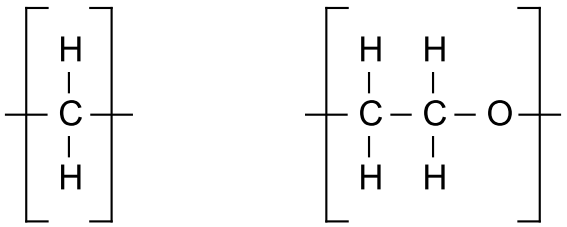

(a) PE (b) PEO

Figure 3.1: Structural formulas of polyethylene (PE) and poly(ethylene oxide) (PEO).

Table 3.1: Molecular weights and melting temperatures [73] of the samples studied in this thesis, as well as the water content of the PEO samples. The melting temperatures of PEO and $C_{16}H_{34}$ were determined by differential scanning calorimetry (Perkin Elmer DSC 8500, scan rate 1 K/min), while the melting point of the $C_{100}H_{202}$ was taken from the literature [74].

n-Alkanes	M_w (g/mol)	T_m (K)
$C_{16}H_{34}$	226	291
$C_{100}H_{202}$	1405	388

PEO	M_w (g/mol)	T_m (K)	w_{H_2O}
PEO200	206	236	0.11 %
PEO600	581	292	0.37 %
PEO1500	1521	321	0.13 %

4 Neutron Scattering

Neutron scattering allows to probe the structure, dynamics and magnetic properties of matter at length scales down to the sub-atomic range and on extended time scales of about 1 fs to 1 μs. This is due to the unique properties of neutrons [75]: (i) Neutrons are uncharged and therefore show no electric interactions with the sample. Hence, in contrast to electrons, protons and electromagnetic waves, neutrons can easily penetrate deeply into the sample where they scatter only at the nuclei by nuclear forces. (ii) Cold and thermal neutrons have energies in the meV-range, which is of the same order as typical potentials for atomic motions in condensed matter. (iii) Due to their mass ($m_\mathrm{n} = 1.675 \cdot 10^{-27}$ kg), the wavelength of cold and thermal neutrons are in the range of 1–20 Å, covering length scales on the order of interatomic distances. X-rays with similar wavelengths have much higher energies on the keV scale. (iv) Because the neutron has a magnetic moment, it can interact with the magnetic field of unpaired electrons, allowing for an analysis of magnetic properties as e. g. the energies of magnetic excitations. Since the magnetic interaction is negligible to the nuclear interaction and also of no concern for the systems studied in this thesis, it will not be further considered.

In the following a short outline of the theory of neutron scattering will be given. More detailed explanations can be found in the literature (see [75, 76], amongst others).

4.1 Theory of Neutron Scattering

In a typical scattering experiments two basic quantities are measured:

- The energy transfer $\hbar(\omega_f - \omega_i) = \hbar\omega$, which is defined as the difference between the final ($E_f = \hbar\omega_f$) and initial ($E_i = \hbar\omega_i$) energies of the neutron.

- The momentum transfer $\Delta\vec{p} = \hbar(\vec{k}_f - \vec{k}_i) = \hbar\vec{Q}$, where $\vec{k}_f$ and $\vec{k}_i$ are the corresponding wave vectors of the neutron. $\vec{Q}$ denotes the scattering vector and its modulus is given by

$$Q = |\vec{Q}| = \sqrt{|\vec{k}_i|^2 + |\vec{k}_f|^2 - 2|\vec{k}_i||\vec{k}_f|\cos(2\theta)} \tag{4.1a}$$

$$\underset{\text{scattering}}{\overset{\text{elastic}}{=}} \frac{4\pi}{\lambda}\sin\left(\frac{2\theta}{2}\right), \tag{4.1b}$$

  with the scattering angle 2θ. The last line only applies to elastic scattering.

The interaction of a neutron with a nucleus occurs via nuclear and magnetic forces. Since the range of the nuclear interaction (in the order of femtometers) is very short compared to the wavelength of a neutron (Å), the nuclei can be treated as point-like [76]. In this way the interaction of a neutron with a nucleus at distance $\vec{r}$ can be described by the Fermi pseudopotential

$$V(\vec{r}) = \frac{2\pi\hbar^2}{m_\mathrm{n}} b\delta(\vec{r}), \tag{4.2}$$

with the scattering length b. This parameter can be complex and its real part can be positive or negative, corresponding to attractive or repulsive interaction, respectively. The imaginary part describes the probability that the neutron is absorbed by the nucleus. The scattering length depends irregularly on the atomic species and isotope, as well as on the spin state of the nucleus-neutron system. Since there is usually a mix of scattering lengths present, the total scattering can be divided into coherent and incoherent scattering. The first one corresponds to the mean scattering of all scatterers, whereas the latter contributes the deviation of the actual scattering lengths of the scatterers as [77]

$$b_\mathrm{coh} = \overline{b}, \tag{4.3a}$$

$$b_\mathrm{inc} = \sqrt{\overline{b^2} - \overline{b}^2}. \tag{4.3b}$$

The scattering cross section is defined as

$$\sigma = 4\pi b^2. \tag{4.4}$$

Table 4.1 lists the cross sections for the elements that are relevant for this thesis.

The double differential cross section is defined as the number of neutrons scattered into a solid angle $\mathrm{d}\Omega$ per second with a final energy energy between E_f and $E_f + \mathrm{d}E_f$,

Table 4.1: Coherent and incoherent scattering cross sections and absorption cross section for 2200 m/s neutrons [78].

Element/Isotope	σ_{coh}	σ_{inc}	σ_{abs}
$^{1}_{1}$H	1.7583	80.27	0.3326
$^{2}_{1}$H	5.592	2.05	0.000519
$_{1}$H	1.7568	80.26	0.3326
^{3}He	4.42	1.6	5333 $\pm$7
$_{2}$C	5.551	0.001	0.0035
$_{8}$O	4.232	0.0008	0.00019
$_{13}$Al	1.495	0.0082	0.231
$_{14}$Si	2.163	0.004	0.171
$_{18}$Ar	0.458	0.225	0.675
$_{23}$V	0.0184	5.08	5.08

normalized to the incoming flux, the solid angle element $\mathrm{d}\Omega$ and the energy range $\mathrm{d}E_f$ [75]. Considering only nuclear scattering, the double differential cross section can be written in the form [75, 77]

$$\frac{\mathrm{d}^2\sigma}{\mathrm{d}\Omega \mathrm{d}E_f} = \frac{k_f}{k_i}\frac{1}{2\pi\hbar}\sum_{l,m}\overline{b_l b_m}\int_{-\infty}^{\infty}\left\langle e^{i\vec{Q}\vec{r}_l(t)}e^{i\vec{Q}\vec{r}_m(0)}\right\rangle e^{-i\omega t}\mathrm{d}t, \tag{4.5}$$

where k_f and k_i are the moduli of the wave vectors, $\vec{r}_i(t)$ is the position of a scatterer i at time t and the brackets denote the ensemble average over all t [3]. Assuming that the distribution of the scattering lengths b among the nuclei is random, the average of the scattering lengths can be subdivided into

$$\overline{b_l b_m} = \begin{cases} \overline{b^2} & \text{for } l = m \\ \overline{b}^2 & \text{for } l \neq m. \end{cases} \tag{4.6}$$

Using these expressions together with equation 4.4, one can rewrite equation 4.5 as

$$\frac{\mathrm{d}^2\sigma}{\mathrm{d}\Omega \mathrm{d}E_f} = \frac{k_f}{k_i}\frac{1}{2\pi\hbar}\,\overline{b}^2\sum_{l,m}\int_{-\infty}^{\infty}\ldots\,\mathrm{d}t + \frac{k_f}{k_i}\frac{1}{2\pi\hbar}\,(\overline{b^2}-\overline{b}^2)\sum_{l}\int_{-\infty}^{\infty}\ldots\,\mathrm{d}t \tag{4.7}$$

$$= \left(\frac{\mathrm{d}^2\sigma}{\mathrm{d}\Omega \mathrm{d}E_f}\right)_{\mathrm{coh}} + \left(\frac{\mathrm{d}^2\sigma}{\mathrm{d}\Omega \mathrm{d}E_f}\right)_{\mathrm{inc}} \tag{4.8}$$

$$= \frac{k_f}{k_i}\frac{N}{4\pi}\left(\sigma_{\mathrm{coh}}S_{\mathrm{coh}}(\vec{Q},\omega) + \sigma_{\mathrm{inc}}S_{\mathrm{inc}}(\vec{Q},\omega)\right), \tag{4.9}$$

with the number of scattering nuclei N and introducing the scattering functions $S(\vec{Q},\omega)$. The coherent part depends on both the time dependent positions of the same nucleus as well as of different nuclei. Hence it describes interference effects and represents both the self and pair correlation. The incoherent term however describes only the self correlation [77]. The scattering functions, also called dynamic structure factors, contain information about both the structure and the dynamics of the sample [79]. They are the time-Fourier transforms ($\mathcal{FT}$)

$$S(\vec{Q},\omega) = \mathcal{FT}\left[I(Q,t)\right] = \frac{1}{2\pi\hbar}\int_{-\infty}^{\infty} I(Q,t)e^{i\omega t}\mathrm{d}t \tag{4.10}$$

of the so-called intermediate scattering functions, which are defined as [76]

$$I_{\mathrm{coh}}(\vec{Q},t) = \frac{1}{N}\sum_{l,m}\left\langle e^{i\vec{Q}\vec{r}_l(t)}e^{-i\vec{Q}\vec{r}_m(0)}\right\rangle \quad \text{and} \tag{4.11a}$$

$$I_{\mathrm{inc}}(\vec{Q},t) = \frac{1}{N}\sum_{l}\left\langle e^{i\vec{Q}\vec{r}_l(t)}e^{-i\vec{Q}\vec{r}_l(0)}\right\rangle. \tag{4.11b}$$

They sum up to the total intermediate scattering function $I(\vec{Q},t)$. This function typically starts at $I(\vec{Q},0) = 1$ and decays in time, if decorrelation takes place. A total decorrelation yields $I(\vec{Q},t) = 0$. By introducing a particle-density operator and its Fourier transform as

$$\begin{aligned}\rho(\vec{r},t) &= \sum_i \delta\left(\vec{r} - \vec{r}_i\left(t\right)\right)\\ \rho(\vec{Q},t) &= \sum_i e^{i\vec{Q}\vec{r}_i(t)},\end{aligned} \tag{4.12}$$

the intermediate scattering function can be expressed in terms of a density-density correlation function as

$$I(\vec{Q},t) = \frac{1}{N}\left\langle \rho(-\vec{Q},0)\rho(\vec{Q},t)\right\rangle. \tag{4.13}$$

This expression will be used to calculate intermediate scattering functions from the computer simulations, vide infra.

A Fourier transformation in space of the intermediate scattering function leads to the van Hove correlation function [79]

$$G(\vec{r},t) = \frac{1}{(2\pi)^3}\int I(\vec{Q},t)e^{-i\vec{Q}t}\mathrm{d}\vec{Q}. \tag{4.14}$$

The space-time correlation functions are defined as [76]

$$G_{\text{pair}}(\vec{r},t) = \frac{1}{N}\sum_{l,m}^{N}\int \langle \delta\left(\vec{r}' - \vec{r}_l(t)\right)\delta\left(\vec{r} - \vec{r}' + \vec{r}_m(0)\right)\rangle \,\mathrm{d}\vec{r}', \tag{4.15a}$$

$$G_{\text{self}}(\vec{r},t) = \frac{1}{N}\sum_{l}^{N}\int \langle \delta\left(\vec{r}' - \vec{r}_l(t)\right)\delta\left(\vec{r} - \vec{r}' + \vec{r}_l(0)\right)\rangle \,\mathrm{d}\vec{r}'. \tag{4.15b}$$

These functions contain the Heisenberg operators $\vec{r}_i(t)$, which do not commute. In the classical approximation, the $\vec{r}_i(t)$ can simply be regarded as the position vectors. Now the integration can be carried out resulting in [76]

$$G^{\text{cl}}_{\text{pair}}(\vec{r},t) = \frac{1}{N}\sum_{l,m}^{N}\langle \delta\left(\vec{r} - \vec{r}_l(t) + \vec{r}_m(0)\right)\rangle\,, \tag{4.16a}$$

$$G^{\text{cl}}_{\text{self}}(\vec{r},t) = \frac{1}{N}\sum_{l}^{N}\langle \delta\left(\vec{r} - \vec{r}_l(t) + \vec{r}_l(0)\right)\rangle\,. \tag{4.16b}$$

Assuming that all nuclei are equivalent allows for the following interpretation of the correlation functions: The pair correlation function $G^{\text{cl}}_{\text{pair}}(\vec{r},t)$ gives the probability density of finding *a* particle at position $\vec{r}(t)$ at time t if *some* particle was at the origin at time $t = 0$. Likewise, the self correlation function $G^{\text{cl}}_{\text{self}}(\vec{r},t)$ gives the probability of finding *a* particle at $\vec{r}(t)$ given that *this* particle was at the origin at time $t = 0$ [3, 80].

The transformation of the different functions described above can be summarized as

$$G_{\text{pair}}(\vec{r},t) \overset{\text{space}-\mathcal{FT}}{\Longrightarrow} I_{\text{coh}}(\vec{Q},t) \overset{\text{time}-\mathcal{FT}}{\Longrightarrow} S_{\text{coh}}(\vec{Q},\omega), \tag{4.17a}$$

$$G_{\text{self}}(\vec{r},t) \overset{\text{space}-\mathcal{FT}}{\Longrightarrow} I_{\text{inc}}(\vec{Q},t) \overset{\text{time}-\mathcal{FT}}{\Longrightarrow} S_{\text{inc}}(\vec{Q},\omega). \tag{4.17b}$$

The dimensions of $S(\vec{Q},\omega)$ and $G(\vec{r},t)$ are $(\text{energy})^{-1}$ and $(\text{volume})^{-1}$, respectively, while $S(\vec{Q},t)$ is dimensionless. Since the systems studied in this thesis behave as ideally powder samples, meaning that they are statistically isotropic under the experimental conditions used, the absolute values r, Q will be used instead of $\vec{r}, \vec{Q}$ in the following.

Dynamics

Motions of single particles are expressed by the self-part of the van Hove correlation function. At $t = 0$ this function is a delta function, since all particles are initially at the origin of their individual coordinate system. Evolving in time, $G_{\mathrm{self}}(r,t)$ will start to smear out, but the integration over space will always yield unity, guaranteeing particle number conservation.

Assuming that the particles perform a random walk allows for the approximation of $G_{\mathrm{self}}(r,t)$ by a Gaussian function [81]

$$G_{\mathrm{self}}^{\mathrm{Gauss}}(r,t) = \left(\frac{3}{2\pi \left\langle r^2(t)\right\rangle}\right)^{3/2} \exp\left(-\frac{3r^2}{2\left\langle r^2(t)\right\rangle}\right), \tag{4.18}$$

introducing the mean-square displacement (MSD) $\left\langle r^2(t)\right\rangle = \left\langle (r(t) - r(0))^2\right\rangle$. With the diffusion coefficient D and the MSD $\left\langle r^2(t)\right\rangle = 6Dt$ which, according to Einstein's theory, describes a Brownian motion, one obtains

$$G_{\mathrm{self}}^{\mathrm{Gauss}}(r,t) = (4\pi Dt)^{-3/2} \exp\left[-\frac{r^2}{4Dt}\right]. \tag{4.19}$$

Fourier transforming leads to

$$I_{\mathrm{inc}}^{\mathrm{Gauss}}(Q,t) = \exp\left[-DQ^2t\right], \tag{4.20}$$

$$S_{\mathrm{inc}}^{\mathrm{Gauss}}(Q,\omega) = \frac{1}{\hbar\pi}\frac{DQ^2}{\omega^2 + (DQ^2)^2}. \tag{4.21}$$

Hence long-range Fickean diffusive motion leads to a single exponential decay of the intermediate scattering function $I_{\mathrm{inc}}^{\mathrm{Gauss}}(Q,t)$. The scattering function 4.21 is a Lorentzian with the half width at half maximum (HWHM) $\Gamma = DQ^2$. Therefore observing a Q^2-dependence of the HWHM of the measured scattering functions indicates diffusive motion. However, this diffusive behavior must not straightforwardly be linked to molecular self-diffusion. It will be pointed out in this thesis that for molecular liquids a Q^2-scaling can be identified on the whole pico- to nanosecond time scale. But especially at short times molecular self-diffusion is not the dominant motion. Hence the diffusion coefficient D characterizing this short-time motion does not have to be the same as the long-time diffusion coefficient obtained with e. g. PFG-NMR, but must be treated as an *apparent* diffusion coefficient D_{a}.

The above expressions are only true if the Gaussian approximation is fulfilled. Otherwise higher-order corrections must be included into the incoherent intermedi-

ate scattering function $I_{\mathrm{inc}}(t)$. Expanding it to higher orders of Q gives a modified function which reads as [82, 83]

$$I_{\mathrm{inc}}(Q,t) = \exp\left\{-\frac{\langle r^2(t)\rangle\, Q^2}{6} + \alpha_2(t)\frac{1}{2}\left(\frac{\langle r^2(t)\rangle\, Q^2}{6}\right)^2 + ...\right\}. \tag{4.22}$$

When terminating the expansion after the second term $\alpha_2(t)$ is called the non-Gaussian parameter. It is defined as a function of the second and fourth moments of the particle displacement by

$$\alpha_2(t) = \frac{\langle r^4(t)\rangle}{(1+2/d)\,\langle r^2(t)\rangle^2} - 1 \tag{4.23}$$

with the spatial dimension d. This parameter gives the time dependence the deviation of the self part of the van Hove correlation function from a Gaussian. The origin of the non-Gaussian behavior can be manifold. Therefore the parameter $\alpha_2(t)$ can be among others considered to find dynamic heterogeneous dynamics [84, 85] and characterize cage motion [86], or used as an order parameter for the glass transition [87].

Statics

The van Hove function at $t = 0$, $G(r, 0)$, can be written as

$$G(r,0) = \delta(r) + g(r) \tag{4.24}$$

by introducing the pair distribution function $g(r)$, which is the radial distribution function for isotropic systems [88, 89]. The transformation of $G(r, 0)$ leads to $I(Q, 0)$ and defines the static structure factor as the zeroth energy moment of the scattering function [75]

$$\begin{aligned} S(Q) := S_{\mathrm{coh}}(Q) &= \int_{-\infty}^{\infty} S_{\mathrm{coh}}(Q,\omega)\mathrm{d}\omega \\ &= \frac{1}{N}\sum_{l,m}\left\langle e^{iQ(r_l - r_m)}\right\rangle \\ &= 1 + \int g(r)e^{iQr}\mathrm{d}r. \end{aligned} \tag{4.25}$$

Since only the coherent part contains the structural information and the incoherent part only adds a constant background, $S_{\mathrm{coh}}(Q)$ will be denoted $S(Q)$.

Assuming that the incoherent neutron scattering is only due to the disorder of the spins, the spin state of the neutron is flipped with a probability of 2/3. Coherent scattering however does not change the spin of the scattered neutron [90, 91]. Hence the coherent and incoherent differential cross sections can be expressed through the scattering with (SF) and without (NSF) spin-flip through

$$\left(\frac{\mathrm{d}\sigma}{\mathrm{d}\Omega}\right)_{\mathrm{inc}} = \frac{3}{2}\left(\frac{\mathrm{d}\sigma}{\mathrm{d}\Omega}\right)_{\mathrm{SF}} \tag{4.26a}$$

$$\left(\frac{\mathrm{d}\sigma}{\mathrm{d}\Omega}\right)_{\mathrm{coh}} = \left(\frac{\mathrm{d}\sigma}{\mathrm{d}\Omega}\right)_{\mathrm{NSF}} - \frac{1}{2}\left(\frac{\mathrm{d}\sigma}{\mathrm{d}\Omega}\right)_{\mathrm{SF}}. \tag{4.26b}$$

Using neutron polarization analysis these coherent and incoherent scattering contributions can be determined.

4.2 Description of the Instruments

The time-of-flight Spectrometer TOFTOF

The direct geometry neutron spectrometer TOFTOF [92, 93] of the Technische Universität München at the FRM II selects the incident energy of the neutrons and determines their final energy both by the time-of-flight (TOF) method. The "S"-shaped neutron guide filters out fast neutrons with wavelengths of $\lambda < 1.38\,\text{Å}$ and gamma rays from the neutron source. The working principle of TOFTOF is sketched in figure 4.1.

The primary spectrometer consists of a multi-chopper system, which selects a certain energy range out of the white neutron beam. Each of the 7 chopper disks is made of carbon fibre composites and coated with neutron-absorbing ^{10}B. The first two counterrotating choppers (pulsing choppers) slice short symmetric pulses out of the continuous, white neutron beam. Since the pulses are polyenergetic, they spread along the way to the last chopper pair (monochromating choppers). These select an almost monoenergetic range of wavelengths out of the broadened pulse. The third and fourth chopper (higher order removal choppers) filter out neutrons which have higher order wavelengths and therefore could pass the chopper system with an unwanted energy. In order to ensure that the scattered neutrons can be detected before the neutrons from the next pulse arrive, the fifth chopper (frame

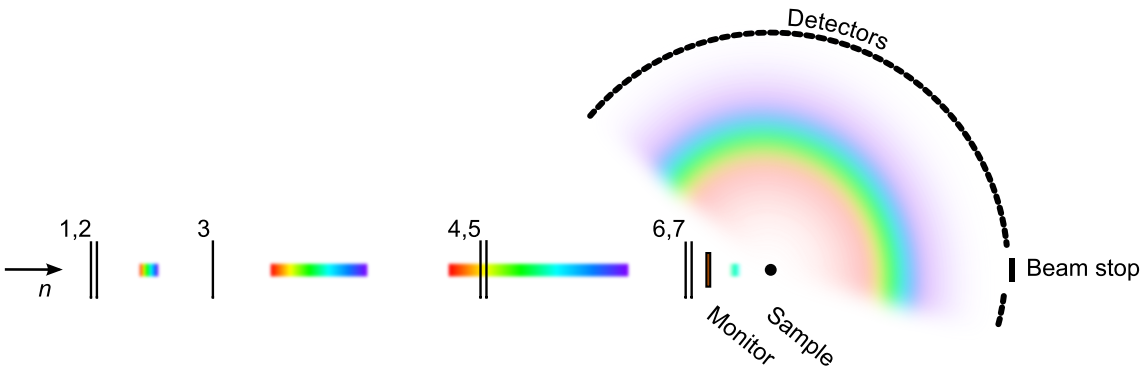

Figure 4.1: Schematic working principle of TOFTOF: The white neutron beam n is pulsed at choppers no. 1 & 2. The pulse broadens, and after a distance of 10 m choppers no. 6 & 7 select neutrons with a defined energy. Also shown are the higher order removal choppers no. 3 & 4, as well as the frame overlap chopper no. 5. After scattering at the sample the neutron energy is determined by the time the neutron needs to reach the detectors at a distance of 4 m, covering scattering angles from 7.5° to 140°. The colors represent the neutrons energy, schematically,

overlap chopper) can be adjusted in its rotation frequency such that only every i^{th} pulse is allowed to pass the chopper system.

The secondary spectrometer contains a variable sample environment and approximately 1000 ^{3}He detectors (active area: $40 \times 3\,\text{cm}$, thickness: $1.5\,\text{cm}$), which are positioned tangential to the Debye-Scherrer-cones and also tangential to a virtual spherical surface with a radius of 4 m around the sample position. The detectors cover an angular range from 7.5° to 140°. The energy of the neutrons is determined by the time-of-flight from the sample to the detectors where they are counted with a gas filled counting detector on the basis of a (n,p)-reaction with ^{3}He [94]. The volume between the sample and the detectors is filled with Argon, to reduce scattering from air.

The energy resolution of the instrument is mainly given by the quality of the selection of monoenergetic neutrons in the primary spectrometer. It can be tuned continuously by changing the chopper speed and selecting a different wavelength of the incident neutrons, respectively. Because of Heisenberg's uncertainty principle ($\Delta E \cdot \Delta t \geq \hbar/2$) [95] a good energy resolution, obtained by a precise selection of the incident neutron wave length, corresponds to a long neutron wave packet and vice versa. Long neutron wave packets take more time to run over the sample, hence they can interact with the nuclei during a longer time. At TOFTOF these observation times t_{obs} can be set in the pico- to nanosecond range by adjusting the energy resolution. The observation times correspond to the decay of the correlation function of a static scatterer to 10 % of its initial value [19].

The Diffuse Neutron Scattering Instrument DNS

The instrument DNS of the Jülich Centre for Neutron Science at the FRM II allows for a simultaneous separation of the coherent, incoherent and magnetic scattering contributions by means of polarization analysis [96–99]. A sketch of DNS is illustrated in figure 4.2.

Out of the white neutron beam from the cold source a monochromatic neutron beam is prepared via Bragg reflection from the (002)-plane of a monochromator crystal made of pyrolytic graphite (PG). By rotating the whole instrument around the monochromator, wavelengths in the range from 2.4 to 6.0 Å can be selected. The beam is polarized using Schärpf bender-type supermirrors (m=3), with a polarization rate of nearly 96 % [97]. Before scattering at the sample, a Mezei-type

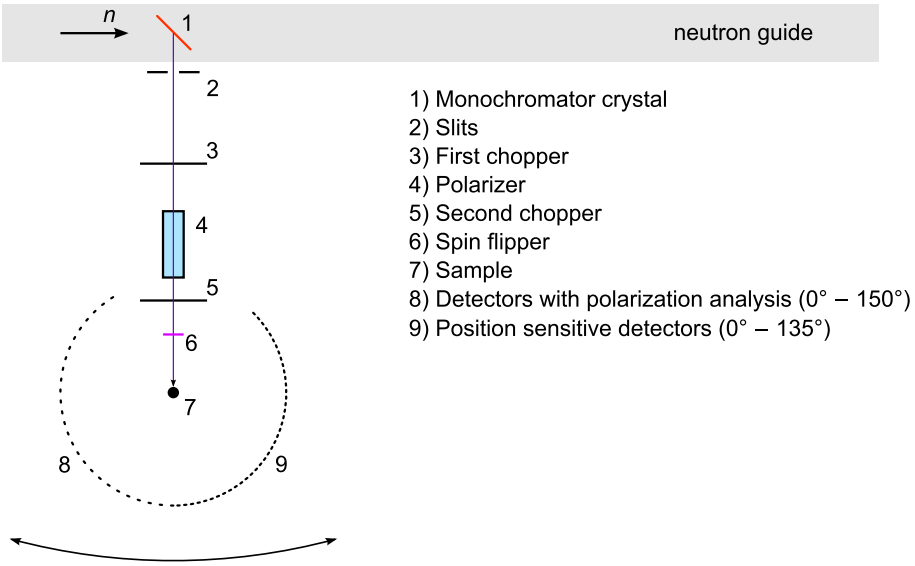

Figure 4.2: Schematic drawing of DNS. A monocromatic beam is prepared out of the white neutron beam n using a monochromator crystal (PG(002), $2.5 \times 2.5\,\mathrm{cm}^2$, lattice spacing $d = 3.355\,\text{Å}$) The wavelength of the neutrons can be adjusted by rotating the whole instrument around the monochromator crystal.

π spin-flipper is installed to reverse the polarization of the neutron beam for spin-flip and non-spin-flip measurements.

To measure the polarization after the scattering, 24 m=3 Schärpf bender-type supermirrors are mounted in front of 24 ^{3}He detector tubes (15 cm long and 2.54 cm in diameter), placed in 5°-steps. The whole range of scattering angles from 0° to 150° can be covered with 1° angular resolution by stepwise moving the whole detector array. Additionally 128 position sensitive ^{3}He detectors (100 cm long and 1.27 cm in diameter) are installed opposite of the polarization analyzers (see fig. 4.2), covering an angular range from 0° to 135°.

The chopper system, which is included in figure 4.2, is planned in order to filter out neutrons with higher-order wavelengths and thus to improve the quality of the data. In combination with the position sensitive detectors DNS will then allow for spectroscopy alongside of polarization analysis. However during the beam time at DNS the chopper system was not in operation yet.

In a first measurement one determines the amount of neutrons which have not performed a spin flip at the sample, and therefore arrive with an unchanged polarization. In a second measurement the π spin-flipper is used. Now only neutrons that have changed their polarization during the scattering are detected. Using equations 4.26, the coherent and incoherent scattering contributions can be separated.

4.3 Experimental Setups and Data Treatment

Measurements were performed both at the time-of-flight spectrometer TOFTOF and at the diffuse neutron scattering instrument DNS. The conducted experiments, which are described in the following, are summarized in table 4.2.

Table 4.2: Temperature ranges measured at TOFTOF (left table) and DNS (right table). Also listed are the instrumental resolutions used for the measurements at TOFTOF, corresponding to tabular 4.3.

TOFTOF	T	ΔE
$C_{16}H_{34}$	283 – 443 K	23 μeV – 3 meV
$C_{100}H_{202}$	393 – 509 K	2, 23 μeV – 3 meV
PEO200	238 – 373 K	4 μeV
	293 – 383 K	55 μeV – 1.5 meV
PEO600	303 – 403 K	55 μeV – 1.5 meV
PEO1500	343 – 403 K	55 μeV – 1.5 meV

DNS	T
$C_{16}H_{34}$	293 – 403 K
$C_{100}H_{202}$	393 – 453 K

Neutron Spectroscopy at TOFTOF

Quasielastic neutron scattering (QENS) experiments were performed at the time-of-flight spectrometer TOFTOF. By adjusting the instrumental resolution of the instrument, the observation times can be varied in the entire pico- to nanosecond time scale. The corresponding chopper settings used for the measurements are given in table 4.3. With these settings a broad Q-range from 0.05 Å^{-1} up to 5.9 Å^{-1} is accessible.

For all measurements except the high resolution (2 and 4 μeV) measurements the samples were filled in thin-walled aluminum hollow cylinders (diameter 23 mm, height 65 mm) with a sample layer thickness of 0.1 mm [100]. The resulting amount of the sample was 0.5 ml. For the 2 and 4 μeV measurement a flat aluminum sample container (width 30 mm, height 70 mm) with a gap of 1 mm was used. In order to decrease the amount of sample an aluminum plate (thickness 0.5 mm) was placed in the sample container. The resulting sample volume was approximately 1 ml. The surface normal of the flat container was oriented to a scattering angle of 45° or 135°, hence the container is shielding the detectors at around 135° or 45°, respectively. The shielded angular range was removed during the data reduction. The empty sample holders were measured, too, to later correct for scattering from the container.

The measurement time was varied to account for the reduced intensity at higher instrumental resolutions. For the lower resolutions ($\Delta E \leq 55\,\mu$eV) the samples were measured for 1 h at each temperature, while the 23 and 4 μeV measurements were performed for a minimum of 2 and 4 h, respectively. The signal rate with the best resolution of 2 μeV was a factor 100 lower than the signal rate of the lowest resolution. To get reasonable statistics a measurement time of 12 h was chosen.

To correct for the detector efficiencies and determine the instrumental resolution a measurement of a vanadium standard or the sample at low temperatures was performed. The latter method was chosen for the 2 μeV measurements of $C_{100}H_{202}$. Chain correlation peaks, which emerge at $Q \approx 1.5\text{Å}^{-1}$, are not accessible with this high resolution configuration, and an isotropic scattering of the sample is observed.

Most of the data reduction and evaluation was performed using the program Frida1 [101]. Several errors are known to exist in Frida1 [3], which were taken into account as far as practicable. The data reduction procedure was done as follows: First the raw data $N(2\theta, \text{tof})$ was normalized to the monitor counts. Following the time-of-flight channels were converted to energy transfer, according to the description in [1]. To correct the detector sensitivities, the elastic line of the resolution spectra was integrated and corrected with the Debye-Waller factor. Then the sample spectra were normalized for the detector efficiencies by dividing the spectra by these numbers. Following a self-absorption correction using the Frida1 routine, the

Table 4.3: Chopper settings at TOFTOF for different instrumental resolutions ΔE (μeV), corresponding to an effective observation time t_{obs}: Chopper rotation frequency f_{ch}, incident wavelength λ_{i} and frame overlap ratio R. Additionally listed is the accessible Q-range and the maximum energy transfer allowed for in the data treatment, as described in the text.

ΔE (μeV)	t_{obs} (ps)	f_{ch} (rpm)	λ_{i} (Å)	R	Q-range (Å^{-1})	E_{max} (meV)
3000	1.1	6000	2	1	0.41 – 5.9	20
1500	2	12000	2	2	0.41 – 5.9	20
900	3.5	12000	2.4	2	0.34 – 4.94	8
450	6.8	12000	3	2	0.27 – 3.94	5
250	13.25	12000	3.6	3	0.23 – 3.28	3
150	19	12000	4.2	3	0.20 – 2.81	2
100	35	12000	5	4	0.16 – 2.36	2
55	50	12000	6	4	0.14 – 1.97	1.45
23	118	12000	8	5	0.10 – 1.48	1.26
4	900	16000	14	8	0.06 – 0.84	0.1
2	1200	14000	16	8	0.05 – 0.74	0.025

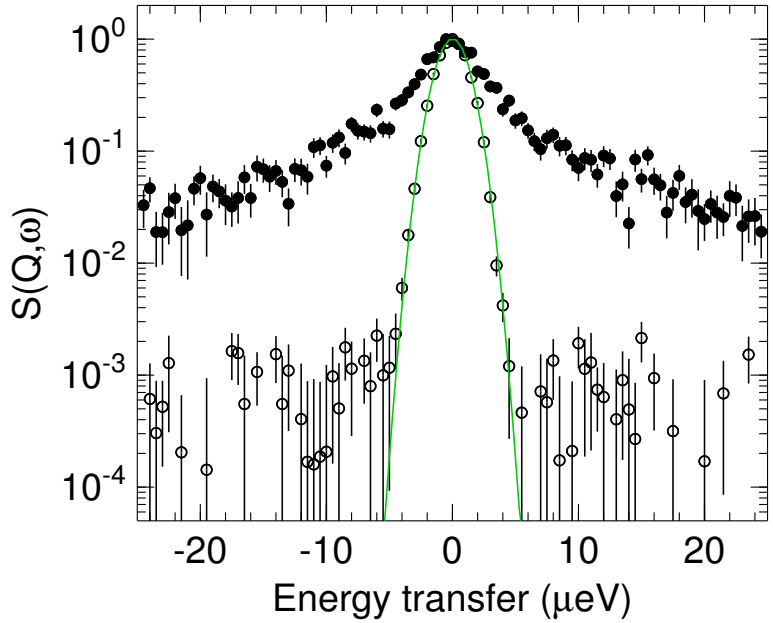

Figure 4.3: $C_{100}H_{202}$ measured at $T = 4\,\mathrm{K}$ (open symbols) and at $T = 509\,\mathrm{K}$ (full symbols) at $Q = 0.2\,\mathrm{\AA}^{-1}$ at TOFTOF, with an instrumental resolution of $2\,\mu\mathrm{eV}$. The low temperature data characterizes the instrumental resolution, which can be described by a Gaussian function (green solid line).

spectra $S(2\theta, \omega)$ were rebinned to spectra of constant Q using the library sihl [102]. For the $2\,\mu\mathrm{eV}$ and $4\,\mu\mathrm{eV}$ data Q-steps of $0.01\,\mathrm{\AA}^{-1}$ were used. The other data were rebinned with Q-steps of $0.1\,\mathrm{\AA}^{-1}$. Subsequently the spectra of the empty can were subtracted from the spectra of the samples. The Q-ranges containing Bragg scattering from the aluminum sample holder were removed and the resulting spectra were corrected for the detailed balance factor.

Figure 4.3 exemplarily illustrates $S(Q, \omega)$ measured for $C_{100}H_{202}$ at the highest resolution of $2\,\mu\mathrm{eV}$ at $4\,\mathrm{K}$ and $509\,\mathrm{K}$, respectively. In the low temperature measurement the quasielastic contribution to the measurement signal is negligible, as the sample is eventually frozen. Hence the shape of the measured $S(Q, \omega)$ determines the instrumental resolution. The scattering function of liquid $C_{100}H_{202}$ at $509\,\mathrm{K}$ is broadened by scattering due to aperiodic, e. g. diffusive motions in the liquid.

Intermediate scattering functions were obtained by a numerical Fourier transformation of the data points with positive energy transfers $0 \leq \hbar\omega \leq E_{\max}$, with the maximum energy transfer $E_{\max}$ as listed in table 4.3. In order to improve the statistics of the $I(Q, t)$ obtained from the high resolution measurements (2 & $4\,\mu\mathrm{eV}$), a numerical Fourier transformation was also performed on the data with negative energy transfer by taking the absolute values $|\hbar\omega|$. This procedure is justified since

the resolution function of TOFTOF is symmetric and can be approximated nicely by a Gaussian [92], as demonstrated in figure 4.3. After the Fourier transformation the sample $I(Q,t)$ were divided by the resolution functions to correct for the instrumental resolution.

Neutron Diffraction at DNS

Neutron polarization analysis was performed at the diffuse neutron scattering instrument DNS. An incident neutron wavelength of $\lambda_\mathrm{i} = 4.2\,\text{Å}$ was selected. Measurements were performed at two positions of the detector bank. Hence 48 angles from 7.5° to 125° were covered in angular steps of 2.5°, resulting in a maximum Q of $2.65\,\text{Å}^{-1}$. The samples were measured either in the aluminum hollow cylinders or flat sample containers, which were also used at TOFTOF. The flat cells were oriented 40° to the incoming beam, the surface normal of the container pointing to a scattering angle of 50°.

The measurement time was 1 h for each detector bank position and each measurement mode (SF: spin-flip and NSF: non-spin-flip), resulting in a total measurement time of 4 h per sample temperature. Additionally the empty sample containers as well as a "black" sample (absorbing 100 %, referred to as background measurement in the following) were measured at room temperature.

The efficiency of the polarizers and the π-flipper, also referred to as the flipping ratio R, was measured using a nickel-chromium-alloy, which is a spin coherent and isotope incoherent scatterer (100 % NSF) [103]. This finite instrument flipping ratio was determined by relating the NSF counts to SF counts [104] to be approximately $R \approx 23$.

Data reduction was carried out based on the program plot.py* [105], which is the standard data handling software at DNS, and following the method applied by Gaspar et al. [91]. The measured intensities $N(2\theta)$ were first normalized to the monitor counts and converted to $N(Q)$ according to equation 4.1b. This conversion is only valid for the case of elastic scattering and will be discussed below. Following the empty can and background measurements were subtracted, and the appropriate

*The data reduction was not performed with plot.py solely, due to some doubtful parts in the plot.py routine.

self-absorption corrections was performed using the Frida1 routine [101]. The finite instrument flipping ratio R was factored in as [91, 104]

$$N_{\mathrm{NSF,corr.}}(Q) = N_{\mathrm{NSF}}(Q) + \frac{1}{R-1}\left(N_{\mathrm{NSF}}(Q) - N_{\mathrm{SF}}(Q)\right) \tag{4.27a}$$

$$N_{\mathrm{SF,corr.}}(Q) = N_{\mathrm{SF}}(Q) + \frac{1}{R-1}\left(N_{\mathrm{SF}}(Q) - N_{\mathrm{NSF}}(Q)\right). \tag{4.27b}$$

From these corrected intensities incoherent $N_{\mathrm{inc}}(Q)$ and coherent $N_{\mathrm{coh}}(Q)$ scattering contributions were obtained according to equation 4.26. The incoherent term should contribute as a constant background and was therefore used to normalize the coherent term [91, 106]. In that way a calibration factor α was calculated as

$$\alpha = \frac{N_{\mathrm{coh}}(Q)}{N_{\mathrm{inc}}(Q)}, \tag{4.28}$$

which was used to obtain normalized scattering intensities as

$$S'_{\mathrm{coh}}(Q) = \frac{\sigma_{\mathrm{inc}}}{\sigma_{\mathrm{tot}}}\alpha, \tag{4.29a}$$

$$S'_{\mathrm{inc}}(Q) = \frac{\sigma_{\mathrm{inc}}}{\sigma_{\mathrm{tot}}}. \tag{4.29b}$$

During the data reduction procedure the angular detector positions 2θ were converted to Q accoring to equation 4.1b. This is correct if the sample scatters only elastically. However, quasielastic scattering contributes significantly to the measured signal of liquid samples. As the detectors integrate over all final energies of the scattered neutrons, it is not possible to discriminate in- or quasielastically scattered neutrons. This integration at constant angle is not identical to the integral at constant Q, as can clearly be seen in figure 4.4. All neutrons with $E_f \neq E_i$ are treated as elastically scattered and are hence allocated to an incorrect Q. As a result the quantity obtained from the experiment is not the structure factor as defined in equation 4.25.

A variation of the neutron energy transfer has a direct effect on $\vec{k}_f$ and hence on $\vec{Q}$, as well as on the detector efficiency. For simple systems the so-called Placzek correction is typically used to correct for the inelastic scattering effects, which is based on a mass expansion and the first and second moments of the scattering function [75, 107–110]. This correction requires that the energy transfer is small compared to the excitation energies of the sample and that the neutron mass is much smaller than the mass of the scattering nuclei. The latter condition is not

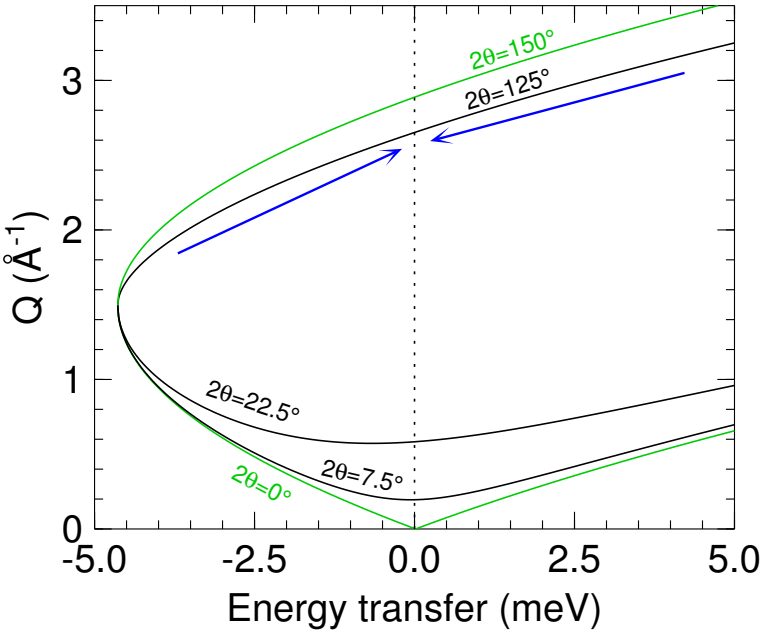

Figure 4.4: Theoretically accessible dynamical range at DNS with an incident neutron wavelength of 4.2 Å (green lines: $2\theta = 0° - 150°$) and the dynamical range accessed during the experiment (black lines). Negative energy transfers correspond to neutron energy loss, and positive values to neutron energy gain. Since the energy transfer cannot be measured at DNS, all quasielastically scattered neutrons detected at a certain angle are treated as elastically scattered and allocated to an incorrect scattering vector Q. This effect is schematically indicated by the blue arrows.

fulfilled for typical molecular liquids, and as a consequence the Placzek correction fails to correct the measured structure factors [110]. Therefore the inelastic scattering effects are (if at all) corrected only by empirical fitting approaches in some studies [111, 112].

In the framework of this thesis neither the Placzek correction nor an empirical correction is applied to the measured data. Instead, the structure factors obtained from the MD simulations are modified to account for the inelastic scattering effects. The intensities calculated from the simulations are shifted along the detector lines to zero energy transfer, as exemplarily indicated in figure 4.4. This procedure is described in section 5.4.

5 Molecular Dynamics Simulations

Molecular dynamics (MD) simulations are a powerful tool to access (in principle) all possible observables of any complex (classical) system, for example to understand molecular genetics on an atomic level [7]. In general, MD simulations are based on the calculation of the net force $\vec{F}_i$ acting on an atom i of mass m_i at position $\vec{r}_i$, defined by the negative derivative of a potential function V

$$\vec{F}_i = -\frac{\partial V}{\partial \vec{r}_i}. \tag{5.1}$$

The resulting displacement of the atom is consequently determined via

$$\frac{\partial^2 \vec{r}_i}{\partial t^2} = \frac{\vec{F}_i}{m_i}. \tag{5.2}$$

These steps are the main parts of the basic global MD algorithm, which is illustrated in figure 5.1.

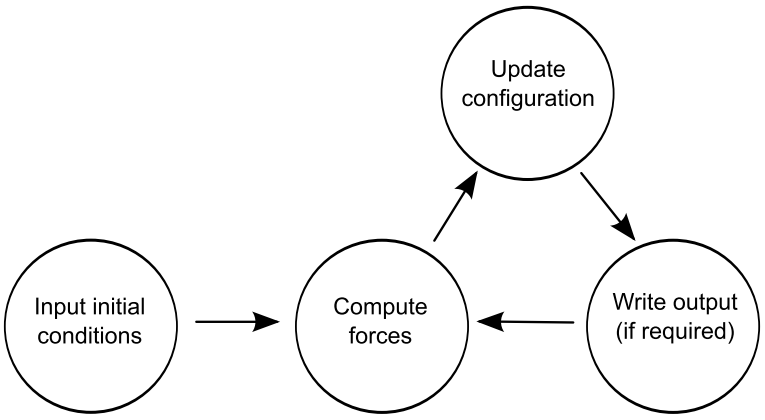

Figure 5.1: Global MD simulation algorithm [113].

Two basic elements have to be specified in order to perform MD simulations: i) The model describing the interaction between atoms. The most accurate way is to calculate the interactions at the quantum level [114]. These ab initio simulations are very CPU-intensive due to the electron-electron-coupling term in the Hamiltonian.

Hence to approximate the interatomic potential, empirical functions are used, called the force field. ii) The method to calculate the movement of the atoms and the way to integrate the equations of motion. Typically Newton's equations of motion (eq. 5.2) are extended to control the temperature and pressure of the system, and then integrated numerically for discrete time steps δt.

The accuracy and validity of the simulations are limited by this framework. The choice of force field is crucial for the correct representation of micro- and macroscopic properties, and already little changes of only one parameter can have huge effects on the resulting structural and dynamical properties. The simulation time step has to be chosen meeting two conditions: On the one hand it has to be as short as possible to improve the precision of the integration of motion. On the other hand the time step should be long in order to achieve reasonable calculation time and to avoid errors due to numerical imprecision.

5.1 Structure of Force Fields

A large number of force fields are available for the simulation of various (bio)molecules [115]. Although they have a similar layout, based on mathematical functional forms, it is the parameters that differentiate the individual force fields. Most force fields are empirical, as the underlying functions are based on several approximations and the parameters are usually derived from experimental data.

In the following a quick overview of the basic components of force fields will be given. In principle a force field can be divided into three basic parts: Bonded and non-bonded interactions as well as constraints. The latter can be applied to confine e. g. bond lengths or bond angles. Since they were not used in the framework of this thesis they will not be further discussed. More detailed descriptions can be found in the literature [113, 116, 117].

Non-Bonded Interactions

The non-bonded interactions describe the pair potential between any two atoms at distance r_{ij}, i. e. they act between inter- and intramolecular atoms. An intermolecular attraction stronger than the average kinetic energy of the atoms leads to the formation of a condensed phase.

Repulsion and Dispersion These terms are usually combined in the Lennard-Jones potential [118]

$$V_{\mathrm{LJ}}(r_{ij}) = 4\epsilon \left[\left(\frac{\sigma}{r_{ij}} \right)^{12} - \left(\frac{\sigma}{r_{ij}} \right)^{6} \right], \tag{5.3}$$

where ϵ characterizes the depth of the potential and σ is the distance at which the energy is zero (cf. fig. 5.2). The attractive r_{ij}^{-6}-term accounts for the van der Waals force, or London force between unpolar molecules or atoms. A spontaneous polarization of an atom induces a dipole in nearby atoms, leading to a weakly attractive force. The repulsive r_{ij}^{-12}-term describes the repulsion at short range, where the electron-electron interaction is strong, resulting from the Pauli exclusion principle. Although the r_{ij}^{-12}-term has no theoretical justification, it fairly describes the Pauli repulsion. Besides the calculation of r^{12} as the square of r^6 is computational efficient. In the Buckingham potential [119] the repulsive term is exponential, which is more realistic, but also more expensive to compute.

The Lennard-Jones interactions are typically calculated up to a specific cut-off distance, justified by the rapid decay of the attractive force with increasing distance.

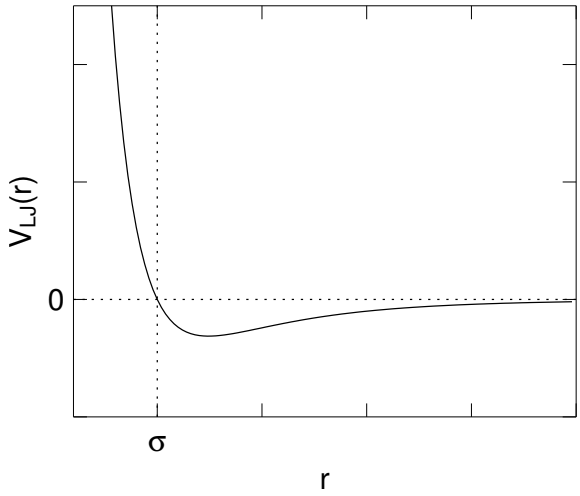

Figure 5.2: Lennard-Jones potential, which is typically applied to model repulsive and dispersive forces.

Electrostatic Interaction This term accounts for the forces between two particles with charges $q_{i,j}$, which is given by the Coulomb potential [120]

$$V_C(r_{ij}) = \frac{1}{4\pi\epsilon_0} \frac{q_i q_j}{r_{ij}} \tag{5.4}$$

with the vacuum permittivity ϵ_0. This term is the computationally most expensive one, because its effect does not decay as rapidly as the interaction modeled by the Lennard-Jones potential. Therefore, this term should be calculated for many pairs of atoms in the system.

Bonded Interactions

The bonded interactions account for the intramolecular potentials which are due to the covalent bonds, or extend over one or two atoms along the chain, as schematically illustrated in figure 5.3. The interactions between first and second neighboring atoms are mainly quantum mechanical, and hence cannot be modeled by a Lennard-Jones potential. They are therefore explicitly excluded from the non-bonded Lennard-Jones interactions and typically modeled by harmonic terms [113].

Concerning third neighbors, also called 1–4 pairs, the Lennard-Jones repulsion is often too strong, especially in the case for carbon-carbon interactions in a *cis*-conformation [113]. To avoid a resulting deformation or breakage of the molecule, non-bonded interactions are reduced for the 1–4 pairs. The factors, by which repulsion, dispersion and electrostatics are scaled are defined within the applied force field.

Figure 5.3 illustrates the basic bonded interactions, which will be described in the following.

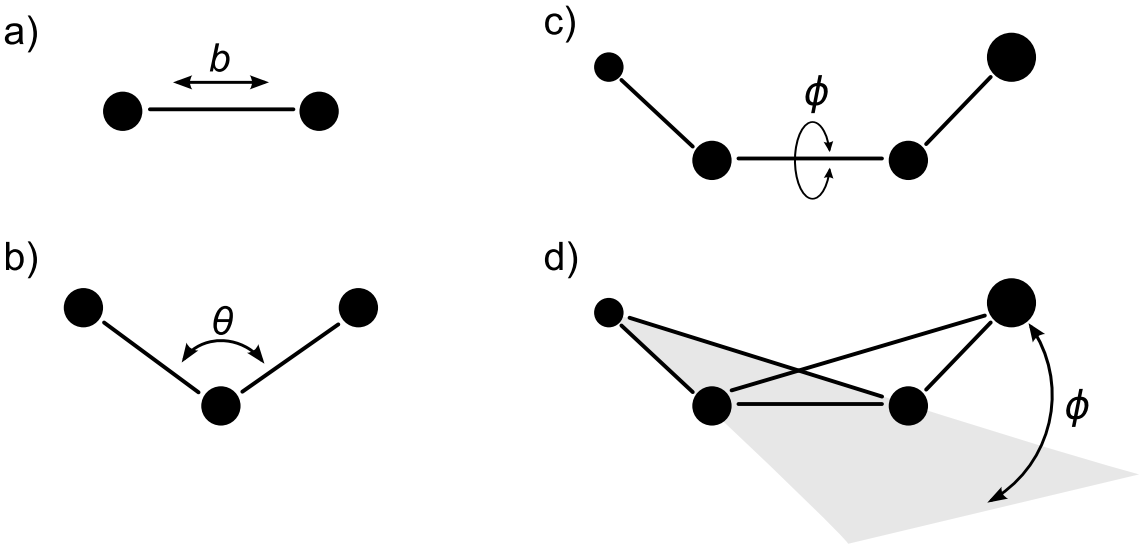

Figure 5.3: Schematic illustration of bonded interactions: a) Bond stretching, b) angle bending, c) proper and d) improper dihedral rotation.

Bond Stretching The bond stretching term describes the force between two covalently bonded atoms. When the bond is compressed the electron cloud of the two atoms overlap, leading to an increase in energy. Stretching the bond will also lead to an increase of energy, and eventually the bond will disassociate. The Morse potential [121, 122] describes this behavior and is a convenient model when simulating diatomic molecules. Since the deviations from the equilibrium bond length is usually very small in molecular dynamics simulations, the potential can be assumed to be approximately harmonic of the form [113]

$$V_{\mathrm{b}}(b) = \frac{1}{2}k^{\mathrm{b}}(b - b_0)^2, \tag{5.5}$$

with a force constant k^{b} and the average distance b_0 between the atoms. The forces due to the covalent bonds are very high in comparison to other forces, justifying the use of the harmonic approximation.

Angle Bending This term models the force due to the deformation of the valence angles between three covalently bonded atoms. The potential is also represented by a harmonic potential [113]

$$V_a(\theta) = \frac{1}{2}k^{\theta}(\theta - \theta_0)^2, \tag{5.6}$$

with a force constant k^{θ} and the equilibrium angle θ_0. These forces are typically smaller than the ones due to bond stretching.

Torsional Terms - Dihedrals Defining the rotational barriers between four covalently bonded atoms. For single bonds the torsional interaction is soft compared to bond stretching and angle bending, hence the changes in dihedral angles can be large. Torsional angle rotation is of utmost importance for the simulation of biomolecules, as large-scale dynamics strongly depend on the interplay of the dihedrals with the non-bonded interactions [123]. There are two types of dihedrals: Proper and improper dihedrals.

In a proper dihedral ϕ is the angle between the planes spanned by atoms (1,2,3) and (2,3,4) of a linear chain (see fig 5.3), and $\phi = 0$ corresponds to the *cis*-configuration of the group. Since the potential is periodic through a 360° rotation, it

cannot be approximated by a Taylor series or harmonic term. It is hence described by a cosine function as [113]

$$V_{\mathrm{d}}(\phi) = k^{\phi} \left[1 + \cos(n\phi - \phi_0)\right] \tag{5.7}$$

with a force constant k^{ϕ}, defining the barrier heights, the periodicity or multiplicity n and the phase ϕ_0. Adding 1 to the cosine sets that the resulting energy is always larger than zero [116]. For alkanes, the Ryckaert-Bellemans function is used to represent the dihedral potential according to

$$V_{\mathrm{rb}}(\phi) = \sum_{n=0}^{5} C_n \left(\cos(\psi)\right)^2 \tag{5.8}$$

with a parameter set C_n and $\psi = \phi - 180°$.

Improper dihedrals are used to retain planar groups (e. g. aromatic rings) and to conserve the chirality in a tetrahedral geometry. As they are not present in linear chains, they are not of interest for this work and therefore not further discussed.

5.2 Temperature & Pressure Control and MD Integrator

In classical MD simulations the total number of atoms N, the volume V and the total energy E of the simulation system are conserved, resulting in a microcanonical (NVE) ensemble. However, rounding and truncation errors will cause a small drift in energy. For large systems the fluctuations in temperature, which is a statistical quantity, are small and can be approximated as constant. NVE ensembles are amongst others useful for the study of constant-energy surfaces of the conformational space [124].

The simulation of biomolecules requires a precise temperature T control to account for the raise in temperature when exothermic conformational changes take place. In the resulting canonical (NVT) ensemble the energy of the system is adjusted to retain the desired temperature, by e. g. rescaling the velocities. The temperature control is needed to simply simulate a constant temperature ensemble or to regulate the temperature when performing simulated annealing.

To meet lab conditions pressure P needs to be conserved instead of the volume. This results in the isothermal-isobaric (NPT) ensemble, where the pressure scales the dimension of the simulation box. This additional coupling results in a greater perturbation compared to those in an NVT ensemble.

In the following several methods for temperature and pressure coupling will be described briefly. These methods give scaling factors which are allowed for in the configuration update step of the global MD algorithm (cf. fig. 5.1). Afterwards these temperature and pressure control algorithms will be compared to each other.

Temperature Coupling

The instantaneous temperature T of the simulation system is calculated as

$$T = \frac{2K}{N_\mathrm{f} k_\mathrm{B}}, \tag{5.9}$$

with the total kinetic energy K, the number of degrees of freedom N_f and the Boltzmann constant k_B [113].

Berendsen The Berendsen algorithm [125] describes a weak coupling to a heat bath with temperature T_0. The principal correction of the system temperature T follows

$$\frac{\mathrm{d}T}{\mathrm{d}t} = \frac{1}{\tau}(T_0 - T), \tag{5.10}$$

resulting in a damped exponential relaxation, with a time constant τ. A short value of τ results in a stronger coupling to the heat bath, while a longer τ has a minor influence. Inserting friction and stochastic terms into the equations of motion results in a scaling of the velocities with the factor

$$\lambda = \left[1 + \frac{\Delta t}{\tau_\mathrm{T}}\left(\frac{T_0}{T} - 1\right)\right]^{1/2} \tag{5.11}$$

for a timestep Δt. The temperature coupling time constant τ_T is not exactly equal to the time constant τ of equation 5.10. As the scaling causes a redistribution of kinetic energy between kinetic and potential energy, the change in temperature is less than desired [113].

The Berendsen thermostat is often used for equilibration purposes, especially when the system is far from equilibrium. However, it has no conserved quantity and does not generate a correct canonical ensemble [113].

Velocity Rescaling The velocity rescaling (v-rescaling) thermostat [126] is an extension of the Berendsen thermostat, producing a correct ensemble. This is done by adding a random force to ensure the correct distribution of the kinetic energy. In principle, the velocities are multiplied by a factor $\alpha = \sqrt{K_0/K}$, to force the total kinetic energy K towards the average kinetic energy at the target temperature K_0. The rescaling is eventually done by using an auxiliary dynamics as

$$\mathrm{d}K = (K_0 - K)\frac{\mathrm{d}t}{\tau_\mathrm{T}} + 2\sqrt{\frac{KK_0}{N_\mathrm{f}}}\frac{\mathrm{d}W}{\sqrt{\tau_\mathrm{T}}}, \tag{5.12}$$

where dW is a Wiener noise [113]. Dropping the additional stochastic term (second term in the equation) again gives the Berendsen thermostat.

This v-rescaling algorithm leads to a fast equilibration when the system is far from equilibrium, just as the Berendsen algorithm does. Furthermore it also samples the correct canonical ensemble once the equilibrium is reached. It is therefore used in the framework of this thesis for the initial equilibration of the simulation system.

Nosé-Hoover The Nosé-Hoover algorithm, or also called the extended-system method, was first introduced by Nosé [127] and later reformulated by Hoover [128]. In this approach the heat bath is considered as an integral part of the system. An artificial dynamical variable s is added, associated with a mass q_s and a momentum p_s. The equations of motion are replaced by

$$\frac{\mathrm{d}^2\vec{r}_i}{\mathrm{d}t^2} = \frac{\vec{F}_i}{m_i} - \xi\frac{\mathrm{d}\vec{r}_i}{\mathrm{d}t}, \tag{5.13}$$

with the thermodynamic friction coefficient $\xi = p_s/q_s$. The equations of motion for the thermostat parameter ξ are

$$\frac{\mathrm{d}p_\xi}{\mathrm{d}t} = \frac{1}{q_s}\left[\sum m\frac{\mathrm{d}\vec{r}}{\mathrm{d}t} - (N_\mathrm{f}+1)k_\mathrm{B}T_0\right] \sim (T - T_0). \tag{5.14}$$

The right-hand term is the difference between the current kinetic energy of the system and the one at the desired temperature. If the current temperature is higher than T_0, the friction will increase, and vice versa.

The mass parameter q_s determines the coupling strength. Large values of q_s correspond to a loose coupling, requiring long equilibration times. A tight coupling however may cause high-frequency oscillations of the temperature. The main difference to the weak coupling thermostats is the oscillatory relaxation of the Nosé-Hoover coupling, resulting in longer equilibration times. The parameter q can be related to a reference temperature T_0 with a time constant τ_T via

$$q_s = N_\mathrm{f}k_\mathrm{B}T_0\tau_\mathrm{T}. \tag{5.15}$$

The time constant should be 4–5 times larger than the value used with the weak coupling algorithms (Berendsen or v-rescaling thermostats) [113].

This thermostat also samples the correct ensemble [129]. In contrast to the weak coupling methods the Nosé-Hoover algorithm allows for fluctuations that produce more natural dynamics. However, because does it allow for these fluctuations, the Nosé-Hoover thermostat is less suited for the equilibration of systems that are far from equilibrium, as will be pointed out later. A detailed comparison with the Berendsen scheme can be found in the literature [130].

Pressure Coupling

Controlling the pressure P means controlling the box volume V. For isotropic systems, which are dealt with in this thesis, the pressure is given by the difference between the kinetic energy K and the virial Ξ by $P = 2(K - \Xi)/(3V)$. The adjustment of the pressure is accomplished by scaling the interparticle distances (by simply scaling the coordinates) and thereby shifting the virial.

Berendsen Analogous to the Berendsen thermostat, the pressure P of the system is relaxed exponentially to a reference pressure P_0 according to

$$\frac{\mathrm{d}P}{\mathrm{d}t} = \frac{P_0 - P}{\tau_\mathrm{P}}, \tag{5.16}$$

with a time constant τ_P [125]. The scaling factor, which is similar to equation 5.11, reads as

$$\mu = \left[1 - \frac{\Delta t}{\tau_\mathrm{P}} \beta \left(P_0 - P(t)\right)\right]^{1/3}. \tag{5.17}$$

The isothermal compressibility β is related to a change in pressure via

$$\frac{\mathrm{d}P}{\mathrm{d}t} = -\frac{1}{\beta V}\frac{\mathrm{d}V}{\mathrm{d}t}. \tag{5.18}$$

Since β only influences the time constant τ_P for coupling, and not the pressure itself, a rough estimate for the compressibility is already sufficient. Typically the compressibility of water at room temperature ($\beta = 4.5 \cdot 10^{-5}\,\mathrm{bar}^{-1}$) is used for many systems. Isothermal compressibilities for various molecular liquids can be found in the literature [131].

The Berendsen barostat does not generate a proper ensemble as it does not reproduce the correct distribution of pressures. It is simply able to reproduce the correct average pressure. If the system pressure is far from the desired reference pressure, the Berendsen barostat allows for a fast equilibration. It is therefore used to perform an initial coarse equilibration of the simulation system in the framework of this thesis.

Parrinello-Rahman Similar to the motivation for implementing the Nosé-Hoover thermostat, the Parrinello-Rahman barostat [132, 133] is used to obtain a more precise behavior of the pressure. It was first developed for simulating crystal struc-

tures, allowing for a necessary change of the shape of the simulation box. Using the Parrinello-Rahman algorithm, the equations of motion become

$$\frac{\mathrm{d}\vec{r}_i^2}{\mathrm{d}t^2} = \frac{\vec{F}_i}{m_i} - \mathbf{M}^{-1}\frac{\mathrm{d}\mathbf{M}}{\mathrm{d}t}\frac{\mathrm{d}\vec{r}_i}{\mathrm{d}t}. \tag{5.19}$$

Here $\mathbf{M} = \mathbf{h}^{\mathrm{T}}\mathbf{h}$ is the metric tensor of the box matrix $\mathbf{h}$, which consists of the box vectors. Eventually the box vectors are coupled to the reference pressure P_0 as

$$\frac{\mathrm{d}\mathbf{h}^2}{\mathrm{d}t^2} = V\mathbf{W}^{-1}(\mathbf{h}^{\mathrm{T}})^{-1}(P - P_0), \tag{5.20}$$

where the mass parameter matrix $\mathbf{W}$ controls the coupling strength. Similar to the Nosé-Hoover thermostat, $\mathbf{W}$ can be related to a time constant τ_{P} as

$$\mathbf{W}^{-1} \sim \frac{\beta}{\tau_{\mathrm{P}}^2}, \tag{5.21}$$

again with the isothermal compressibility β.

In combination with a proper thermostat the Parrinello-Rahman barostat allows for the generation of a proper NPT ensemble. However, it might produce large volume oscillations, especially if the system is not well equilibrated. Hence the Parrinello-Rahman coupling scheme is unfavorable if the system pressure is far off the reference pressure, as will be demonstrated in the following comparison. It is used in this thesis only after a thorough equilibration with the Berendsen barostat.

Comparison of the Coupling Algorithms

In the preceding paragraphs two general principles for coupling to a heat- or pressure-bath were described. Additional algorithms exist, as e. g. the stochastic dynamics algorithm [134–136] or stochastic-coupling method [137]. But since these are less commonly used for MD simulations they will not be further considered.

The effect of the different coupling methods is exemplarily illustrated in figure 5.4. There are advantages and disadvantages for the use of these algorithms, which will be briefly outlined in the following.

Berendsen and Velocity Rescaling Algorithm These weak coupling methods allow for a fast and smooth first-order approach to equilibrium, as can be seen in figure 5.4. But once equilibrium is reached the Berendsen algorithm is less useful,

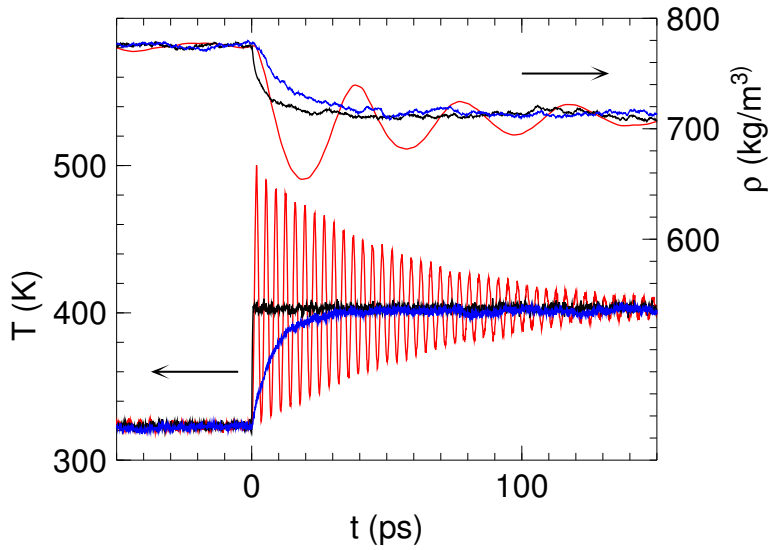

Figure 5.4: Response of the temperature (lower graphs) and density (upper graphs) during a instantaneous change of the reference temperature T_0 from 50°C to 130°C at $t = 0\,\text{ps}$. The reference pressure was set to 1 atm. The simulation system contains 512 $C_{16}H_{34}$ molecules. Different methods for temperature- and pressure-coupling were applied:
Red: Nosé-Hoover ($\tau_T = 4\,\text{ps}$) and Parrinello-Rahman ($\tau_P = 20\,\text{ps}$)
Black: v-Rescaling ($\tau_T = 0.1\,\text{ps}$) and Berendsen ($\tau_P = 1.0\,\text{ps}$)
Blue: v-Rescaling ($\tau_T = 4\,\text{ps}$) and Berendsen ($\tau_P = 1\,\text{ps}$)
Note that the absolute densities are slightly incorrect, as will be discussed later.

since it cannot produce a correct canonical ensemble. The symplectic v-rescaling thermostat, published some years ago, replaces the quite old Berendsen temperature coupling scheme. In this work the v-rescaling coupling method was used together with the Berendsen barostat to create starting structures at the desired temperature and pressure. After this coarse equilibration a fine equilibration was performed by applying the Nosé-Hoover and Parrinello-Rahman coupling methods.

Nosé-Hoover and & Parrinello-Rahman Algorithm These methods cause a slow second-order approach to equilibrium and are hence less applicable for equilibration. When the system is far from equilibration, an initial equilibration using the Nosé-Hoover and & Parrinello-Rahman coupling schemes can take relatively long, or can even cause a blowing up of the system. As can clearly be seen in figure 5.4, these algorithms cause large oscillations when temperature or pressure is a little off. But since they maintain a canonical ensemble they are the first choice for simulation after equilibrium has been reached using weak coupling schemes. They were hence applied after the desired temperature and pressure was reached with the weak coupling methods. A detailed overview of the equilibration procedure will be given later.

Integration of the Equations of Motion

From the potential energy V the force $\vec{F} = -\vec{\nabla}V$ acting on an atom and eventually its acceleration $\vec{a} = \vec{F}/m$ is known. But since the potential energy is a function of the positions of all atoms in the system, the equations of motion cannot be solved analytically. The integrator is needed to numerically calculate the displacements of the atoms at discreet time steps δt. After the integration the time point is updated as $t = t + \delta t$. The integration algorithm should allow for energy and momentum conservation.

Both integrators presented below have three important characteristics [138]: First of all they are invariant under time reversal, just as Newton's equations of motion. Secondly they guarantee an exact conservation of angular momentum, however energy is not exactly conserved. Finally both integrators are symplectic, in other words they preserve phase space density [123]. This results in good energy conservation which guarantees the stability of the integration scheme [123, 139]. A detailed comparison of several algorithms for molecular dynamics can be found in [140].

The Leap-Frog Integrator In the so-called leap-frog algorithm [141] the velocities are calculated at intermediate time steps $t + 1/2\,\delta t$. With these the positions at $t + \delta t$ are calculated. Hence the positions leap over the velocities and vice versa as

$$\vec{r}(t + \delta t) = \vec{r}(t) + \vec{v}\left(t + \frac{1}{2}\delta t\right)\delta t, \tag{5.22}$$

$$\vec{v}(t + \frac{1}{2}\delta t) = \vec{v}\left(t - \frac{1}{2}\delta t\right) + \vec{a}(t)\delta t. \tag{5.23}$$

A disadvantage of this integrator is that the velocities are not calculated explicitly at time t. They can only be approximated by*

$$\vec{v}(t) = \frac{1}{2}\left[\vec{v}\left(t - \frac{1}{2}\delta t\right) + \vec{v}\left(t + \frac{1}{2}\delta t\right)\right]. \tag{5.24}$$

Because of its simplicity and therefore fast computation the leap-frog integrator was applied for all simulations presented in this thesis.

*Only necessary if explicit velocities are needed in the output file.

The Velocity Verlet Integrator With the velocity Verlet algorithm [142] positions, velocities and accelerations are calculated a the same time step $t + \delta t$ using the equations

$$\vec{r}(t + \delta t) = \vec{r}(t) + \vec{v}(t)\delta t + \frac{1}{2}\vec{a}(t)\delta t^2, \tag{5.25}$$

$$\vec{v}(t + \delta t) = \vec{v}(t) + \frac{1}{2}\left[\vec{a}(t) + \vec{a}(t + \delta t)\right]\delta t. \tag{5.26}$$

This method has the advantage that the kinetic energy is available at each time step and provides a higher precision than the leap-frog integrator. The drawback is however a less efficient computation, due to the more complex form of the integrator.

5.3 Simulation Procedure

In the preceding section the basics of classical MD simulations were briefly explained. In the framework of this thesis the program package GROMACS[†] [143] was used to carry out the simulations. The GROMACS project was started by the Herman Berendsen group of the Biophysical Chemistry department of Groningen University in the early 1990s. Nowadays it is maintained and further developed by numerous contributors across the world.

Since the beginning GROMACS has been continuously optimized[‡]. It was chosen in the framework of this thesis because of its relatively high performance and popularity, which comes along with broad support.

In the following the choice of force field used for the simulations will be motivated, following by a summary of the simulation procedure.

Used Force Fields

MD simulations allow for the calculation of the motion of molecules, which are subject to several forces, as outlined above. To account for the internal structure of the molecules, two general approaches exist to divide the chains into single subunits. The first approach is to treat several atoms as a single interaction site [145]. For alkanes each carbon atom with its bonded hydrogen forms such a pseudo-atom, hence the equations of motion are only integrated for methyl and methanediyl groups as a whole. This coarse-graining is called the united atom (UA) or extended atom representation. For the simulation of n-alkanes the UA models are known to overestimate the self-diffusion and local dynamics [19, 21, 27, 146].

The second approach is to include all atoms explicitly, including nonpolar hydrogen atoms [147]. These all atom (AA) or explicit atom simulations are obviously more realistic but are also much slower in computation, due to the increased number of interaction sites. In this thesis all atom simulations were performed to account for the motion of the individual hydrogen atoms, which are eventually observed with quasielastic neutron scattering on the picosecond time scale.

Many all atom force fields exist for the simulation of of alkanes. One of the more popular ones is the OPLS-AA force field ("Optimized Potentials for Liquid Simula-

[†]Short for GROningen MAchine for Chemical Simulations.
[‡]Total estimated effort: 451 person years (03/13) [144].

tions") [148][§]. It was parameterized for organic liquids by optimizing liquid densities and heats of vaporization. However, the OPLS-AA force field has some drawbacks: It gives deviations for the heats of vaporization for alkane chains longer than hexane (C_6H_{14}) [149], predicts a incorrect critical temperatures for short alkanes [150, 151] and yields phase transition temperatures for pentadecane ($C_{15}H_{32}$) that are far above the experimental value [152].

Chang and Sandler reparameterized the Lennard-Jones parameters for interatomic interactions, keeping the original intramolecular potentials as defined in the OPLS-AA force field [153]. Since this reparameterized force field already predicted fair agreement with quasielastic neutron scattering data for dotriacontane ($C_{32}H_{66}$) [19], it was adapted for the simulation work in this thesis. It is able to better reproduce experimental liquid densities and enthalpies of vaporization [153], but still yields a too high melting temperature, as will be presented later. In order to lower the melting temperature, the explicit 1–4 pair interactions (see section 5.1) were neglected in this thesis. In the original Chang & Sandler force field both the Coulomb and Lennard-Jones forces for third neighbors along the molecular chain are scaled with a factor of 0.5. Neglecting the nonbonded interactions for these 1–4 pairs results in a lower melting temperature, with only a marginal effect on the dynamics. Throughout this thesis all simulations and respective results were obtained using the Chang & Sandler force field without explicit non-bonded 1–4 pair interactions, unless otherwise stated.

In a recent work Siu et al. refined the torsional parameters and Lennard-Jones potential for long hydrocarbons [152]. This optimized parameter set, named L-OPLS, produces phase transition temperatures, diffusion coefficients and viscosities which are in better agreement with experimental results than the other force fields described above. As will be demonstrated later, first comparisons show that the L-OPLS force field reproduces very similar short-time dynamics as obtained with the force field parameters of Chang & Sangler, but can describe static properties more accurately. However, the simulation expense increases due to a more sophisticated simulation procedure, including amongst others a switch function to shift the Lennard-Jones potential and the use of long range dispersion corrections for energy and pressure [154].

[§]Cited more than 3000 times (02/13).

Building a Simulation System

In the following a quick guideline will be given, to illustrate how the n-alkane simulation systems were prepared in general.

1. Write molecule backbone in a stretched conformation, with bond lengths and bond angles according to the force field.
2. Add hydrogen atoms, either manually or by using e. g. the software PYMOL [155].
3. Generate a simulation box, using the GROMACS program genbox, and use this program to randomly fill in the molecules (or molecule clusters).
4. Perform an energy minimization routine, in case molecules were placed too close to each other resulting in huge repulsion forces.
5. Equilibrate the system in an NVT ensemble.
6. Equilibrate the system in an NPT ensemble.

To generate large systems (>100,000 atoms), a small cluster of molecules was generated with the above procedure. This cluster was then multiple placed in a large simulation box according to step 3. Afterwards the system was equilibrated analogous to steps 4–6.

In this way two systems were generated: A hexadecane system containing 512 $C_{16}H_{34}$ molecules (25,600 atoms), and a hectane system with 4096 $C_{100}H_{202}$ chains (1,236,992 atoms). Furthermore short simulation runs were performed on a tetratetracontane simulation system, containing 2048 $C_{44}H_{90}$ molecules (274,432 atoms), to test among others the scaling behavior of GROMACS. The resulting box length of all simulation systems is more than twice as long as a stretched molecule. This should suppress any artifacts resulting from the finite box size in combination with periodic boundary conditions.

Simulation Parameters

All simulations were performed using the leap-frog method to integrate the equations of motion with a time step of $\delta t = 1\,\mathrm{fs}$. Periodic boundary conditions were applied in all directions. The neighborlist, based on which of the non-bonded interactions are computed, is updated every 10 fs with an cutoff radius of 1.0 nm. All forces due to non-bonded interactions with distances between 1.0 nm and the Lennard-Jones cutoff of 2.0 nm are calculated only during the update routine of the neighborlist.

Electrostatics were calculated using the Particle-Mesh Ewald (PME) method [156]. With this the total electrostatic energy is split into a short-range part, a long-range part and a constant term. The short-range part is directly calculated in real space, while the long-range summation is done in reciprocal space. In this procedure the charges are assigned to a mesh, which is then Fourier transformed. The allocation of load between the real and reciprocal space calculation of the Ewald sum allows for an effective calculation of the electrostatic potential when simulating on a computer cluster. For the short-range interactions a Coulomb-cutoff of 1.0 nm was chosen.

Slightly different simulation parameters were applied when the L-OPLS force field of Siu et al. was used. The differences are apparent from the partial simulation input parameters given in appendix B on page 177.

Coarse Equilibration Initial velocities were generated according to a Maxwell-Boltzmann distribution. For the initial equilibrations, when the system was far from equilibrium, the velocity-rescaling thermostat with a time constant $\tau_T = 0.1\,\mathrm{ps}$ and the Berendsen barostat with a time constant of $\tau_P = 1.0\,\mathrm{ps}$ were applied.

Fine Equilibration and Production Run When equilibrium was reached, the temperature and pressure coupling algorithms were changed to the Nosé-Hoover ($\tau_T = 4\,\mathrm{ps}$) and Parrinello-Rahman ($\tau_P = 20\,\mathrm{ps}$) methods, respectively. After a fine equilibration routine production runs were performed with the same parameters.

If pressure coupling was applied, the reference pressure was set to $1.01325 \cdot 10^5\,\mathrm{Pa}$, and a compressibility of $4.5 \cdot 10^{-10}\,\mathrm{Pa}^{-1}$ was used. The temperature was shifted by applying the v-rescaling thermostat with $\tau_T = 4\,\mathrm{ps}$, followed by the fine equilibration routine described above.

Table 5.1: Overview of the n-alkane simulation systems used in the framework of this thesis.

System	total length	output step
$512 \times C_{16}H_{34}$	1 ns	0.1 ps
	5 ns	0.5 ps
$4096 \times C_{100}H_{202}$	20 ps	0.1 ps
	200 ps	1 ps
	2 ns	10 ps
	20 ns	100 ps

The total length and output-frequency of the individual production runs were adjusted to result in manageable sizes of the output files. An overview listing these characteristics is given in table 5.1.

In this way simulations were performed for $C_{16}H_{34}$ at $T = 293, 303, 363, 403, 443\,\mathrm{K}$ and for $C_{100}H_{202}$ at $T = 393, 453, 509\,\mathrm{K}$.

The $C_{16}H_{34}$ simulations were run on a 16-node cluster located at the Maier-Leibnitz Zentrum as well as on the Linux cluster of the Leibniz-Rechenzentrum (LRZ) [5]. The $C_{44}H_{90}$ and $C_{100}H_{202}$ systems were simulated on the latter cluster, while parts of the $C_{100}H_{202}$ simulations were performed on SuperMUC, the new supercomputer of the LRZ [5], using 960 nodes. The computation speed of production runs are illustrated in figure 5.5. A linear scaling can be observed for the $C_{100}H_{202}$ simulations performed on the Linux cluster. Using 960 nodes on SuperMUC results in an enhanced performance than expected by extrapolating the simulation speed obtained on the Linux cluster. Simulating the $C_{16}H_{34}$ system gives deviations from a linear scaling when using more than 100 processors. This is due to the relatively small system size, which is decomposed into small domains which are then allocated to the processors. Part of the total run time is then spent on inefficient communication between the processors.

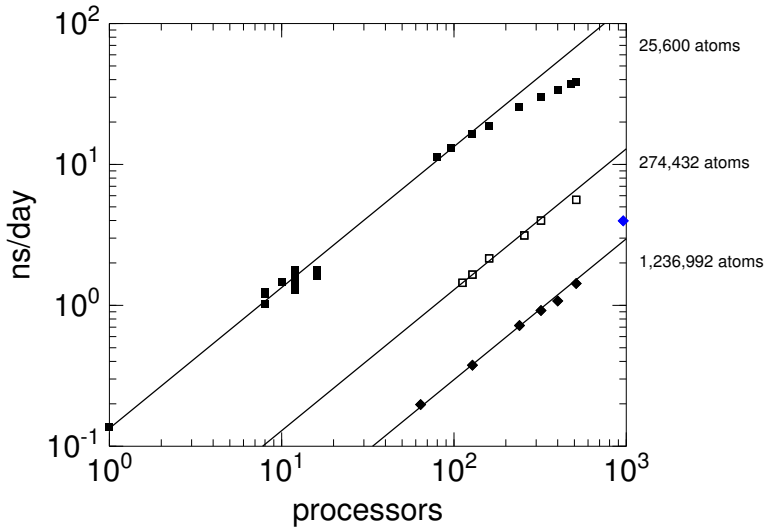

Figure 5.5: Scaling behavior of the production runs performed in the framework of this thesis. The solid lines illustrates a linear scaling behavior. The blue symbol represents the simulation performed on SuperMUC.

5.4 Data Analysis

On the one hand increasing computing power allows for performing extensive MD simulations, but on the other hand increasing computing power is needed to improve the analysis of the simulations. While a visual inspection of the trajectories allows for an initial evaluation of the prevailing molecular dynamics, the main part of the data analysis focuses on the efficient extraction of physical properties of interest from the trajectories.

Trajectory Conversion

netCDF The input file format for the program package *n*MOLDYN which was used to calculate scattering functions, is the netCDF format. Although *n*MOLDYN comes with several converters, GROMACS trajectories cannot directly be converted to netCDF (yet), but this is on the to-do list of the *n*MOLDYN developers [157]. Therefore the following conversion routine via the software VMD [158] was applied:

1. Create a snapshot in the pdb-format of the data at time $t = 0$, using the GROMACS program trjconv as:
   `trjconv -f trajectory.trr -s input.tpr -dump 0 -o snapshot.pdb`
2. In VMD: Read the *snapshot.pdb* file and then load the GROMACS trajectory file into the snapshot. Afterwards delete frame 0, which corresponds to the t=0 snapshot of the *snapshot.pdb* file. Finally save the trajectories as *trajectory.dcd*.
3. In *n*MOLDYN: Convert *snapshot.pdb* & *trajectory.dcd* to *trajectory.nc*.

In doing so the original time step information is lost. Either VMD does not translate the time step information correctly or writes a different variant of the dcd-format than *n*MOLDYN expects [157]. Therefore the time step of the *trajectory.nc* file is always 49 fs, and any time-dependent analysis produced with *n*MOLDYN must be corrected according to the true time step.

XYZ The conversion of the binary *trajectory.trr* file into human readable coordinate-files was done by using the GROMACS programs trjconv and g_traj as follows:

1. `trjconv -f trajectory.trr -s input.tpr -pbc mol`
   `-o trajectory_pbc.trr`
   With this procedure jumps across the periodic boundaries are removed.

2a. `g_traj -f trajectory_pbc.trr -s input.tpr -nojump -fp -ox trajectory_pbc.xyz`

2b. `g_traj -f trajectory_pbc.trr -s input.tpr -nojump -fp -ox trajectory_pbc_subgroup.xyz -n subgroup.ndx`

2c. `g_traj -f trajectory_pbc.trr -s input.tpr -nojump -fp -ox trajectory_pbc_com.xyz -n molecules.ndx -ng` (# of molecules) `-com`

The output using command 2a contains all trajectories from the input file. Optionally a subgroup, for example a certain chemical element, can be selected by providing the corresponding index file generated with the GROMACS program make_ndx in command 2b [113]. Similar the center-of-mass coordinates can be extracted by listing a subgroup for each molecule in a *molecules.ndx* index file and executing command 2c.

Real-Space Analysis of the Simulations

The GROMACS package offers many programs for analysis of the simulated trajectories, which are documented elsewhere [113]. Few of them were used in the framework of this thesis, among others:

g_msd Calculates mean-square displacements, averaged over all atoms or those provided in an optional index file. Hence by providing an index file *molecules.ndx*, which lists a subgroup for each molecule, MSDs for the center-of-mass coordinates were obtained.

g_vanhove Produces van Hove correlation functions. Using the option `-or`, the respective probabilities of atomic displacements during a certain time interval t are calculated as a function of distance r.

g_analyze This program was used to produce autocorrelation functions of ASCII data sets, by using the option `-ac`.

These programs allow for a straightforward evaluation of the simulated dynamics. More sophisticate analysis was performed by running self-written Python scripts to calculate non-Gaussian parameter, dihedral autocorrelation functions or vector orientation autocorrelation functions among others. These scripts are given in appendix A on page 165.

Calculation of the Scattering Functions

The program package *n*MOLDYN [159, 160] is designed to perform analysis of MD simulation data. It was first written in Fortran 77 in the early 90's by Gerald Kneller and coworkers, and has meanwhile been adapted to Python. In this thesis *n*MOLDYN was mainly used to calculate scattering functions from the simulated trajectories.

For the calculation of time correlation functions from data with N_t time steps *n*MOLDYN uses the Fast Correlation Algorithm (FCA) [159], which is an efficient Fast Fourier Transform [161] ($\mathcal{FFT}$)-based method. With this method the complexity is reduced from $\mathcal{O}(N_t^2)$ to $\mathcal{O}(N_t \log N_t)$.

To account for the different weighting when calculating coherent and incoherent properties, specific weighting schemes for atom α in the system of N atoms are used as [162]

$$\sqrt{w_{\alpha,\mathrm{coh}}} = \frac{b_{\alpha,\mathrm{coh}}}{\sqrt{\sum_{\alpha=1}^{N} b_{\alpha,\mathrm{coh}}^2}}, \tag{5.27a}$$

$$w_{\alpha,\mathrm{inc}} = \frac{b_{\alpha,\mathrm{inc}}^2}{\sum_{\alpha=1}^{N} b_{\alpha,\mathrm{inc}}^2}. \tag{5.27b}$$

Here b is the scattering length, corresponding to the definitions in equations (4.3), averaged over both the isotopes and the relative spin orientations of neutrons and nuclei.

Note that these weighting schemes only account for the different scattering lengths of the atoms when calculating the incoherent and coherent dynamic structure factors. They do not take the ratio of incoherent and coherent scattering with respect to the total scattering into account, hence $\mathcal{I}_{\mathrm{inc}}(Q,t)$ and $\mathcal{I}_{\mathrm{coh}}(Q,t)$, calculated as described below, need to be weighted corresponding to the respective scattering cross sections before summing them to obtain the total dynamic structure factors $\mathcal{I}(Q,t)$.

Dynamic Incoherent Structure Factor The incoherent intermediate scattering function is computed as

$$\mathcal{I}_{\mathrm{inc}}(Q,t) \doteq \sum_{\alpha} w_{\alpha.\mathrm{inc}} \mathcal{I}_{\alpha,\mathrm{inc}}(Q,t). \tag{5.28}$$

The atomic incoherent scattering function

$$\mathcal{I}_{\alpha,\mathrm{inc}}(Q,t) = \overline{\left\langle \exp[-i\vec{Q}\vec{r}_\alpha(0)] \exp[i\vec{Q}\vec{r}_\alpha(t)] \right\rangle}^{Q}, \tag{5.29}$$

where $\overline{\ldots}^{Q}$ denotes an averaging over Q-vectors having approximately the same modulus, is calculated using the FCA algorithm.

Hence the incoherent scattering function is the sum of the correlation function for each atom. The cost is therefore $\mathcal{O}(N \cdot (N_t \log N_t))$. Moreover, the incoherent scattering function requires more I/O operations than the coherent scattering function, which adds even more overhead. As a result, the incoherent scattering function is one of the slowest analyses in *n*MOLDYN [157].

In order to reduce the calculation time of $\mathcal{I}_{\mathrm{inc}}(Q,t)$ for the $C_{100}H_{202}$ system, which contains more than 1.2 million atoms, dynamic incoherent structure factors were computed taking only 512 of total 4096 molecules into account. For the analysis of the $C_{16}H_{34}$ system all 512 molecules were considered. Q-values from 0.1 to 4 Å^{-1} were used, with Q-steps of 0.1 Å^{-1}. For each vector of Q 50 additional Q-vectors were computed in a shell $Q \pm 0.05\,\text{Å}^{-1}$, to account for a proper averaging in equation 5.29.

Dynamic Coherent Structure Factor The coherent intermediate scattering function, corresponding to equation 4.13, is calculated as

$$\mathcal{I}_{\mathrm{coh}}(Q,t) \doteq \overline{\left\langle \rho(-\vec{Q},0)\rho(\vec{Q},t) \right\rangle}^{Q}. \tag{5.30}$$

The Fourier transformed particle density is defined as

$$\rho(\vec{Q},t) = \sum_\alpha \sqrt{w_{\alpha,\mathrm{coh}}} \exp\left[i\vec{Q}\vec{r}_\alpha(t)\right]. \tag{5.31}$$

In this way the double sum in the definition of the coherent scattering function (eq. 4.11a) can be expressed as an autocorrelation function of the Fourier-transformed particle density. *n*MOLDYN calculates that density at $\mathcal{O}(N \cdot N_t)$ cost, and then uses the efficient FCA algorithm ($\mathcal{O}(N_t \log N_t)$) to calculate the scattering function.

The dynamic coherent structure factors were calculated taking all molecules in the systems into account. Analogous to the previous descriptions, 40 equidistant Q-values from 0.1 to 4 Å^{-1} were used with 50 sub-Q-shells.

Static Coherent Structure Factor The static structure factor is obtained by calculating equation 5.30 at $t = 0$

$$\mathcal{S}(Q) = \mathcal{I}_{\mathrm{coh}}(Q, 0). \tag{5.32}$$

For the $C_{16}H_{34}$ system $\mathcal{S}(Q)$ was calculated by averaging over 1000 time frames, while only 20 time frames were used for the larger $C_{100}H_{202}$ system. In both cases Q-values from 0.1 to 3 $\mathrm{Å}^{-1}$ were used, again with Q-steps of 0.1 $\mathrm{Å}^{-1}$. As before, 50 sub-Q-shells were averaged for each individual scattering vector.

Modification of the Simulated Static Structure Factor

During the neutron scattering experiment at DNS all inelastically scattered neutrons are treated as elastically scattered, as described in section 4.3 . Hence, at a constant angle, the detectors at DNS measure the total intensity

$$\int\limits_{\mathrm{const.}\theta} \mathrm{d}E_f \left(\frac{\mathrm{d}^2\sigma}{\mathrm{d}\Omega \mathrm{d}E_f} \right)_{\mathrm{coh}}. \tag{5.33}$$

However, the calculation of the static structure factor from the simulations takes these effects into account, as the integration is done at constant Q (cf. eq. 4.25). Hence the measured quantity cannot directly be compared with the static structure factor calculated with equation 5.32.

Since there is no precise procedure to correct the data measured at DNS, the intensities calculated from the MD simulations are allocated to a different Q-grid instead, corresponding to the experimental setup. This was done as follows: First the coherent intermediate scattering function $\mathcal{I}_{\mathrm{coh}}(Q, t)$ (eq. 5.30), calculated for a Q-range from 0.1 to 10 $\mathrm{Å}^{-1}$ with Q-steps of 0.1 $\mathrm{Å}^{-1}$ in this case, is Fourier transformed. From these scattering functions double differential scattering cross sections were obtained, according to (cf. eqs. 4.8, 4.9)

$$\left(\frac{\mathrm{d}^2\sigma}{\mathrm{d}\Omega \mathrm{d}E_f} \right)_{\mathrm{coh}} = \frac{k_f}{k_i} \frac{N}{4\pi} \mathcal{S}_{\mathrm{coh}}(Q, \omega). \tag{5.34}$$

With the approriate neutron wave length that was used at DNS the scattering angle 2θ is determined for each point in the spectra, corresponding to equation 4.1a. Following the scattering vector Q^{el} for elastic scattering is calculated by applying equation 4.1b. The integral of equation 5.33 was thereby calculated numerically.

The resulting $\mathcal{S}'_{\mathrm{coh}}(Q^{\mathrm{el}})$ is now comparable to the $S'_{\mathrm{coh}}(Q)$ as obtained from the neutron diffraction measurements at DNS.

The corresponding Python script is given in the appendix on page 175.

6 Dynamics Observed with Quasielastic Neutron Scattering

In a previous study [18], Smuda et al. performed quasielastic neutron scattering (QENS) experiments on 11 n-alkanes from octane (C_8H_{18}) to tetrapentacontane ($C_{54}H_{110}$). They evaluated both the measured scattering functions $S(Q,\omega)$ and intermediate scattering functions $I(Q,t)$ using various models to account for different local motions besides Fickean diffusion. The obtained diffusion coefficients were model-independent.

The instrumental resolutions used in their study corresponds to effective observation times of $55\,\text{ps} \leq t_{\text{obs}} \leq 70\,\text{ps}$. For all samples a clear Q^2-dependency of the quasielastic broadening was identified, indicating a diffusive motion of the atoms (cf. eq. 4.21). The short molecules showed the same diffusivity as observed with pulsed-field-gradient nuclear magnetic resonance (PFG-NMR) [11], which probes the dynamics on an extended time scale of milliseconds to seconds [1]. The long chains, however, moved too fast compared to the long-time PFG-NMR results (cf. fig. 6.1). Hence a Q^2-behavior of the broadening of the elastic line, which will be further on treated as characteristic for a diffusive motion according to Einstein's random walk theory, does not necessarily represent long range center-of-mass molecular self-diffusion. As a consequence the diffusion coefficients extracted from QENS will be termed apparent diffusion coefficients, unless they truly describe long range molecular self-diffusion.

Smuda et al. concluded that rather intramolecular motions were observed for the long n-alkanes, with a smaller activation energy compared to the one for long-range diffusion. The contribution of center-of-mass molecular self-diffusion on the overall observed short-time dynamics increased with decreasing chain length. A detailed study of the dynamics of liquid alkane systems on the pico- to nanosecond time scale allows for probing the fundamental steps of self-diffusion. The time scales on which

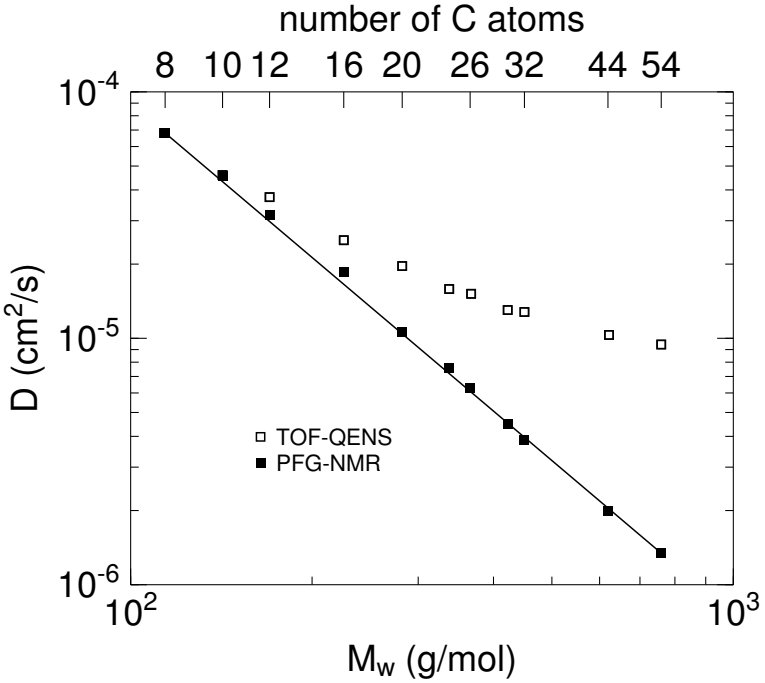

Figure 6.1: Diffusion coefficients of several n-alkanes measured with TOF-QENS (open symbols, $t_{\mathrm{obs}} = 50\,\mathrm{ps}$) and PFG-NMR (full symbols) [1, 11, 18] at $T = 383\,\mathrm{K}$.

the individual molecular motions occur can be moved by variation of molecular weight and temperature.

In order to gain a more detailed picture on the motions taking place at the onset of molecular self-diffusion, extensive QENS studies were performed in this work on the following model systems: Hexadecane ($C_{16}H_{34}$), hectane ($C_{100}H_{202}$) and poly(ethylene oxide) (PEO) with similar molecular weight as the n-alkane samples (cf. table 3.1).

For $C_{16}H_{34}$ the transition from local motions to translational self-diffusion takes place on the time window accessible with TOF-QENS. On a 55 ps time scale slight variations from long-range molecular self-diffusion can still be detected (cf. fig. 6.1). However, long range diffusion already dominates the signal observed with backscattering techniques on the short nanosecond time scale [163].

For $C_{100}H_{202}$ only minor contributions of molecular self-diffusion are expected on the picosecond time scale. A study of this system hence allows for classifying the local dynamics.

The structure of PEO is similar to the one of n-alkanes. The effect of the oxygen atom introduced in the molecular backbone is analyzed and the observed dynamics are compared to the n-alkane dynamics.

6.1 Hexadecane ($C_{16}H_{34}$)

In order to analyze all $C_{16}H_{34}$ measurements performed at TOFTOF with different observation times together, the scattering functions evaluated from the measured double differential cross sections were Fourier transformed to the corresponding intermediate scattering functions $I(Q,t)$. These are more convenient for direct comparision with MD simulation results and interpretation with respect to physical models. With quasielastic neutron scattering one mainly observes the self motion of the hydrogen atoms, due to their dominating incoherent scattering cross section. Hence the decay of the $I(Q,t)$ mainly reflects the autocorrelation of the hydrogen atoms.

The resulting $I(Q,t)$ cover several orders of magnitude in time, and can be empirically described using stretched exponential functions, as the Kohlrausch–William–Watts (KWW) function

$$I^{\mathrm{KWW}}(t) = A \exp\left[-\left(\frac{t}{\tau}\right)^{\beta}\right]. \tag{6.1}$$

A is a prefactor, τ is the characteristic relaxation time quantifying the decay of the correlation function to 1/e of its initial value, and β is the stretching parameter. A stretching parameter $\beta = 1$ corresponds to a single exponential decay, and a stretching of the decay leads to $\beta < 1$ [164]. Such a stretched exponential decay can be due to the superposition of single exponentials [165, 166]. A broadening of the distribution of the single relaxation times then causes a stretching of the overall correlation function. In other words in a heterogeneous system the local environment and consequently the exponential relaxation time differs from particle to particle. In many cases the different relaxations can be approximated by a stretched exponential, with a mean, average relaxation time [167]. Mean relaxation times are calculated as

$$\langle\tau\rangle = \int_0^\infty \mathrm{d}t\, I^{\mathrm{KWW}}(t) = \frac{\Gamma(\beta^{-1})}{\beta}\tau, \tag{6.2}$$

where Γ is the gamma function.

The behavior of the intermediate scattering functions $I(Q,t)$ obtained for the $C_{16}H_{34}$ melt is illustrated in figure 6.2. These curves were obtained by merging the data points resulting from the measurements with eight different instrumental resolutions for each temperature. The separate spectra overlap perfectly, collapsing

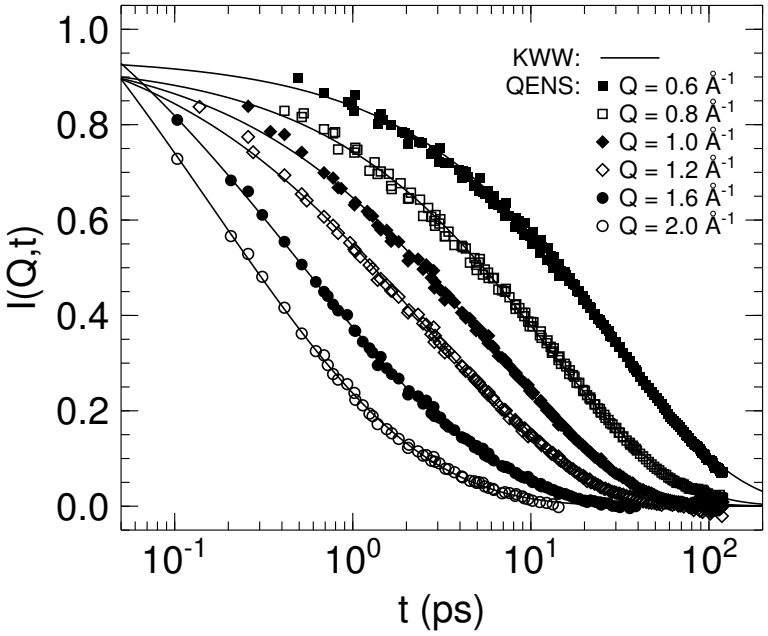

Figure 6.2: Measured intermediate scattering functions of $C_{16}H_{34}$ (symbols) together with stretched exponential fits (solid lines) at $T = 293\,\mathrm{K}$ (cf. [168]).

into single master curves. These master curves cover three orders of magnitude in time. The individual error-bars are smaller than the symbols, except for times close to or longer than the respective observation time. These data points were removed from the spectra.

The decay of the master curves can be satisfactory described using the KWW function. In contrast to this, Smuda et al. could model their $C_{32}H_{66}$ data well only when considering a two-step exponential decay [18], while Arrighi et al. also observed a single-step decay of the $I(Q,t)$ for several n-alkanes [20].

The extracted stretching parameters β are displayed in figure 6.3 and are partially consistent with the findings of other quasielastic neutron scattering studies of triacontane ($C_{30}H_{62}$) [20] and $C_{44}H_{90}$ [17]. For small scattering vectors $Q \leq 0.6\,\mathrm{Å}^{-1}$ the extracted stretching exponents give a temperature independent value of $\beta \approx 0.65$, which corresponds to a moderately stretched decay of the $I(Q,t)$. The corresponding dynamics take place over large distances in real space, since these low values of Q correspond to a nanometer length scale. Such large-scale motions can be pictured as e. g. molecular rotation or translational self-diffusion of the entire molecules. It has to be assumed that different large-scale dynamics cause different relaxation times of the individual atoms. The atoms at the ends of the chain see a rotational motion of the entire molecules slightly differently than the atoms located at the chain center, for instance, resulting in a stretched form of the intermediate scattering function.

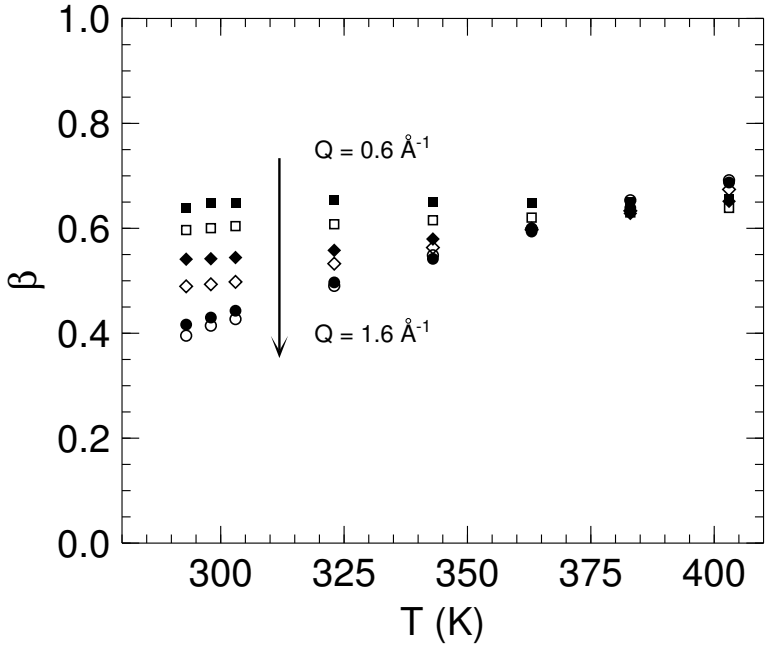

Figure 6.3: Stretching parameter β from a stretched exponential fit to the measured $I(Q,t)$ of $C_{16}H_{34}$. The arrow points into the direction of increasing scattering vector Q. For the measured Q smaller than $0.6\,\text{Å}^{-1}$ or larger than $1.6\,\text{Å}^{-1}$ the temperature dependency does not change any further.

With increasing scattering vector Q a change becomes obvious: Now the stretching increases with decreasing temperature. This is contrary to the behavior of increasing β with increasing Q found for $C_{30}H_{62}$ [20] and polyethylene (PE) [169]. The present data imply that at lower temperatures and large scattering vector a broader distribution of relaxation times is observed, which might be due to different dynamic processes with similar relaxation times but slightly different activation energies in the $C_{16}H_{34}$ melt. With increasing temperature some of the dynamics then occur at very short times and are hence not in the time window accessed with TOFTOF any longer. The resulting distribution of relaxation times then narrows, hence β increases.

Also local processes acting at different positions along the molecular backbone might cause a broadening of the $I(Q,t)$ at low temperatures. It is easy to imagine that torsional dynamics are faster close to the chain ends than at the center of the chain, due to the locally increased degrees of freedom. The superposition of the relaxation times then results in a decreasing β.

The mean characteristic relaxation times $\langle\tau\rangle$ obtained from the KWW fits are presented in figure 6.4 and 6.5 as a function of scattering vector Q and temperature T, respectively. With increasing temperature and scattering vector the relaxation times

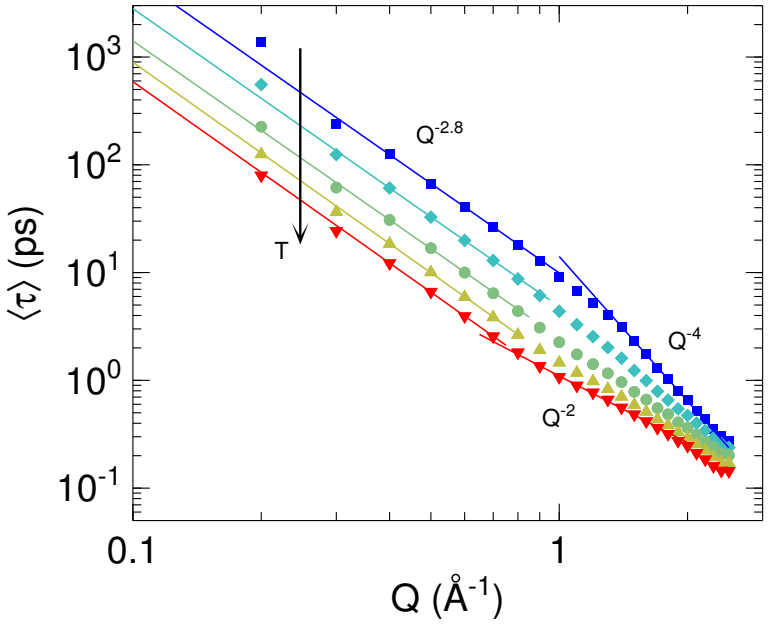

Figure 6.4: Mean relaxation times extracted from stretched exponential fits to the measured $I(Q,t)$ of $C_{16}H_{34}$ (symbols). Also shown are different Q-scalings (solid lines). The arrow points into the direction of rising temperature.

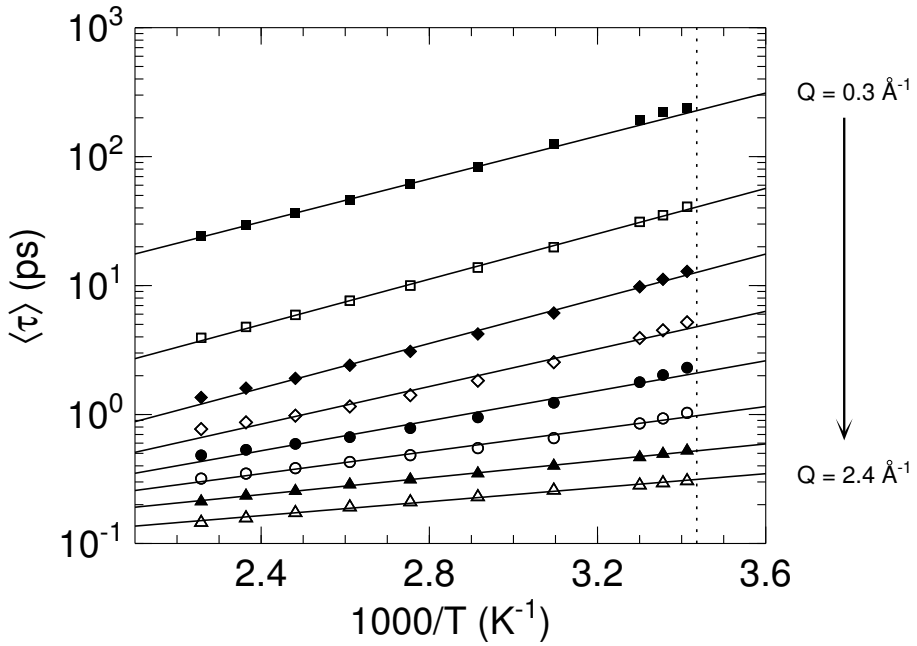

Figure 6.5: Mean relaxation times from a stretched exponential fit to the measured $I(Q,t)$ of $C_{16}H_{34}$ (symbols), fitted with the Arrhenius equation (solid lines). The dotted line indicates the melting temperature of $C_{16}H_{34}$, and the arrow points into the direction of increasing scattering vector Q.

decrease. Consequently the dynamics are faster on local length scales and high temperatures. A non-uniform Q-dependency of $\langle\tau\rangle$ can be identified. A $Q^{-2.8}$ scaling

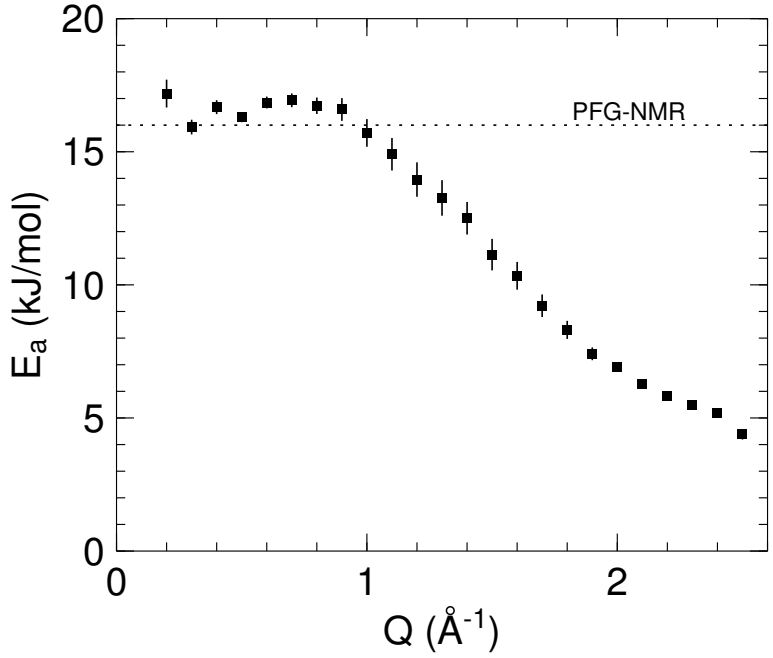

Figure 6.6: Activation energies as extracted from an Arrhenius fit to the mean relaxation times for $C_{16}H_{34}$. The dotted line represents the value measured with PFG-NMR [11] (cf. [168]).

is present for low values of scattering vector $Q \leq 1\text{Å}^{-1}$, which is independent of temperature. For larger Q the scaling changes from Q^{-4} at $T = 293\,\text{K}$ to Q^{-2} at $T = 443\,\text{K}$. Obviously different dynamics are observed when looking on different length scales. The crossover from small to large length scales also shows a slight temperature dependence, as the change in the Q-scaling seems to occur at lower values of Q with increasing T.

The temperature dependency in figure 6.5 can be described by the Arrhenius equation

$$\langle \tau \rangle = \langle \tau_0 \rangle \exp\left(-\frac{E_\text{a}}{RT}\right), \tag{6.3}$$

with an pre-exponential factor $\langle \tau_0 \rangle$, an activation energy E_a and the universal gas constant R. The Arrhenius fit describes the data neatly, except at temperatures close the melting point of $C_{16}H_{34}$. Here the observed motions are slightly slower than modeled by the Arrhenius equation. The corresponding activation energies are plotted in figure 6.6. For large values of Q, corresponding to motions on local length scales, lower values of E_a are obtained than for motions on an extended length scale. In this low-Q regime the extracted E_a matches the values determined by PFG-NMR [11]. It can therefore be assumed that all processes leading to molecular self-diffusion already take place on the time scale under study. By evaluating only the slow,

diffusive component of the scattering functions $S(Q, \omega)$, as will be demonstrated for the analysis of the $C_{100}H_{202}$ measurements in the following, Smuda et al. extracted an activation energy of approximately 13.8 kJ/mol, which is lower than the expected for true long-range Fickean diffusion [18]. It is to be assumed that the observed dynamics result from a combination of torsional vibrations and conformational relaxations, which must also be active for the longer $C_{100}H_{202}$ chains [20].

The analysis of the QENS spectra of $C_{16}H_{34}$ reveals that many different motions are observed, occurring on several length and time scales. At high temperatures the intermediate scattering functions follow approximately a $\exp(-Q^2t)$ behavior, when motions on local length scales are considered. According to equation 4.20 this corresponds to diffusive motion. With decreasing temperature this scaling is lost, and a stretching of the $I(Q, t)$ is observed, indicating that a complex composition of different dynamics dominates the observed dynamics. The Q- and T-dependency of the stretching parameter β allows for the conclusion that the various motions are characterized by different activation energies. The analysis of the MD simulations will yield additional information which allow for the identification of the prevailing motions.

6.2 Hectane ($C_{100}H_{202}$)

The dynamics in the $C_{100}H_{202}$ melt were evaluated in the frequency domain, allowing for a straightforward comparison with the results for shorter n-alkanes published by Smuda et al. [18]. The scattering functions $S(Q,\omega)$ were quantitatively modeled by a sum of a narrow and broad Lorentzian

$$S^{2\mathcal{L}}(Q,\omega) = F(Q)\big[A_0(Q)\mathcal{L}_1(Q,\omega) + (1 - A_0(Q))\,\mathcal{L}_{1,2}(Q,\omega)\big]. \tag{6.4}$$

The prefactor $F(Q)$ comprises the Debye-Waller factor and $A_0(Q)$ is the elastic incoherent structure factor [170]. The Lorentzian function

$$\mathcal{L}(Q,\omega) = \frac{1}{\pi}\frac{\Gamma(Q)}{\Gamma^2(Q) + \omega^2} \tag{6.5}$$

is characterized by its half width at half maximum (HWHM) $\Gamma(Q)$. The narrow component $\mathcal{L}_1$ describes slow, translational motion of the whole molecules. All fast, local molecular motions are approximated by the second, broad Lorentzian $\mathcal{L}_{1,2}$. Multiple scattering effects accumulate to a broad background, which is absorbed in the broad Lorentzian component [171]. By decreasing the observation time the narrow Lorentzian models the dynamics which prior contributed to the broad Lorentzian. This allows for the study of different dynamics by varying the observation times and simply treating only the narrow component [19].

All scattering functions show a clear broadening of the elastic line line. The fit of two Lorentzian functions describes all data with instrumental resolutions $\geq 23\,\mu$eV fine. Figures 6.7 illustrate several measured $S(Q,\omega)$ together with a fit of equation 6.4, plotted as solid black lines. The fits are hardly visible because they perfectly coincide with the data points. The two components of the fit, plotted as dotted and dashed lines, are well separated.

For all fits the extracted HWHM of the first, narrow Lorentzian $\Gamma_1(Q)$ follows a Q^2-dependency. Hence a diffusive motion of the hydrogen atoms is observed. As already mentioned, this feature must not be linked to Fickean self-diffusion of the entire molecules, especially when short observation times (lower instrumental resolutions) are considered. By fitting a linear function to the $\sqrt{\Gamma(Q)}$ data, as exemplarily illustrated in figure 6.7, apparent diffusion coefficients D_a were extracted according to equation 4.21. The HWHM of the second, broad Lorentzian $\Gamma_2(Q) = \Gamma_{1,2}(Q) - \Gamma_1(Q)$, which accounts for all fast, internal motions, is not independent

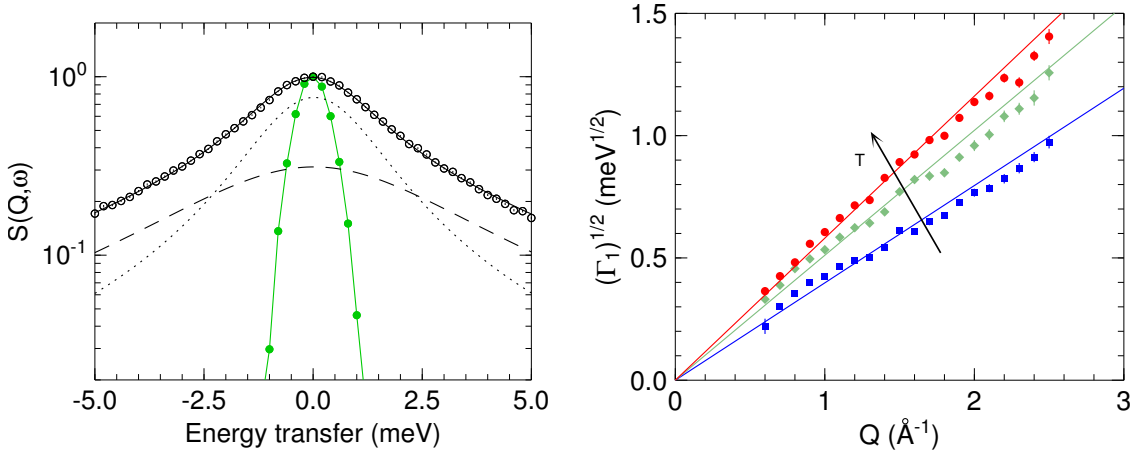

(a) $\Delta E = 900\,\mu$eV. The scattering function is plotted for $T = 509\,$K and $Q = 2.0\,$Å^{-1}.

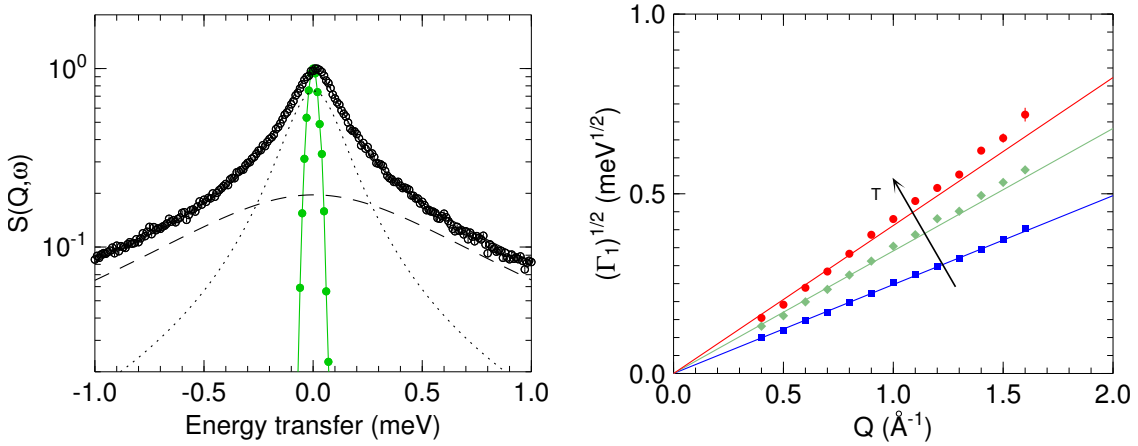

(b) $\Delta E = 55\,\mu$eV. The scattering function is plotted for $T = 453\,$K and $Q = 1.0\,$Å^{-1}.

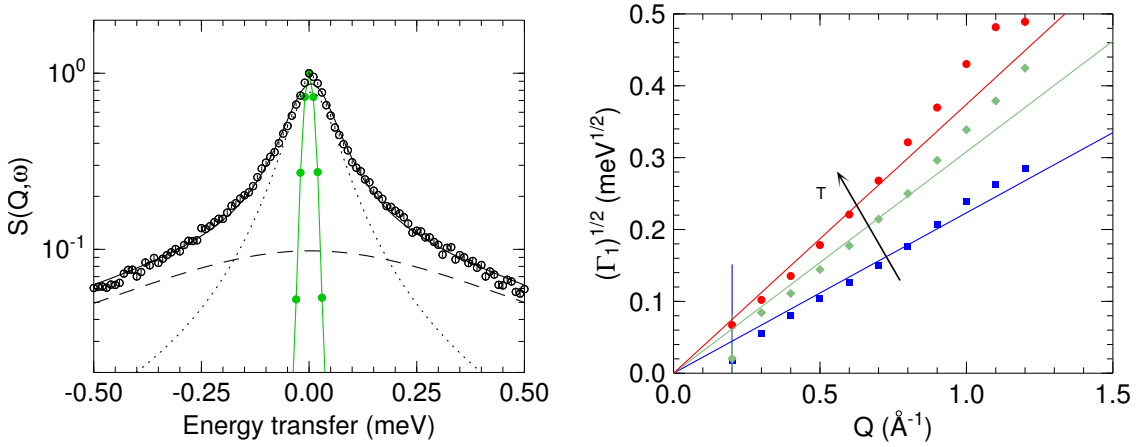

(c) $\Delta E = 23\,\mu$eV. The scattering function is plotted for $T = 393\,$K and $Q = 1.0\,$Å^{-1}.

Figure 6.7: Left figures: Scattering functions measured with different instrumental resolutions ΔE for $C_{100}H_{202}$. The measured resolution functions are represented in green. A two-Lorentzian fit is indicated by the black solid lines, the narrow and broad components of the fit are plotted as dotted and dashed lines, respectively. Right figures: Square root of the extracted half width at half maximum $\Gamma_1(Q)$ of the narrow Lorentzian component at $T = 393$, 453 and 509 K. The arrows point into the direction of rising temperature.

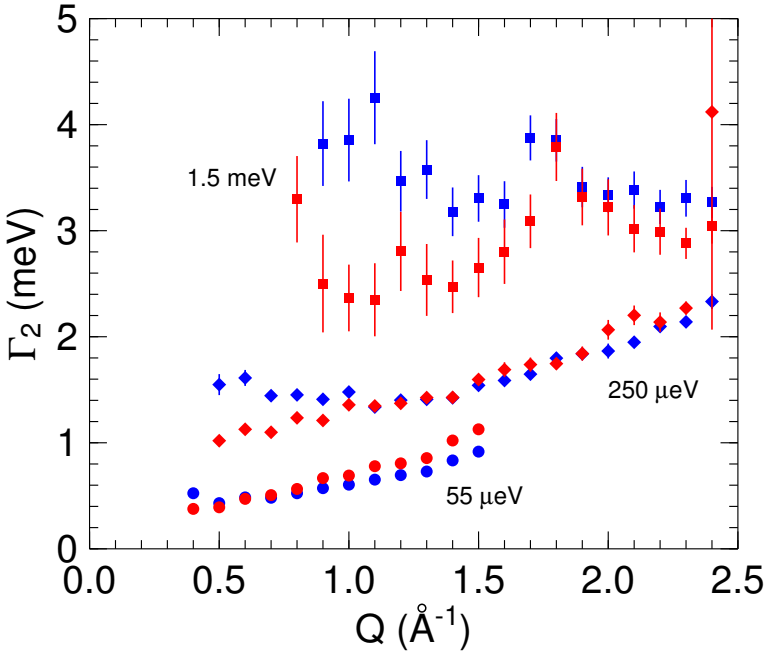

Figure 6.8: Half width at half maximum of the broad component of a two-Lorentzian fit to the $S(Q,\omega)$ of $C_{100}H_{202}$ with different instrumental resolutions at $T = 393\,\mathrm{K}$ (red symbols) and 509 K (blue symbols).

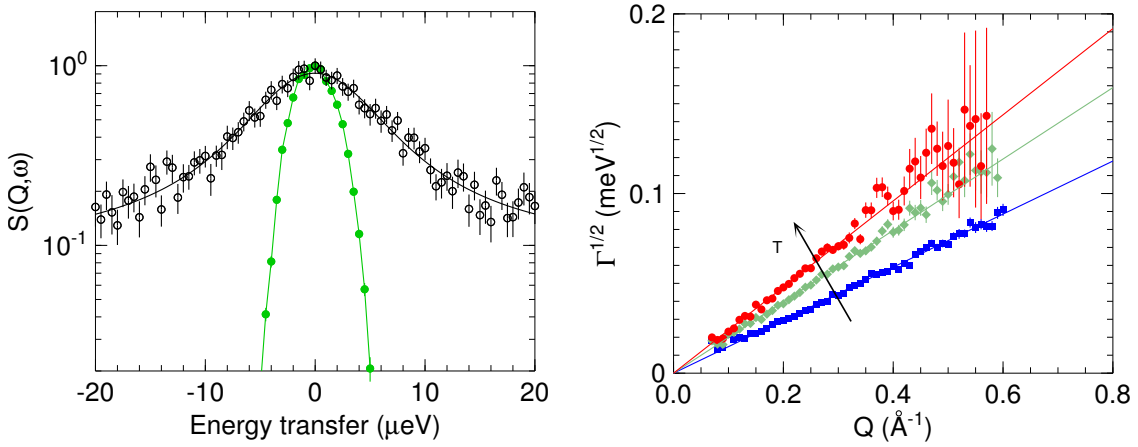

Figure 6.9: Instrumental resolution of 2 μeV, corresponding to an effective observation time of 1.2 ns. Left figure: The measured scattering function for $C_{100}H_{202}$ at $T = 393\,\mathrm{K}$ and $Q = 0.5\,\mathrm{Å}^{-1}$ (symbols) together with a fit of a single Lorentzian function (solid black line) and the resolution function (green). Right figure: Square root of the extracted half width at half maximum at $T = 393$, 453 and 509 K together with linear fits. The arrows point into the direction of rising temperature.

of Q and instrumental resolution (cf. fig. 6.8). With a decreasing observation time (higher instrumental resolution) the width broadens. Hence faster motions, which are not accessible with long observation times, are now observed and accumulated in the second Lorentzian.

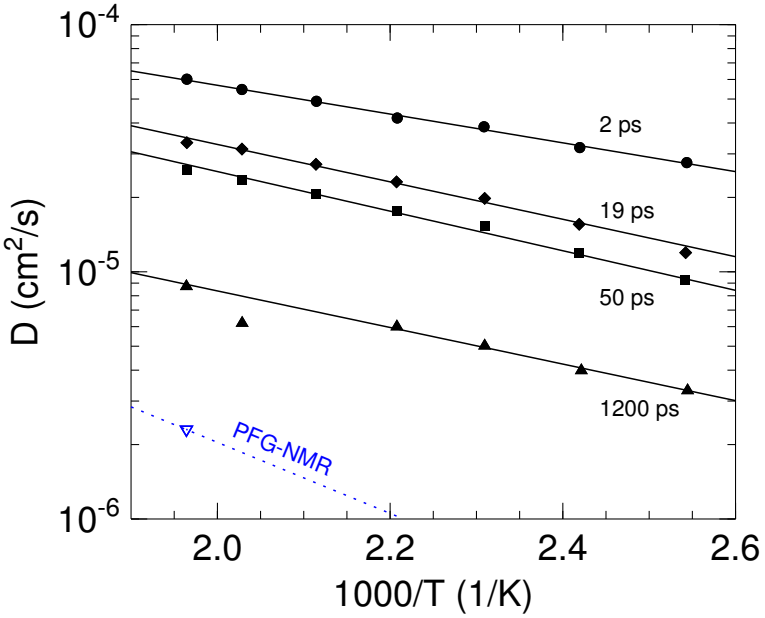

Figure 6.10: Apparent diffusion coefficients obtained from fitting the measured $S(Q,\omega)$ of $C_{100}H_{202}$ with different instrumental resolutions or observation times. The solid lines represent Arrhenius fits. For the 2 μeV data ($t_{obs} = 1.2$ ns) the value at $T = 493$ K seems to be erroneous and was ignored during the fitting procedure. Also shown is the value extrapolated from PFG-NMR data [172, 173], together with an temperature dependency according to an extrapolated activation energy of 27.5 kJ/mol, as described in the text.

The scattering functions measured with the highest instrumental resolution of 2 μeV can already be well described by a single Lorentzian function (eq. 6.5) plus a constant background, as exemplarily displayed in figure 6.9. Certainly also a two-Lorentzian function can fit the data, with similar results. However, substituting the broad Lorentzian by a constant background results in smaller errors of the extracted HWHM of the narrow Lorentzian. This specifically applies to the high temperature data: For large scattering vectors Q a broad quasielastic signal is measured, resulting in already large fitting errors (cf. fig. 6.9).

The extracted HWHM of the 2 μeV measurements again shows a Q^2-scaling, allowing for the calculation of an apparent diffusion coefficients D_a from the $\Gamma(Q)$-slope. The error-bars for the $T = 509$ K data points are relatively large at high Q, since the self-correlation at these local length scales is pretty much lost, resulting in low intensity.

The resulting apparent diffusion coefficients are plotted in figure 6.10. The values strongly depend on the instrumental resolution and thus on the effective observation time t_{obs}. With increasing t_{obs} the diffusive motion becomes slower. Even for the longest observation time of 1.2 ns (corresponding to the instrumental resolution of

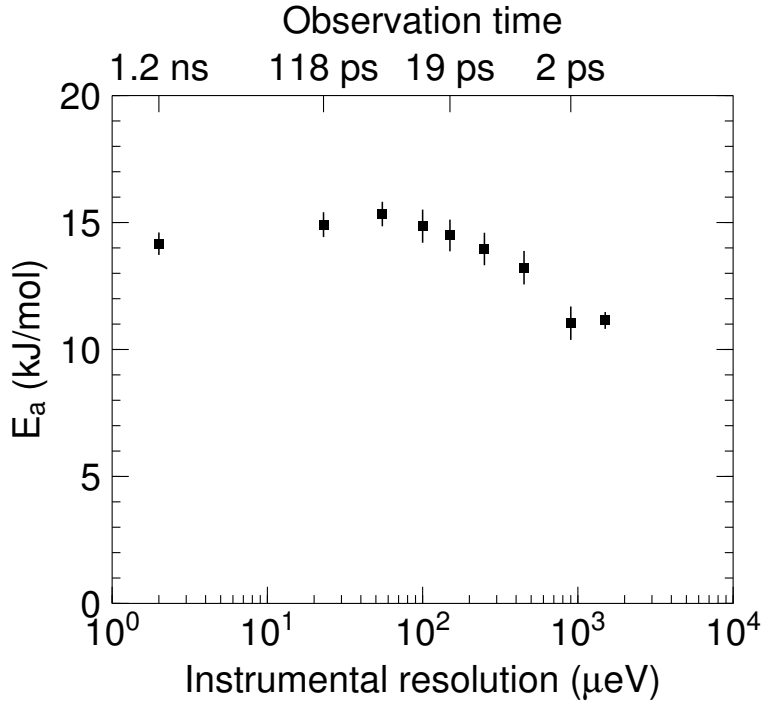

Figure 6.11: Activation energies as extracted from an Arrhenius fit to the apparent diffusion coefficients of $C_{100}H_{202}$. The best and worse instrumental resolutions of 2 μeV and 1.5 meV corresponds to effective observation times of 1.2 ns and 2 ps. All values are smaller than $E_a \approx 27.5$ kJ/mol, as expected for molecular self-diffusion (see text).

2 μeV) the apparent diffusion coefficient is nearly an order of magnitude larger than the value of $D^{NMR} \approx 2.3 \cdot 10^{-6}$ cm^2/s for $T = 509$ K, as extracted from PFG-NMR data from Pearson et al. [172, 173], extrapolating both chain length and temperature. Hence molecular self-diffusion contributes only little to the observed motions on the pico- to nanosecond time scale.

Using the Arrhenius equation 6.3 allows for the description of the temperature dependence of the apparent diffusion coefficient. The resulting activation energies E_a of the diffusive-like motions are given in figure 6.11. Dynamics occurring on the nanosecond time scales, and hence with rather large displacements, are characterized by a relatively high activation energy. Local, short time dynamics show a smaller activation energy. This tendency is in agreement with the results obtained from the evaluation of the $C_{16}H_{34}$ dynamics.

The increasing activation energy with decreasing instrumental resolution (increasing observation time) can be observed up to 55 μeV, where a maximum of 15.3 kJ/mol is reached. This E_a is smaller than the value determined by Smuda et al. for long n-alkanes. Using an instrumental resolution of 55 μeV they found an

activation energy of about 17 kJ/mol, which was independent of molecular weight and attributed this to the contribution of internal motions.

The activation energies obtained from the high-resolution measurements are slightly lower. The motions detected with observation times in the 100 ps to 1 ns range can approximately be characterized by a constant E_a between 14 and 15 kJ/mol. However, this value is much smaller than the value expected for molecular self-diffusion: Extrapolating PFG-NMR data [11] yields an activation energy of approximately 27.5 kJ/mol.

Mainly local, intramolecular motions of $C_{100}H_{202}$ seem to prevail on the whole pico- to nanosecond time scale. The scattering functions show a diffusive-like motion on all length and time scales, which cannot be attributed to molecular self-diffusion, since the apparent diffusion is too fast. The analysis of the activation energies shows almost constant values for observation times of 100 ps and 1 ns, framed by larger values obtained with much longer (PFG-NMR) and slightly shorter (55 μeV) observation times. The latter yields an E_a which is smaller than expected from extrapolating the data of Smuda et al. to long chains [18]. This can be explained by different fitting procedures to obtain diffusion coefficients, which eventually lead to slight deviations of the resulting activation energy.

With increasing observation time the extracted activation energy does not approach the value expected for self-diffusion, but remains more or less constant on the 10 ps – 1 ns time scale instead. The analysis of the MD simulations will reveal that not only intramolecular motions occur before molecular self-diffusion sets in, but collective intermolecular dynamics dominate on this extended time scale: It will be demonstrated that many atoms in extended clusters move collectively and flow-like in similar directions. It is especially the decorrelation of these flow-like motions which result in an enhanced chain relaxation on the pico- to nanosecond time scale. It is hence to be assumed that the activation energy characterizes both these collective features and single chain dynamics and cannot be attributed to a specific motion. As will be concluded from the analysis of the MD simulations, global rotational and translational motions of the center-of-mass molecules contribute only little to the overall dynamics on the sub-nanosecond time regime. Besides the collective flow-like motions it is mainly torsional dynamics, characterized by an activation energy of about $14 - 15$ kJ/mol, which dominate the pico- to nanosecond dynamics of $C_{100}H_{202}$.

Rouse Analysis Since the $C_{100}H_{202}$ chains at $T = 509\,\mathrm{K}$ are on the one hand slightly shorter than the entanglement length of $N_e = 136$ [31, 174] of polyethylene at this temperature and on the other hand long enough to show Gaussian chain characteristics [33], the Rouse model was tested to describe the short time motion observed with QENS.

The incoherent intermediate scattering function in terms of the Rouse model is obtained by inserting the approximated Rouse-MSD (eq. 2.25) into the Fourier-transformed expression of the Gaussian van Hove correlation function 4.18 resulting in

$$\begin{aligned} I_{\mathrm{inc}}^{\mathrm{R,approx}}(Q,t) &= \exp\left(-\frac{Q^2}{6}\left\langle R_{\mathrm{R}}^2(t)\right\rangle\right) \\ &= \exp\left(-Q^2 D_{\mathrm{R}} t\right) \exp\left(-\sqrt{\frac{t}{\tau_{\mathrm{inc}}^{\mathrm{R}}(Q)}}\right), \end{aligned} \tag{6.6}$$

with the Q-dependent Rouse relaxation time

$$\tau_{\mathrm{self}}^{\mathrm{R}}(Q) = \frac{9\pi}{W\ell^4 Q^4}. \tag{6.7}$$

The expression of the coherent correlation function is more complex. The formulation reads [58]

$$\begin{aligned} I_{\mathrm{coh}}^{\mathrm{R}}(Q,t) =& \frac{1}{N}\exp\left(-Q^2 D_{\mathrm{R}} t\right) \sum_{n,m=1}^{N} \exp\left(-\frac{|n-m|}{6} Q^2\ell^2\right) \times \\ & \exp\left\{-\frac{2}{3}\frac{R_{\mathrm{E}}^2 Q^2}{\pi^2}\sum_{p=1}^{N-1}\frac{1}{p^2}\left[\cos\left(\frac{p\pi n}{N}\right)\cos\left(\frac{p\pi m}{N}\right)\left(1-\exp\left(-\frac{p^2}{\tau_{\mathrm{R}}}t\right)\right)\right]\right\}, \end{aligned} \tag{6.8}$$

with the end-to-end chain distance $R_{\mathrm{E}} = \sqrt{N}\ell$. Using this formulation the incoherent not-approximated expression was obtained by setting $n = m$:

$$\begin{aligned} I_{\mathrm{inc}}^{\mathrm{R}}(Q,t) =& \frac{1}{N}\exp\left(-Q^2 D_{\mathrm{R}} t\right) \times \\ & \sum_{n=1}^{N}\exp\left\{-\frac{2}{3}\frac{R_{\mathrm{E}}^2 Q^2}{\pi^2}\sum_{p=1}^{N-1}\frac{1}{p^2}\left[\cos^2\left(\frac{p\pi n}{N}\right)\left(1-\exp\left(-\frac{p^2}{\tau_{\mathrm{R}}}t\right)\right)\right]\right\} \end{aligned} \tag{6.9}$$

For small values of Q only the first term in both the coherent and incoherent expression is significant, describing the center-of-mass self-diffusion of the chain. The statistical segment length and segmental friction coefficient were taken from the lit-

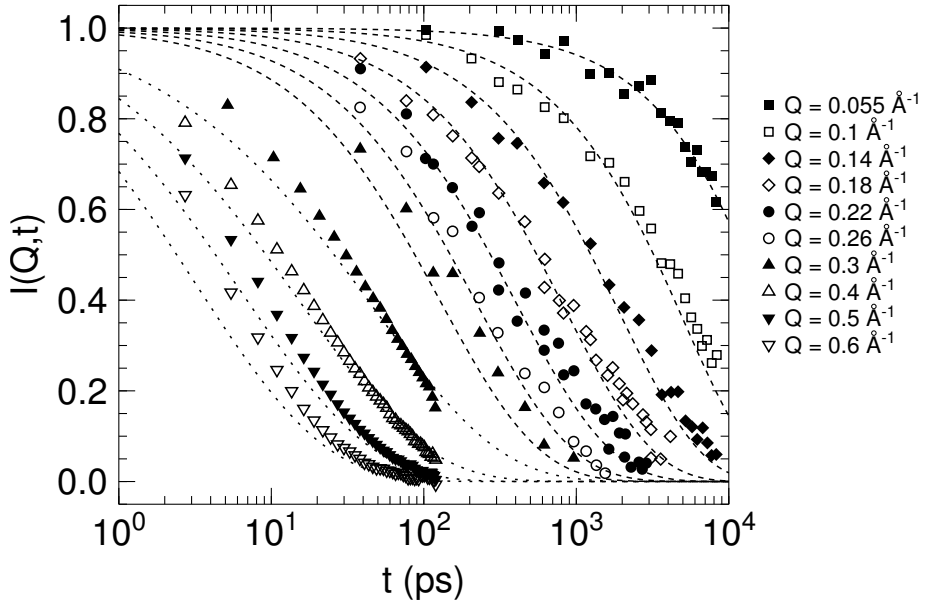

Figure 6.12: Symbols: Intermediate scattering functions as obtained for $C_{100}H_{202}$ at $T = 509\,\mathrm{K}$ with quasielastic neutron scattering (QENS, instrumental resolution of $23\,\mu\mathrm{eV}$) and neutron spin echo (NSE, [31]). The four leftmost datasets are the QENS data, while the long-time data with scattering vectors $Q \leq 0.3\mathrm{\AA}^{-1}$ were measured by Paul et al. [31]. Lines: Intermediate scattering functions as predicted by the Rouse model using the incoherent (dotted lines) and coherent (dashed lines) expressions for the QENS and NSE data, respectively.

erature ($\ell^2 = 13.76\,\mathrm{\AA}^2$ [31] and $\zeta = 0.048 \cdot 10^{-11}\,\mathrm{Ns/m}$ [58]), while a self-diffusion coefficient of $D = 1.8 \cdot 10^{-6}\,\mathrm{cm}^2/\mathrm{s}$ was chosen in agreement with the results of Paul et al. [31].

The measured scattering functions $S(Q, \omega)$ were numerically Fourier transformed and divided by the respective spectra of the instrumental resolutions to obtain the intermediate scattering functions $I(Q, t)$ corrected for instrumental resolution. The resulting data are illustrated in figure 6.12 together with the prediction by the Rouse model. QENS data are displayed together with the data obtained with neutron spin echo (NSE) by Paul et al. [31]. To describe the QENS data the Rouse model was calculated using the exact incoherent expression (eq. 6.9), while the coherent notation (eq. 6.8) was taken to test the NSE data, as done by Paul et al. [31].

The Rouse prediction of the QENS data show a poor match for all values of Q. The motions predicted by the Rouse model are too fast, as the measured intermediate scattering functions are consistently above the Rouse predictions. This trend continues for the NSE-data, and only for the lowest Q values a reasonable agreement between the NSE data and the Rouse model can be found. At large Q-values mainly

molecular self-diffusion is observed, to which the Rouse model passes over on long time scales.

Besides the fact that the Rouse model predicts a dynamics in the ps-range which is too fast, the overall shape of the experimentally measured intermediate scattering functions cannot be reproduced. The dynamics observed experimentally decay in a more narrow time range and exhibit a larger relaxation time than expected from the Rouse predictions. Obviously some additional motions not accounted for by the Rouse model are present in the real system.

A detailed Rouse analysis of the simulated data will reveal that only the first modes (modeling rather global chain dynamics) can be applied to describe the molecular dynamics of the $C_{100}H_{202}$ molecules. The Rouse model is doomed to fail as it does not account for collective intermolecular motions. It will be clearly demonstrated in section 7.4 of this thesis that such motions take place within the whole picosecond time range, which is well in the Rouse regime.

6.3 Poly(ethylene oxide) (PEO)

The dynamics of poly(ethylene oxide) (PEO) with different molecular weights (cf. table 3.1), measured using three instrumental resolutions (4 μeV, 55 μeV and 1.5 meV), was studied analogous to the preceeding evaluation of the $C_{100}H_{202}$ measurements. The scattering functions obtained with a resolutions of 55 μeV and 1.5 meV were fitted with a sum of two Lorentzians (eq. 6.4), as exemplarily illustrated in figure 6.13. The width of the narrow component again follows a Q^2-behavior, indicating diffusive

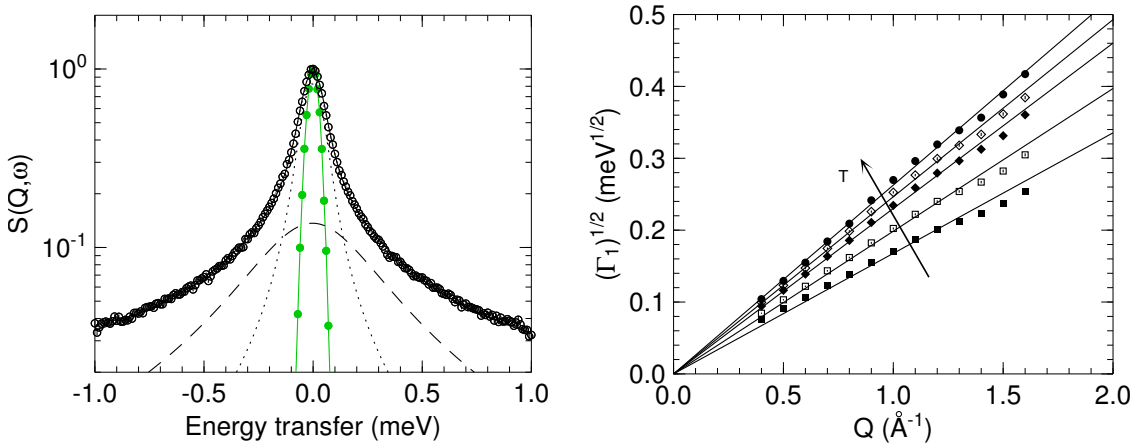

(a) $\Delta E = 55\,\mu$eV, $M_w = 1521$ g/mol. The scattering function is plotted for $T = 341$ K and $Q = 1.5$ Å^{-1}. The HWHM are displayed for $T = 341, 360, 379, 388$ and 398 K.

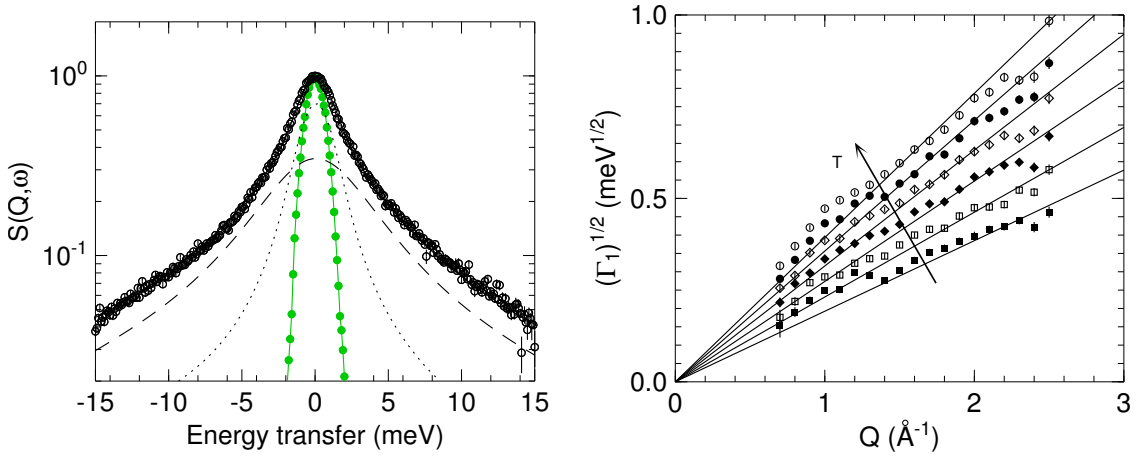

(b) $\Delta E = 1.5$ meV, $M_w = 581$ g/mol. The scattering function is plotted for $T = 398$ K and $Q = 2.5$ Å^{-1}. The HWHM are displayed for $T = 303, 322, 341, 360, 379$ and 398 K.

Figure 6.13: Left figures: Scattering functions measured with different instrumental resolutions ΔE for PEO with different molecular weight M_w. The resolution functions are plotted in green. Fits of the sum of two Lorentzians are plotted as black lines, and the corresponding narrow and broad components as dotted and dashed lines, respectively. Right figures: Square root of the extracted half width at half maximum (HWHM) $\Gamma_1(Q)$ of the narrower Lorentzian. The arrows point into the direction of rising temperature.

motion. These motions can thus be characterized by apparent diffusion coefficients D_a.

High resolution measurements were performed on the low molecular weight sample ($M_w = 206\,g/mol$). Only at temperatures well above the melting temperature a broadening of the elastic line could be detected, as illustrated in figure 6.14. The scattering functions obtained at temperatures below 300 K coincide with the resolution function. Hence at these low temperatures no pronounced motions were observed on the nanometer length and nanosecond time scale accessed with an instrumental resolution of 4 μeV. It is to be assumed that analogous measurements of higher molecular weight PEO would yield a quasielastic signal only at temperatures much higher than their respective melting temperatures.

Only the high resolution spectra measured at temperatures above 300 K (i. e. $T = 308$ and 373 K) was evaluated. As pictured in figure 6.14, the data can be well fitted with a single Lorentzian function (eq. 6.5) and a constant background. A sum of two Lorentzians can fit the data just as well, but the larger number of parameters results in larger errors of the individual parameters. Apparent diffusion coefficients were obtained by assuming a Q^2-scaling of the extracted half width at half maximum (HWHM). This condition is nicely fulfilled for the high temperature data. The scattering functions at $T = 308$ K almost coincide with the instrumental resolution. Hence the quasielstic broadening is marginal and its determination is limited by the ω-spacing of the data points. As a result the $\Gamma(Q)$ levels off at

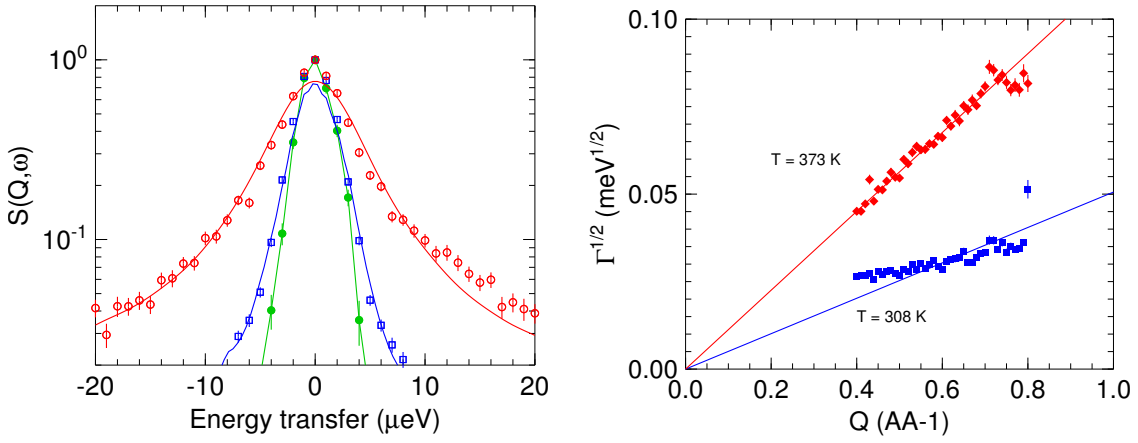

Figure 6.14: Scattering functions of the low molecular weight PEO ($M_w = 206\,g/mol$, symbols) and the respective square root of the extracted half width at half maximum, as described in the text. The scattering functions were obtained with an instrumental resolution of 4 μeV (green), corresponding to an effective observation time of 900 ps, at $T = 308$ (blue) and 373 K (red) and fitted using a single Lorentzian function.

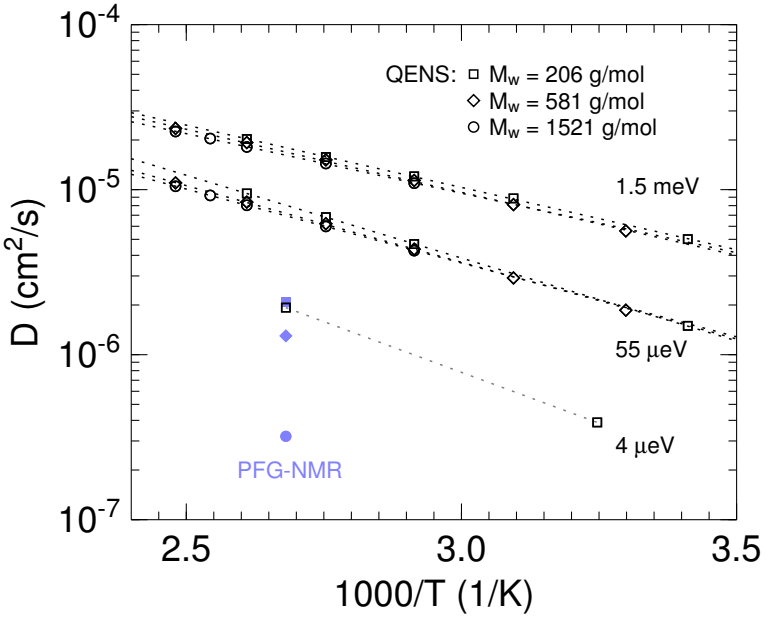

Figure 6.15: Apparent diffusion coefficients extracted from the $S(Q,\omega)$ of the three PRO samples, measured with different instrumental resolutions. The values are about an order of magnitude larger than those determined by PFG-NMR [175]. The instrumental resolutions of $4\,\mu$eV, $55\,\mu$eV and 1.5 meV correspond to effective observation times of 900 ps, 50 ps and 2 ps, respectively. Also plotted are the results from PFG-NMR [175] as filled blue symbols, which were determined for PEO with slightly different molecular masses: $M_\mathrm{w} = 330$ (square), 580 (diamond) and 1470 g/mol (circle).

small Q. A Q^2-scaling was assumed nonetheless to extract an upper estimation of the apparent diffusion coefficient. The actual value might be lower, as the slope of the data points seems to be flatter than the fit.

The apparent diffusion coefficients extracted from all measurements performed on PEO are summarized in figure 6.15. Motions observed with lower instrumental resolutions (shorter observation times) are characterized by larger values of D_a. This spread increases with decreasing temperature. Only a slight chain length dependence can be determined for the $55\,\mu$eV ($t_\mathrm{obs} = 50$ ps) measurement. At high temperatures the observed motions of the shorter PEO chains are slightly faster than the dynamics of the higher molecular weight PEO samples. At low temperatures the fast motion ($t_\mathrm{obs} = 2$ ps) is independent of the chain length. Hence only intramolecular motions are observed, and the chain-length dependent contribution from molecular self-diffusion is indistinguishable.

The high-temperature apparent diffusion coefficients for the fast motions are about an order of magnitude larger than those determined by Appel & Fleischer using PFG-NMR [175]. For $T = 373$ K they obtained the following long-time self-diffusion coef-

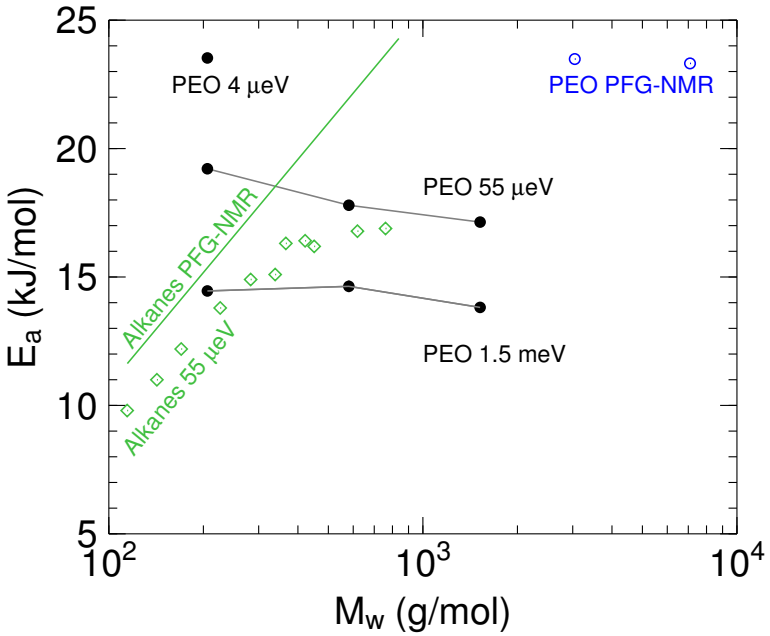

Figure 6.16: Activation energies obtained from an Arrhenius fit to the temperature dependent apparent diffusion coefficients measured for PEO (black symbols). Also shown are the values determined with PFG-NMR [175] (blue symbols). To compare the dynamics of the PEO chains with that of *n*-alkanes, the values measured with QENS [18] and PFG-NMR [11] are added to the figure (green, cf. fig. 6.1).

ficients: $D^{\mathrm{NMR}}(330\,\mathrm{g/mol}) = 2.1 \cdot 10^{-6}\,\mathrm{cm^2/s}$, $D^{\mathrm{NMR}}(580\,\mathrm{g/mol}) = 1.3 \cdot 10^{-6}\,\mathrm{cm^2/s}$ and $D^{\mathrm{NMR}}(1470\,\mathrm{g/mol}) = 3.2 \cdot 10^{-7}\,\mathrm{cm^2/s}$. However, the nanosecond dynamics of the short PEO chains measured with high resolution QENS are in good agreement with the PFG-NMR results. Self-diffusion of the entire molecules dominates the observed signal of the low molecular weight PEO on the nanosecond time scale. The dynamics on shorter time scales are faster than this relatively slow global molecular self-diffusion. These fast motions are rather caused by contributions of internal motions of the molecules than by a translational motion of the entire molecules.

Using the Arrhenius equation 6.3 activation energies E_a were calculated. For the $4\,\mu$eV data an Arrhenius behavior cannot be implied from the data, since only two apparent diffusion constants were obtained. Nonetheless the Arrhenius equation was applied to obtain an approximate activation energy. Keeping in mind that the approximate diffusion coefficient at $T = 308\,\mathrm{K}$ is rather too high, the resulting E_a can also be interpreted as an upper limit estimation. The resulting values are given in figure 6.16. The activation energies for the fast motions (instrumental resolution of 1.5 meV) are about independent of the chain length, as can already be concluded from the nearly coinciding apparent diffusion coefficient D_a in figure 6.15. On a 50 ps time scale (instrumental resolution of $55\,\mu$eV) the activation energies are higher than

on a 2 ps time scale (instrumental resolution of 4 μeV). This is in agreement with the results obtained for n-alkanes: Fast, local motions are characterized by smaller activation energies.

The chain length dependence of the activation energy extracted from the 55 μeV data is opposite to the behavior detected for n-alkanes: The values determined by Smuda et al. (see fig. 6.16) increase with increasing chain length, analogue to PFG-NMR data, and level off for high molecular weight. They concluded that for these long chains only local, intramolecular motions are observed, which are independent of the molecular dimension. This is not the case for the PEO dynamics on the same time scale. The dynamics of the smaller PEO molecules are subject to higher activation energies. Shorter chains approach the regime of global translational motion, which is characterized by an higher E_a, faster than the long chains. Hence the dynamics on the 50 ps time scale can be linked to the very onset of molecular self-diffusion for the low molecular weight PEO.

The motions of the short PEO sample observed with an instrumental resolution of 4 μeV are in line with the long-time PFG-NMR values, obtained for PEO with higher molecular weight [175, 176]. This confirms that these short PEO chains reach the self-diffusive regime on the sub-nanosecond time scale.

The slightly different chemical composition of the PEO chains has a huge effect on the global chain dynamics. Intermolecular hydrogen bonding causes a slow down of the motions, resulting in a relatively high activation energy for short PEO chains and a delayed crossover to molecular self-diffusion compared to the n-alkane dynamics. The internal motions observed for the longer PEO chains with a 50 ps observation time are characterized by the same activation energy as found for the the high molecular weight n-alkanes. Whether the local, intramolecular dynamics are identical on this time scale for the PEO and n-alkane chains needs to be addressed in future simulation work.

7 Motions Identified using MD Simulations

The quasielastic neutron scattering measurements allowed for a study of the motions on the pico- to nanosecond time scale. The resulting data of the short hexadecane ($C_{16}H_{34}$) molecules revealed that a superposition of various motions dominates the observed signal at low temperatures. Activation energies were extracted characterizing the dynamics on different time and length scales. For the long hectane ($C_{100}H_{202}$) molecules almost constant activation energies were determined, characterizing the motions observed with observation times in the range of 10 ps to 1 ns.

In order to identify the present motions leading to molecular self-diffusion, detailed molecular dynamics (MD) simulations were performed on a $C_{16}H_{34}$ and $C_{100}H_{202}$ system. Poly(ethylene oxide) has not been simulated in the framework of this thesis. However such simulations have been started to complement the respective neutron scattering data.

In the following a throughout validation of the simulated dynamics will be presented, before the dynamics of the *n*-alkane chains will be analyzed. By this local, global and collective motions of the atoms will be differentiated, which dominate the prevailing dynamics on different time scales.

7.1 Validation of the MD Simulations

Before simulated trajectories can be analyzed for any purpose, a validation of the subject under interest must be performed [177]. In the framework of this thesis the simulations are performed to obtain complementary information to the quasielastic neutron scattering (QENS) data. Therefore the focus of the validation is directed to the short-time dynamics. Structural information are of minor interest. High quality force fields, however, need to be able to reproduce spectroscopy and diffraction patterns, obtained by neutron or x-ray scattering on a wide temperature range. It

will be pointed out that optimizing structural details as e. g. density strongly affects the short-time dynamics.

Dynamics

The validation of the short time dynamics was done by calculating the intermediate scattering functions $I(Q,t)$ from the MD simulations and comparing them with the data measured with QENS at TOFTOF. From the simulations coherent and incoherent dynamic structure factors were computed with *n*MOLDYN as described in section 5.4.

The measured $I(Q,t)$ cannot be straightforward normalized. $I(Q,0)$ for instance corresponds to the Fourier transform of $S(Q,\omega \to \infty)$. As the measured energy range is finite $I(Q,0)$ is not clearly defined. The measured spectra were therefore divided single constant values to align them with the simulated data.

The comparison of the $C_{16}H_{34}$ dynamics simulted with the force field of Chang & Sandler [153] at 293 K is illustrated in figure 7.1. For all scattering vectors Q the simulated and measured data coincide perfectly on the whole time scale accessed with QENS. The accordance is of similar quality for the other temperatures. As already referred to before, explicit 1–4 pair interactions in the force field were ne-

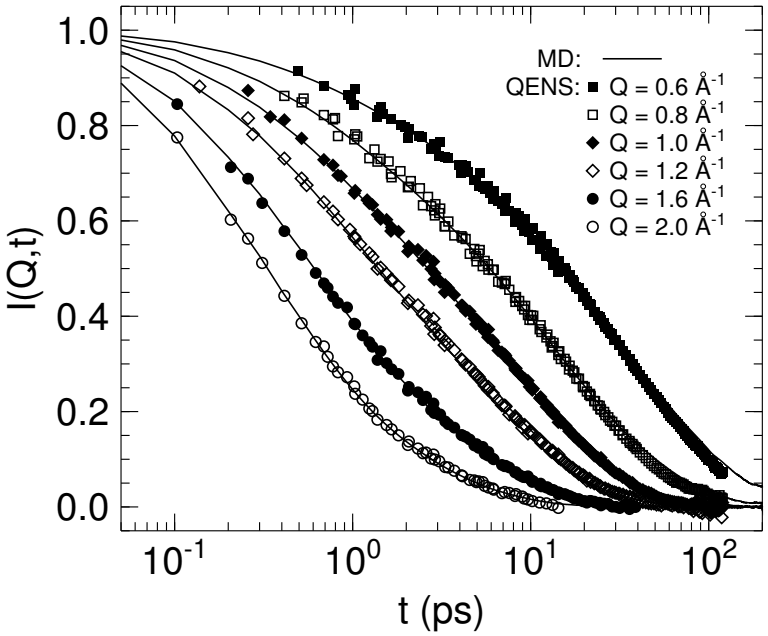

Figure 7.1: $C_{16}H_{34}$ - Intermediate scattering functions as calculated from the MD simulations (solid lines) and measured with quasielastic neutron scattering (QENS) at TOFTOF (symbols) at $T = 293\,\mathrm{K}$ (cf. [168]).

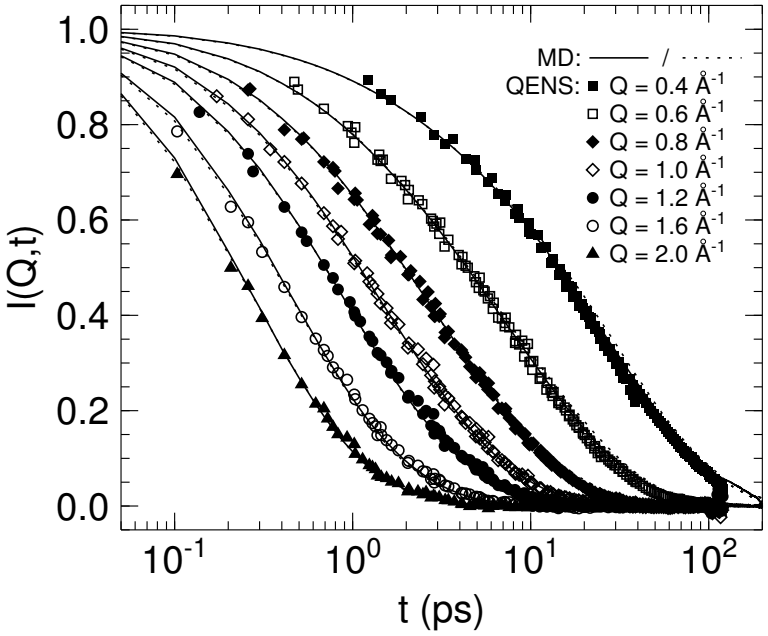

Figure 7.2: $C_{16}H_{34}$ - Intermediate scattering functions as calculated from the MD simulations using (dotted lines) and neglecting (solid lines) explicit 1–4 pair interactions in the force field, together with the data measured with quasielastic neutron scattering (QENS) at TOFTOF (symbols) at $T = 363\,\mathrm{K}$ (cf. [168]).

glected in order to lower the melting temperature, which is considerably too high otherwise, as will be pointed out later. To identify the impact of this procedure on the short time dynamics, intermediate scattering functions were calculated from simulations with and without these 1–4 interactions. The comparison in figure 7.2 for $T = 363\,\mathrm{K}$ confirms no major difference of the short time dynamics. The data from both simulation sets lie on top of each other and also coincide with the QENS data. This justifies the procedure of neglecting non-bonded interactions for the first three neighbors to lower the incorrect melting temperature without a severe influence on the dynamics.

Besides the force field of Chang & Sandler, which reproduces the $C_{16}H_{34}$ dynamics excellently, the L-OPLS force field reparametrization of Siu et al. [152] was tested. A comparison of the resulting dynamic structure factors resulting from simulations using both force fields is presented in figure 7.3. Only marginal differences in the shape of the curves can be identified, although the dynamics resulting from the Chang & Sandler force field are negligible faster. The dynamics simulated with both force fields are very similar to each other and are both within the errors of the experimentally measured intermediate scattering functions (cf. fig. 7.2). Both force fields hence reproduce the observed dynamics very accurately. The Chang &

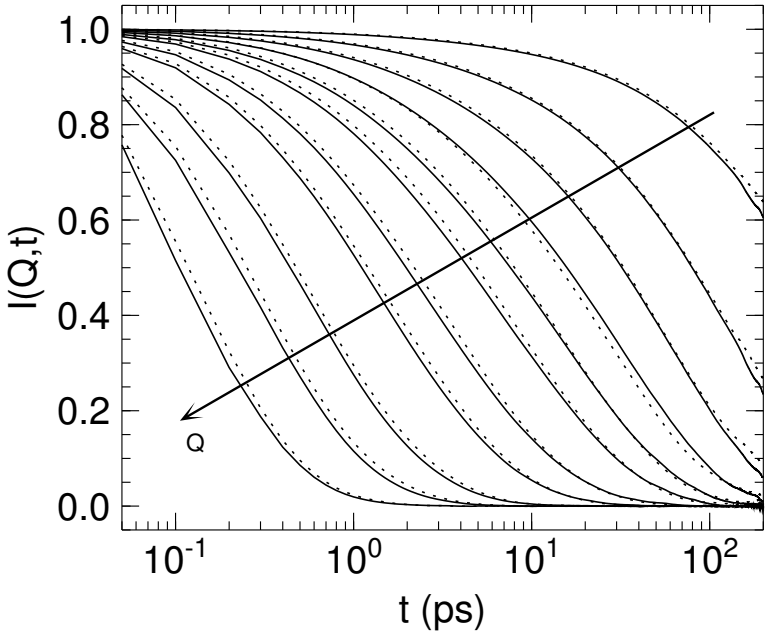

Figure 7.3: $C_{16}H_{34}$ - Comparison of the dynamic structure factors at $T = 363\,\mathrm{K}$ obtained from simulations with the force field parameters of Chang & Sandler (solid lines, [153]) and Siu et al. (dotted lines, [152]). Both simulations were performed using explicit 1–4 pair interactions. The arrow points into the direction of increasing scattering vector Q, ranging from 0.1 to 3.0 $\mathrm{Å}^{-1}$ (0.1, 0.2, 0.3, 0.4, 0.5, 0.6, 0.8, 1.0, 1.5, 2.0, 3.0 $\mathrm{Å}^{-1}$).

Sandler force field results in a better simulation performance compared to the use of the L-OPLS force field and was hence standardly used in the framework of this thesis.

The $C_{100}H_{202}$ melt, which is expected to show slower dynamics than the $C_{16}H_{34}$ system, was also measured with even higher instrumental resolutions. The master curves, obtained by joining intermediate scattering functions measured for different instrumental resolutions, cover four orders of magnitude in time, as can be seen in figure 7.4 for $T = 509\,\mathrm{K}$. Again, an outstanding agreement between the data points obtained from the MD simulation and neutron spectroscopy can be identified for $C_{100}H_{202}$, which extends from the sub-picosecond to nanosecond time scale. This is also the case for the lower temperatures.

In this high quality validation on the atomic scale the simulated short-time dynamics represent the motions observed with neutron scattering excellently. Hence the simulated motions complement the quasielastic neutron scattering data by providing equivalent information in real space. The validation also proves the value of neutron spectroscopy to directly probe the dynamics which directly result from the force field parameters.

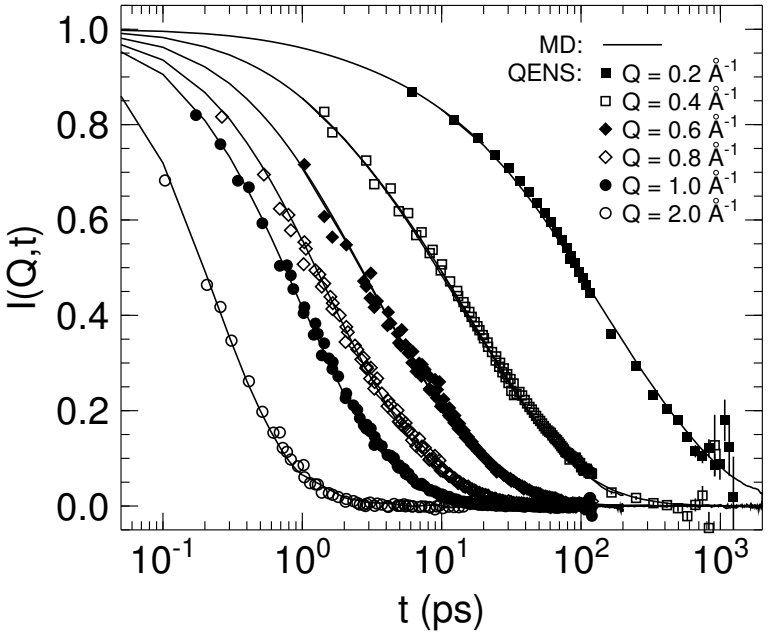

Figure 7.4: $C_{100}H_{202}$ - Intermediate scattering functions as calculated from the MD simulations (solid lines) and measured with quasielastic neutron scattering (QENS) at TOFTOF (symbols) at $T = 509\,\mathrm{K}$ (cf. [178]).

Structure

Density A first test of the simulated structure is a validation of the simulated density. Table 7.1 contains the densities of all simulated systems and allows for a comparison of the results from different force fields with the literature values from the Landolt-Börnstein database [179]. The resulting densities using the force field from Chang & Sandler are too large, and the relative error decreases with increasing temperature. The relative errors are below 5 %, which is fair enough, considering that the size of the simulation box is not a fixed parameter in the simulation of an NPT ensemble.

Including explicit 1–4 pair interactions into the force field results in a crystallization of the n-alkane systems at low temperatures above the literature melting temperature. Neglecting these 1–4 terms resulted in a artificially low melting point. The resulting densities are found to be too large compared to the experimental values, similar to the values obtained from the simulations neglecting non-bonded 1–4 interactions.

The L-OPLS force field presented by Siu et al. yields a more precise density of the $C_{16}H_{34}$ system at low temperatures, with relative errors below 1 %. However, for higher temperatures the densities are too low compared to the literature values

Table 7.1: Comparison of the simulated densities (kg/m^3) with literature values from the Landolt-Börnstein (L.-B.) database [179] for the simulated n-alkane systems at different temperatures T. The densities are listed for the simulations using the Chang & Sandler (C&S) force field [153] with (4^{th} column) and without (5^{th} column) calculating explicit non-bonded 1–4 pair interactions. Using 1–4 pairs may result in crystallization (cryst.) above the melting temperature. Also listed are the densities obtained using the L-OPLS force field parameters of Siu et al. [152].

System	T	L.-B.	C&S with 1–4 pairs	C&S without 1–4 pairs	Siu et al.
$C_{16}H_{34}$	293 K	773.44	cryst.	799.97	770.58
	323 K	752.81	cryst.	775.74	-
	363 K	724.89	745.76	743.36	708.77
	403 K	696.55	712.03	710.37	-
	443 K	667.83	677.44	676.55	636.36
$C_{100}H_{202}$	393 K	-	cryst.	804.92	-
	453 K	-	-	762.72	-
	509 K	-	726.09	724.09	679.40

and the relative error increases with inceasing temperature. The L-OPLS force field was developed to simulate biologically relevant systems at room temperature and was therefore not optimized at higher temperatures [154].

The Lennard-Jones potential is an empiric function which is applied to model van der Waals forces in the MD simulations. The simulated density strongly depends on the cutoff length r_{LJ} used to truncate the Lennard-Jones interaction. To study the dependency of the density on the Lennard-Jones cutoff length short MD simulation runs were performed with varying r_{LJ}. As tabulated in table 7.2, a decrease of the cutoff length resulted in lowering the density. It is generally believed that a realistic potential should yield more precise simulation results by increasing the cutoff length. The results from bulk water simulations showed that this tendency is not true [180]. For $C_{16}H_{34}$ at 363 K intermediate scattering functions were calculated for simulations with a modified cutoff length $r_{\text{LJ}} = 1.15$ nm and compared with the otherwise simulated system ($r_{\text{LJ}} = 2.00$ nm). The resulting dynamic coherent and incoherent structure factors are plotted in figure 7.5 and 7.6, respectively. The dominant co-

Table 7.2: Density of the $C_{16}H_{34}$ system at 363 K with a variable Lennard-Jones (LJ)-cutoff.

LJ-cutoff (nm)	1.10	1.15	1.20	1.30	2.00
density (kg/m^3)	722	725	728	732	743

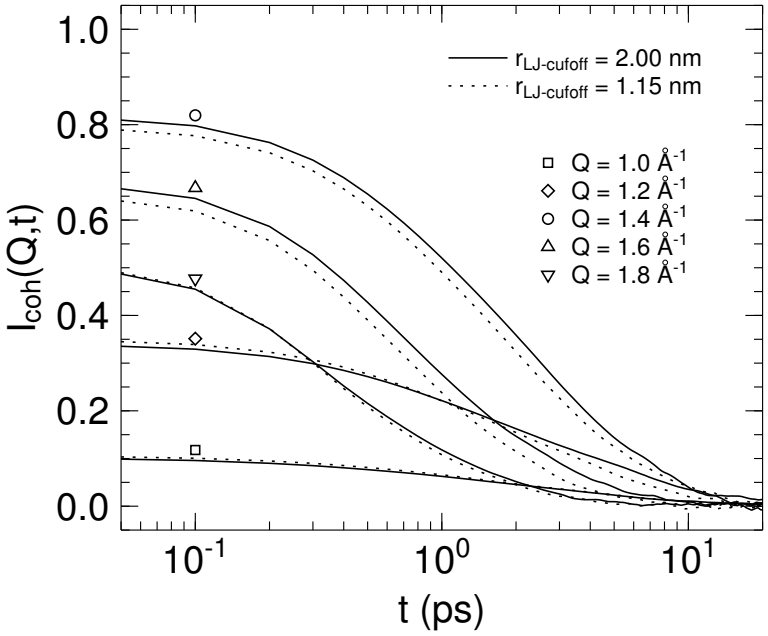

Figure 7.5: $C_{16}H_{34}$ - Dynamic coherent structure factors as obtained from the MD simulations at 363 K. The simulations were performed using two different Lennard-Jones cutoff lengths $r_{\mathrm{LJ-cutoff}}$. The symbols label the different values of scattering vector Q.

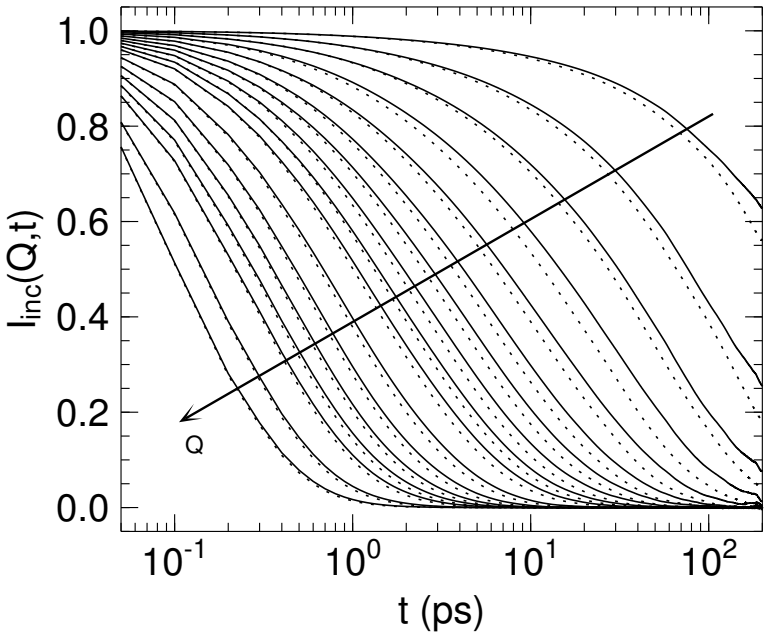

Figure 7.6: $C_{16}H_{34}$ - Dynamic incoherent structure factors as calculated from the MD simulations at 363 K simulated using two different Lennard-Jones cutoff lengths $r_{\mathrm{LJ-cutoff}} = 2.00$ nm (solid lines) and 1.15 nm (dotted lines). The arrow points into the direction of increasing scattering vector Q, ranging from 0.1 to 3.0 Å^{-1} (0.1, 0.2, 0.3, 0.4, 0.5, 0.6, 0.7, 0.8, 0.9, 1.0, 1.2, 1.4, 1.6, 1.8, 2.0, 2.5, 3.0 Å^{-1}). The change of $r_{\mathrm{LJ-cutoff}}$ results in an altered form of the spectra at low values of Q.

herent structure factor at $Q \approx 1.4\,\text{Å}^{-1}$ corresponds to the chain-chain correlation. With the reduced Lennard-Jones cutoff the density of the system decreases, and the coherent structure factor $I_{\text{coh}}(Q, t = 0)$ also decreases slightly.

The incoherent part shows clear differences for low values of $Q < 1\,\text{Å}^{-1}$. The simulated dynamics with the modified Lennard-Jones cutoff r_{LJ} yield a faster decay of the self part of the correlation function. Hence the short-time motions of the atoms are strongly influenced by adjusting the Lennard-Jones cutoff. Bending the density into shape in this way leads to dynamics which do not represent the experimentally measured intermediate scattering functions.

Since the simulated dynamics are nicely reproduced using the advanced Lennard-Jones cutoff length $r_{\text{LJ}} = 2\,\text{nm}$, the minor error in density is accepted. If precise representations of the simulated structures at low temperatures are needed, the new L-OPLS force field parameters of Siu et al. [152] should be applied for the simulation of n-alkanes. A reparametrization of the L-OPLS force field parameters to simulate the correct temperature dependence of hydrocarbons is the focus of current work [154].

Static Structure Factor The static structure factors $S(Q)$ was measured with neutron polarization analysis at DNS and calculated from the MD simulations. Te latter intensities were modified to account for the inelasticity effects, as described in section 5.4. The data obtained from both methods are illustrated in figure 7.7 for $C_{16}H_{34}$ and $C_{100}H_{202}$ at all measured temperatures.

For both systems the overall shape of the measured $S(Q)$ is well reproduced by the simulations. Due to the low coherent scattering of the sample the measured signal is quite noisy. The position of the chain correlation peak at $Q \approx 1.4\,\text{Å}^{-1}$ in the MD simulations is at the right position, although the simulated densities are slightly too high. Hence this has no effect on the intermolecular chain distances, but rather on the local conformation of the molecules.

At low values of $Q < 1\,\text{Å}^{-1}$ an increasing deviation of the measured and simulated $S(Q)$ can be observed, in particular for the static structure factors of $C_{100}H_{202}$. It is to be assumed that this feature is an artifact resulting from the data reduction. It is especially a proper measurement and subtraction of the experimental background which affects the low-Q behavior of the $S(Q)$.

It is to be noted that the modification of the simulated intensities is essential for a direct comparison with the neutron scattering data obtained at DNS. The

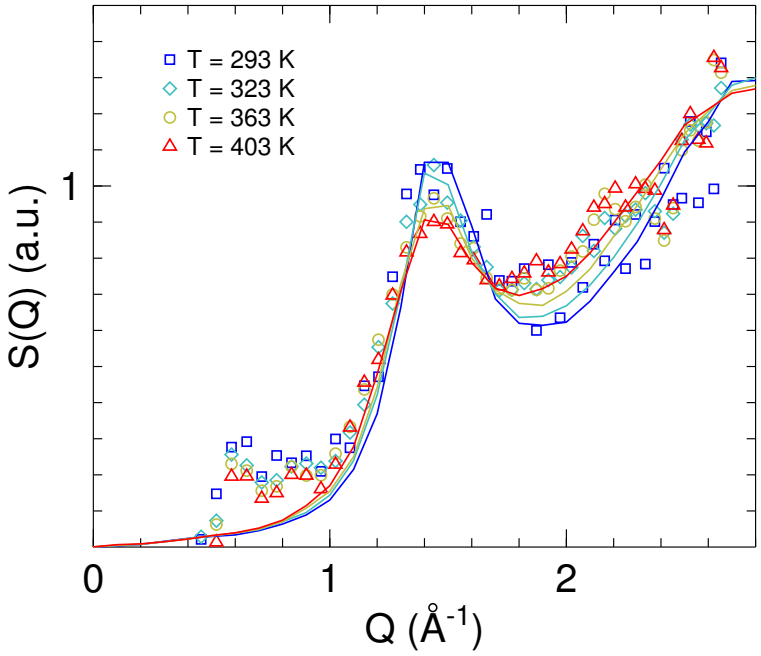

(a) $C_{16}H_{34}$

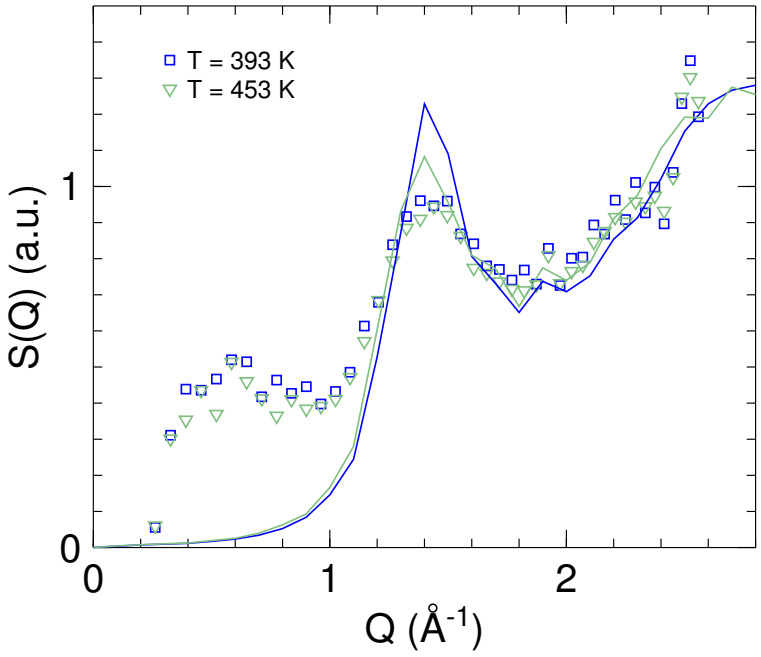

(b) $C_{100}H_{202}$

Figure 7.7: Static structure factors as measured with neutron polarization analysis at DNS (symbols) and as calculated from the MD simulations (lines) for $C_{16}H_{34}$ (upper image) and $C_{100}H_{202}$ (lower image) at several temperatures T. The values obtained from the simulations were modified to account for the inelasticity effects.

temperature dependence of the chain correlation peak is in great accordance and also the width of this peak at $Q \approx 1.4\,\text{Å}^{-1}$ is nicely reproduced by the MD simulations, particularly for the $C_{16}H_{34}$ system. For the $C_{100}H_{202}$ system the simulated amplitude of the chain correlation peak is too pronounced. Compared to the data analysis of the $C_{16}H_{34}$ system, less time frames were used to calculate the static structure factor for the simulated $C_{100}H_{202}$ melt, as the computation effort increases magnificantly with increasing system size. The overestimation of the chain correlation peak may result from the less detailed analysis.

Also for large scattering vectors of $Q \gtrsim 2\,\text{Å}^{-1}$ the simulated values agree with the measured ones, mostly due to the correction performed on the simulated values. The impact of this modification is illustrated in figure 7.8, where the unaltered static structure factor is plotted together with the modified data set for the $C_{16}H_{34}$ system. The relocation of intensities, as described in section 5.4 results in a amplification of the data points at $Q \gtrsim 2\,\text{Å}^{-1}$, making a comparison to the neutron scatteing data possible.

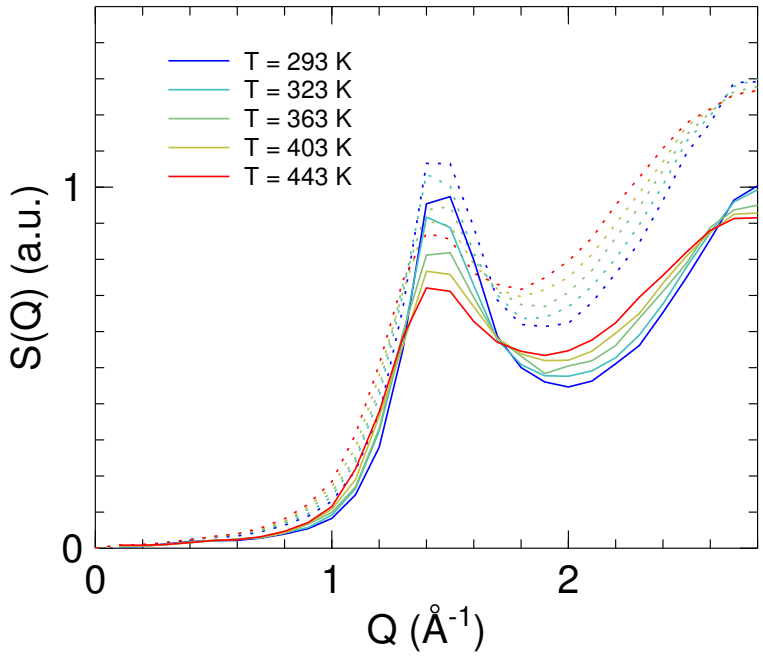

Figure 7.8: $C_{16}H_{34}$ - Static structure factors as calculated from the MD simulations (solid lines), compared to the results obtained when accounting for the inelsticity effects (dotted lines).

7.2 Atomic and Molecular Self Motion

Since the quasielastic neutron scattering data verify the simulated dynamics on a wide length and time scale, the motion of the atoms and molecules will be analyzed in real space in the following. This analysis will focus on the displacements of individual atoms and of the whole molecules, i. .e. their center-of-mass (com) coordinates, before the simulated trajectories will be used to test the validity and applicability of the Rouse model.

Radial Distribution Function

The self-motion of the atoms in real space is represented by the self-part of the van Hove correlation function $G_{\mathrm{self}}(r,t)$. As introduced in section 4.1, this function describes the probability of finding a particle at distance r from its origin after time t. For $t=0$ this function results in a δ-function, since the particles have not moved at all. With increasing time the function starts to broaden, as exemplarily illustrated in figures 7.9 and 7.10 for $C_{16}H_{34}$ and $C_{100}H_{202}$, respectively. The peak maximum shifts to larger displacements and decreases in height with increasing temperature and time.

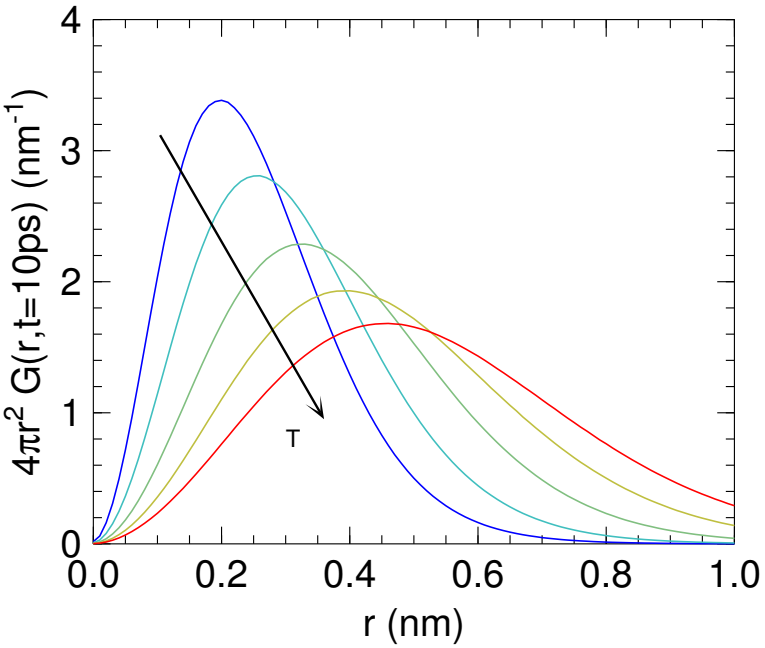

Figure 7.9: $C_{16}H_{34}$ - Self-part of the van Hove correlation function at $t = 10\,\mathrm{ps}$. The arrow points into the direction of rising temperature. With increasing temperature the peak maximum shifts to larger distances while the peak height decreases.

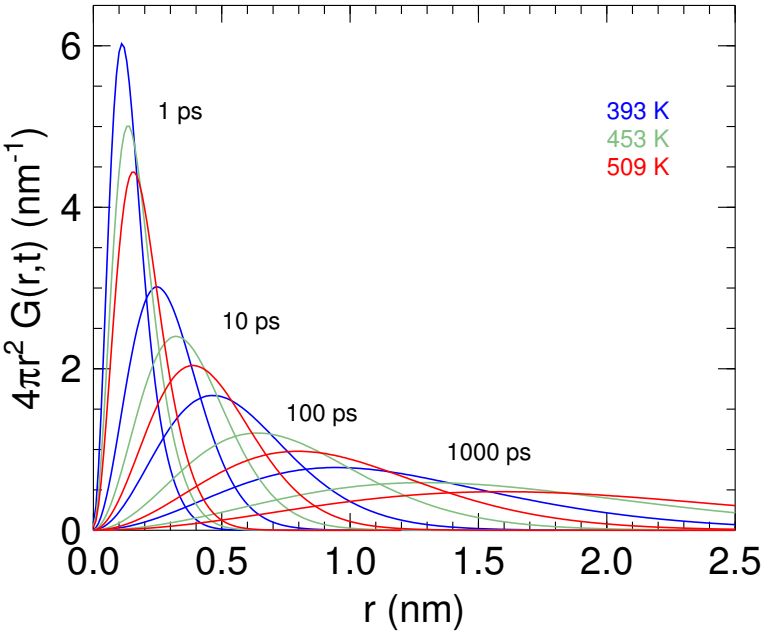

Figure 7.10: $C_{100}H_{202}$ - Self-part of the van Hove correlation function. With increasing time the peak maximum shifts to larger distances while the peak height decreases.

At very short times ($t \to 0$) the individual atoms move ballistically. Therefore, due to the equilibrium distribution of velocities, the self-part of the van Hove correlation function has a Gaussian form as a function of r [89]. In the long time limit ($t \to \infty$) the purely diffusive regime is reached, hence $G_{\text{self}}(r,t)$ is again a Gaussian [181, 182]. Using a Gaussian function, $G_{\text{self}}(r,t)$ can be described according to equation 4.18 [85]. For the calculation of the Gaussian expression of the radial distribution function, the mean-square displacement is required as an input. It was obtained from the simulations as

$$\left\langle r^2(t) \right\rangle = \int_0^\infty r^2 \left(4\pi r^2 G_{\text{self}}(r,t)\right) \mathrm{d}r \tag{7.1}$$

for this purpose. Figure 7.11 exemplarily presents a comparison of the simulated $G_{\text{self}}(r,t)$ with the results obtained from equation 4.19 for $C_{16}H_{34}$ at 443 K.

At $t = 1$ ps and $t = 10$ ps clear deviations from a Gaussian distribution are present in the $C_{16}H_{34}$ system at high temperatures. The peak of the Gaussian approximation $G_{\text{self}}^{\text{Gauss}}(r,t)$ occurs at larger distances than observed from the simulations. With increasing time the correlation function can be modeled increasingly better by Gaussians, as can be seen from the only minor differences of the e. g. $t = 100$ ps data.

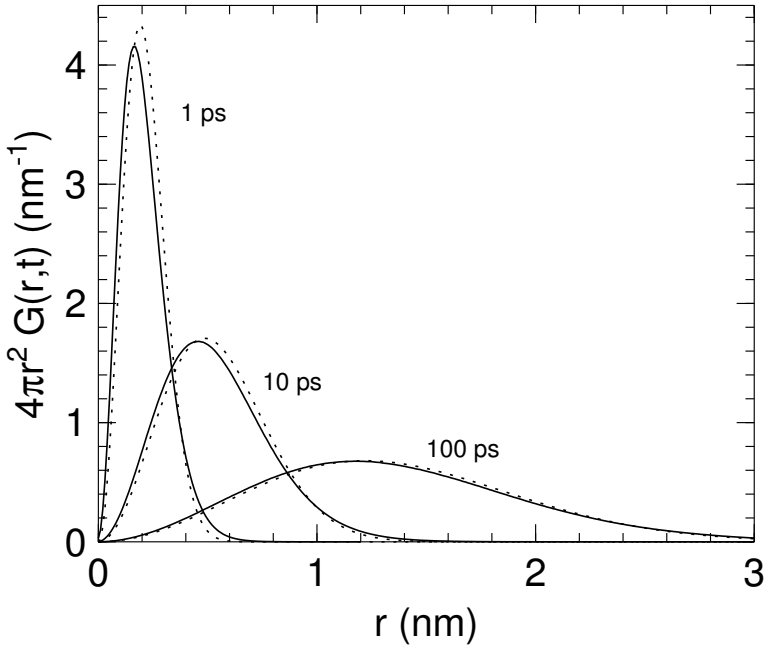

Figure 7.11: $C_{16}H_{34}$ - Self-part of the van Hove correlation function at $T = 443\,\mathrm{K}$ as calculated from the simulated trajectories (solid lines). In addition the standard Gaussian function is shown (dotted lines). Clear deviations from the Gaussian distribution function can be identified on the short picosecond time scale.

Non-Gaussian Parameter

The deviations of the self-part of the van Hove correlation function $G_{\mathrm{self}}(r,t)$ from a Gaussian distribution are quantitatively determined by the non-Gaussian parameter $\alpha_2(t)$ (eq. 4.23). The parameter $\alpha_2(t)$ was calculated for the center-of-mass coordinates of the molecules and for the coordinates of the individual carbon atoms separately. Only carbon atoms are treated in the latter case to reduce the calculation effort, justified by the fact that the motions of the hydrogen atoms are strongly linked to the carbon dynamics.

$C_{16}H_{34}$ For the displacements of the whole $C_{16}H_{34}$ molecules, i. e. for their com coordinates, a clear non-Gaussian behavior can be identified on intermediate times with a maximum at $5\,\mathrm{ps} \lesssim t \lesssim 20\,\mathrm{ps}$ (see fig. 7.12(a)). The peak maximum is temperature dependent and shifts to shorter times with increasing temperature. Furthermore the deviations from a Gaussian behavior decrease with increasing temperature. Neglecting explicit 1–4 pair interactions in the force field leads to a reduced value of $\alpha_2(t)$, however the peak position seems unchanged. Similar observations were reported for simple Lennard-Jones systems [84], underlining that this behavior is not related to intramolecular motions. The maximum amplitude of the

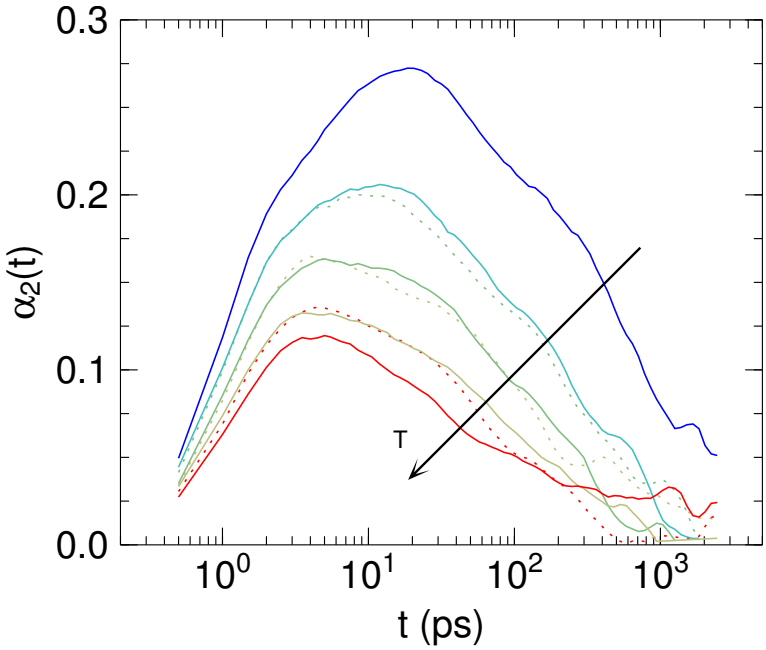

(a) $C_{16}H_{34}$ - Center-of-mass coordinates of the molecules.

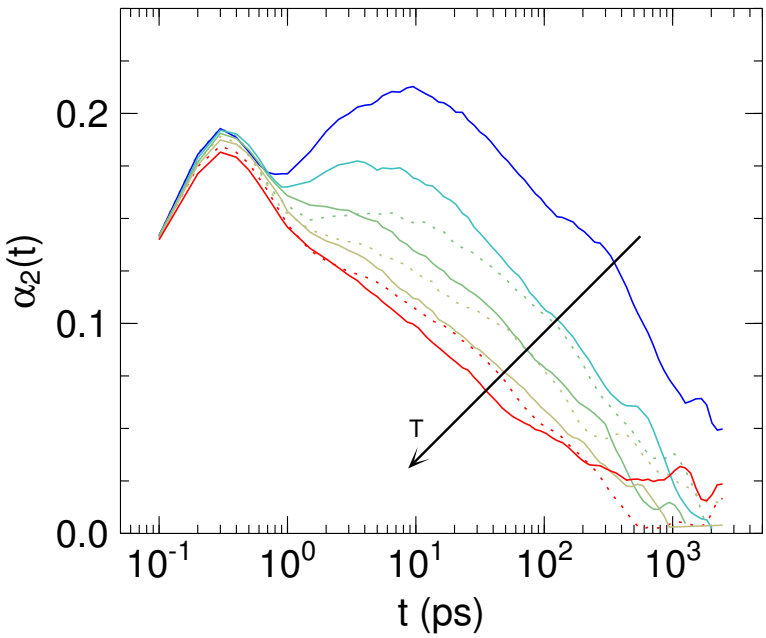

(b) $C_{16}H_{34}$ - Carbon atoms.

Figure 7.12: $C_{16}H_{34}$ - Non-Gaussian parameter calculated for the center-of-mass coordinates of the whole molecules (upper image) and for only the carbon atoms (lower image). The MD simulations were performed with (dotted lines) and without (solid lines) explicit 1–4 pair interactions. The arrow points into the direction of rising temperature.

non-Gaussian parameter can be linked to the crossover to a subdiffusive motion of the com molecules, which is very pronounced at low temperatures. This will be addressed in the following section. In addition to the strong maximum a shoulder appears at longer times. For the lowest simulated temperature ($T = 293\,\mathrm{K}$) this feature is at $t \approx 500\,\mathrm{ps}$ and also shifts to shorter times with increasing temperature. However, it is difficult to clearly identify this feature, since the peak is very dominant. As will be pointed later, this shoulder corresponds to the crossover from the subdiffusive to the diffusive regime.

A similar behavior can be noticed for the non-Gaussian parameter calculated for the individual carbon atoms in the $C_{16}H_{34}$ melt. As can be seen in figure 7.12(b), the peak and the shoulder that was identified for the com $C_{16}H_{34}$ coordinates is also present here. The peak is more difficult so localize with increasing temperature. This is due to the appearance of an additional distinct peak, which reaches its maximum at $t \approx 0.3\,\mathrm{ps}$. There is only a slight temperature dependence of the peak height. This characteristic can be is related to fast librational motions of the covalent bonds [183, 184], and is hence not visible in simple Lennard-Jones or colloidal systems.

$C_{100}H_{202}$ The com trajectories of the $C_{100}H_{202}$ molecules, plotted in figure 7.13(a) show similar non-Gaussian features. The first peak of $\alpha_2(t)$ is observed between 3 and 10 ps. No clear temperature dependence for this feature could be determined. Again this short-time feature corresponds to the crossover to a subdiffusive behavior of the com motions, as will be concluded from the analysis of the mean-square displacements in the following section. This crossover is reflected in a relatively little amplitude of the non-Gaussian parameter, compared to the dominant peak of the com $\alpha_2(t)$ of the $C_{16}H_{34}$ data (cf. fig. 7.12(a)).

With increasing time the non-Gaussianity of the $C_{100}H_{202}$ com motion increases and reaches a maximum at long times. For the simulated temperature of $T = 453\,\mathrm{K}$ and 509 K the maximum of $\alpha_2(t)$ can be identified at $t_{\max} \approx 3\,\mathrm{ns}$ and $t_{\max} \approx 1\,\mathrm{ns}$, respectively. For $T = 393\,\mathrm{K}$ the maximum is at $t > 10\,\mathrm{ns}$. The maximum again shifts to shorter times and the value of $\alpha_2(t_{\max})$ decreases with increasing temperature. The crossover from the subdiffusive regime to a freely diffusive motion takes place on these time scales.

The non-Gaussian dynamics of the carbon atoms in the $C_{100}H_{202}$ melt also show the additional feature at $t \approx 0.3\,\mathrm{ps}$, as illustrated in figure 7.13(b). This feature corresponds to the observations for the dynamics of the carbon atoms in the $C_{16}H_{34}$ melt. There is only a slight temperature dependence of the peak height, but the

position of the peak shows no dependence of the chain length. In this microscopic regime the atoms start feeling the covalent bonds and the observed dynamics are again due to local vibrations [184].

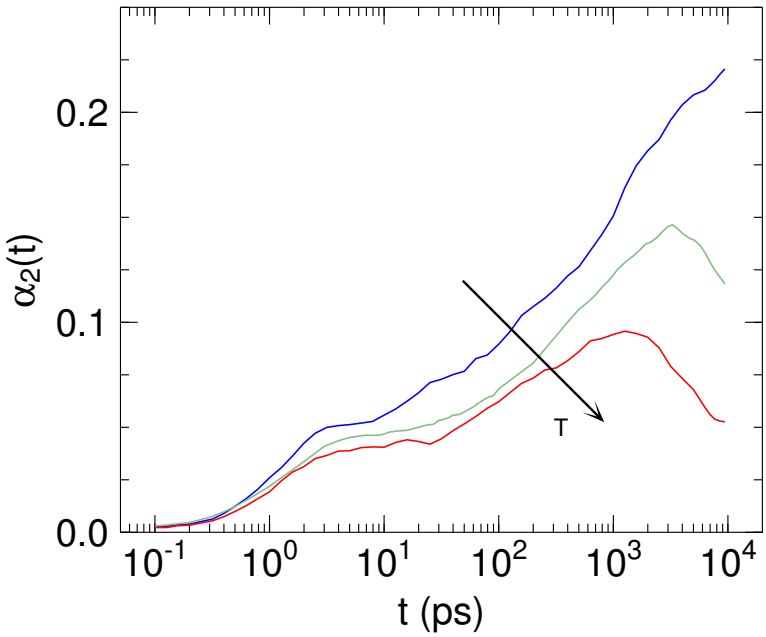

(a) $C_{100}H_{202}$ - Center-of-mass coordinates of the molecules.

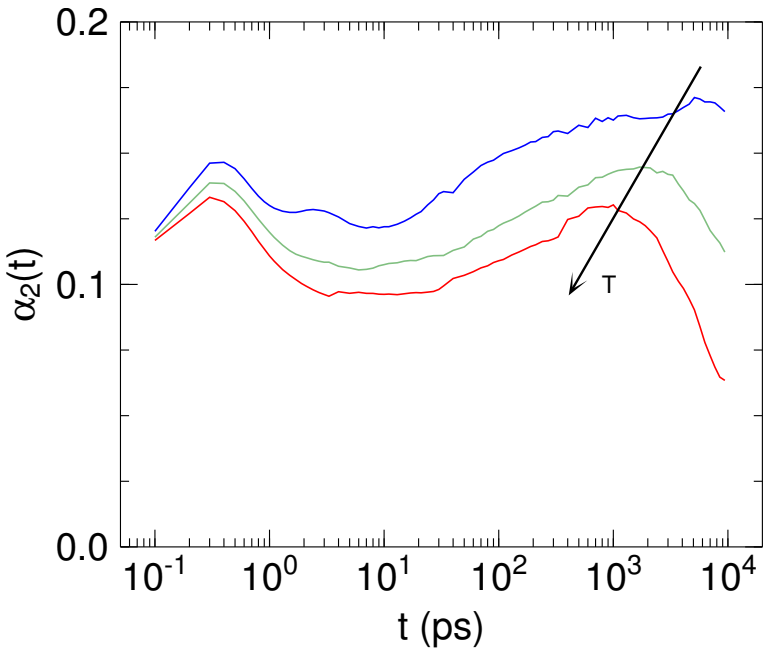

(b) $C_{100}H_{202}$ - Carbon atoms.

Figure 7.13: $C_{100}H_{202}$ - Non-Gaussian parameter calculated for the center-of-mass coordinates of the molecules (upper image) and for only the carbon atoms (lower image). The arrow points into the direction of rising temperature.

Mean-Square Displacement

The mean-square displacement (MSD) was calculated for the coordinates of all individual atoms and for the the center-of-mass coordinates of the molecules as well.

$C_{16}H_{34}$ Any translational motion of the whole molecular chain is reflected in the displacement of the individual atoms of the chain. To characterize the extend to which the atomic motion is affected by global molecular dynamics, the MSD of the individual atoms is compared to the MSD of the com molecules in figure 7.14 at three different temperatures. The MSD of the individual atoms is enhanced, and merges with the MSD of the com molecules at $500\,\mathrm{ps} \lesssim t \lesssim 5\,\mathrm{ns}$, whereas this point shifts to shorter times with increasing temperature. Hence the motions of the single atoms on the picosecond time scale is not entirely driven by the com motion, but is rather due to intramolecular motions.

The whole molecules show a subdiffusive, i. e. $t^{<1}$ behavior, which is more pronounced at lower temperatures. A fit of a power law $\langle r^2(t)\rangle \propto t^x$ to the MSD of the com coordinates at $T = 293\,\mathrm{K}$ yields an exponent of $x = 0.6$ (fit range 1–10 ps). For this temperature the crossover to the freely diffusive regime ($x = 1.0$) occurs

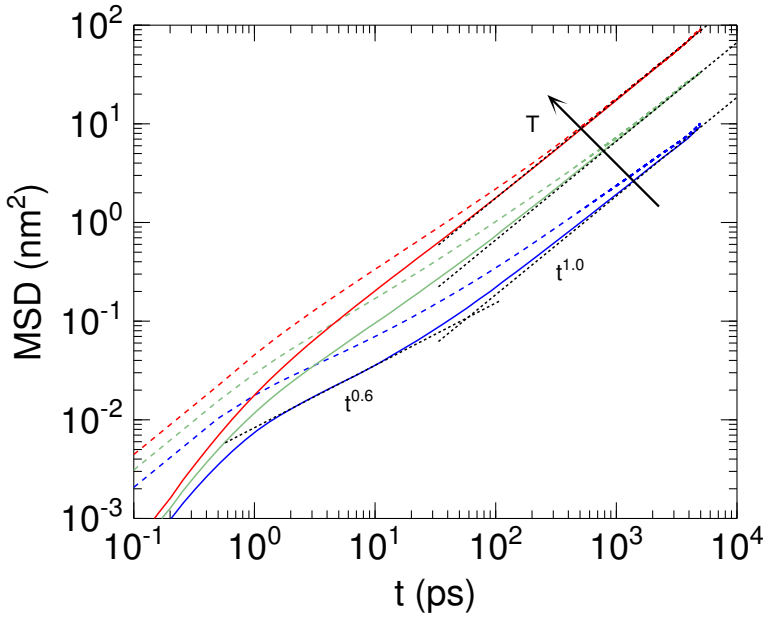

Figure 7.14: $C_{16}H_{34}$ - Mean-square displacement (MSD) at $T = 293$, 363 and 443 K. The solid lines represent the MSD of the center-of-mass coordinates of the whole molecules, while the dashed lines present the MSD calculated for all atoms in the system. The black dotted lines are power laws. The linear t^1-range corresponds to the diffusive regime. The arrow points into the direction of rising temperature.

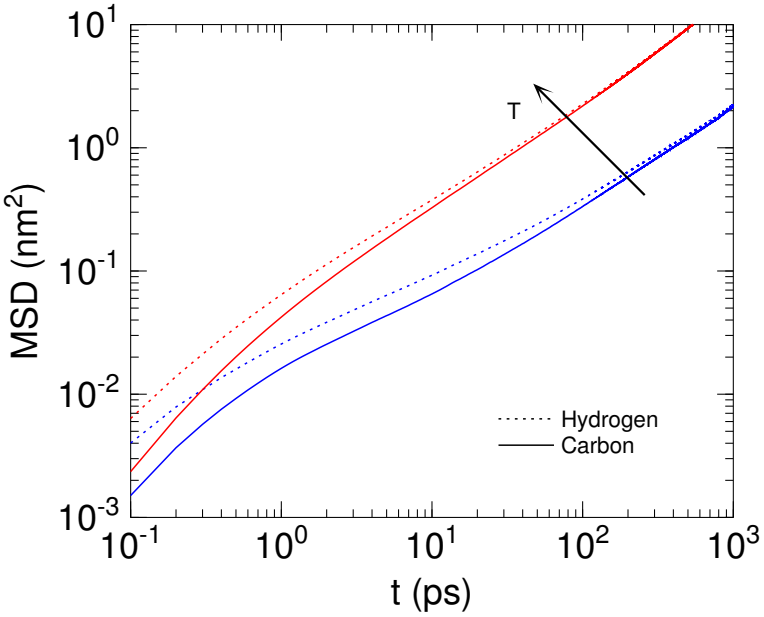

Figure 7.15: $C_{16}H_{34}$ - Mean-square displacement (MSD) of the hydrogen atoms (dotted lines) and carbon atoms (solid lines) at $T = 293$ and 443 K. At short times the MSD of the hydrogen atoms is enhanced due to e. g. bond vibrations or methyl group rotations.

at roughly $t \approx 100$ ps. With increasing temperature this crossover takes place at shorter times.

In order to study the chain dynamics of the $C_{16}H_{34}$ molecules only the MSD of the carbon atoms is considered in the following. The fact that the overall dynamics of the hydrogen atoms are highly correlated to the motions of the carbon atoms of the molecular backbone allows for this simplification. At very short times independent motions such as methyl group rotations provide extra contributions to the MSD of the hydrogen atoms [185–187] (cf. fig. 7.15).

The relative MSD of the chain ends to the MSD of the chain center is illustrated in figure 7.16(a), showing that the ends of the chains perform larger displacements than the atoms at the center of the chain on the whole pico- to nanosecond time range studied. The first, short time decay of the curves is due to the enhanced flexibility of the chain ends. The carbon atoms at the chain ends are covalently bonded to only one neighboring carbon atom. Hence fast sub-picosecond dynamics as e. g. bond vibrations have a more distinct effect on the MSD of the atoms at the chain ends. However, with increasing time the relative effect of these local vibrational motions get lost in more global dynamics.

A second rise of the relative MSD occurs between 10 ps and 1 ns, with the peak maximum shifting to shorter times with increasing temperature. The maximum

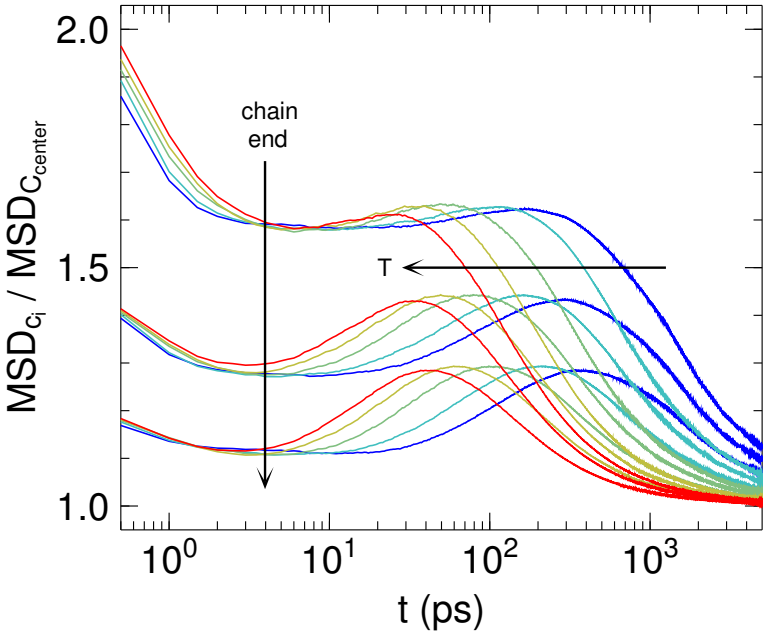

(a)

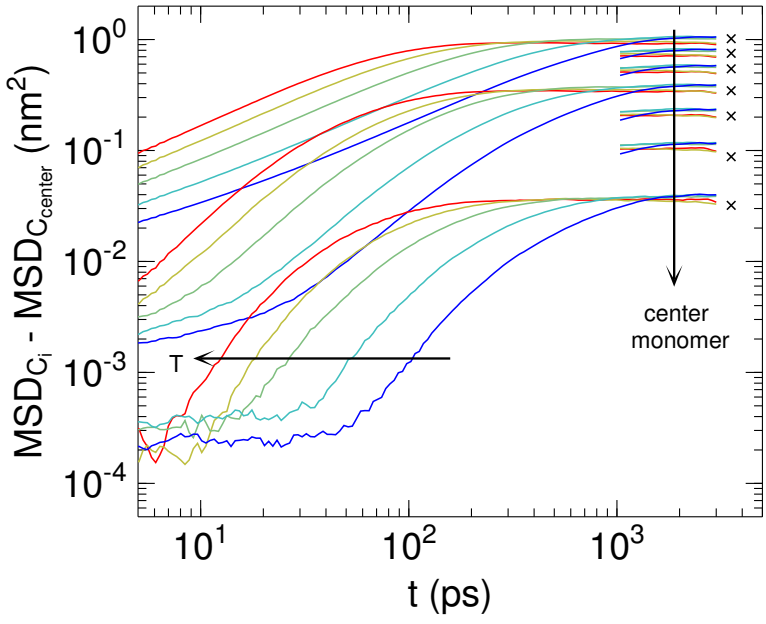

(b)

Figure 7.16: $C_{16}H_{34}$ - Mean-square displacement (MSD) of carbon atoms C_i at different positions along the molecule divided (upper image) and subtracted (lower image) respectively by the MSD of the carbon atoms C_{center} at the central positions of the molecular backbone (cf. [168]). The horizontal arrow points into the direction of rising temperature, while the other illustrates the position of the carbon atom C_i along the molecule.
The black marks in the lower image represent the maximum displacement of the carbon atoms due to a centered rotational motion of the $C_{16}H_{34}$ molecule, as listed in table 7.3.

Table 7.3: Most probable distance between carbon atoms separated connected by # bonds along entire $C_{16}H_{34}$ chains. Also listed are the averaged additional MSD values, calculated for $C_{16}H_{34}$ molecules at $T = 403\,\mathrm{K}$, which perform a centered rotational motion, as described in the text and illustrated in figure 7.17.

# bonds	1	2	3	4	5	6	7
most probable distance (nm)	0.154	0.256	0.389	0.505	0.633	0.752	0.875
additional MSD (nm^2)	0.032	0.087	0.201	0.339	0.533	0.752	1.018

value of the peak is mainly independent of temperature, indicating that geometrical aspects of the molecules are the reason for this behavior. A sole centered rotational motion of the entire molecule would give rise to an enhanced relative MSD, since the center of the chain would not move at all in this case.

Subtracting the MSD of the carbon atoms at the center of the chain from the MSD data of the other carbon atoms effectively removes the long-range displacement of the whole molecule. The resulting data, as pictured in figure 7.16(b) gives information only on reorientational dynamics of the molecules. On a time scale $10\,\mathrm{ps} \lesssim t \lesssim 1\,\mathrm{ns}$ the MSD of the chain ends increases more compared to the MSD of the chain center, analogous to the observations of the relative MSD in figure 7.16(a). Afterwards, on the nanosecond time scale, the curves approach a constant value, which can be interpreted as the maximum displacement of the carbon atoms due to a rotational motion of the whole molecules.

The constant values of the curves in figure 7.16(b) for large times correspond to the maximum displacement of the atoms of a stiff molecule performing a centered rotational motion. The distance of a carbon–carbon bond is 0.154 nm. Moving

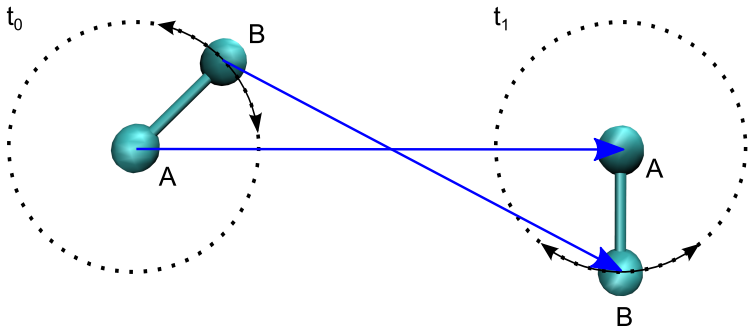

Figure 7.17: Illustration of the additional displacement due to a rotational motion of covalently bonded atoms. Atom A moves into any direction and atom B rotates around A. The displacement of atom B can be greater or smaller than the displacement of atom A. Considering all starting positions of atom B at time t_0 and all final positions at t_1 results in the additional mean-square displacement as listed in table 7.3.

one carbon atom (which is located at a central position of the molecular backbone) steadily in one direction and rotating the other one around it, results in an additional averaged MSD of $0.032\,\mathrm{nm}^2$ of the second carbon atom (cf. fig. 7.17). For atoms connected via several covalent bonds along the molecular backbone the most probable distance between these atoms was extracted from the simulations. This procedure takes into consideration that the molecules are in different configuration, due to geometric isomerism. The respective most probable distances and the resulting additional averaged MSD are listed in table 7.3.

$C_{100}H_{202}$ In the whole picosecond time scale the MSD of the com $C_{100}H_{202}$ molecules shows only little movement of the entire chains. As can be seen in figure 7.18, the displacement during a time interval of 100 ps is of only a few Å, even at the highest simulated temperature. The MSD shows a subdiffusive behavior, which spans into the nanosecond time range. As determined for the $C_{16}H_{34}$ molecules, the crossover to the diffusive regime ($\sim t^1$) is temperature dependent, and shifts to shorter times with increasing temperature. At $T = 509\,\mathrm{K}$ this crossover takes place at $t \approx 10\,\mathrm{ns}$, which coincides with corresponding neutron spin echo results [39]. By

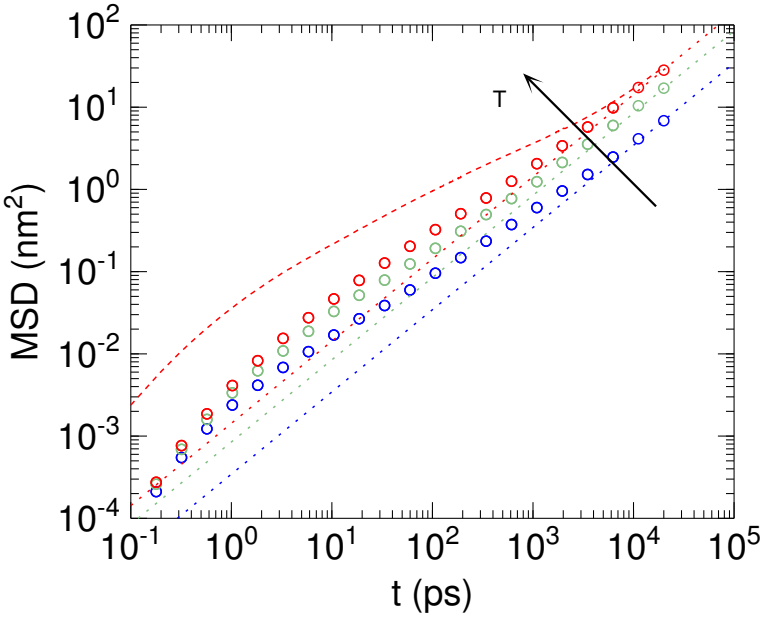

Figure 7.18: $C_{100}H_{202}$ - Mean-square displacement (MSD) at $T = 393$, 453 and 509 K. The symbols represent the MSDs of the center-of-mass coordinates of the whole molecules, while the dashed red line represents the MSDs calculated for the carbon atoms at the center of the molecule backbone at the highest temperature of $T = 509\,\mathrm{K}$. The dotted lines are linear functions fitted to the center-of-mass MSDs at all temperatures. The arrow points into the direction of rising temperature.

fitting a linear function to the MSD of the com coordinates a self-diffusion coefficient can be determined yielding $D_{\mathrm{com}}^{\mathrm{MSD}} = 2.38 \cdot 10^{-6}\,\mathrm{cm}^2/\mathrm{s}$ at $T = 509\,\mathrm{K}$. Pearson et al. determined diffusion coefficients for shorter n-alkanes with PFG-NMR [172, 173]. An extrapolation of their data results in a value of $D^{\mathrm{NMR}} \approx 2.3 \cdot 10^{-6}\,\mathrm{cm}^2/\mathrm{s}$ for $C_{100}H_{202}$ at $T = 509\,\mathrm{K}$. This is in good agreement with the simulated long time diffusion coefficient, regarding the uncertainty involved in the extrapolation of temperature and chain length.

Although the whole molecules translate only marginally, the MSD of the individual atoms is more pronounced than the MSD of the com coordinates of the whole molecules. The MSD of the carbon atoms and of the com molecules coincide on time scales which were barely accessed with the MD simulations performed in the framework of this thesis*. At $T = 509\,\mathrm{K}$ the MSDs match on a time scale of about $t \gtrsim 20\,\mathrm{ns}$ (cf. fig. 7.18). This time scale shifts to longer times with decreasing temperature (not shown). Hence the atomic motions are only little driven by the self-diffusion of the $C_{100}H_{202}$ molecules on the studied time scale. Therefore the atomic motions are only little driven by the self-diffusion of the $C_{100}H_{202}$ molecules on the studied time scale.

Different behavior can be identified for the MSD of the whole $C_{100}H_{202}$ molecules, as indicated in figure 7.19 for $T = 509\,\mathrm{K}$. The dynamics on very short times are characterized by a t^2 scaling, corresponding to an initial ballistic regime. This is followed by a short superdiffusive ($t^{5/4}$) and the subdiffusive regime, with a $t^{3/4}$ scaling as predicted by the theories of Farago et al., accounting for either viscoelastic hydrodynamic interactions (VHIs) [46] or density fluctuations [72]. However, both models were not prepared to describe the superdiffusive or ballistic regime.

To test the two models, the respective mean-square displacements (eqs. 2.27 and 2.28) were plotted. The only free parameter W, accounting for a time constant, was obtained according to the method described by Farago et al. [46]: $b^2\sqrt{Wt}$ was fitted to the subdiffusive regime of the MSD of the carbon atoms at the center of the $C_{100}H_{202}$ molecule, resulting in $W \approx 0.5\,\mathrm{ps}^{-1}$. The statistical segment length $b = 0.4\,\mathrm{nm}$ and the particle number density $n = 31\,\mathrm{nm}^{-3}$ was chosen in accordance with other studies [30, 31]. It is to be noted that neither model contains free parameters which need to be fitted to the com MSD. A comparison of the MSD with the predictions of both theories, which is illustrated in figure 7.19, clearly illustrates that the effect of density fluctuations is weak to account for the subdiffusive behav-

*The maximum simulation time was 20 ns

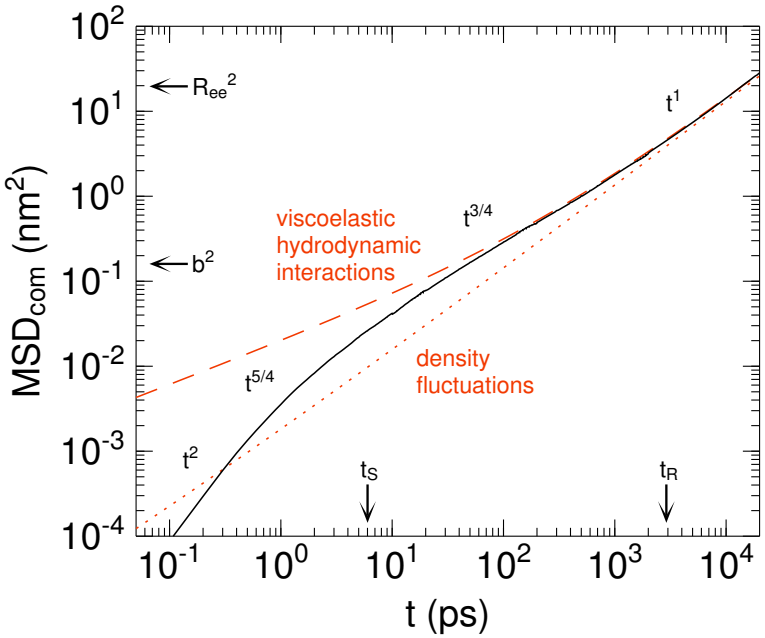

Figure 7.19: $C_{100}H_{202}$ - Mean-square displacement (MSD) of the center-of-mass coordinates at $T = 509\,\mathrm{K}$ (solid black line). Also plotted are the predictions from two theories to model the subdiffusive ($t^{<1}$) regime: One accounting for viscoelastic hydrodynamic interactions [46] (dashed red line) and one including density fluctuations [72] (dotted red line). The arrows indicate the validity of the two models, which is framed by the mean-square chain end-to-end distance R_{ee}^2 and the squared statistical segment length b as well as the segmental t_S and Rouse t_R relaxation time, which were derived from the Rouse analysis presented in the following section (cf. [178]).

ior. The VHI-model, however, nicely describes the subdiffusive regime as well as the crossover to Fickean diffusion.

Further verification of the model needs to test the scaling of the long-time com velocity autocorrelation function (VAF), which is predicted as $-N^{-1/2}t^{-3/2}$ by the VHI-model. A straightforward computation of the VAF for the simulated trajectories results in very noisy data and is hence impractical to test the VHI-model [188]. Nevertheless the experimentally validated simulation presented here strongly supports the VHI-theory, pointing out that hydrodynamic effects lead to the anomalous com diffusion. Although this theory was developed to model the motions of very long, unentangles flexible molecules, it is very capable of describing the com dynamics of the $C_{100}H_{202}$ chains.

Rouse Analysis

The Rouse model was developed to describe the dynamics of short polymer chains, which are long enough to show Gaussian chain statistics. The distributions of the end-to-end chain distances of the $C_{100}H_{202}$ chains calculated from the simulations are displayed in figure 7.20 for two different temperatures. Also plotted are radial Gaussian distribution functions [33]

$$w(r) = 4\pi r^2 \left(\frac{3}{2\pi \langle \vec{r}_{ee}^{\,2} \rangle} \right)^{3/2} \exp\left(-\frac{3r^2}{2\langle \vec{r}_{ee}^{\,2} \rangle} \right), \tag{7.2}$$

calculated using the mean-square end-to-end distance $\langle \vec{r}_{ee}^{\,2} \rangle$ taken from the simulations. The comparison shows that the results can be roughly described with a Gaussian distribution. The chains are in a more elongated conformation than modeled, as the distribution shifts to larger r. Other force fields can yield better Gaussian chain statistics [33], which must not reflect the true end-to-end chain distance distribution of a $C_{100}H_{202}$ melt. It is hence doubtful that these force fields can reproduce the simulated dynamics with the same quality as demonstrated in this thesis.

Since the simulated chains exhibit roughly a Gaussian chain statistics, the dynamics of the $C_{100}H_{202}$ chains were analyzed in terms of the Rouse model in more detail.

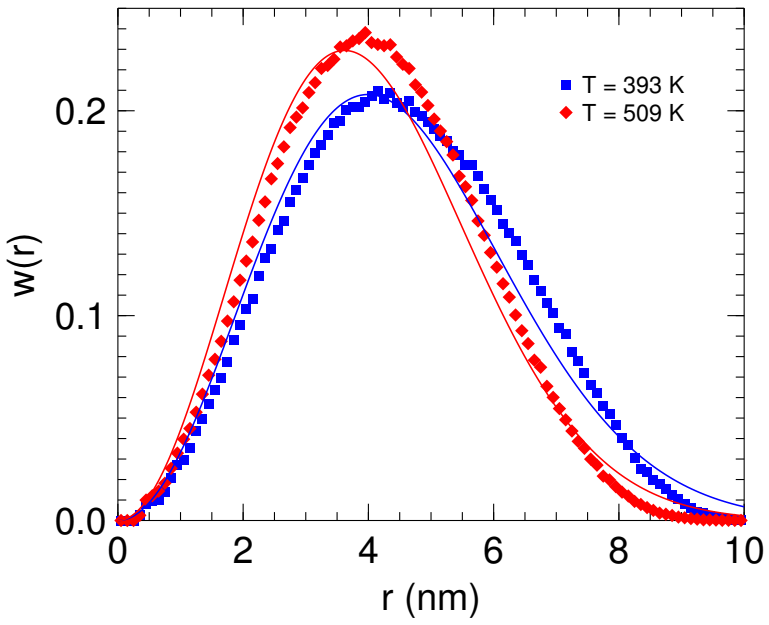

Figure 7.20: End-to-end chain distance distribution of the simulated $C_{100}H_{202}$ molecules (symbols), together with a Gaussian distribution function (solid lines).

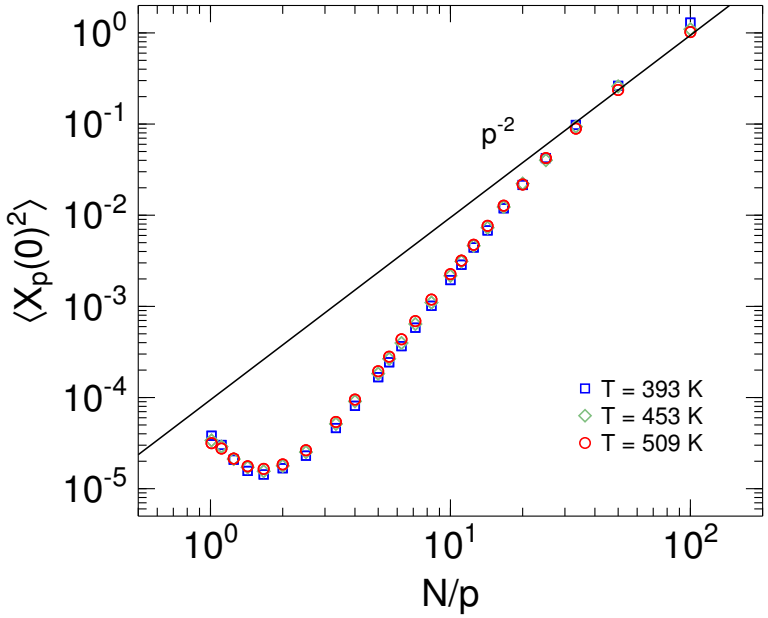

Figure 7.21: Amplitudes of the normal amplitudes in terms of the Rouse model for several mode numbers p and all simulated temperatures. The Rouse model predicts no temperature dependence and a p^{-2}-scaling of the amplitudes, which is fulfilled only for low p.

As pointed out in section 2.2, the chain dynamics are described by normal coordinates $\vec{X}_p(t)$ of the Rouse modes p. Small mode numbers correspond to more spatially extended motions of the chain. The mode amplitudes should scale as p^{-2} (cf. eq. 2.22). As it can be seen in figure 7.21 this scaling is fulfilled for the low mode numbers $p \leq 3$ only. For higher mode numbers, describing dynamics on small spatial extensions, the mode amplitudes are lower than predicted. As the amplitudes are mainly governed the restoring forces of the artificial springs connecting neighboring beads (cf. eq. 2.22), the deviation of the p^{-2} scaling indicates that the actual restoring forces are stronger than those considered in the Rouse model.

Figure 7.22 shows the Rouse correlators $\Phi_{pp}(t)$ (eq. 2.23), which are the time correlation functions of the normal coordinates. For all modes > 0 these functions should exhibit a single exponential decay. In order to test this behavior, the Rouse correlators were fitted using stretched exponential functions. As can be seen in figure 7.22, the relaxation of the Rouse correlators for all simulated temperatures can be well described in this way.

However, the decay of the Rouse correlators are not perfectly single exponential, which would result in a stretching parameter $\beta = 1$. In figure 7.23 the extracted stretching parameters are displayed. For all values of N/p the parameter β is found to be smaller than 1. Only for the first two modes the value of β is close to unity.

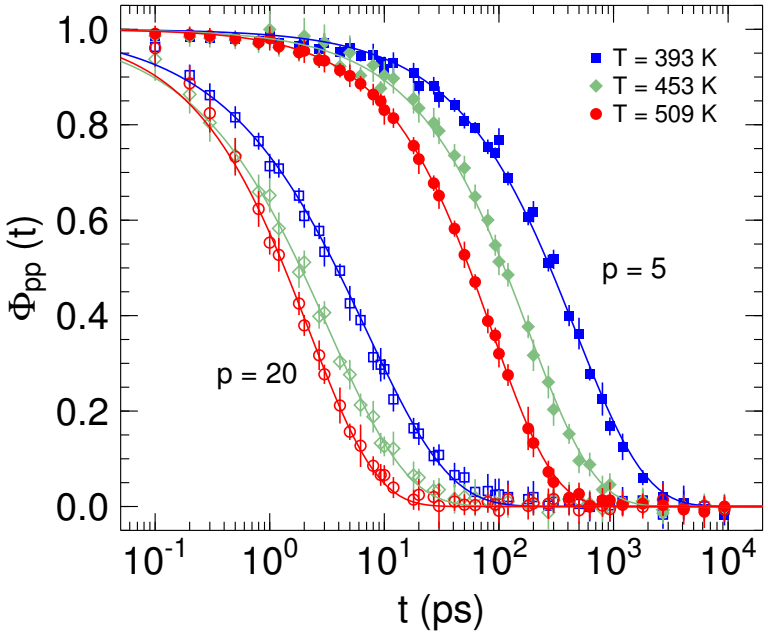

Figure 7.22: $C_{100}H_{202}$ - Rouse correlators for all simulated temperatures and two mode numbers (full symbols: $p = 5$, open symbols: $p = 20$). The decay of the correlators is fitted by stretched exponential functions (solid lines).

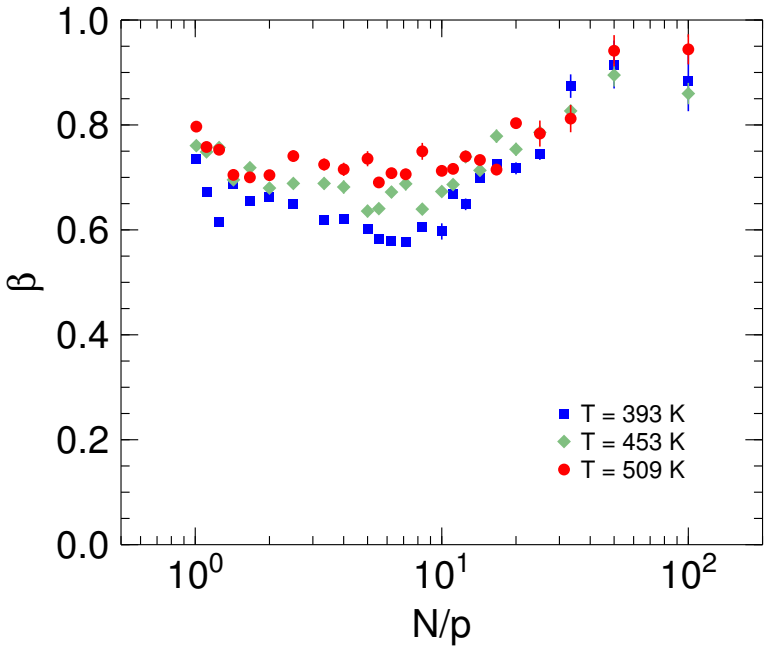

Figure 7.23: $C_{100}H_{202}$ - Stretching parameters as extracted from a stretched exponential fit to the Rouse correlators.

There is only a slight temperature dependence of β: The stretching increases with decreasing temperature. In conclusion it is to state that the Rouse model starts to fail to describe the dynamics characterized by higher mode numbers and lower

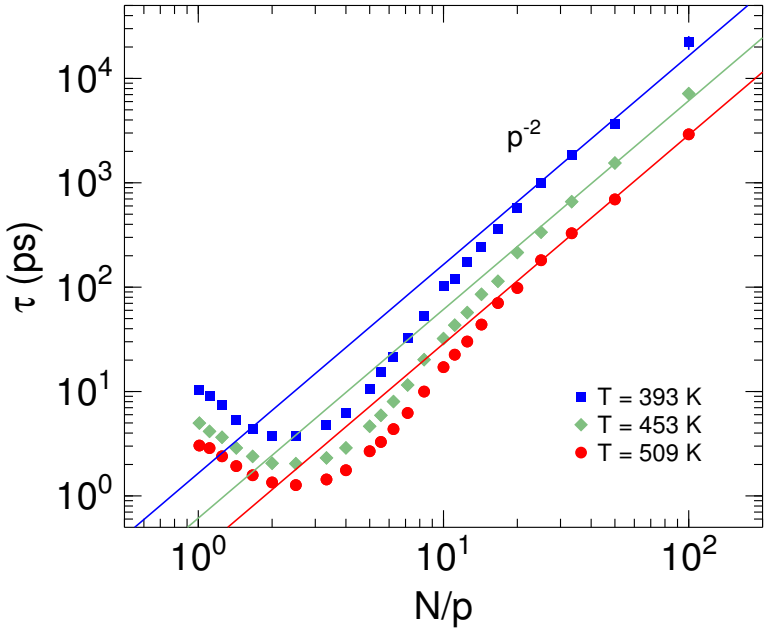

Figure 7.24: Relaxation times of a stretched exponential fit to the Rouse correlators (symbols). The p^{-2}-scaling as predicted by the Rouse model holds only for low mode numbers p.

temperatures. Local chemical interactions contribute to the decay of the Rouse correlators, resulting in a non-exponential decay [189].

The mean relaxation times $\langle \tau_p \rangle$ as obtained from the stretched exponential fits are plotted in figure 7.24. The relaxation time of the first mode corresponds to the Rouse time τ_R. For the three simulated temperatures the Rouse times are: 22.1 ns (393 K), 7.15 ns (453 K) and 2.91 ns (509 K). The Rouse model predicts a scaling $\langle \tau_p \rangle \sim p^{-2}$ (eq. 2.19), which applies for the lower modes $p \lesssim 6$. Hence the Rouse model starts to fail on length scales corresponding to the size of 16 monomers and less. Obviously on these length scales local chemical interactions start to suppress the Rouse correlators [40].

The mean relaxation times $\langle \tau_p \rangle$ of the Rouse correlators depend on both the restoring forces of the artificial springs (as the amplitudes of the Rouse correlators) and a friction coefficient, which represents the background friction, or white noise, to include intermolecular effects (cf. eq. 2.19). The analysis of the mean-square displacement revealed a dominant subdiffusive regime on the pico- to nanosecond time scale (cf. sec. 7.2). This subdiffusive behavior of the whole molecules is not modeled by the Rouse model, which predicts a simple Fickean diffusion for all times, could be well described by accounting for viscoelastic and hydrodynamic interactions. As the Rouse model misses the effect of collective flows induced by hydrodynamic in-

teractions, the assumption of white noise fails and alongside the mean relaxation times of the Rouse correlators start to deviate from the Rouse predictions. As will be described later, these intermolecular collective motions have a strong effect on the chain dynamics.

7.3 Local and Global Chain Reorientations

The results of the preceding section showed that the $C_{100}H_{202}$ dynamics cannot be described in terms of the Rouse model, as it was only able to predict dynamics on a length scale of the whole molecules satisfactorily. However, accounting for viscoelastic and hydrodynamic interactions allowed for describing the anomalous diffusion of the whole molecules. In the following local and global chain relaxations will be treated separately for both $C_{16}H_{34}$ and $C_{100}H_{202}$.

Local Chain Dynamics: Torsional Rotation

The torsional dynamics were studied by calculating the C-C-C-C torsional angle autocorrelation function [190] as

$$P^{\mathrm{dih}}(t) = \frac{\langle \cos\phi(t)\cos\phi(0)\rangle - \langle\cos\phi(0)\rangle^2}{\langle\cos^2\phi(0)\rangle - \langle\cos\phi(0)\rangle^2}, \tag{7.3}$$

with the torsional angle ϕ, which is 180° in *trans*-conformation and 0° in *cis*-conformation of the molecular backbone (cf. fig. 7.25). The resulting data show an exponential decay, as exemplarily illustrated in figure 7.26. It is known that the autocorrelation function of the torsional motion for bonds closer to the chain ends decays more rapidly [191]. This is also observed for the present data: $P^{\mathrm{dih}}(t)$ for dihedrals at the chain end decays slightly faster than for dihedrals at the chain center as can be seen from the inset of figure 7.26.

The curves were fitted by KWW functions (eq. 6.1) with the prefactor A set to 1. Mean relaxation times $\langle\tau^{\mathrm{dih}}\rangle$ were obtained using equation 6.2. As can be seen

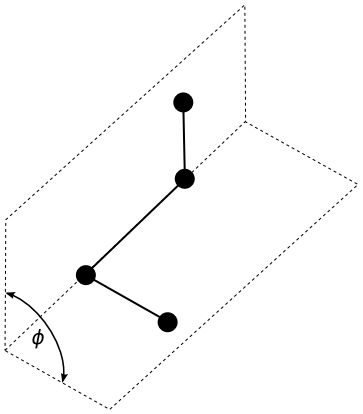

Figure 7.25: Definition of the torsional angle ϕ.

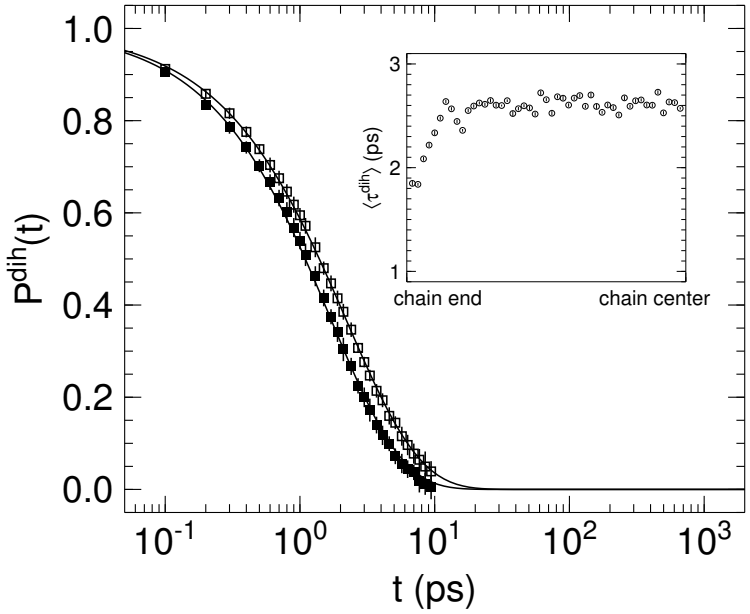

Figure 7.26: $C_{100}H_{202}$ - Backbone torsional angle autocorrelation function calculated at $T = 509\,\mathrm{K}$. The data is plotted for two positions of the dihedral: At the end (full squares) and at the central position (open squares) along the molecular backbone. The full lines are fits of stretched exponential functions, the corresponding mean relaxation times for all different positions of the dihedral are presented in the inset.

from the inset in figure 7.26 the torsional motion of the dihedrals close to the chain ends is enhanced. The unequal dihedral dynamics along the molecular backbone causes a broadening of the total distribution of the torsional relaxation times. This distribution narrows with increasing chain length, as the relative contribution of the chain ends is reduced. The averaged values of $\langle\tau^{\mathrm{dih}}\rangle$ are listed in table 7.4.

The variance of the dihedral relaxation times confirms the assumed chain length dependence: The relative variance is much larger for the shorter $C_{16}H_{34}$ molecules than for the long $C_{100}H_{202}$ chains. In long chains most dihedrals are far from the chain ends, hence the resulting mean relaxation times fluctuate less.

The temperature dependence of $\langle\tau^{\mathrm{dih}}\rangle_{\mathrm{avg}}$ can be described by an Arrhenius behavior (not shown). From an Arrhenius fit (eq. 6.3) activation energies were extracted for the torsional dynamics of both the $C_{16}H_{34}$and $C_{100}H_{202}$molecules. The corresponding energies are 11.5 ± 0.5 and $14.1 \pm 0.3\,\mathrm{kJ/mol}$, respectively. A non-Arrhenius Vogel-Fulcher behavior of the temperature dependence of the relaxation times, as reported for bulk polyethylene [192], is not observed. Other simulation studies studied the temperature dependence of the conformational transition rates of tridecane ($C_{13}H_{27}$) and tetratetracontane ($C_{44}H_{90}$) [21, 22]. The resulting acti-

Table 7.4: Mean relaxation times $\langle \tau^{\mathrm{dih}} \rangle_{\mathrm{avg}}$ of torsional dynamics averaged over all dihedrals along the molecular backbone for $C_{16}H_{34}$ and $C_{100}H_{202}$ for all simulated temperatures. The temperature dependence follows an Arrhenius behavior, with activation energies as listed.

$C_{16}H_{34}$	$\langle \tau^{\mathrm{dih}} \rangle_{\mathrm{avg}}$ (ps)
293 K	13.5 ± 1.1
323 K	10.2 ± 0.6
363 K	5.89 ± 0.29
403 K	4.15 ± 0.21
443 K	2.93 ± 0.14
E_{a} (kJ/mol)	11.5 ± 0.5

$C_{100}H_{202}$	$\langle \tau^{\mathrm{dih}} \rangle_{\mathrm{avg}}$ (ps)
393 K	6.84 ± 0.12
453 K	3.78 ± 0.04
509 K	2.53 ± 0.02
E_{a} (kJ/mol)	14.1 ± 0.3

vation energies of 13.0 kJ/mol and 13.4 kJ/mol, respectively, are fairly comparable with the results found in this study.

Global Chain Dynamics: Molecular Rotation

The orientation of a linear, unentangled molecule is reflected by its end-to-end vector. Consequently, a reorientation of the end-to-end vector reflects the rotation of the entire molecules. The orientation autocorrelation function (OACF) of the end-to-end vector was calculated corresponding to the first and second Legendre polynomials as

$$P_1^{\mathrm{ee}}(t) = \langle \vec{e}_{\mathrm{ee}}(t)\, \vec{e}_{\mathrm{ee}}(0) \rangle \tag{7.4}$$

$$P_2^{\mathrm{ee}}(t) = \frac{1}{2} \left[3 \langle \left(\vec{e}_{\mathrm{ee}}(t)\, \vec{e}_{\mathrm{ee}}(0) \right)^2 \rangle - 1 \right], \tag{7.5}$$

with the unit vector $\vec{e}_{\mathrm{ee}}$ lying in the direction of the chain end-to-end vector (eq. 2.2). The two functions are related to the spectral bandshapes measured with infrared absorption and Raman or depolarized light scattering experiments, respectively [89]. As can be seen in figure 7.27, the end-to-end vector OACFs are approximately exponential in form. The correlation functions were fitted with a KWW function (eq. 6.1), again with the prefactor A set to 1. Fitting the end-to-end vector OACF of the $C_{100}H_{202}$ molecules at lower temperatures provided less accurate values, since the correlation functions decayed only to 40 % of its initial values within the simulated time frame (cf. fig. 7.27).

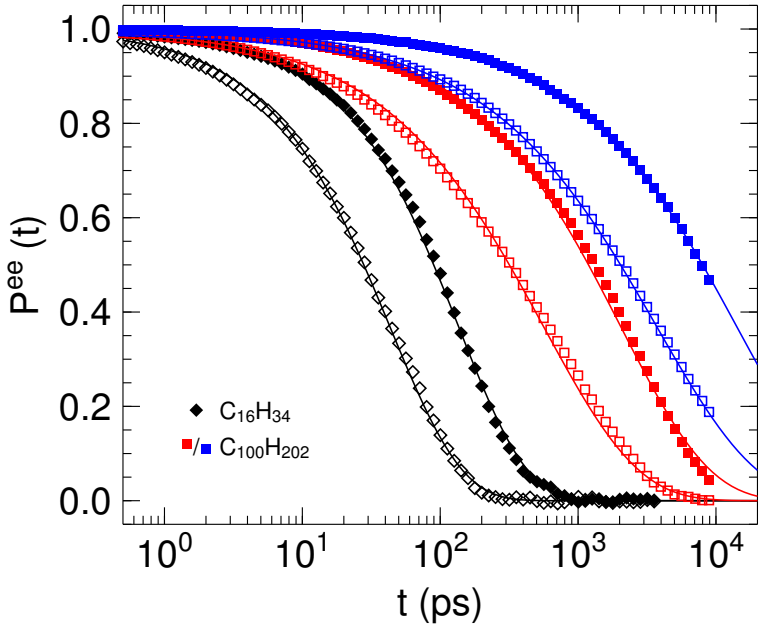

Figure 7.27: First (full symbols) and second (empty symbols) Legendre polynomials of the end-to-end vector orientation for $C_{16}H_{34}$ at $T = 363\,\mathrm{K}$ (black symbols) and $C_{100}H_{202}$ at $T = 393\,\mathrm{K}$ (blue symbols) and $509\,\mathrm{K}$ (red symbols). The data are modeled with stretched exponential functions (solid lines).

Assuming that the P^{ee} decay exponentially, i. e. $\beta = 1$, the rotation can be approximated with a rotational diffusion rate W_{rot} via [89]

$$P_l^{ee}(t) = \exp\left[-l(l+1)W_{rot}t\right]. \tag{7.6}$$

Corresponding to diffusive behavior of the motion, the characteristic relaxation times $\tau_l = [l(l+1)]^{-1}$ should then be related by [193]

$$\frac{\tau_l}{\tau_{l+1}} = \frac{(l+1)(l+2)}{l(l+1)} = \frac{l+2}{l}. \tag{7.7}$$

As can be seen in table 7.5, the single exponential behavior is fairly well fulfilled for the $C_{16}H_{34}$ molecules. The mean correlation times decrease with increasing temperature and the ratio $\langle\tau_1^{ee}\rangle/\langle\tau_2^{ee}\rangle$ is close to 3, indicating a diffusive motion in accordance with equation 7.7.

For the $C_{100}H_{202}$ molecules this behavior is not as clear. This can be explained by the fact that the $C_{100}H_{202}$ chains are not in a elongated conformation as the $C_{16}H_{34}$ molecules. Hence, the decorrelation of the end-to-end vector is not as sharp, resulting in a stretched form of $P^{ee}(t)$. Furthermore the total simulation time is too short to obtain good statistics for the low temperature data.

Table 7.5: Parameters obtained from a KWW fit to the end-to-end vector orientation autocorrelation functions (eq. 7.4 and 7.5). Activation energies were obtained from an Arrhenius fit to the mean relaxation times.

Molecule	T	$\langle\tau_1^{ee}\rangle$ (ps)	β_1^{ee}	$\langle\tau_2^{ee}\rangle$ (ps)	β_2^{ee}	$\langle\tau_1^{ee}\rangle/\langle\tau_2^{ee}\rangle$
$C_{16}H_{34}$	293 K	598.7	0.921	221.8	0.780	2.70
	323 K	330.4	0.851	105.9	0.802	3.12
	363 K	145.7	0.876	47.71	0.834	3.05
	403 K	86.16	0.901	27.70	0.873	3.11
	443 K	49.89	0.932	16.56	0.912	3.01
	E_a (kJ/mol)	17.9 ± 0.6		18.7 ± 0.3		
$C_{100}H_{202}$	393 K	19893	0.637	5611.63	0.601	3.54
	453 K	5985	0.649	1660	0.617	3.61
	509 K	2689	0.675	792.8	0.635	3.39
	E_a (kJ/mol)	28.8 ± 0.6		28.5 ± 1.1		

Activation energies were obtained from the temperature dependence of the correlation times with an Arrhenius fit (eq. 6.3). The respective values are listed in table 7.5. The MD simulations of $C_{16}H_{34}$ with explicit 1–4 pair interactions resulted in slower molecular rotation. The respective mean relaxation times were about 20 % longer than the values listed in table 7.5. This is plausible, since neglecting non-bonded 1–4 interactions results in a slightly increased flexibility of the chains, leading to an enhancement of the rotational motion of the whole molecules. However, the time scales are still alike and clearly separated from other relaxation processes. The activation energies obtained from the simulation of $C_{16}H_{34}$ with 1–4 pair interactions are only slightly larger: $E_{a,\,l=1} = 19.2 \pm 0.1\,\mathrm{kJ/mol}$ and $E_{a,\,l=2} = 19.6 \pm 0.3\,\mathrm{kJ/mol}$, compared to the activation energies as listed in table 7.5.

A random walk on a circle results in a linear increase of the MSD at short times [194], just as expected for a diffusive long-range motion. During this initial short time the respective intermediate scattering function can be described by a single exponential decay and a Q^2 dependence characteristic for a diffusive motion (cf. eq. 4.20). Only for longer times deviations from these characteristics indicate a localized motion. It is to be assumed that a global molecular reorientation significantly contributes to the signal observed with QENS on the respective time scales. At the onset of this rotational motion the observed Q^2-dependence of the intermediate scattering function, which is detected for a large number of n-alkanes [18, 19], is due to this localized diffusive motion.

Reorientation of Backbone Bonds

With the unit vector $\vec{e}_i$ pointing into the direction of a single carbon–carbon backbone bond, the reorientation of this bond is analyzed by calculating the respective vector OACF as

$$P_i^{\mathrm{C-C}}(t) = \langle \vec{e}_i(t)\, \vec{e}_i(0) \rangle \,. \tag{7.8}$$

The index i gives the different positions of the carbon–carbon bond along the molecular backbone, ranging from the end of the chain, i. e. $i = 1$, to the chain center. The analysis of this correlation function gives information on processes leading to a change of the local and global conformations of the chain, as will be presented in the following. Purely translational motions however give no contribution to the reorientation of the backbone bonds.

$C_{16}H_{34}$ The OACF of the backbone bonds for the short oligomer $C_{16}H_{34}$ is exemplarily shown in figure 7.28 for two temperatures. The correlation decays faster with increasing temperature and the chain dynamics are enhanced at the ends of the molecular backbone. The functions exhibit a clear two-step decay for all temperatures and positions of the backbone bond along the chain, and the time scales

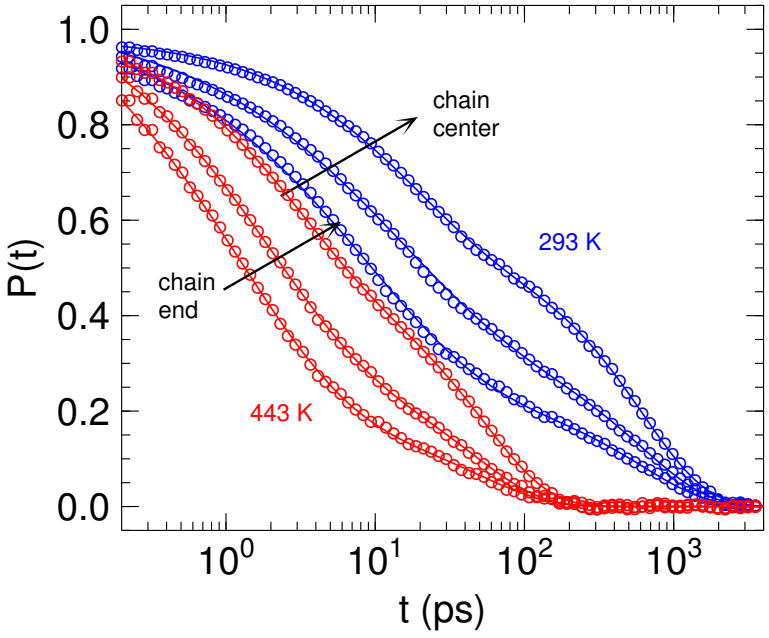

Figure 7.28: $C_{16}H_{34}$ - Orientation autocorrelation function calculated for the carbon–carbon bond vector orientation (symbols) at $T = 293$ and 443 K (cf. [168]). Displayed is the data for the end and second-to-end carbon pairs as well as for the carbon pair at the center of the molecular backbone, as indicated by the arrows. The data points are fitted by double exponential functions (solid lines).

of the two steps are separated by about one order of magnitude in time. The data were fitted by double exponential functions of the form

$$I^{\mathrm{KWW}} = A \exp\left[-\left(\frac{t}{\tau_{\mathrm{A}}}\right)^{\beta_{\mathrm{A}}}\right] + B \exp\left[-\left(\frac{t}{\tau_{\mathrm{B}}}\right)^{\beta_{\mathrm{B}}}\right], \tag{7.9}$$

with the prefactors A, B, the characteristic relaxation times $\tau_{\mathrm{A}}, \tau_{\mathrm{B}}$ and the stretching parameters $\beta_{\mathrm{A}}, \beta_{\mathrm{B}}$. The stretching parameter of the second, long-time decay was ≈ 1. In order to reduce the number of fit parameters β_{B} was set to unity. The sum of the prefactors yield 1.023 ± 0.003, underlining that the OACF decays entirely within the simulated time frame. The first decay dominates the overall loss of the correlation of the orientation of bonds which are closer to the ends of the molecules, which can be concluded from the relatively high values of the first prefactor A ($A/(A+B) \gtrsim 80\,\%$ (cf. table 7.6).

The mean characteristic relaxation times $\langle\tau\rangle$, also listed in table 7.6, are illustrated in figure 7.29. Comparing the relaxation times with the results obtained so far, the two decays can be attributed to dihedral and molecular rotation: The first, fast decay of the autocorrelation function on the short picosecond time scale occurs more rapidly closer to the ends of the chains, as the respective relaxation times $\langle\tau_{\mathrm{A}}\rangle$ are about 20 - 30 % shorter. The average relaxation times are in good agreement

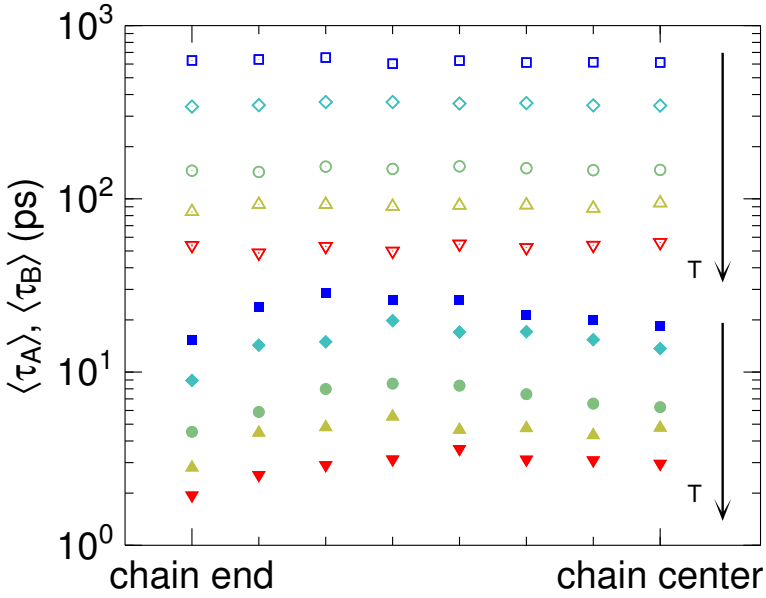

Figure 7.29: $C_{16}H_{34}$ - Mean relaxation times extracted from a double exponential fit to the orientation autocorrelation function of backbone bonds. Full symbols: $\langle\tau_{\mathrm{A}}\rangle$, empty symbols: $\langle\tau_{\mathrm{B}}\rangle$, according to equation 7.9. The arrows point into the direction of rising temperature (T = 293, 323, 363, 403, 443 K).

with the values listed in table 7.4. Accordingly, this first relaxation of the backbone bond orientation can be attributed to dihedral dynamics.

The characteristic relaxation times of the second decay $\langle\tau_B\rangle$ are approximately independent of the position of the carbon–carbon bond along the molecular backbone, the variations are on the order of only a few percent. Such a behavior is expected for a rotational motion of the whole, stiff molecule. In line with this, the corresponding relaxation times of this second decay $\langle\tau_B\rangle$ coincide with the values determined for global molecular reorientation (as listed in table 7.5).

Activation energies were obtained from the temperature dependence of the mean relaxation times according to Arrhenius equation 6.3. As can be seen from figure 7.30, the activation energy corresponding to the second, slow decay of the correlation function is almost constant with respect to the position of the carbon–carbon bond. The average value of $17.6 \pm 0.7\,\mathrm{kJ/mol}$ is again in good agreement with the value determined for molecular rotation. The activation energy for the first, fast decay averages to $14.7 \pm 0.9\,\mathrm{kJ/mol}$, which is a little higher than the respective value obtained for torsional motions of $11.5 \pm 0.5\,\mathrm{kJ/mol}$. It is to be assumed that this discrepancy results from the use of different methods to characterize torsional dynamics.

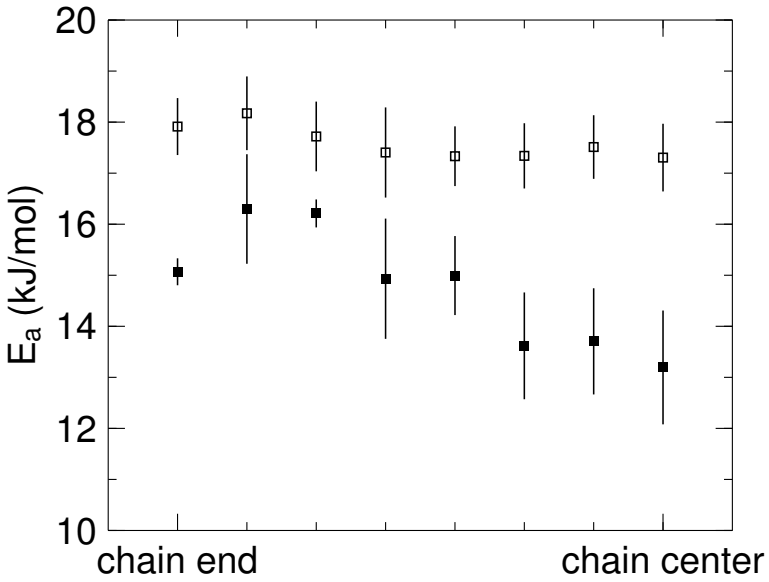

Figure 7.30: $C_{16}H_{34}$ - Activation energies from an Arrhenius fit to $\langle\tau_A\rangle$ (full symbols, representing the faster relaxation) and $\langle\tau_B\rangle$ (empty symbols, representing the slower relaxation), according to equation 7.9.

Table 7.6: $C_{16}H_{34}$ - Parameters extracted from a double exponential fit to the orientation autocorrelation function of carbon–carbon bonds, for different positions of the carbon pairs along the chain, where $i = 1$ and $i = 8$ corresponds to the position at the end and center of the chain, respectively. The parameter β_B is set to unity, as described in the text.

T	i	$\frac{A}{(A+B)}$	$\langle\tau_A\rangle$ (ps)	β_A	$\langle\tau_B\rangle$ (ps)
20 °C	1	0.782	15.3	0.532	629
	2	0.685	23.8	0.526	638
	3	0.645	28.7	0.560	653
	4	0.556	26.2	0.610	603
	5	0.530	26.2	0.631	628
	6	0.470	21.2	0.676	612
	7	0.458	20.1	0.720	615
	8	0.440	18.4	0.717	612
50 °C	1	0.811	8.94	0.527	341
	2	0.722	14.3	0.533	347
	3	0.670	14.9	0.585	362
	4	0.628	19.8	0.586	362
	5	0.567	17.0	0.611	355
	6	0.537	17.1	0.639	357
	7	0.511	15.4	0.636	346
	8	0.496	13.7	0.685	345
90 °C	1	0.824	4.52	0.561	145
	2	0.716	5.59	0.595	143
	3	0.695	7.98	0.591	153
	4	0.619	8.58	0.638	149
	5	0.580	8.35	0.645	154
	6	0.527	7.45	0.698	150
	7	0.497	6.57	0.712	146
	8	0.486	6.27	0.740	147
130 °C	1	0.839	2.81	0.562	84.3
	2	0.766	4.47	0.565	93.8
	3	0.706	4.80	0.629	92.8
	4	0.645	5.53	0.656	90.4
	5	0.577	4.64	0.711	91.7
	6	0.544	4.74	0.706	92.1
	7	0.508	4.32	0.722	88.2
	8	0.524	4.77	0.722	94.6
170 °C	1	0.856	1.94	0.569	53.9
	2	0.747	2.55	0.616	48.7
	3	0.696	2.91	0.682	53.2
	4	0.613	3.13	0.722	49.9
	5	0.606	3.60	0.694	54.8
	6	0.542	3.13	0.738	52.3
	7	0.527	3.10	0.746	54.0
	8	0.527	2.94	0.748	56.0

$C_{100}H_{202}$ The OACF of single backbone bond vectors was also calculated for the $C_{100}H_{202}$ chains. In contrast to the results obtained for the $C_{16}H_{34}$ chains, the resulting autocorrelation functions do not show a clear two-step decay. As illustrated in figure 7.31, at positions closer to the chain ends a two-step decay can still be distinguished, where the second decay occurs on time scales of some hundred picoseconds. However, at more central positions of the carbon–carbon bonds along the chain, rather three relaxations can be observed: A detailed analysis of the reorientation of the bond vector at the center of the chain reveals a third process causing a relaxation on the nanosecond time scale (cf. fig. 7.31), which is even visible to the unaided eye.

The separation of the second from the third relaxation is difficult to qualify by fitting three stretched exponential functions to the data, since the two processes seem to overlap and their amplitudes are relatively low. In order to characterize the data in a model-independent way, a CONTIN [195] analysis was performed. The CONTIN algorithm is widely used for the data evaluation in light scattering experiments, and is also applied to evaluate intermediate scattering functions obtained

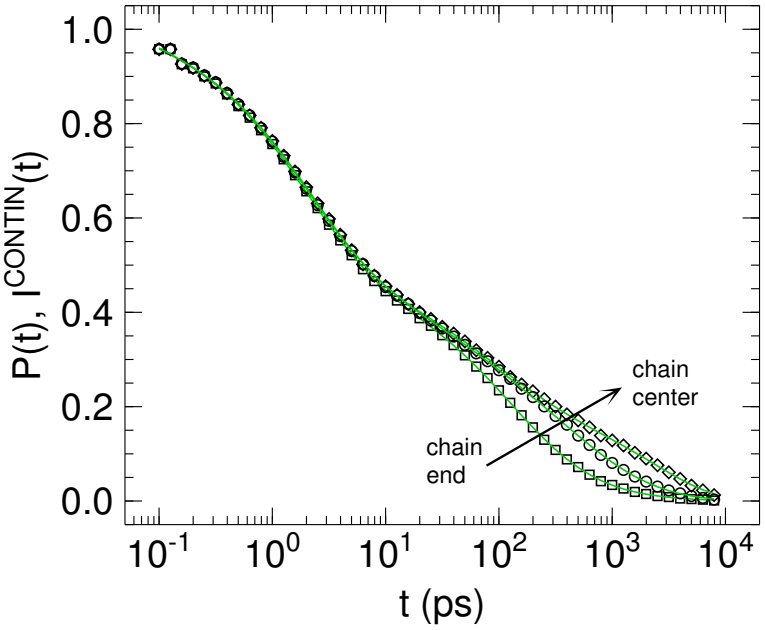

Figure 7.31: $C_{100}H_{202}$ - Orientation autocorrelation function of the carbon–carbon bond vector at $T = 509\,\mathrm{K}$ (symbols). The plotted data were calculated for three different positions of the bonds along the molecular backbone, as indicated by the arrow. Fitting a continuous distribution of exponentials (green solid lines) perfectly describes the shape of the data.

with quasielastic neutron scattering [20] †. It allows to fit a continuous linear combination of exponential functions to a correlation function, where the single exponentials are weighted by a normalized distribution of relaxation times (DRT) $F[\ln(\tau)]$, according to

$$I^{\text{CONTIN}}(t) = \int_{-\infty}^{\infty} \mathrm{d}\ln(\tau) F[\ln(\tau)] \exp\left(-\frac{t}{\tau}\right). \tag{7.10}$$

Using this approach the OACFs can be described nicely, as illustrated in figure 7.31. The resulting DRT provides information about the number of distinct relaxation processes, their amplitudes and the dispersion of the exponential decays that are needed to describe the the spectrum. DRTs for some positions along the molecular backbone are illustrated in figure 7.32, while the entire trend can be determined from the colorplot in figure 7.33.

The fastest relaxation process (at about 2 ps at $T = 509\,\mathrm{K}$), which is present at all bond positions, is again due to the torsional motion of the dihedrals. The average relaxation time $\left\langle \tau^{\text{dih}} \right\rangle_{\text{avg}}$, determined for the dihedral relaxation at $T = 509\,\mathrm{K}$, can

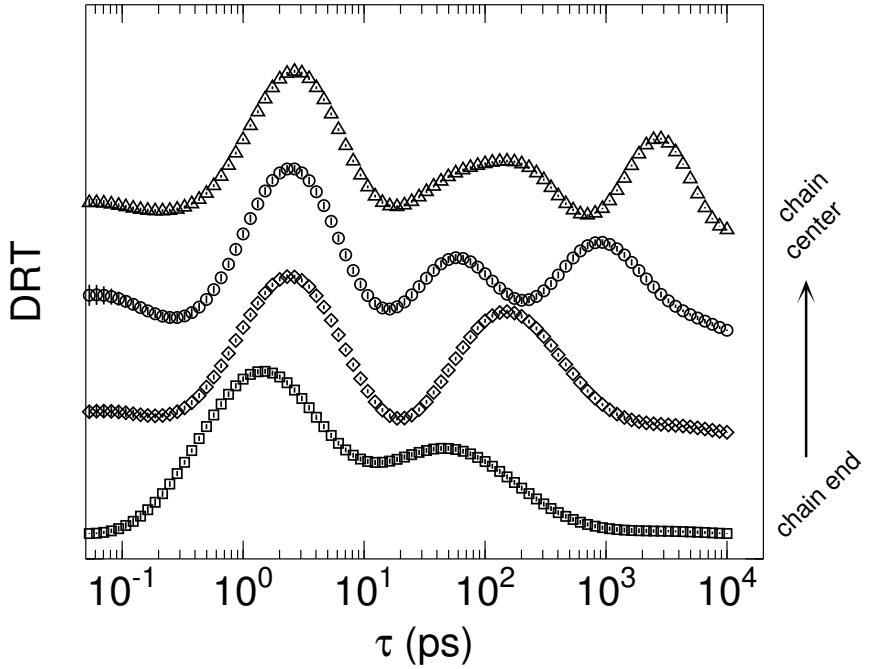

Figure 7.32: $C_{100}H_{202}$ - Distribution of relaxation times (DRT) of the backbone bond reorientation at $T = 509\,\mathrm{K}$, plotted for four positions of the carbon–carbon bonds along the molecule, as indicated by the arrow. The spectra are shifted along the y-axis for better visualization.

†Further developments of this method will also allow for a similar evaluation of the scattering functions $S(Q, \omega)$ [196].

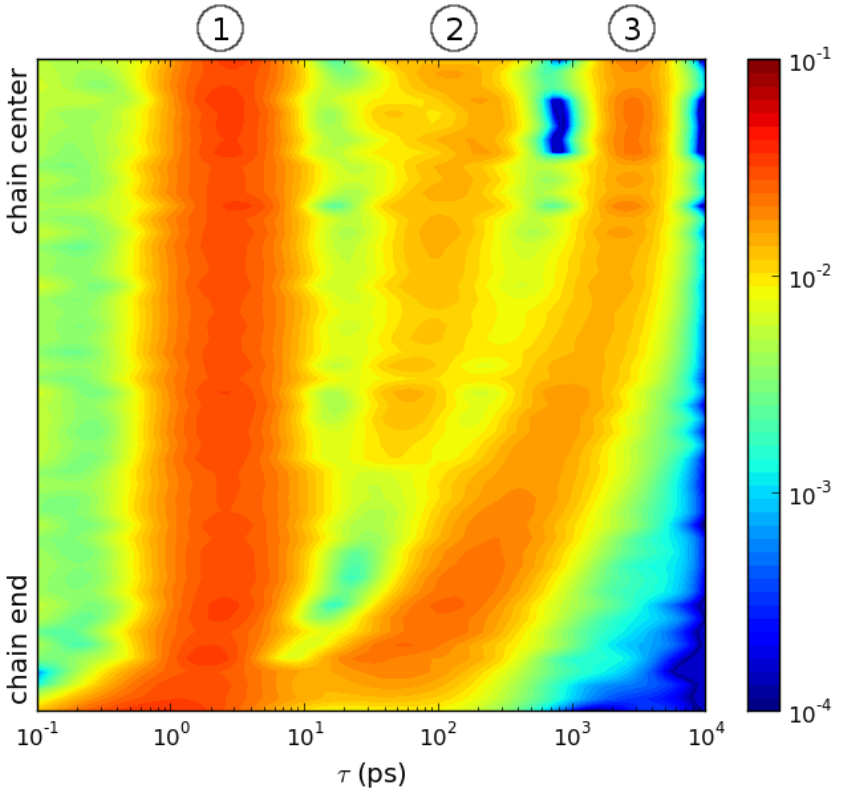

Figure 7.33: $C_{100}H_{202}$ - Distribution of relaxation times of backbone bond reorientations at $T = 509\,\mathrm{K}$, for different positions of the carbon–carbon bonds along the molecule (cf. [178]). The three distinct relaxation processes are labeled at the top.

be recovered from the first peak of the DRTs. Close to the chain ends the dihedral motion is enhanced, as the first relaxation peak shift to shorter times. This is in agreement with the results obtained from the analysis of the backbone torsional dynamics (cf. fig. 7.26).

A distinct relaxation process can be detected at intermediate times for bondings close to the central positions. This relaxation has the smallest amplitude of the three processes, and occurs on time scales of about 10 ps to 1 ns at $T = 509\,\mathrm{K}$. Close to the chain ends this relaxation seems to mix up with the third, long time relaxation process. In contrast to the 1^{st} and 3^{rd} relaxation process, this 2^{nd} relaxation could not be assigned to a local or global single-chain dynamics. Its origin is probably due to an intermolecular collective flow-like motion of the atoms which will be treated in detail in the following section. To anticipate the outcome (at 509 K): During a timespan of several picoseconds many atoms in large clusters of thousands of atoms move flow-like into the same direction. This behavior is most pronounced after a duration of 25 ps. During this time the dihedrals turn several times, but the overall

direction of the carbon-carbon pair is fixed by the motion of its surrounding. The decorrelation of these flow patterns, which extends to the nanosecond regime, allows for the atoms to move into different directions. This slight reorientation is reflected by the intermediate relaxation of the backbone bond vector and applies to the atoms at all positions along the molecular backbone. However, the resulting intermediate relaxation cannot be identified for the bonds close to the chain ends as it coincides with the 3$^{\text{rd}}$ relaxation process, which causes the bond orientation autocorrelation function to fully decorrelate.

The slowest, 3$^{\text{rd}}$ relaxation shows a strong dependence on the position of the respective carbon–carbon bond. The characteristic relaxation time shifts from tens of picoseconds at the chain end to approximately 3 ns at the chain center. At these central positions the relaxation time agrees with the value determined for a rotational motion of the whole $C_{100}H_{202}$ chains. Therefore the whole branch of the 3$^{\text{rd}}$ relaxation in figure 7.33 can be attributed to global reorientations. This process is non-uniformly, in contrary to the findings for $C_{16}H_{34}$ where the relaxation time was independent of the position along the molecule. Since the $C_{100}H_{202}$ molecules cannot be treated as stiff elongated molecules, it is obvious that large segments at the ends of the chains can reorientate by $\pi/2$ more or less independent from the rest of the chain due to the increased flexibility at the chain end. This causes a total decorrelation of the carbon–carbon bond orientation, already at times when the central bond orientation is not fully relaxe yet.

The distribution of relaxation times at the lower temperatures of $T = 393\,\text{K}$ and 453 K show a similar behavior. The corresponding colorplots are given in figure 7.34. However, the carbon–carbon bond OACF does not decay to zero during the simulation length, since the dynamics, which are temperature dependent, are slowed down. Only close to the chain ends the dynamics are fast enough and the correlation function decays close to zero during the probed time scale. As a consequence the CONTIN algorithm does not produce smooth results as for the $T = 509\,\text{K}$ case [197]. Longer simulations would be necessary to analyze the DRTs at lower temperatures in more detail. Nevertheless the data allow for a estimation of the time scale of the intermediate relaxation process. At $T = 393\,\text{K}$ a relatively strong relaxation can be identified with a maximum at roughly 600–700 ps, which shifts to 400–500 ps at $T = 453\,\text{K}$. Additional weak relaxations appear at about 100 ps in the 393 and 453 K colorplots. These relaxations might be artifacts from the CONTIN algorithm, resulting from the fact that the total function does not fully decay within the probed time window.

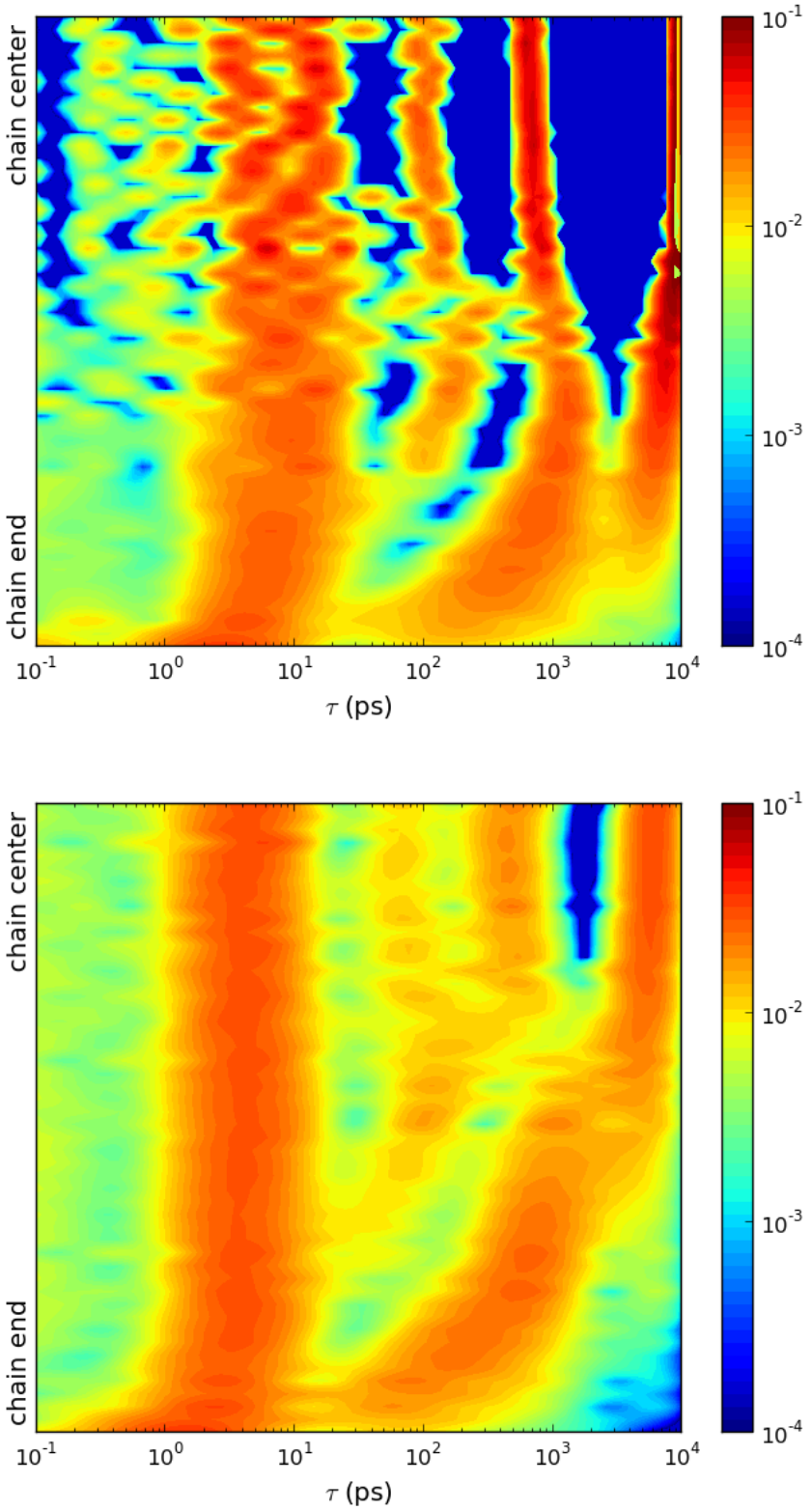

Figure 7.34: $C_{100}H_{202}$ - Distribution of relaxation times of backbone bond reorientations at $T = 393\,\mathrm{K}$ (top) and $453\,\mathrm{K}$ (bottom), for different positions of the carbon–carbon bonds along the molecule.

In order to verify the presence of the relaxation process detected at intermediate times for the reorientation of bond vectors along the $C_{100}H_{202}$ backbone, a coarse graining of the molecules was performed. In this process the coordinates of four neighboring backbone atoms were combined to obtain the coordinates of small segments. Thereby the $C_{100}H_{202}$ molecule is transformed to a coarse grained molecule, consisting of 25 segments.

Following the orientation autocorrelation function (OACF) of the vectors connecting neighboring segments were calculated, according to equation 7.8. By applying the CONTIN algorithm, distribution of relaxation times (DRTs) were obtained for each spectrum. The resulting DRTs obtained from the OACF for different positions of the segments along the molecular chain are illustrated in figures 7.35 and 7.36 for all simulated temperatures T.

In contrast to the images obtained without this coarse graining (cf. fig. 7.33, 7.34), only two relaxation processes can be determined. The fast process, reflecting

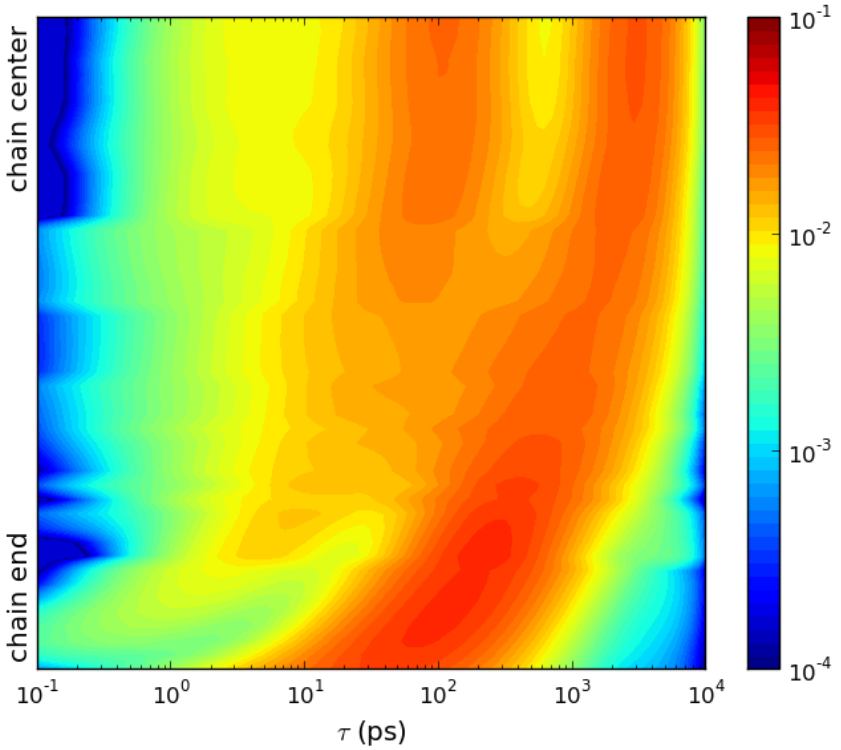

Figure 7.35: $C_{100}H_{202}$ - Distribution of relaxation times of the reorientation of vectors connecting neighboring segments at different positions along the molecule at $T = 509\,\mathrm{K}$. Each segment consists of four backbone atoms, in that way dihedral dynamics (corresponding to the 1^{st} relaxation process in figure 7.33) are masked out.

dihedral dynamics, has vanished. In the coarse grained molecule these torsional motions take place inside of a segment, which was formed by four neighboring atoms, and do not affect the reorientation of the segments, and are hence masked out. The resulting OACFs are dominated by the remaining two relaxation processes, with the slower one being due to molecular rotation and the faster one coinciding with the intermediate relaxation observed for the atomic, i. e. carbon-carbon reorientation. This clarifies that this intermediate relaxation is not an artifact of the CONTIN algorithm, but causes a clear decay of the carbon–carbon orientation autocorrelation function.

For the lower temperatures of additional weak peaks can be observed in the color-plots besides the two dominant relaxations. It is to be assumed that these artificial features result from the fact that the total OACF does not fully decay within the accessed time window.

Such distinct dynamical relaxations on intermediate time scales were also found previously for polyisobutylene, *cis*-1,4-polybutadiene, polypropylene, polyethylene terephthalate and polyethylene [197–200]. However, in those studies intermediate relaxation processes appeared only when considering the reorientation of large segments. For the carbon–carbon OACF just two relaxations were found. This can be explained by the analysis used in those studies: The local relaxations were studied by averaging over the entire molecular backbone, i. e. the DRTs from different positions along the molecular backbone were merged. This procedure causes the intermediate and long time relaxation process in figure 7.33 to collapse to one broad peak only. Resolving the correlation function along the chain, as done in this thesis, reveals a more detailed picture on the local chain dynamics.

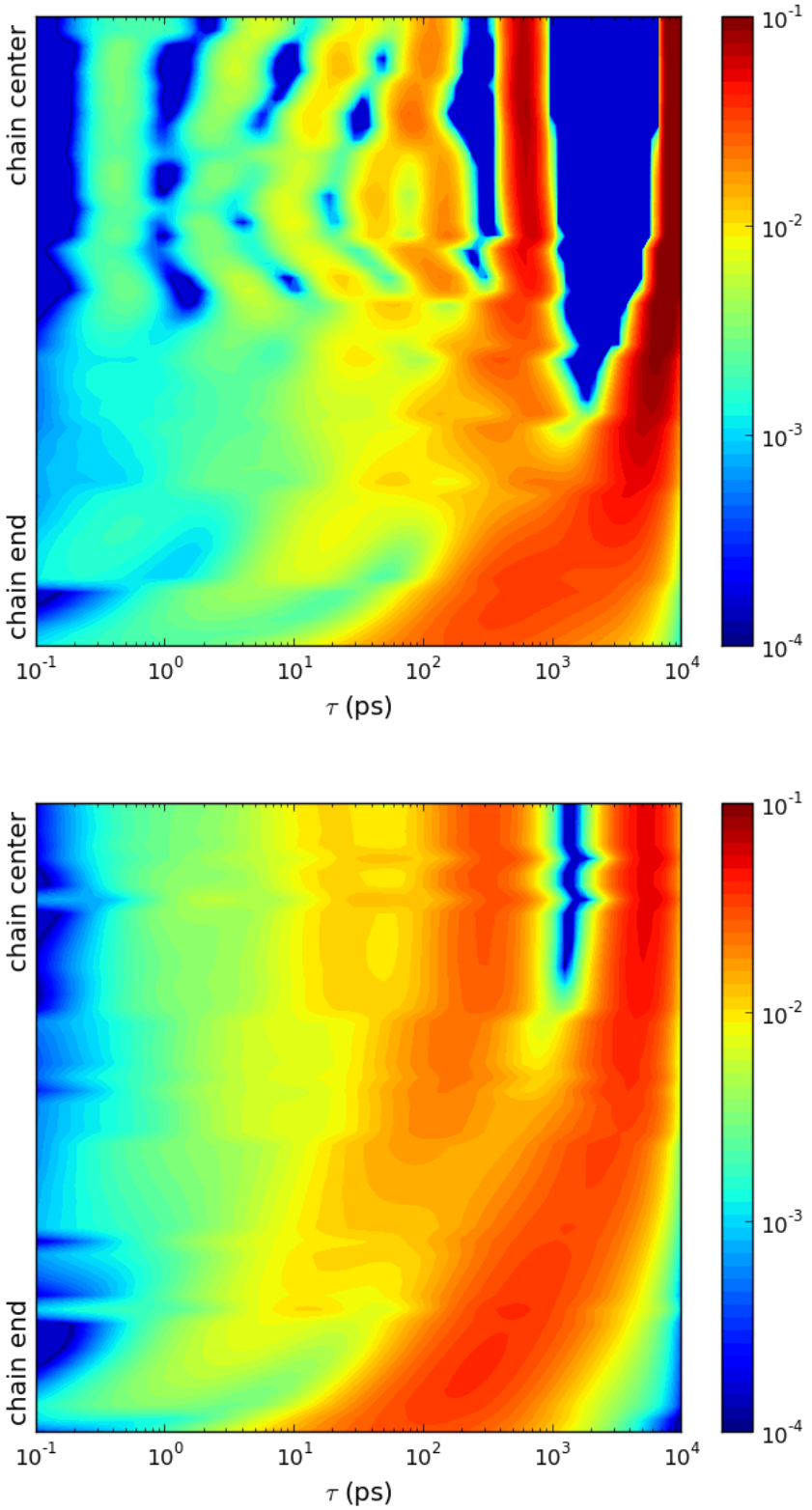

Figure 7.36: $C_{100}H_{202}$ - Distribution of relaxation times of the reorientation of vectors connecting neighboring segments at different positions along the molecule at $T = 393\,\mathrm{K}$ (top) and $453\,\mathrm{K}$ (bottom), respectively.

7.4 Collective Motion in the Melt

Detecting and quantifying collective behavior is quite challenging, due to the manifold correlations between many particles. In two-dimensional systems, as e. g. 2D-Lennard-Jones liquids, collective motions can be easily visualized by generating a spatial map of single particle displacements [201]. In such systems particles in extended regions move with similar (relatively high) velocities in similar directions. Meanwhile other regions are nearly static. Such a transient spatial fluctuation of the dynamics is termed dynamic heterogeneity.

In order to describe such dynamic heterogeneities or similar collective motions correlations functions designed to specifically highlight intermolecular correlations are needed. In an approach by Berthier, heterogeneous dynamics in time and space are characterized by correlating the mobilities of the particles [202]. In this approach the mobilities are defined as $\exp(-\langle r^2(t)\rangle)$, with the mean-square displacement $\langle r^2(t)\rangle$. In the $C_{100}H_{202}$ system under study the correlated motions are expected on time scales up to hundreds of picoseconds as suggested in section 7.3. Within e. g. 100 ps[‡] the atoms move quite far (cf. fig. 7.18) and thus the mobility defined is not a meaningful measure of the collective behavior.

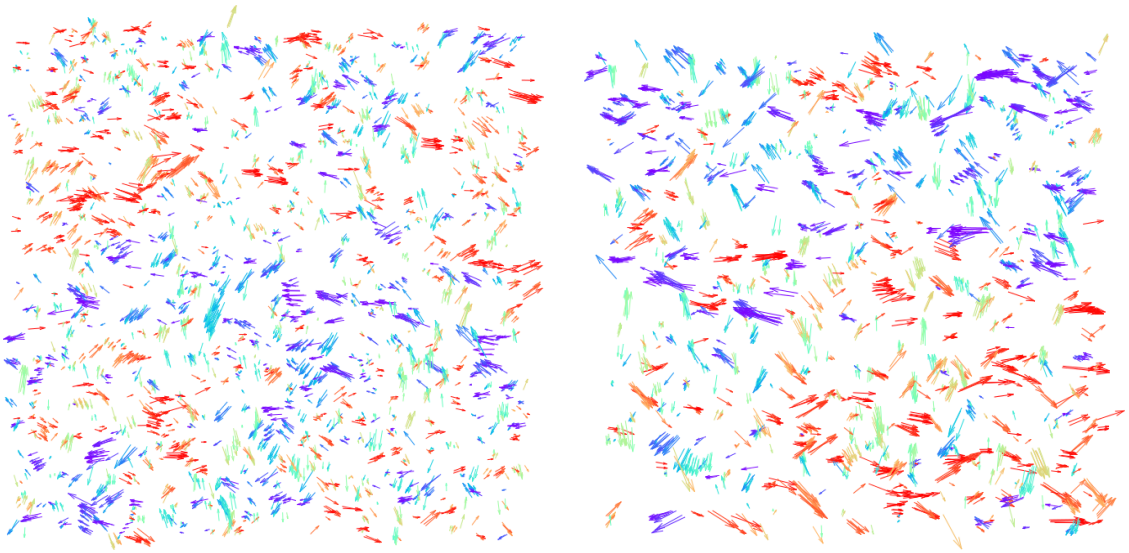

Figure 7.37: $C_{100}H_{202}$ - Displacement vectors in a 0.25 nm thick 2D cut at $T = 509\,\mathrm{K}$ (cf. [178]). The timespan extends over 20 ps (left image) and 100 ps (right image), respectively. The vectors are colored according to their orientation for better visualization. The dimensions are about $23.5^2\,\mathrm{nm}^2$.

[‡]Expected order of duration of the correlated dynamics at $T = 509\,\mathrm{K}$.

To detect collective motions displacement vectors were plotted in two-dimensional cuts. In figure 7.37 such 0.25 nm thick 2D cuts are presented, with atomic displacements during 20 ps (left image) and 100 ps (right image) at $T = 509\,\mathrm{K}$, respectively. The colors represent the direction of the displacement and reveal that many atoms in large clusters move into the same direction on both time scales. Separated regions with fast and slow dynamics could not be observed. Dynamic heterogeneities, as can be observed in 2D systems, are not present on the evaluated time scale in the 3D $C_{100}H_{202}$ melt.

The collectivity was quantified by the following method, which is also illustrated in figure 7.38: By picking one carbon atom j and its nearest intermolecular neighboring carbon atom j' at time t, the collective motions in the three-dimensional molecular melt were characterized by determining the extent to which atoms j and j' move into similar directions during $t + \tau$. The displacement vectors are defined as $\vec{u}_{i,t}(\tau) = \vec{r}_i(t+\tau) - \vec{r}_i(t)$, with the position vectors $\vec{r}$. The magnitude of the correlated dynamics was qualified by calculating the scalar product of the unit displacement vectors of nearest intermolecular neighbors as

$$s(\tau) = \left\langle \frac{\vec{u}_{j,t}(\tau)\vec{u}_{j',t}(\tau)}{|\vec{u}_{j,t}(\tau)|\,|\vec{u}_{j',t}(\tau)|} \right\rangle_{j,t} . \tag{7.11}$$

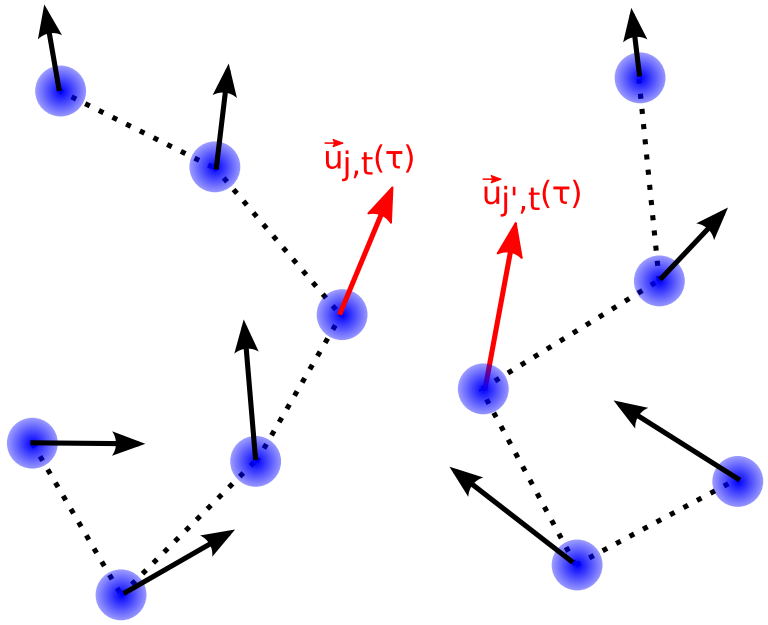

Figure 7.38: Illustration of equation 7.11: The relative orientation of the displacements of nearest intermolecular neighbors (red arrows) is used as a measure to characterize collective motions.

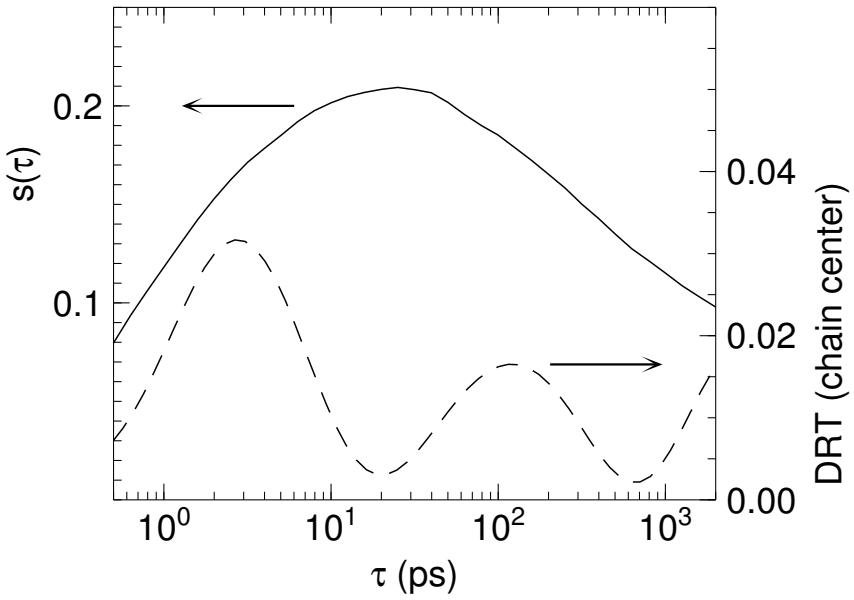

Figure 7.39: $C_{100}H_{202}$ - Scalar product according to equation 7.11 (solid line) and distribution of relaxation times (DRT, dashed line) for the relaxation of carbon–carbon bonds at central positions of the $C_{100}H_{202}$ molecules (cf. fig. 7.32) at $T = 509\,\mathrm{K}$ (cf. [178]).

If collective flow-like motions are present in the system, neighboring atoms move into the same direction, resulting in a positive scalar product of their displacement vectors. However, entirely random orientations of the displacements results in an average scalar product of $s(\tau) = 0$.

A resulting $s(\tau)$ spectrum for $C_{100}H_{202}$ at $T = 509\,\mathrm{K}$ is plotted in figure 7.39. At short τ the intermolecular dynamics are barely correlated, as can be seen from the small values of $s(\tau)$. In this regime the atomic motions are mostly driven by dihedral dynamics. With increasing time an increasing strength of the correlation between the atomic displacements can be observed, indicating that the intermolecular neighbors move preferably into the same direction. The same behavior was also found when extending equation 7.11 by allowing j' to be any atom within a sphere of radius $R < 2\,\mathrm{nm}$ around atom j, and averaging $s(\tau)$ for all these atoms. Hence this increasing correlation can be pictured as a flow-like motion of many neighboring atoms. Such flow patterns can also easily be captured and identified in 2D plots (cf. fig. 7.37).

At the time $\tau_{\max} \approx 25\,\mathrm{ps}$ the maximal correlation is reached. The displacement of the atoms is determined by the motion of their surroundings. With increasing time $\tau > \tau_{\max}$ the flow-like behavior starts to decorrelate. This results in a decreasing effect of the surrounding dynamics on the individual chain dynamics, which is reflected in a relaxation of the local bond vectors. As can be seen in figure 7.39, the

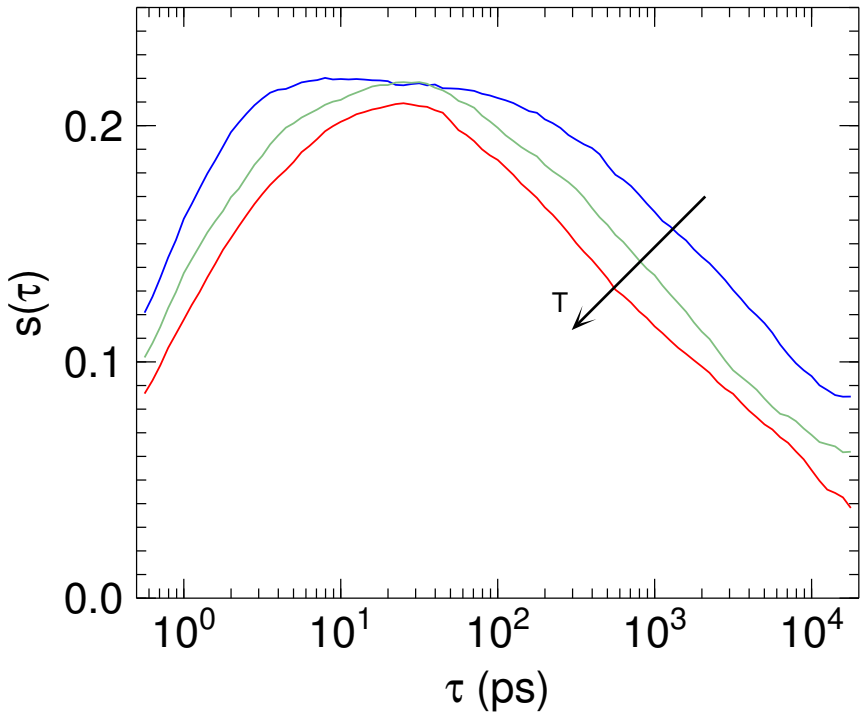

Figure 7.40: $C_{100}H_{202}$ - Scalar product of unit displacement vectors of intermolecular neighboring carbon atoms in the molecular melt for T =393, 453 and 509 K. The arrow points into the direction of rising temperature.

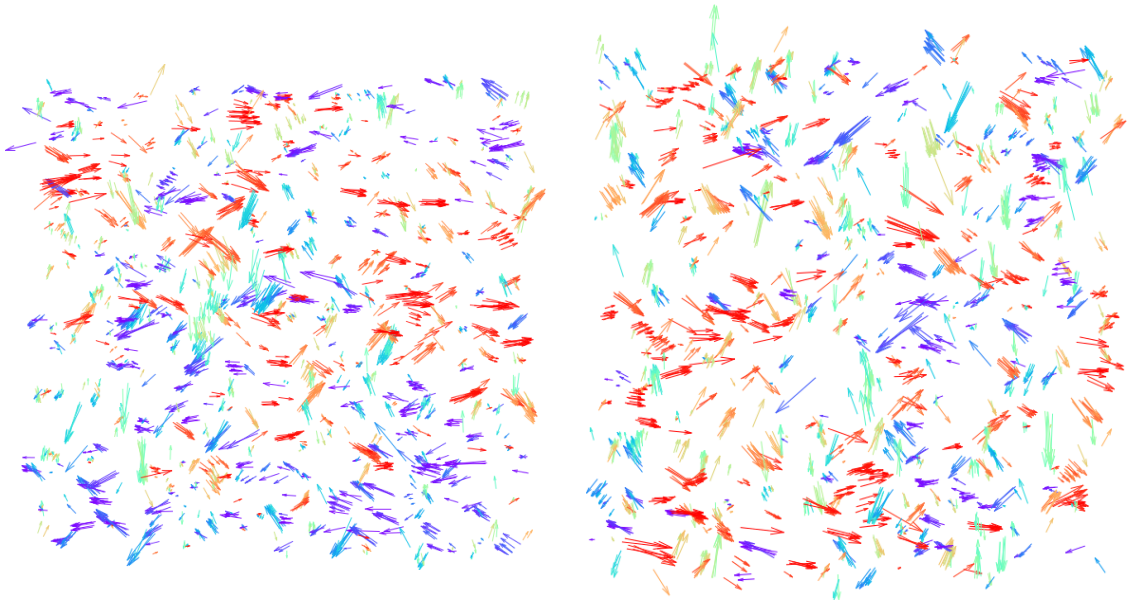

Figure 7.41: $C_{100}H_{202}$ - Displacement vectors in a 0.25 nm thick 2D cut at $T = 393$ K. The timespan extends over 500 ps (left image) and 1000 ps (right image), respectively. The vectors are colored according to their orientation for better visualization. The dimensions are about 23^2 nm^2.

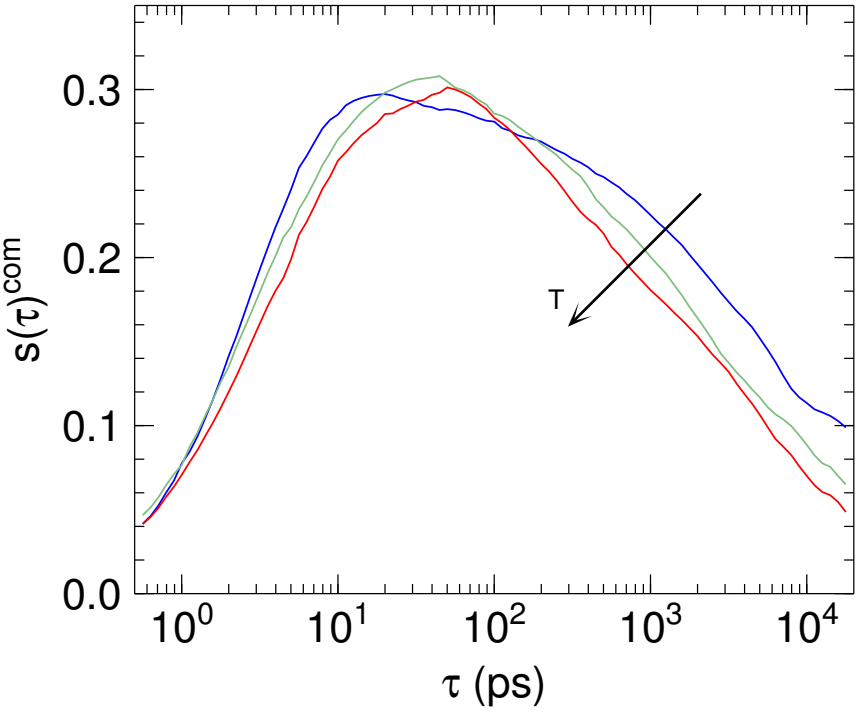

Figure 7.42: $C_{100}H_{202}$ - Scalar product of unit displacement vectors of neighboring com molecules at T =393, 453 and 509 K. The arrow points into the direction of rising temperature.

maximum of $s(\tau)$ corresponds to the onset of the intermediate relaxation process of the carbon–carbon bond reorientation. The decorrelation of the collective dynamics occurs on a wide time scale, characterized by the slow decay of $s(\tau > \tau_{\max})$, corresponding to the broad DRT of the intermediate relaxation process.

Similar effects can be observed at lower temperatures. At first the collective behavor of the displacements increases. With decreasing temperature this process seems to take place at shorter times and the directed motions persist on a longer time scale. At $T = 393\,\mathrm{K}$ the time $\tau_{\max}$ is not as definite as at high temperatures and seems to cover about one order of magnitude in time. At this low temperatures the flow-like motions of the atoms takes place on an extended time scale, and can be identified in 2D cuts even on the nanosecond time scale (see fig. 7.41).

The decorrelation of the collective motions shifts to longer times with decreasing temperature. This is expected as the onset of the intermediate relaxation process shifts similarly to longer times. The fading of the flow-like behavior takes place on a wide time scale for all temperatures, which is linked to the relaxation of the molecular backbone.

In order to study the collectivity of the whole molecules, equation 7.11 was computed using center-of-mass coordinates of the $C_{100}H_{202}$ molecules. Thereby the scalar product was calculated for the unit displacement vectors of neighboring molecules. The resulting data is plotted in figure 7.42 for all simulated temperatures. The curves show the same shape and trend as was oberved before: At first the dynamics of the whole molecules are barely correlated. With increasing time τ the molecules move collectively in clusters. This effect reaches a maximum during approximately 10 ps and 100 ps, and extends into the nanosecond regime at low temperatures. This intermolecular collectivity of the atomic motion is reflected by the strong non-Gaussian characteristics observed in section 7.2.

It is these hydrodynamic effects which are considered by the theory of VHI-controlled dynamics proposed by Farago et. al. [44, 46] and allowed for a proper modeling of the center-of-mass mean-square displacement in section 7.2. Although melts of $C_{100}H_{202}$ have been simulated previously [30, 31], collective features as presented here were not reported. The simulation system used in this thesis is significantly larger compared to the systems simulated in most other studies, which makes it possible for hydrodynamic interctions to fully develop.

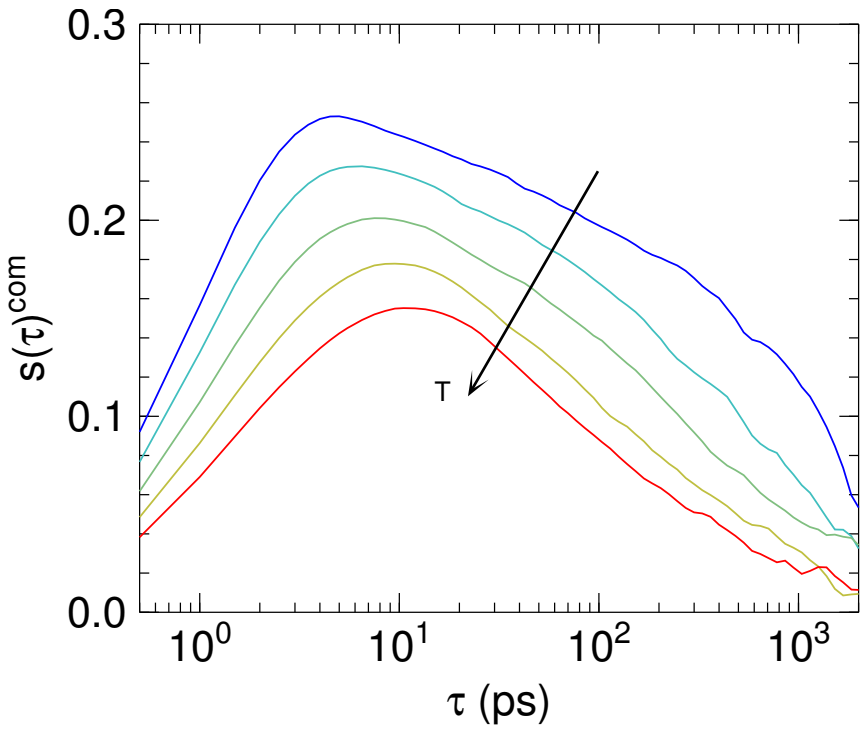

Figure 7.43: $C_{16}H_{34}$ - Scalar product of unit displacement vectors of neighboring com molecules at T =293, 323, 363, 403 and 443 K. The arrow points into the direction of rising temperature.

To study the effect of correlated dynamics in the short chain $C_{16}H_{34}$ melt, the same procedure was applied as described above. Thereby the scalar product was calculated for the displacements of the com $C_{16}H_{34}$ molecules. The results are presented in figure 7.43. In accordance with the findings for the $C_{100}H_{202}$ molecules it can clearly be seen that hydrodynamic effects are pronounced, and increase with decreasing temperature. In contrast to the $C_{100}H_{202}$ chain dynamics no explicit influence of these correlated dynamics on the reorientation of $C_{16}H_{34}$ backbone bond vectors could be identified, as the decorrelation of these flow-like motions coincide with the characteristic relaxation of global molecular.

This study shows that correlated dynamics of many atoms take place in molecular melts on an extended time scale, which connects to the onset of molecular self-diffusion. Accounting for these hydrodynamic effects allows for a proper description of the motion of whole molecules. Consequently these fluid correlations also apply for the individual atoms. The analysis of collective motions in polymer melts is subject to extensive research. Many other studies quantify cooperative motions at low temperatures, close to or below the glass transition temperature, by detecting stringlike cooperative rearrangements [203, 204]. In this thesis the existence of intermolecular collectivity could be visualized and further on quantified by the use of special correlation functions at temperatures well above the melting temperature. These hydrodynamic interactions not only cause the pronounced anomalous subdiffusive behavior of the atoms and molecules, but also have a strong effect on the relaxation of the molecular backbone.

8 Conclusion

In this thesis extensive quasielastic neutron scattering (QENS) experiments and molecular dynamics (MD) simulations were performed and analyzed to study the dynamics taking place at the onset of self-diffusion in molecular liquids.

With resolution resolved QENS, performed at the time-of-flight spectrometer TOFTOF, time scales ranging from 0.1 ps to 1 ns were probed. The neutron scattering data allowed for a characterization of the prevailing atomic dynamics with high statistics. The resulting spectra were not only used for precise evaluation, but also for a throughout validation of the simulated dynamics on a time scale sensitive to the force field parameters applied in the MD simulations. The comparison yields an outstanding quantitative agreement between the measured and simulated dynamics. Hence the study of the simulated trajectories in real space can be used to visualize molecular motions which significantly helps to find models describing the transport mechanism in molecular liquids. It is to be mentioned that the state-of-the-art MD simulations performed in the framework of this thesis cannot reproduce all static and dynamic properties precisely. The features extracted from the simulations can only be utilized to the extend to which the simulated trajectories have been validated. Enhanced experimental capabilities are thus indispensable for a more precise validation of simulation data. In addition state-of-the-art neutron scattering data should directly be used to parameterize force fields in the first place.

The analysis of the QENS data indicated that several dynamical processes are present on the pico- to nanosecond time scale, eventually leading to molecular self-diffusion. The evaluation of the complementary MD simulations allowed for an identification of these motions, which are of both intra- and intermolecular nature. The results will be summarized and discussed in the following.

The intermediate scattering functions measured at TOFTOF on a $C_{16}H_{34}$ melt mainly represent the hydrogen motion on the 0.1 to 100 ps time scale. It was found that by variation of temperature a crossover of different dynamics is observed on local length scales ($Q \gtrsim 1\,\text{Å}^{-1}$). At low temperatures a broad distribution of relaxations

contributes to the signal, which can be assigned to torsional motion of the dihedrals. The analysis of the simulated trajectories revealed that the dihedral rotation is faster close to the ends of the $C_{16}H_{34}$ chains. At low temperatures these motions are slow enough to considerably contribute to the observed signal, and the relative spread of the relaxation times along the molecular chain results in a stretched form of the measured $I(Q,t)$.

On the same time scale where dihedral motions occur a strong non-Gaussian behavior of the center-of-mass (com) displacement arises. This time scale coincides with the subdiffusive regime of the com mean-square displacement (MSD), which lasts until the freely diffusive regime is reached. The corresponding motions of the atoms seem to dominate the measured signal on larger length scales ($Q \lesssim 1\,\text{Å}^{-1}$). An analysis of the simulated $C_{16}H_{34}$ dynamics in terms of collective motions showed that intermolecular correlations of the molecular dynamics are present and are reflected by the non-Gaussian behavior of the com dynamics. Since the $C_{16}H_{34}$ molecules are quite stiff compared to the long $C_{100}H_{202}$ chains, it has to be assumed that these collective motions of the whole molecules strongly impact the dynamics of the individual atoms.

With increasing temperature torsional motions disappear from the time window accessed with QENS, and a more global relaxation of the $C_{16}H_{34}$ chains dominates: Rotation of the whole molecules. The corresponding activation energy of this process can be associated to the activation energy of molecular self-diffusion, and the time scale where these global rotations take place is linked to the crossover from the subdiffusive to the freely diffusive regime of the molecular dynamics.

The Rouse model, which was developed to describe single-chain motions in short polymer melts, was tested to describe the the dynamics in a $C_{100}H_{202}$ melt. The comparison of the $I(Q,t)$ obtained with QENS and predicted by the Rouse model showed that the Rouse theory can only describe the motions on a macromolecular length scale in the time regime where self-diffusion dominates the overall dynamics. In order to monitor the apparent shortcomings of the Rouse predictions, a detailed analysis of the simulated $C_{100}H_{202}$ motions was performed in terms of the Rouse model. This showed that only global chain dynamics are described accurately by the first Rouse modes. On more local length scales the entropic springs of the Rouse model cannot model the actual restoring forces.

Further deviations of the Rouse model were found by analyzing the MSD of the com coordinates of the $C_{100}H_{202}$ molecules. The Rouse model predicts a simple

Fickean diffusive motion, but a clear subdiffusive behavior was found on an extended time scale, framed by the ballistic and freely diffusive regime. The experimentally validated simulation presented in this thesis could be used to test two different theoretical approaches to account for this subdiffusive scaling. It could thereby be demonstrated that the recent theory of Farago et al., who have explicitly accounted for viscoelastic and hydrodynamic interactions (VHI) can successfully describe the subdiffusive molecular motions. Such hydrodynamic effects are not represented by the classical Rouse model.

The scattering functions measured at TOFTOF on a $C_{100}H_{202}$ melt were studied with regard to slow, long-range motions. For all observation times surveyed with TOFTOF, ranging from 2 ps to more than 1 ns, diffusive-like motions were found, which were characterized by apparent diffusion coefficients D_a. However, all observed motions were too fast, as the values of D_a were larger than expected for long-range long-time molecular self-diffusivity.

In the long chain $C_{100}H_{202}$ system overall chain relaxations are relatively slow, hence the onset of self-diffusion is prolonged. The characteristic time scales of local and global chain motions are well separated. Torsional motions were again found to dominate the chain relaxations on short time scales of few picoseconds. Large scale molecular rotations take place in the nanoseconds regime, shortly before the atoms start to show freely diffusive behavior.

The analysis of local chain reorientation revealed that a third, intermediate relaxation process is present on time scales framed by the torsional and global chain dynamics. The origin of this feature could be attributed to decay of intermolecular flow-like motions in large clusters. These collective flow effects coincide with the subdiffusive regime of the MSD and contribute significantly to the observed chain dynamics.

The observation of highly collective motions in the molecular melt is contrary to the concept of total hydrodynamic shielding derived by de Gennes for polymer melts. A model explicitly taking VHI into account gives first results to describe the subdiffusive behavior of the whole molecules. Consequently also the motions of the individual atoms, which are strongly coupled to the com motion on this intermediate time scale, are affected by these hydrodynamic effects. An analytic model for the atomic transport mechanism in molecular liquids has to take this intermolecular collectivity into account.

In the shorter $C_{16}H_{34}$ melt such an intermediate relaxation processes of the backbone bond reorientations could not be identified. The time scales of local and global chain relaxations are much closer to each other, and the decorrelation of collective flow-like motions superimposes with the intramolecular chain relaxations.

In addition a detailed QENS study of poly(ethylene oxide) (PEO), having a similar structure as *n*-alkanes, was presented. The observed dynamics were carefully compared to the ones found for *n*-alkanes. The overall motions are strongly slowed down due to the existence of intermolecular hydrogen bonds. An increase of the extracted activation energies for motions on a 50 ps time scale was found with decreasing chain length, opposite to the trend found for *n*-alkanes. In order to identify the effect of hydrogen bonding on the observed intramolecular dynamics and on the expected collective behavior, future MD simulations need to be performed and evaluated following the methods presented in this thesis.

Bibliography

[1] C. Smuda. "Diffusive Bewegungen in molekularen Flüssigkeiten". PhD thesis. Technische Universität München, 2009.

[2] R. Solaro, F. Chiellini, and A. Battisti. "Targeted Delivery of Protein Drugs by Nanocarriers". *Materials*, vol. 3, pp. 1928–1980 (2010).

[3] S. Busch. "The Pico- to Nanosecond Dynamics of Phospholipid Molecules". PhD thesis. Technische Universität München, 2012.

[4] K. Zuse, F. L. Bauer, and H. Zemanek. *Der Computer – Mein Lebenswerk*. Springer, 2007.

[5] URL: `http://www.lrz.de/services/compute/linux-cluster/`.

[6] D. Feller and E. R. Davidson. "Basis Sets for Ab Initio Molecular Orbital Calculations and Intermolecular Interactions". *Reviews in Computational Chemistry*, vol. 1, pp. 1–43 (2007).

[7] W. F. van Gunsteren and H. J. C. Berendsen. "Computer Simulation of Molecular Dynamics: Methodology, Applications, and Perspectives in Chemistry". *Angewandte Chemie International Edition in English*, vol. 29, no. 9, pp. 992–1023 (1990).

[8] W. F. van Gunsteren and A. E. Mark. "Validation of molecular dynamics simulation". *The Journal of Chemical Physics*, vol. 108, p. 6109 (1998).

[9] D. C. Douglass and D. W. McCall. "Diffusion in Paraffin Hydrocarbons". *The Journal of Physical Chemistry*, vol. 62, no. 9, pp. 1102–1107 (1958).

[10] H. Ertl and F. A. L. Dullien. "Self-diffusion and viscosity of some liquids as a function of temperature". *AIChE Journal*, vol. 19, no. 6, pp. 1215–1223 (1973).

[11] E. von Meerwall, S. Beckman, J. Jang, and W. Mattice. "Diffusion of liquid n-alkanes: Free-volume and density effects". *The Journal of Chemical Physics*, vol. 108, p. 4299 (1998).

[12] P. E. Rouse Jr. "A theory of the linear viscoelastic properties of dilute solutions of coiling polymers". *The Journal of Chemical Physics*, vol. 21, p. 1272 (1953).

[13] A. R. Rennie, W. Petry, and B. Stühn. "Motion of long alkanes in polyethylene melts". *Springer Proceedings in Physics*, vol. 29. Ed. by D. Richter and T. Springer, pp. 235–239 (1988).

[14] K. E. Larsson, L. Q. D. O. Amaral, N. Ivanchev, S. Ripeanu, L. Bergstedt, and U. Dahlborg. "Proton Motions in Complex Hydrogenous Liquids. II. Results Gained from Some Neutron-Scattering Experiments". *Physical Review*, vol. 151, no. 1, p. 126 (1966).

[15] K. F. Bradley, S.-H. Chen, and T. O. Brun. "Quasielastic neutron scattering measurements of n-butane in its crystalline, plastic, and liquid phases". *The Journal of Chemical Physics*, vol. 95, p. 5273 (1991).

[16] D. Fuhrmann, L. Criswell, H. Mo, U. G. Volkmann, K. W. Herwig, H. Taub, and F. Y. Hansen. "Diffusive motion in model soft matter systems: quasielastic neutron scattering study of short-and intermediate-length alkane layers". *Physica B: Condensed Matter*, vol. 276, pp. 345–346 (2000).

[17] G. Arialdi, K. Karatasos, J.-P. Ryckaert, V. Arrighi, F. Saggio, A. Triolo, A. Desmedt, J. Pieper, and R. E. Lechner. "Local Dynamics of Polyethylene and Its Oligomers: A Molecular Dynamics Interpretation of the Incoherent Dynamic Structure Factor". *Macromolecules*, vol. 36, no. 23, pp. 8864–8875 (2003).

[18] C. Smuda, S. Busch, G. Gemmecker, and T. Unruh. "Self-diffusion in molecular liquids: Medium-chain n-alkanes and coenzyme Q_{10} studied by quasielastic neutron scattering". *The Journal of Chemical Physics*, vol. 129, p. 014513 (2008).

[19] T. Unruh, C. Smuda, S. Busch, J. Neuhaus, and W. Petry. "Diffusive motions in liquid medium-chain n-alkanes as seen by quasielastic time-of-flight neutron spectroscopy". *The Journal of Chemical Physics*, vol. 129, p. 121106 (2008).

[20] V. Arrighi, J. Tanchawanich, and M. T. F. Telling. "Molar Mass Dependence of Polyethylene Chain Dynamics. A Quasi-Elastic Neutron Scattering Investigation". *Macromolecules*, vol. 46, no. 1, pp. 216–225 (2012).

[21] G. D. Smith and D. Y. Yoon. "Equilibrium and dynamic properties of polymethylene melts from molecular dynamics simulations. I. n-Tridecane". *The Journal of Chemical Physics*, vol. 100, no. 1, pp. 649–658 (1994).

[22] G. D. Smith, D. Y. Yoon, W. Zhu, and M. D. Ediger. "Comparison of equilibrium and dynamic properties of polymethylene melts of n-C44H90 chains from simulations and experiments". *Macromolecules*, vol. 27, no. 20, pp. 5563–5569 (1994).

[23] G. D. Smith, D. Y. Yoon, and R. L. Jaffe. "Long-time molecular motions and local chain dynamics in n-C44H90 melts by molecular dynamics simulations". *Macromolecules*, vol. 28, no. 17, pp. 5897–5905 (1995).

[24] Y. Zhang, R. M. Venable, and R. W. Pastor. "Molecular Dynamics Simulations of Neat Alkanes: The Viscosity Dependence of Rotational Relaxation". *The Journal of Physical Chemistry*, vol. 100, no. 7, pp. 2652–2660 (1996).

[25] V. A. Harmandaris, M. Doxastakis, V. G. Mavrantzas, and D. N. Theodorou. "Detailed molecular dynamics simulation of the self-diffusion of n-alkane and cis-1,4 polyisoprene oligomer melts". *The Journal of Chemical Physics*, vol. 116, p. 436 (2002).

[26] G. H. Goo, G. Sung, S. H. Lee, and T. Chang. "Diffusion behavior of n-alkanes by molecular dynamics simulations". *Bulletin of the Korean Chemical Society*, vol. 23, no. 11, pp. 1595–1603 (2002).

[27] S. H. Lee and T. Chang. "Viscosity and diffusion constants calculation of n-alkanes by molecular dynamics simulations". *Bulletin of the Korean Chemical Society*, vol. 24, no. 11, pp. 1590–1598 (2003).

[28] M. Mondello, G. S. Grest, E. B. Webb III, and P. Peczak. "Dynamics of n-alkanes: Comparison to Rouse model". *The Journal of Chemical Physics*, vol. 109, p. 798 (1998).

[29] G. D. Smith, W. Paul, D. Y. Yoon, A. Zirkel, J. Hendricks, D. Richter, and H. Schober. "Local dynamics in a long-chain alkane melt from molecular dynamics simulations and neutron scattering experiments". *The Journal of Chemical Physics*, vol. 107, p. 4751 (1997).

[30] W. Paul, G. D. Smith, and D. Y. Yoon. "Static and Dynamic Properties of a n-C100H202 Melt from Molecular Dynamics Simulations". *Macromolecules*, vol. 30, no. 25, pp. 7772–7780 (1997).

[31] W. Paul, G. Smith, D. Y. Yoon, B. Farago, S. Rathgeber, A. Zirkel, L. Willner, and D. Richter. "Chain Motion in an Unentangled Polyethylene Melt: A Critical Test of the Rouse Model by Molecular Dynamics Simulations and Neutron Spin Echo Spectroscopy". *Physical Review Letters*, vol. 80, no. 11, pp. 2346–2349 (1998).

[32] X. Qiu and M. D. Ediger. "Local and global dynamics of unentangled polyethylene melts by 13C NMR". *Macromolecules*, vol. 33, no. 2, pp. 490–498 (2000).

[33] J. Han, R. L. Jaffe, and D. Y. Yoon. "Conformational characteristics of polymethylene chains in melts and in various phantom chains from explicit atom molecular dynamics simulations". *Macromolecules*, vol. 30, no. 23, pp. 7245–7252 (1997).

[34] K. Binder and W. Paul. "Monte Carlo simulations of polymer dynamics: Recent advances". *Journal of Polymer Science Part B: Polymer Physics*, vol. 35, no. 1, pp. 1–31 (1997).

[35] G. Smith, W. Paul, M. Monkenbusch, and D. Richter. "A comparison of neutron scattering studies and computer simulations of polymer melts". *Chemical Physics*, vol. 261, no. 1, pp. 61–74 (2000).

[36] G. D. Smith, W. Paul, M. Monkenbusch, and D. Richter. "On the non-Gaussianity of chain motion in unentangled polymer melts". *The Journal of Chemical Physics*, vol. 114, p. 4285 (2001).

[37] W. Paul. "Anomalous diffusion in polymer melts". *Chemical Physics*, vol. 284, no. 1, pp. 59–66 (2002).

[38] N. C. Karayiannis, V. G. Mavrantzas, and D. N. Theodorou. "A novel Monte Carlo scheme for the rapid equilibration of atomistic model polymer systems of precisely defined molecular architecture". *Physical Review Letters*, vol. 88, no. 10, p. 105503 (2002).

[39] M. Zamponi, A. Wischnewski, M. Monkenbusch, L. Willner, D. Richter, P. Falus, B. Farago, and M. Guenza. "Cooperative Dynamics in Homopolymer Melts: A Comparison of Theoretical Predictions with Neutron Spin Echo Experiments". *The Journal of Physical Chemistry B*, vol. 112, no. 50, pp. 16220–16229 (2008).

[40] M. Brodeck, F. Alvarez, A. Arbe, F. Juranyi, T. Unruh, O. Holderer, J. Colmenero, and D. Richter. "Study of the dynamics of poly(ethylene oxide) by combining molecular dynamic simulations and neutron scattering experiments". *The Journal of Chemical Physics*, vol. 130, p. 094908 (2009).

[41] A. R. Brás, R. Pasquino, T. Koukoulas, G. Tsolou, O. Holderer, A. Radulescu, J. Allgaier, V. G. Mavrantzas, W. Pyckhout-Hintzen, A. Wischnewski, D. Vlassopoulos, and D. Richter. "Structure and dynamics of polymer rings by neutron scattering: breakdown of the Rouse model". *Soft Matter*, vol. 7, no. 23, pp. 11169–11176 (2011).

[42] M. Guenza. "Theoretical models for bridging timescales in polymer dynamics". *Journal of Physics: Condensed Matter*, vol. 20, no. 3, p. 033101 (2008).

[43] M. Guenza. "Cooperative dynamics in unentangled polymer fluids". *Physical Review Letters*, vol. 88, no. 2, p. 025901 (2001).

[44] J. Farago, H. Meyer, and A. N. Semenov. "Anomalous diffusion of a polymer chain in an unentangled melt". *Physical Review Letters*, vol. 107, no. 17, p. 178301 (2011).

[45] J. Farago, H. Meyer, J. Baschnagel, and A. Semenov. "Hydrodynamic and viscoelastic effects in polymer diffusion". *Journal of Physics: Condensed Matter*, vol. 24, no. 28, p. 284105 (2012).

[46] J. Farago, H. Meyer, J. Baschnagel, and A. Semenov. "Mode-coupling approach to polymer diffusion in an unentangled melt. II. The effect of viscoelastic hydrodynamic interactions". *Physical Review E*, vol. 85, no. 5, p. 051807 (2012).

[47] S. C. Glotzer. "Spatially heterogeneous dynamics in liquids: insights from simulation". *Journal of Non-Crystalline Solids*, vol. 274, no. 1, pp. 342–355 (2000).

[48] P. G. Debenedetti and F. H. Stillinger. "Supercooled liquids and the glass transition". *Nature*, vol. 410, no. 6825, pp. 259–267 (2001).

[49] L. Berthier and G. Biroli. "Theoretical perspective on the glass transition and amorphous materials". *Reviews of Modern Physics*, vol. 83, no. 2, p. 587 (2011).

[50] C. Bennemann, C. Donati, J. Baschnagel, and S. C. Glotzer. "Growing range of correlated motion in a polymer melt on cooling towards the glass transition". *Nature*, vol. 399, no. 6733, pp. 246–249 (1999).

[51] D. P. Zitterbart, B. Wienecke, J. P. Butler, and B. Fabry. "Coordinated Movements Prevent Jamming in an Emperor Penguin Huddle". *PLoS ONE*, vol. 6, no. 6, e20260 (2011).

[52] K. Tunstrøm, Y. Katz, C. C. Ioannou, C. Huepe, M. J. Lutz, and I. D. Couzin. "Collective States, Multistability and Transitional Behavior in Schooling Fish". *PLOS Computational Biology*, vol. 9, no. 2, e1002915 (2013).

[53] R. Faller. "Influence of Chain Stiffness on Structure and Dynamics of Polymers in the Melt". PhD thesis. Johannes Gutenberg-Universität Mainz, 2000.

[54] J. E. Mark. *Physical properties of polymers handbook*. Springer, 2006.

[55] A. Gurtovenko and A. Blumen. "Generalized Gaussian Structures: Models for Polymer Systems with Complex Topologies". *Advances in Polymer Science*, vol. 182, pp. 171–282 (2005).

[56] N. Fatkullin, T. Shakirov, and N. Balakirev. "Why does the Rouse Model Fairly Describe the Dynamic Characteristics of Polymer Melts at Molecular Masses below Critical Mass?" *Polymer Science Series A*, vol. 52, no. 1, pp. 72–81 (2010).

[57] P. de Gennes. "Reptation of a Polymer Chain in the Presence of Fixed Obstacles". *The Journal of Chemical Physics*, vol. 55, p. 572 (1971).

[58] D. Richter, M. Monkenbusch, A. Arbe, and J. Colmenero. *Advances in Polymer Science*, vol. 174, pp. 1–221 (2005).

[59] M. Doi and S. F. Edwards. *The Theory of Polymer Dynamics*. Oxford University Press, USA, 1988.

[60] A. E. Likhtman. "Viscoelasticity and molecular rheology". *Polymer Science: A Comprehesive Reference*, vol. 1, pp. 133–179 (2011).

[61] A. Kloczkowski, J. Mark, and H. Frisch. "The relaxation spectrum for Gaussian networks". *Macromolecules*, vol. 23, no. 14, pp. 3481–3490 (1990).

[62] J.-U. Sommer and A. Blumen. "On the statistics of generalized Gaussian structures: collapse and random external fields". *Journal of Physics A: Mathematical and General*, vol. 28, no. 23, p. 6669 (1999).

[63] R. Pérez-Aparicio, J. Colmenero, F. Alvarez, J. Padding, and W. Briels. "Chain dynamics of poly(ethylene-alt-propylene) melts by means of coarse-grained simulations based on atomistic molecular dynamics". *The Journal of Chemical Physics*, vol. 132, p. 024904 (2010).

[64] B. H. Zimm. "Dynamics of Polymer Molecules in Dilute Solution: Viscoelasticity, Flow Birefringence and Dielectric Loss". *The Journal of Chemical Physics*, vol. 24, p. 269 (1956).

[65] P. Ahlrichs, R. Everaers, and B. Dünweg. "Screening of hydrodynamic interactions in semidilute polymer solutions: A computer simulation study". *Physical Review E*, vol. 64, no. 4, p. 040501 (2001).

[66] P. de Gennes. "Dynamics of entangled polymer solutions. II. Inclusion of hydrodynamic interactions". *Macromolecules*, vol. 9, no. 4, pp. 594–598 (1976).

[67] H. Meyer. Institut Charles Sadron. Private communication.

[68] P. de Gennes. "Dynamics of entangled polymer solutions. I. The Rouse model". *Macromolecules*, vol. 9, no. 4, pp. 587–593 (1976).

[69] W. Paul and G. D. Smith. "Structure and dynamics of amorphous polymers: computer simulations compared to experiment and theory". *Reports on Progress in Physics*, vol. 67, no. 7, p. 1117 (2004).

[70] D. Richter. Forschungszentrum Jülich. Private communication.

[71] T. Unruh. Friedrich-Alexander-Universität Erlangen-Nürnberg. Private communication.

[72] J. Farago, A. N. Semenov, H. Meyer, J. P. Wittmer, A. Johner, and J. Baschnagel. "Mode-coupling approach to polymer diffusion in an unentangled melt. I. The effect of density fluctuations". *Physical Review E*, vol. 85, no. 5, p. 051806 (2012).

[73] F. Rust. "Intermolekulare Bewegung von Polyethylenglykol". Seminar paper. TUMKolleg, 2013.

[74] P. Flory and A Vrij. "Melting Points of Linear-Chain Homologs. The Normal Paraffin Hydrocarbons". *Journal of the American Chemical Society*, vol. 85, no. 22, pp. 3548–3553 (1963).

[75] G. Squires. *Introduction to the theory of thermal neutron scattering*. Cambridge University Press, 2012.

[76] M. Bée. *Quasielastic neutron scattering: Principles and Applications in Solid State Chemistry, Biology and Materials Science*. Adam Hilger, 1988.

[77] S. Busch. "Protein Diffusion in Concentrated Solutions". Diploma thesis. Technische Universität München, 2007.

[78] V. Sears. "Neutron scattering lengths and cross sections". *Neutron News*, vol. 3, no. 3, pp. 26–37 (1992).

[79] L. Van Hove. "Correlations in space and time and Born approximation scattering in systems of interacting particles". *Physical Review*, vol. 95, no. 1, p. 249 (1954).

[80] H. Morhenn, S. Busch, G. Simeoni, and T. Unruh. "TOFTOF - Time-of-flight spectrometer". In: *Laboratory Course Neutron Scattering, Experiment Manuals*. Ed. by T. Brückel, G. Heger, D. Richter, G. Roth, and R. Zorn. Vol. 28. Schlüsseltechnologien / Key Technologies. Forschungszentrum Jülich GmbH, 2011. URL: `http://www.fz-juelich.de/zb/jewel`.

[81] J. P. Boon and S. Yip. *Molecular hydrodynamics*. McGraw-Hill, 1980.

[82] A. Rahman, K. Singwi, and A. Sjölander. "Theory of Slow Neutron Scattering by Liquids. I". *Physical Review*, vol. 126, no. 3, p. 986 (1962).

[83] R. Zorn. "Deviation from Gaussian behavior in the self-correlation function of the proton motion in polybutadiene". *Physical Review B*, vol. 55, no. 10, p. 6249 (1997).

[84] W. Kob, C. Donati, S. J. Plimpton, P. H. Poole, and S. C. Glotzer. "Dynamical heterogeneities in a supercooled Lennard-Jones liquid". *Physical Review Letters*, vol. 79, no. 15, pp. 2827–2830 (1997).

[85] Z. Hu and C. J. Margulis. "Heterogeneity in a room-temperature ionic liquid: Persistent local environments and the red-edge effect". *Proceedings of the National Academy of Sciences of the United States of America*, vol. 103, no. 4, pp. 831–836 (2006).

[86] B. Vorselaars, A. V. Lyulin, K. Karatasos, and M. Michels. "Non-Gaussian nature of glassy dynamics by cage to cage motion". *Physical Review E*, vol. 75, no. 1, p. 011504 (2007).

[87] T. Odagaki and Y. Hiwatari. "Gaussian–to–non-Gaussian transition in supercooled fluids". *Physical Review A*, vol. 43, no. 2, p. 1103 (1991).

[88] B. R. A. Nijboer and A. Rahman. "Time expansion of correlation functions and the theory of slow neutron scattering". *Physica*, vol. 32, no. 2, pp. 415–432 (1966).

[89] J.-P. Hansen and I. R. McDonald. *Theory of simple liquids*. Academic Press, 2006.

[90] A. Furrer, J. Mesot, and T. Strässle. *Neutron Scattering in Condensed Matter Physics*. World Scientific Publishing Co. Pte. Ltd., 2009.

[91] A. M. Gaspar, S. Busch, M.-S. Appavou, W. Häussler, R. Georgii, Y. Su, and W. Doster. "Using polarization analysis to separate the coherent and incoherent scattering from protein samples". *Biochimica et Biophysica Acta (BBA)-Proteins & Proteomics*, vol. 1804, no. 1, pp. 76–82 (2010).

[92] T. Unruh, J. Neuhaus, and W. Petry. "The high-resolution time-of-flight spectrometer TOFTOF". *Nuclear Instruments and Methods in Physics Research Section A*, vol. 580, no. 3, pp. 1414–1422 (2007).

[93] T. Unruh, J. Neuhaus, and W. Petry. "Erratum to "The high-resolution time-of-flight spectrometer TOFTOF [92]". *Nuclear Instruments and Methods in Physics Research Section A*, vol. 585, pp. 201–201 (2008).

[94] L. Dobrzynski and K. Blinowski. *Neutrons and solid state physics*. Ellis Horwood Ltd., 1994.

[95] W. Heisenberg. "Über den anschaulichen Inhalt der quantentheoretischen Kinematik und Mechanik". *Zeitschrift für Physik*, vol. 43, pp. 172–198 (1927).

[96] URL: `http://www.frm2.tum.de/en/science/spectrometry/dns/`.

[97] Y. Su. "DNS - Neutron Polarization Analysis". In: *Laboratory Course Neutron Scattering, Experiment Manuals*. Ed. by T. Brückel, G. Heger, D. Richter, G. Roth, and R. Zorn. Vol. 28. Schlüsseltechnologien / Key Technologies. Forschungszentrum Jülich GmbH, 2011. URL: `http://www.fz-juelich.de/zb/jewel`.

[98] O. Schärpf and H. Capellmann. "The XYZ-Difference Method with Polarized Neutrons and the Separation of Coherent, Spin Incoherent, and Magnetic Scattering Cross Sections in a Multidetector". *physica status solidi (a)*, vol. 135, no. 2, pp. 359–379 (1993).

[99] J. Stewart, K. Andersen, R. Cywinski, and A. Murani. "Magnetic diffuse scattering in disordered systems studied by neutron polarization analysis". *Journal of Applied Physics*, vol. 87, no. 9, pp. 5425–5430 (2000).

[100] J. Wuttke. "Improved sample holder for multidetector neutron spectrometers". *Physica B: Condensed Matter*, vol. 266, no. 1-2, p. 112 (1999).

[101] J. Wuttke. *Frida1: Fast reliable inelastic data analysis*. 1990. URL: `http://sourceforge.net/projects/frida/`.

[102] S. Busch. *sihl: scattered intensity handling library*. 2009. URL: `http://www.thamnos.de/repos/sihl/`.

[103] B. Chiffey and T. Hicks. "The spontaneous moment of nickel-chromium alloys". *Physics Letters A*, vol. 34, no. 5, pp. 267–268 (1971).

[104] O. Schärpf. *The Spin of the Neutron as a Measuring Probe*. 2010. URL: `http://82.135.31.182/neutronpol.pdf`.

[105] A. Glavic. *plot.py 0.7.14*. 2011. URL: `http://sourceforge.net/projects/plotpy/`.

[106] B. Gabryś and O. Schärpf. "Scattering from polymers using polarised neutrons: a new development". *Physica B: Condensed Matter*, vol. 180, pp. 495–498 (1992).

[107] G. Placzek. "The scattering of neutrons by systems of heavy nuclei". *Physical Review*, vol. 86, no. 3, p. 377 (1952).

[108] U. Dahlborg and B. Kunsch. "On the Placzek Correction for Simple Liquids and Gases". *Physics and Chemistry of Liquids*, vol. 12, no. 3, pp. 237–254 (1983).

[109] H. E. Fischer, A. C. Barnes, and P. S. Salmon. "Neutron and x-ray diffraction studies of liquids and glasses". *Reports on Progress in Physics*, vol. 69, no. 1, p. 233 (2006).

[110] A. K. Soper. "Inelasticity corrections for time-of-flight and fixed wavelength neutron diffraction experiments". *Molecular Physics*, vol. 107, no. 16, pp. 1667–1684 (2009).

[111] F. Alvarez, J. Colmenero, R. Zorn, L. Willner, and D. Richter. "Partial Structure Factors of Polyisoprene: Neutron Scattering and Molecular Dynamics Simulation". *Macromolecules*, vol. 36, no. 1, pp. 238–248 (2003).

[112] G. Venturi, F. Formisano, G. J. Cuello, M. R. Johnson, E. Pellegrini, U. Bafile, and E. Guarini. "Structure of liquid n-hexane". *The Journal of Chemical Physics*, vol. 131, p. 034508 (2009).

[113] D. van der Spoel, E. Lindahl, B. Hess, A. R. van Buuren, E. Apol, P. J. Meulenhoff, D. P. Tieleman, A. L. T. M. Sijbers, K. A. Feenstra, R. van Drunen, and H. J. C. Berendsen. *Gromacs User Manual version 4.5.4*. 2010.

[114] Y. Shao, L. F. Molnar, Y. Jung, J. Kussmann, C. Ochsenfeld, S. T. Brown, A. T. Gilbert, L. V. Slipchenko, S. V. Levchenko, D. P. O'Neill, et al. "Advances in methods and algorithms in a modern quantum chemistry program package". *Physical Chemistry Chemical Physics*, vol. 8, no. 27, pp. 3172–3191 (2006).

[115] A. D. Mackerell Jr. “Empirical Force Fields for Biological Macromolecules: Overview and Issues”. *Journal of Computational Chemistry*, vol. 25, no. 13, pp. 1584–1604 (2004).

[116] A. Kukol. *Molecular Modeling of Proteins*. Methods in Molecular Biology. Humana Press, 2008.

[117] G. Schneider and K.-H. Baringhaus. *Molecular Design: Concepts and Applications*. Wiley-VCH, 2008.

[118] J. E. Jones. “On the determination of molecular fields. II. From the equation of state of a gas”. *Proceedings of the Royal Society of London. Series A: Mathematical and Physical Sciences.* Vol. 106, no. 738, pp. 463–477 (1924).

[119] R. Buckingham. “The classical equation of state of gaseous helium, neon and argon”. *Proceedings of the Royal Society of London. Series A: Mathematical and Physical Sciences.* Vol. 168, no. 933, pp. 264–283 (1938).

[120] W. Demtröder. *Experimentalphysik 2: Elektrizität und Optik*. Vol. 2. Springer, 2009.

[121] P. M. Morse. “Diatomic molecules according to the wave mechanics. II. Vibrational levels”. *Physical Review*, vol. 34, no. 1, p. 57 (1929).

[122] W. Demtröder. *Experimentalphysik 3: Atome, Moleküle und Festkörper*. Vol. 3. Springer, 2005.

[123] T. Becker. “Protein Dynamics - Comparison of Incoherent Neutron Scattering and Molecular Dynamics Simulation”. PhD thesis. Universität Heidelberg, 2004.

[124] J. Chen, W. Im, and C. L. Brooks. “Application of torsion angle molecular dynamics for efficient sampling of protein conformations”. *Journal of Computational Chemistry*, vol. 26, no. 15, pp. 1565–1578 (2005).

[125] H. J. C. Berendsen, J. P. M. Postma, W. F. van Gunsteren, A. DiNola, and J. R. Haak. “Molecular dynamics with coupling to an external bath”. *The Journal of Chemical Physics*, vol. 81, no. 8, pp. 3684–3690 (1984).

[126] G. Bussi, D. Donadio, and M. Parrinello. “Canonical sampling through velocity rescaling”. *The Journal of Chemical Physics*, vol. 126, no. 1, pp. 014101–014101 (2007).

[127] S. Nosé. “A molecular dynamics method for simulations in the canonical ensemble”. *Molecular Physics*, vol. 52, no. 2, pp. 255–268 (1984).

[128] W. Hoover. "Canonical dynamics: Equilibrium phase-space distributions". *Physical Review A*, vol. 31, no. 3, p. 1695 (1985).

[129] P. H. Hünenberger. "Thermostat algorithms for molecular dynamics simulations". *Advanced Computer Simulation*, pp. 105–149 (2005).

[130] H. J. C. Berendsen. "Transport properties computed by linear response through weak coupling to a bath". *Computer Simulations in Material Science*. Ed. by Kluwer, pp. 139–155 (1991).

[131] D. Lide. *CRC: Handbook of Chemistry and Physics, 88^{th} edition*. CRC Press/ Taylor and Francis, 2007.

[132] M. Parrinello and A. Rahman. "Polymorphic transitions in single crystals: A new molecular dynamics method". *Journal of Applied Physics*, vol. 52, no. 12, pp. 7182–7190 (1981).

[133] S. Nosé and M. L. Klein. "Constant pressure molecular dynamics for molecular systems". *Molecular Physics*, vol. 50, no. 5, pp. 1055–1076 (1983).

[134] T. Schneider and E. Stoll. "Molecular-dynamics study of a three-dimensional one-component model for distortive phase transitions". *Physical Review B*, vol. 17, no. 3, p. 1302 (1978).

[135] T. Schneider and E. Stoll. "Molecular-dynamics study of second sound". *Physical Review B*, vol. 18, no. 12, p. 6468 (1978).

[136] W. van Gunsteren and H. Berendsen. "A leap-frog algorithm for stochastic dynamics". *Molecular Simulation*, vol. 1, no. 3, pp. 173–185 (1988).

[137] H. C. Andersen. "Molecular dynamics at constant temperature and/or pressure". *The Journal of Chemical Physics*, vol. 72, p. 2384 (1980).

[138] P. Young. *The leapfrog method and other "symplectic" algorithms for integrating Newton's laws of motion*. Lecture notes in University of California, Santa Cruz. 2013. URL: `http://physics.ucsc.edu/~peter/242/leapfrog.pdf`.

[139] E. Hairer, C. Lubich, and G. Wanner. "Geometric numerical integration illustrated by the Störmer/Verlet method". *Acta Numerica*, vol. 12, pp. 399–450 (2003).

[140] H. Berendsen and W. Van Gunsteren. "Practical algorithms for dynamic simulations". *Molecular-Dynamics Simulation of Statistical-Mechanical Systems, North-Holland, Amsterdam*, pp. 43–65 (1986).

[141] R. W. Hockney and J. W. Eastwood. *Computer simulation using particles*. McGraw-Hill, 1981.

[142] W. C. Swope, H. C. Andersen, P. H. Berens, and K. R. Wilson. "A computer simulation method for the calculation of equilibrium constants for the formation of physical clusters of molecules: Application to small water clusters". *The Journal of Chemical Physics*, vol. 76, no. 1, pp. 637–649 (1982).

[143] B. Hess, C. Kutzner, D. van der Spoel, and E. Lindahl. "GROMACS 4: Algorithms for highly efficient, load-balanced, and scalable molecular simulation". *Journal of Chemical Theory and Computation*, vol. 4, no. 3, pp. 435–447 (2008).

[144] URL: `http://www.gromacs.org`.

[145] J.-P. Ryckaert and A. Bellemans. "Molecular dynamics of liquid alkanes". *Faraday Discussions of the Chemical Society*, vol. 66, pp. 95–106 (1978).

[146] J. Chang, J. Han, L. Yang, R. L. Jaffe, and D. Y. Yoon. "Structure and properties of polymethylene melt surfaces from molecular dynamics simulations". *The Journal of Chemical Physics*, vol. 115, p. 2831 (2001).

[147] D. E. Williams. "Nonbonded potential parameters derived from crystalline hydrocarbons". *The Journal of Chemical Physics*, vol. 47, p. 4680 (1967).

[148] W. L. Jorgensen, D. S. Maxwell, and J. Tirado-Rives. "Development and testing of the OPLS all-atom force field on conformational energetics and properties of organic liquids". *Journal of the American Chemical Society*, vol. 118, no. 45, pp. 11225–11236 (1996).

[149] L. L. Thomas, T. J. Christakis, and W. L. Jorgensen. "Conformation of alkanes in the gas phase and pure liquids". *The Journal of Physical Chemistry B*, vol. 110, no. 42, pp. 21198–21204 (2006).

[150] B. Chen, M. G. Martin, and J. I. Siepmann. "Thermodynamic properties of the williams, opls-aa, and mmff94 all-atom force fields for normal alkanes". *The Journal of Physical Chemistry B*, vol. 102, no. 14, pp. 2578–2586 (1998).

[151] B. Chen and J. I. Siepmann. "Transferable potentials for phase equilibria. 3. Explicit-hydrogen description of normal alkanes". *The Journal of Physical Chemistry B*, vol. 103, no. 25, pp. 5370–5379 (1999).

[152] S. W. Siu, K. Pluhackova, and R. A. Böckmann. "Optimization of the OPLS-AA Force Field for Long Hydrocarbons". *Journal of Chemical Theory and Computation*, vol. 8, no. 4, p. 1459 (2012).

[153] J. Chang and S. I. Sandler. "Interatomic Lennard-Jones potentials of linear and branched alkanes calibrated by Gibbs ensemble simulations for vapor-liquid equilibria". *The Journal of Chemical Physics*, vol. 121, p. 7474 (2004).

[154] R. A. Böckmann. Friedrich-Alexander-Universität Erlangen-Nürnberg. Private communication.

[155] URL: `http://www.pymol.org`.

[156] T. Darden, D. York, and L. Pedersen. "Particle mesh Ewald: An Nâ log (N) method for Ewald sums in large systems". *The Journal of Chemical Physics*, vol. 98, p. 10089 (1993).

[157] K. Hinsen. CNRS Orleans (France). Private communication.

[158] W. Humphrey, A. Dalke, and K. Schulten. "VMD: visual molecular dynamics". *Journal of Molecular Graphics*, vol. 14, no. 1, pp. 33–38 (1996).

[159] G. R. Kneller, V. Keiner, M. Kneller, and M. Schiller. "*n*MOLDYN: A program package for a neutron scattering oriented analysis of Molecular Dynamics simulations". *Computer Physics Communications*, vol. 91, no. 1, pp. 191–214 (1995).

[160] T. Róg, K. Murzyn, K. Hinsen, and G. R. Kneller. "nMoldyn: A program package for a neutron scattering oriented analysis of molecular dynamics simulations". *Journal of Computational Chemistry*, vol. 24, no. 5, pp. 657–667 (2003).

[161] E. O. Brigham. *The Fast Fourier Transform*. Prentice-Hall, Inc., 1974.

[162] V. Calandrini, P. Calligari, K. Hinsen, and G. R. Kneller. *nMOLDYN: User's Guide*. 2006. URL: `http://dirac.cnrs-orleans.fr/plone/software/nmoldyn/nmoldyn_user_guide.pdf`.

[163] M. Wolff, B. Frick, A. Magerl, and H. Zabel. "Flow cell for neutron spectroscopy". *Physical Chemistry Chemical Physics*, vol. 7, no. 6, pp. 1262–1265 (2005).

[164] G. Williams and D. C. Watts. "Non-symmetrical dielectric relaxation behaviour arising from a simple empirical decay function". *Trans. Faraday Soc.* Vol. 66, pp. 80–85 (1970).

[165] R. Bergman, F. Alvarez, A. Alegria, and J. Colmenero. "The merging of the dielectric α-and β-relaxations in poly-(methyl methacrylate)". *The Journal of Chemical Physics*, vol. 109, p. 7546 (1998).

[166] A. Triolo, O. Russina, V. Arrighi, F. Juranyi, S. Janssen, and C. M. Gordon. "Quasielastic neutron scattering characterization of the relaxation processes in a room temperature ionic liquid". *The Journal of Chemical Physics*, vol. 119, p. 8549 (2003).

[167] K. Binder and W. Kob. *Glassy materials and disordered solids: An introduction to their statistical mechanics*. World Scientific Publishing Co. Pte. Ltd., 2011.

[168] H. Morhenn, S. Busch, and T. Unruh. "Chain dynamics in a hexadecane melt as seen by neutron scattering and identified by molecular dynamics simulations". *Journal of Physics: Condensed Matter*, vol. 24, no. 37, p. 375108 (2012).

[169] A. Arbe and J. Colmenero. "Characterization of the "simple-liquid" state in a polymeric system: Coherent and incoherent scattering functions". *Physical Review E*, vol. 80, no. 4, p. 041805 (2009).

[170] M. Bée. "A physical insight into the elastic incoherent structure factor". *Physica B: Condensed Matter*, vol. 182, no. 4, pp. 323–336 (1992).

[171] S. Busch and T. Unruh. "The slow short-time motions of phospholipid molecules with a focus on the influence of multiple scattering and fitting artefacts". *Journal of Physics: Condensed Matter*, vol. 23, no. 25, p. 254205 (2011).

[172] D. S. Pearson, G. Ver Strate, E. von Meerwall, and F. C. Schilling. "Viscosity and self-diffusion coefficient of linear polyethylene". *Macromolecules*, vol. 20, no. 5, pp. 1133–1141 (1987).

[173] D. S. Pearson, L. J. Fetters, W. W. Graessley, G. Ver Strate, and E. von Meerwall. "Viscosity and self-diffusion coefficient of hydrogenated polybutadiene". *Macromolecules*, vol. 27, no. 3, pp. 711–719 (1994).

[174] D. Richter, L. Willner, A. Zirkel, B. Farago, L. J. Fetters, and J. S. Huang. "Polymer motion at the crossover from Rouse to reptation dynamics". *Macromolecules*, vol. 27, no. 25, pp. 7437–7446 (1994).

[175] M. Appel and G. Fleischer. "Investigation of the chain length dependence of self-diffusion of poly(dimethylsiloxane) and poly(ethylene oxide) in the melt with pulsed field gradient NMR". *Macromolecules*, vol. 26, no. 20, pp. 5520–5525 (1993).

[176] S. Z. D. Cheng, J. S. Barley, and E. D. von Meerwall. "Self-Diffusion of Poly(ethylene Oxide) Fractions and Its Influence on the Crystalline Texture". *Journal of Polymer Science Part B: Polymer Physics*, vol. 29, no. 5, pp. 515–525 (1991).

[177] H. Berendsen. "The eternal truth of physics". Presented at the First Annual NBIA Meeting on ESS Science, Copenhagen, Denmark. 2011. URL: `https://indico.nbi.ku.dk/conferenceDisplay.py?confId=291`.

[178] H. Morhenn, S. Busch, H. Meyer, D. Richter, W. Petry, and T. Unruh. "Collective Intermolecular Motions Dominate the Picosecond Dynamics of Short Polymer Chains". *Physical Review Letters*, vol. 111, no. 17, p. 173003 (2013).

[179] R. Wilhoit, X. Hong, K. Marsh, and W. Martienssen. *Landolt-Börnstein: Physical Chemistry: Thermodynamic Properties of Organic Compounds and Their Mixtures, Subvolume B, Densities of Aliphatic Hydrocarbons: Alkanes.* Springer, 1996.

[180] Y. Yonetani. "Liquid water simulation: A critical examination of cutoff length". *The Journal of chemical physics*, vol. 124, p. 204501 (2006).

[181] M. Aichele, Y. Gebremichael, F. Starr, J. Baschnagel, and S. Glotzer. "String-like correlated motion in the dynamics of supercooled polymer melts". *Journal of Chemical Physics*, vol. 119, pp. 5290–5304 (2003).

[182] M. S. Shell, P. G. Debenedetti, and F. H. Stillinger. "Dynamic heterogeneity and non-Gaussian behaviour in a model supercooled liquid". *Journal of Physics: Condensed Matter*, vol. 17, no. 49, p. 4035 (2005).

[183] J. Colmenero, F. Alvarez, and A. Arbe. "Self-motion and the α relaxation in a simulated glass-forming polymer: Crossover from Gaussian to non-Gaussian dynamic behavior". *Physical Review E*, vol. 65, no. 4, p. 041804 (2002).

[184] M. Brodeck. "A Study of Polymer Melts Combining MD Simulations and Neutron Scattering Experiments". PhD thesis. Westfälische Wilhelms-Universität Münster, 2009.

[185] C. Smuda, G. Gemmecker, and T. Unruh. "Quasielastic and inelastic neutron scattering study of methyl group rotation in solid and liquid pentafluoroanisole and pentafluorotoluene". *The Journal of Chemical Physics*, vol. 128, p. 194502 (2008).

[186] C. Smuda, S. Busch, B. Wagner, and T. Unruh. "Methyl group dynamics in glassy, polycrystalline, and liquid coenzyme Q_{10} studied by quasielastic neutron scattering". *The Journal of Chemical Physics*, vol. 129, p. 074507 (2008).

[187] C. Smuda, S. Busch, R. Schellenberg, and T. Unruh. "Methyl Group Dynamics in Polycrystalline and Liquid Ubiquinone Q_0 Studied by Neutron Scattering". *The Journal of Physical Chemistry B*, vol. 113, no. 4, pp. 916–922 (2009).

[188] A. N. Semenov and H. Meyer. "Anomalous diffusion in polymer monolayers". *Soft Matter*, vol. 9, no. 16, pp. 4249–4272 (2013).

[189] M. Brodeck, F. Alvarez, A. J. Moreno, J. Colmenero, and D. Richter. "Chain Motion in Nonentangled Dynamically Asymmetric Polymer Blends: Comparison between Atomistic Simulations of PEO/PMMA and a Generic Bead-Spring Model". *Macromolecules*, vol. 43, no. 6, pp. 3036–3051 (2010).

[190] H. Takeuchi and K. Okazaki. "Molecular dynamics simulation of diffusion of simple gas molecules in a short chain polymer". *The Journal of Chemical Physics*, vol. 92, no. 9, pp. 5643–5652 (1990).

[191] J. Clarke and D. Brown. "Molecular dynamics computer simulation of chain molecule liquids". *Molecular Physics*, vol. 58, no. 4, pp. 815–825 (1986).

[192] R. H. Boyd, R. H. Gee, J. Han, and Y. Jin. "Conformational dynamics in bulk polyethylene: A molecular dynamics simulation study". *The Journal of Chemical Physics*, vol. 101, p. 788 (1994).

[193] G. F. Signorini, J.-L. Barrat, and M. L. Klein. "Structural relaxation and dynamical correlations in a molten state near the liquid–glass transition: A molecular dynamics study". *The Journal of Chemical Physics*, vol. 92, p. 1294 (1990).

[194] T. Unruh. *Structure and dynamics of colloidal dispersions on molecular scale.* Habilitation thesis, Technische Univerität München. 2010.

[195] S. W. Provencher. "CONTIN: a general purpose constrained regularization program for inverting noisy linear algebraic and integral equations". *Computer Physics Communications*, vol. 27, no. 3, pp. 229–242 (1982).

[196] T. Kikuchi, K. Nakajima, S. Ohira-Kawamura, Y. Inamura, O. Yamamuro, M. Kofu, Y. Kawakita, K. Suszya, M. Nakamura, and M. Arai. "Mode Distribution Analysis: A New Method for Model-free Analysis on Quasi-elastic Neutron Scattering". Presented at the Tenth International Conference on Quasielastic Neutron Scattering (QENS 2012), Nikko, Japan. 2012. URL: `http://j-parc.jp/researcher/MatLife/en/meetings/QENS-WINS2012/index.html`.

[197] D. M. Whitley and D. B. Adolf. "Local segmental dynamics of cis-1,4-polybutadiene, polypropylene and polyethylene terephthalate via molecular dynamics simulations". *Molecular Simulation*, vol. 38, no. 2, pp. 119–123 (2012).

[198] K. Karatasos and D. Adolf. "Slow modes in local polymer dynamics". *The Journal of Chemical Physics*, vol. 112, p. 8225 (2000).

[199] K. Karatasos and J.-P. Ryckaert. "Local dynamics of polyisobutylene revisited". *Macromolecules*, vol. 34, no. 21, pp. 7232–7235 (2001).

[200] S. Hotston, D. Adolf, and K. Karatasos. "An investigation into the local segmental dynamics of polyethylene: An isothermal/isobaric molecular dynamics study". *The Journal of Chemical Physics*, vol. 115, p. 2359 (2001).

[201] S. Busch and T. Unruh. "The influence of additives on the nanoscopic dynamics of the phospholipid dimyristoylphosphatidylcholine". *Biochimica et Biophysica Acta (BBA)-Biomembranes*, vol. 1808, no. 1, pp. 199–208 (2011).

[202] L. Berthier. "Dynamic Heterogeneity in Amorphous Materials". *Physics*, vol. 4, p. 42 (2011).

[203] C. Donati, J. F. Douglas, W. Kob, S. J. Plimpton, P. H. Poole, and S. C. Glotzer. "Stringlike Cooperative Motion in a Supercooled Liquid". *Physical Review Letters*, vol. 80, no. 11, pp. 2338–2341 (1998).

[204] F. W. Starr and J. F. Douglas. "Modifying Fragility and Collective Motion in Polymer Melts with Nanoparticles". *Physical Review Letters*, vol. 106, no. 11, p. 115702 (2011).

Appendix

A Python Scripts

This section lists the python scripts that were used to extract information from the simulated dynamics. The ASCII input files were generated as described in section 5.4. Note that all comments in the input file need to be deleted before starting any of the following scripts.

A.1 Non-Gaussian parameter

Calculates the non-Gaussian parameter, according to equation 4.23 on a logarithmic x-grid. Call the script with the total number of timesteps, total number of molecules, and number of xyz-coordinates per molecule in the input file (e. g. 1 for center-of-mass coordinates) as:

`python ngp.py trajectory_pbc.xvg` (#timesteps) (#molecules) (#coordinates per molecule)

Content of ngp.py:

```
#! /usr/bin/env python
import sys
from scipy import *
from matplotlib.pyplot import *

filein=sys.argv[1]
par={}
par['#t'] = int(sys.argv[2])
par['#mol'] = int(sys.argv[3])
par['#coord/mol'] = int(sys.argv[4])

a=reshape(fromfile(filein,dtype=float,sep=" "),
          (par['#t'],par['#mol']*par['#coord/mol']*3+1))

mol=par['#coord/mol']*par['#mol']

factor=1.1
```

```
xtime=0.1
ttime=[]

aaa=[]
for ti in range(101):
    aaa.append([])

while ceil(xtime*factor)<100:
    xtime=ceil(xtime*factor)
    ttime.append(a[xtime][0])
    for j in range(0,par['#t']/2,1):
        zaehler=0.
        nenner=0.
        jtime=j+xtime
        b=a[jtime]-a[j]
        b=b[1:].reshape((len(b[1:])/3,3))
        zaehlertemp = (b**2).sum(axis=1)
        nennertemp = zaehlertemp
        zaehlertemp = zaehlertemp**2
        zaehler = zaehlertemp.sum()
        nenner = nennertemp.sum()
        nenner=nenner**2
        aaa[int(xtime)].append((3./5.*zaehler/nenner*mol)-1)

NGP=[]
errNGP=[]

for ti in range(len(aaa)):
    if aaa[ti]!=[]:
        NGP.append(average(aaa[ti]))
        errNGP.append(std(aaa[ti],ddof=1))

errorbar(ttime,NGP,yerr=errNGP)
xscale('log')
show()
```

A.2 End-to-End and Carbon-Carbon Vector Orientation Autocorrelation Function

Calculates the autocorrelation function for the reorientation of the end-to-end vector and the single backbone bonds, according to equations 7.4, 7.5 and 7.8. The output is saved using the packages chaste and sihl (http://www.thamnos.de/repos/).
Call the script with the total number of timesteps, total number of molecules, and total number of backbone bonds as:

`python cpos.py trajectory_carbon_pbc.xvg` (#timesteps) (#molecules) (backbone chain length)

Content of cpos.py:

```
#! /usr/bin/env python
import sys
from scipy import *
from chaste import Dataset, Data
from sihl.general import Measurement

filein=sys.argv[1]
timesteps=int(sys.argv[2])
molecule=int(sys.argv[3])
cl=int(sys.argv[4])

a=reshape(fromfile(filein,dtype=float,sep=" "),
          (timesteps,cl*molecule*3+1))

xlist={2:{},100:{}}
for x in xlist:
    for i in range(1,cl/x,1):
        xlist[x][i]=[i,cl-i]
    xlist[x][cl/x]=[cl/x]

length=timesteps/2
time=[]

factor=1.01
xtime=0.1
while ceil(xtime*factor)<length:
    xtime=ceil(xtime*factor)
    time.append(a[xtime][0])

for x in xlist:
```

```
g=Measurement(name="")
g.whatis['x']=['t','ps']
g.whatis['y']=['C(t)1','']
g.whatis['z']=['cpos','']
h=Measurement(name="")
h.whatis['x']=['t','ps']
h.whatis['y']=['C(t)2','']
h.whatis['z']=['cpos','']
for ci in xlist[x]:
    sca1=[]
    sca2=[]
    err1=[]
    err2=[]
    aaa1=[]
    aaa2=[]
    for i in range(length):
        aaa1.append([])
        aaa2.append([])
    for t0 in range(length):
        xtime=0.1
        while ceil(xtime*factor)<length:
            xtime=ceil(xtime*factor)
            ti=xtime
            bbb1=0
            bbb2=0
            for m in range(molecule):
                for c in xlist[x][ci][0]:
                    cx=c+x-1
                    t1=ti+t0
                    dist0=((float(a[t0][c*1+(cl*3)*m])
                          -float(a[t0][cx*1+(cl*3)*m]))**2
                        +(float(a[t0][c*2+(cl*3)*m])
                          -float(a[t0][cx*2+(cl*3)*m]))**2
                        +(float(a[t0][c*3+(cl*3)*m])-
                          -float(a[t0][cx*3+(cl*3)*m]))**2)**0.5
                    e0x=(float(a[t0][c*1+(cl*3)*m])
                          -float(a[t0][cx*3-2+(cl*3)*m]))/dist0
                    e0y=(float(a[t0][c*2+(cl*3)*m])
                          -float(a[t0][cx*3-1+(cl*3)*m]))/dsti0
                    e0z=(float(a[t0][c*3+(cl*3)*m])
                          -float(a[t0][cx*3-0+(cl*3)*m]))/dist0
                    dist1=((float(a[t1][c*3-2+(cl*3)*m])
                          -float(a[t1][cx*3-2+(cl*3)*m]))**2
                        +(float(a[t1][c*3-1+(cl*3)*m])
```

```
                                -float(a[t1][cx*3-1+(cl*3)*m]))**2
                            +(float(a[t1][c*3-0+(cl*3)*m])
                                -float(a[t1][cx*3-0+(cl*3)*m]))**2)**0.5
                        e1x=(float(a[t1][c*3-2+(cl*3)*m])
                                -float(a[t1][cx*3-2+(cl*3)*m]))/dist1
                        e1y=(float(a[t1][c*3-1+(cl*3)*m])
                                -float(a[t1][cx*3-1+(cl*3)*m]))/dist1
                        e1z=(float(a[t1][c*3-0+(cl*3)*m])
                                -float(a[t1][cx*3-0+(cl*3)*m]))/dist1
                        do=(e1x*e0x+e1y*e0y+e1z*e0z)
                        bbb1+=do
                        bbb2+=(do**2)
                rel=molecule/len(xlist[x][ci][0])
                aaa1[int(ti)].append(bbb1/rel)
                aaa2[int(ti)].append(0.5*(3*(bbb2/rel)-1))
    for ti in range(length):
        if aaa1[ti]!=[]:
            sca1.append(average(aaa1[ti]))
        if aaa1[ti]!=[]:
            err1.append(std(aaa1[ti],ddof=1))
        if aaa2[ti]!=[]:
            sca2.append(average(aaa2[ti]))
        if aaa2[ti]!=[]:
            err2.append(std(aaa2[ti],ddof=1))
    g.append(Dataset(x=time,y=sca1,dy=err1,z=ci))
    h.append(Dataset(x=time,y=sca2,dy=err2,z=ci))
del g[0]
g.write_i96(str(filein[:-4])+"_P1_1_"+str(x))
del h[0]
h.write_i96(str(filein[:-4])+"_P2_1_"+str(x))
```

A.3 Dihedral Autocorrelation Function

Calculates the C-C-C-C torsional angle autocorrelation function, according to equation 7.3, for all dihedrals along the molecular backbone. The output is saved using the packages chaste and sihl (http://www.thamnos.de/repos/). Call the script with the total number of timesteps, total numper of molecules, and total number of backbone atoms as:

`python dihedral.py trajectory_carbon_pbc.xvg` (#timesteps) (#molecules) (backbone chain length)

Content of dihedral.py:

```
#! /usr/bin/env python
import sys
from chaste import Dataset, Data
from sihl.general import Measurement
from scipy import *
from matplotlib.pyplot import *

filein=sys.argv[1]
timesteps=int(sys.argv[2])
molecule=int(sys.argv[3])
chainlength=int(sys.argv[4])

a=reshape(fromfile(filein,dtype=float,sep=" "),
          (timesteps,cl*molecule*3+1))

length=timesteps/2
chlist=range(1,chainlength-2,1)

g=Measurement(name="")
g.whatis['x']=['t','ps']
g.whatis['y']=['C(t)','']
g.whatis['z']=['position','']

time=[]
factor=1.1
xtime=0.1
while ceil(xtime*factor)<length:
    xtime=ceil(xtime*factor)
    time.append(a[xtime][0])

def dihedralangle(a,i,mol,chpos,chainlength,deg):
    """
```

```
    call with
    a: xyz carbon file
    i: timestep
    mol: which molecule (starting with 1)
    chpos: which position (1 chain end)
    number of backbone atoms of a molecule
    deg: in deg (1) or rad (0)
    """
    mol=(mol-1)*chainlength*3
    b1x=float(a[i][mol+chpos*3+1])-float(a[i][mol+chpos*3-2])
    b1y=float(a[i][mol+chpos*3+2])-float(a[i][mol+chpos*3-1])
    b1z=float(a[i][mol+chpos*3+3])-float(a[i][mol+chpos*3-0])
    b1=array((b1x,b1y,b1z))
    b2x=float(a[i][mol+chpos*3+4])-float(a[i][mol+chpos*3+1])
    b2y=float(a[i][mol+chpos*3+5])-float(a[i][mol+chpos*3+2])
    b2z=float(a[i][mol+chpos*3+6])-float(a[i][mol+chpos*3+3])
    b2=array((b2x,b2y,b2z))
    b3x=float(a[i][mol+chpos*3+7])-float(a[i][mol+chpos*3+4])
    b3y=float(a[i][mol+chpos*3+8])-float(a[i][mol+chpos*3+5])
    b3z=float(a[i][mol+chpos*3+9])-float(a[i][mol+chpos*3+6])
    b3=array((b3x,b3y,b3z))
    x1x=b1y*b2z-b1z*b2y
    x1y=b1z*b2x-b1x*b2z
    x1z=b1x*b2y-b1y*b2x
    x1=array((x1x,x1y,x1z))
    x2x=b2y*b3z-b2z*b3y
    x2y=b2z*b3x-b2x*b3z
    x2z=b2x*b3y-b2y*b3x
    x2=array((x2x,x2y,x2z))
    n1=x1/((x1x**2+x1y**2+x1z**2)**0.5)
    n2=x2/((x2x**2+x2y**2+x2z**2)**0.5)
    aaa=n1[0]*n2[0]+n1[1]*n2[1]+n1[2]*n2[2]
    ang=(arccos(aaa))
    if deg == 1:
        ang=degrees(arccos(aaa))
    else:
        ang=arccos(aaa)
    return ang

corlist=[]
errlist=[]
for ch in chlist:
    print ch
    out=[]
```

```
    for ti in range(length):
        out.append([])
    for t0 in range(length):
        xtime=0.1
        while ceil(xtime*factor)<length:
            xtime=ceil(xtime*factor)
            ti=xtime
            t1=ti+t0
            bbb1=0
            bbb2=0
            bbb3=0
            for m in range(molecule):
                m=m+1
                cos0=cos(dihedralangle(a,t0,m,ch,chainlength,0))
                cost=cos(dihedralangle(a,t1,m,ch,chainlength,0))
                bbb1+=(cost*cos0)
                bbb2+=cos0
                bbb3+=cos0*cos0
            bbb1/=m
            bbb2/=m
            bbb3/=m
            do1=bbb1-bbb2**2
            do2=bbb3-bbb2**2
            out[int(ti)].append(do1/do2)
    cor=[]
    err=[]
    for ti in range(length):
        if out[ti]!=[]:
            cor.append(average(out[ti]))
            err.append(std(out[ti],ddof=1))
    corlist.append(cor)
    errlist.append(err)

for i in range(len(corlist)):
    g.append(Dataset(x=time,y=corlist[i],dy=errlist[i],z=chlist[i]))

del g[0]
g.write_i96(str(filein[:-4])+"dih")
```

A.4 Higher-Order Dynamic Correlation Functions

Respective equation 7.11, this script calculates the scalar products of unit displacements vectors of nearest intermolecular neighbors. The output is saved using the packages chaste and sihl (http://www.thamnos.de/repos/). Call the script with the total number of timesteps, total number of molecules, and the total number of backbone atoms as:

`python sca.py trajectory_carbon_pbc.xvg` (#timesteps) (#molecules) (backbone chain length)

Content of sca.py:

```
#! /usr/bin/env python
from scipy import *
from chaste import Dataset, Data
from sihl.general import Measurement
from random import choice

filein=sys.argv[1]

par={}
par['#t'] = int(sys.argv[2])
par['#mol'] = int(sys.argv[3])
par['#coord/mol'] = int(sys.argv[4])

a=reshape(fromfile(filein,dtype=float,sep=" "),
          (par['#t'],par['#mol']*par['#coord/mol']*3+1))

mlist=[]
for m in range(par['#mol']):
    for c in range(par['#coord/mol']):
        mlist.append(m)
mlist=array(mlist)

out=[]
counterlist=[]
for i in range(len(a)):
    out.append(0)
    counterlist.append(0)

dlist=[]

for m1 in range(par['#mol'] ):
    c1=choice(range(par['#coord/mol']))
```

```
    aa=m1*par['#coord/mol']+c1
    for t0 in range(len(a)):
        a0      =   a[t0][1:].reshape((len(a[t0][1:])/3,3))
        aa0 =   a0[aa]
        dl      = array((((a0 - aa0)**2).sum(axis=1))**0.5)
        bb=(ma.array(dl,mask=(mlist == m1))).argmin()
        dlist.append(dl[bb])
        bb0 =   a0[bb]
        for taustep in range(1,len(a)):
            ti=t0+taustep
            if ti >= par['#t']:
                break
            else:
                anow    = a[ti][1:].reshape((len(a[ti][1:])/3,3))
                aa1     = anow[aa]
                aar     = aa1-aa0
                aare    = aar/(((aar**2).sum())**.5)
                bb1     = anow[bb]
                bbr     = bb1-bb0
                bbre    = bbr/(((bbr**2).sum())**.5)
                skalar  = (aare*bbre).sum()
                out[taustep]+=skalar
                counterlist[taustep]+=1

tauscale=[]
ave=[]
err=[]

for taustep in range(len(a)):
    tauscale.append(a[taustep][0])
    if counterlist[taustep]==0.:
        ave.append(0)
    else:
        ave.append(out[taustep]/counterlist[taustep])

g=Measurement(name="")
g.append(Dataset(x=tauscale,y=ave))

del g[0]
g.whatis['x']=['tau','ps']
g.whatis['y']=['s(tau)','']
g.whatis['z']=['','']
g.write_i96(filein[:-4]+"inter_scalar")
```

A.5 Modified Static Structure Factor from Coherent Scattering Function

Calculates the modified static structure factor from the simulated scattering functions, as explained in section 5.4. The input $\mathcal{S}_{\mathrm{coh}}(Q, w)$ should be in the Frida1 format. The input and output files are handled using the packages chaste and sihl (http://www.thamnos.de/repos/). The resulting intensities must be multiplied with the stepsize of energy transfer $\mathrm{d}E_f$. Call the script with the neutron wave length of the experimental setup as:

`python modify_sq.py Sqw.i96` (neutron wave length)

Content of modify_sq.py:

```
#!/usr/bin/env python
from scipy import *
from chaste import Dataset, Data
from sihl.general import Measurement

filein=sys.argv[1]
laa=sys.argv[2]

ki=2*pi/laa
Ei=81.81/laa**2
hbar=1.05457173e-34
m=1.674927351e-27
h=6.62606957e-34
el=1.602176565e-19
Efactor=h**2/2/m/el/(1e-3)/(1e-20)
kfactor=Efactor/(2*pi)**2

g=Measurement(name="")
g.read_i96(filein)

factor=int(round(1./(float(g.z[len(g.z)/2][0]-g.z[len(g.z)/2-1][0]))))
moddata=zeros((len(g.z)*2))

for i in range(len(g.z)):
    q=round(g.z[i][0],5)
    elist=g.x[i]
    vlist=g.y[i]
    for j in range(len(elist)):
        e=elist[j]
        Ef=Ei+e
```

```
            if Ef<=0.:
                continue
            kf=(Ef/kfactor)**.5
            temp=(ki**2+kf**2-q**2)/(2*ki*kf)
            try:
                deg=degrees(arccos(temp))
            except:
                continue
            q_elastic=4*pi/laa*sin(radians(deg/2))
            vlist[j]=vlist[j]*kf/ki
            moddata[int(round(q_elastic*factor))]+=vlist[j]

qlist=[]
for i in range(len(moddata)):
    qlist.append(float(i)/factor)

h=Measurement(name="")
h.append(Dataset(x=qlist,y=moddata))
del h[0]
h.whatis['x']=['Q','AA-1']
h.whatis['y']=['S(Q)','']
h.whatis['z']=['','']
h.write_i96(filein[:-4]+"mod")
```

B Simulation Parameters

In the following two specific GROMACS simulation input files used in this thesis are given. The first one was applied with the force field parameters of Chang & Sandler [153]. The second input file was used in combination with the L-OPLS force field of Siu et al. [152].

Specific simulation parameters as e. g. simulation length, output frequency, temperature and pressure coupling were applied as described in section 5.3.

B.1 changsandler.mdp

```
; RUN CONTROL PARAMETERS
integrator               = md
; mode for center of mass motion removal
comm-mode                = Linear
; number of steps for center of mass motion removal
nstcomm                  = 1

; NEIGHBORSEARCHING PARAMETERS
; nblist update frequency
nstlist                  = 10
; ns algorithm (simple or grid)
ns_type                  = grid
; Periodic boundary conditions: xyz, no, xy
pbc                      = xyz
periodic_molecules       = no
; nblist cut-off
rlist                    = 1.0
; long-range cut-off for switched potentials
rlistlong                = -1

; OPTIONS FOR ELECTROSTATICS AND VDW
; Method for doing electrostatics
coulombtype              = PME
```

```
rcoulomb-switch          = 0
rcoulomb                 = 1.0
; Relative dielectric constant for the medium and the reaction field
epsilon_r                = 1
epsilon_rf               = 1
; Method for doing Van der Waals
vdw-type                 = Cut-off
; cut-off lengths
rvdw-switch              = 0
rvdw                     = 2.0
; Apply long range dispersion corrections for Energy and Pressure
DispCorr                 = No
; Extension of the potential lookup tables beyond the cut-off
table-extension          = 1
; Seperate tables between energy group pairs
energygrp_table          =
; Spacing for the PME/PPPM FFT grid
fourierspacing           = 0.15
; FFT grid size, when a value is 0 fourierspacing will be used
fourier_nx               = 0
fourier_ny               = 0
fourier_nz               = 0
; EWALD/PME/PPPM parameters
pme_order                = 4
ewald_rtol               = 1e-5
ewald_geometry           = 3d
epsilon_surface          = 0
optimize_fft             = yes
```

B.2 siu.mdp

```
; RUN CONTROL PARAMETERS
integrator               = md
; mode for center of mass motion removal
comm-mode                = Linear
; number of steps for center of mass motion removal
nstcomm                  = 1

; NEIGHBORSEARCHING PARAMETERS
; nblist update frequency
nstlist                  = 10
; ns algorithm (simple or grid)
ns_type                  = grid
; Periodic boundary conditions: xyz, no, xy
pbc                      = xyz
periodic_molecules       = no
; nblist cut-off
rlist                    = 1.5
; long-range cut-off for switched potentials
rlistlong                = 2.0

; OPTIONS FOR ELECTROSTATICS AND VDW
; Method for doing electrostatics
coulombtype              = PME
rcoulomb-switch          = 0
rcoulomb                 = 1.5
; Relative dielectric constant for the medium and the reaction field
epsilon_r                = 1
epsilon_rf               = 1
; Method for doing Van der Waals
vdw-type                 = switch
; cut-off lengths
rvdw-switch              = 1.1
rvdw                     = 1.3
; Apply long range dispersion corrections for Energy and Pressure
DispCorr                 = EnerPres
; Extension of the potential lookup tables beyond the cut-off
table-extension          = 1
; Seperate tables between energy group pairs
energygrp_table          =
; Spacing for the PME/PPPM FFT grid
fourierspacing           = 0.12
; FFT grid size, when a value is 0 fourierspacing will be used
```

```
fourier_nx                = 0
fourier_ny                = 0
fourier_nz                = 0
; EWALD/PME/PPPM parameters
pme_order                 = 4
ewald_rtol                = 1e-5
ewald_geometry            = 3d
epsilon_surface           = 0
optimize_fft              = yes
```

Acknowledgements

First of all I would like to thank Prof. Winfried Petry for giving me the opportunity to write this thesis at the Heinz Maier-Leibnitz Zentrum (MLZ), for his constant interest in my studies and supervision of my research. I also thank Prof. Martin Zacharias, who accepted to chair this dissertation.

I would like to thank Prof. Tobias Unruh for introducing me to neutron scattering and soft matter physics. I highly appreciate his support and enjoyed our fruitful discussions. In particular I thank Sebastian Busch for practically introducing me to neutron scattering, efficient data treatment and for his willingness to discuss any topic with me.

I would like to thank Marie-Sousai Appavou for the friendly company during lunches, Jean-François Moulin for supporting me with advanced scripting, and Wolfgang Häussler for an open ear, tips and explanations.

The scientists and technicians at TOFTOF and DNS helped alot during the neutron scattering experiments and data evaluation, I appreciate their support. Most of the simulations were performed at the Leibniz-Rechenzentrum (LRZ) der Bayerischen Akademie der Wissenschaften. I am grateful for the support during the simulations and for millions of CPU hours granted on both the Linux-Cluster and SuperMUC, the 3 PetaFLOP/s machine at LRZ.

I further appreciate the cooperation with Hendrik Meyer, who explained and discussed the theoretical framework of hydrodynamic interactions with me, and with Prof. Rainer Böckmann, who supported my simulation efforts. I especially thank Prof. Dieter Richter for stimulating discussions and many supporting information to tackle polymer dynamics.

Friederike Rust supported my research during her seminar work with great experimental dexterity, I am very thankful for her assistance.

I finally would like to thank my collegues from the Lehrstuhl für Kristallographie und Strukturphysik, the chair E13 at the physics department of the TUM, the

positron group of the MLZ and the students of JCNS for the great atmosphere in Erlangen, Garching and any conference or workshop where we met.

The financial support by the DFG (grant UN267/4-1) is gratefully acknowledged.